FEM SOLUTIONS OF MAGNETOHYDRODYNAMIC AND BIOMAGNETIC
FLUID FLOWS IN CHANNELS

A THESIS SUBMITTED TO
THE GRADUATE SCHOOL OF APPLIED MATHEMATICS
OF
MIDDLE EAST TECHNICAL UNIVERSITY

BY

ÖNDER TÜRK

IN PARTIAL FULFILLMENT OF THE REQUIREMENTS
FOR
THE DEGREE OF DOCTOR OF PHILOSOPHY
IN
SCIENTIFIC COMPUTING

JANUARY 2014

Approval of the thesis:

FEM SOLUTIONS OF MAGNETOHYDRODYNAMIC AND BIOMAGNETIC FLUID FLOWS IN CHANNELS

submitted by **ÖNDER TÜRK** in partial fulfillment of the requirements for the degree of **Doctor of Philosophy in Department of Scientific Computing, Middle East Technical University** by,

Prof. Dr. Bülent Karasözen
Director, Graduate School of **Applied Mathematics** _____

Prof. Dr. Bülent Karasözen
Head of Department, **Scientific Computing** _____

Prof. Dr. Münevver Tezer-Sezgin
Supervisor, **Mathematics, METU** _____

Examining Committee Members:

Prof. Dr. Bülent Karasözen
Scientific Computing, METU _____

Prof. Dr. Münevver Tezer-Sezgin
Mathematics, METU _____

Prof. Dr. Tanıl Ergenç
Mathematics, Atılım University _____

Prof. Dr. M. Haluk Aksel
Mechanical Engineering, METU _____

Prof. Dr. I. Hakan Tarman
Engineering Sciences, METU _____

Date: _____

I hereby declare that all information in this document has been obtained and presented in accordance with academic rules and ethical conduct. I also declare that, as required by these rules and conduct, I have fully cited and referenced all material and results that are not original to this work.

Name, Last Name: ÖNDER TÜRK

Signature   :

ABSTRACT

FEM SOLUTIONS OF MAGNETOHYDRODYNAMIC AND BIOMAGNETIC FLUID FLOWS IN CHANNELS

Türk, Önder

Ph.D., Department of Scientific Computing

Supervisor   : Prof. Dr. Münevver Tezer-Sezgin

January 2014, 157 pages

In this thesis, solutions to steady and unsteady flow problems of incompressible viscous fluids are obtained numerically. In computational aspects, the primary focus is on the finite element analysis, however, spectral collocation and boundary element methods are also employed. The two-dimensional Navier-Stokes (N-S) equations in stream function-vorticity form are solved by using both finite element method (FEM) and Chebyshev spectral collocation method (CSCM). The accuracy of the FEM and CSCM methodologies is investigated by solving some benchmark fluid flow problems such as lid-driven cavity flow, and natural convection flow in enclosures. The natural convection flow problem is also considered under the effect of an externally applied magnetic field. The magnetohydrodynamic (MHD) system is coupled with the temperature effects through the gravitational force by means of the Boussinesq approximation. Different flow configurations with various boundary conditions are examined on both inclined and non-inclined enclosures, and the solutions are obtained by using FEM and CSCM for the case of small magnetic Reynolds number.

The problem of unsteady, one-dimensional MHD flow and heat transfer between parallel plates, is solved with CSCM due to its simplicity in computations. For the time discretization, an implicit backward finite difference scheme is presented. The effect of the movement of the upper plate on the flow, and the convection action in terms of inflow/outflow through plates are examined. The MHD flow

between parallel plates is extended to the case of dusty fluid by including differential equations for the dust particles. The Navier-slip conditions for both the fluid and dust particle velocities are introduced. The Hartmann number, viscosity parameter, and Navier-slip parameter influences on the flow and temperature are visualized in terms of graphics together with discussions.

The biomagnetic fluid flow (blood flow) and heat transfer in channels between plates with various physical configurations are simulated. A blood model consistent with biomagnetic fluid dynamics (BFD), which includes the principles of MHD and ferrohydrodynamics (FHD), is considered. The fluid is assumed to be Newtonian, and both electrically conducting and nonconducting fluid flows are separately considered. The FEM and DRBEM applications are introduced for the steady biomagnetic fluid flow model where the fluid is considered as electrically non-conducting. The effects of the externally applied magnetic field on the flow and heat distribution are analyzed in details. FEM applications are also presented for the solution of biomagnetic fluid flow through channels between plates with differing constriction profiles. Alterations in the behaviors of the flow and temperature of the biomagnetic fluid due to the stenoses in the channel and location and intensity of the magnetic source are analyzed.

Keywords: FEM, DRBEM, Spectral method, MHD flow, Biomagnetic flow

ÖZ

MAGNETOHİDRODİNAMİK VE BİYOMANYETİK AKIŞKAN KANAL AKIMLARININ SONLU ELEMANLAR YÖNTEMİ İLE ÇÖZÜMÜ

Türk, Önder

Doktora, Bilimsel Hesaplama Bölümü

Tez Yöneticisi   : Prof. Dr. Münevver Tezer-Sezgin

Ocak 2014, 157 sayfa

Bu tezde, sıkıştırılamaz viskoz akışkanların zamana bağlı ve zamandan bağımsız akış problemleri nümerik olarak çözülmektedir. Hesaplamalarda sayısal yöntemler bakımından ağırlıklı olarak sonlu elemanlar yöntemi uygulanmakta, ancak belirli problemlerin çözümünde spektral kollokasyon ve sınır elemanları yöntemleri kullanılmaktadır. İki boyutlu Navier-Stokes denklemlerinin stream fonksiyonu, vortisite bilinmeyenleri cinsinden çözümleri sonlu elemanlar ve Chebyshev spektral kollokasyon yöntemleri ile elde edilmektedir. Bu yöntemler ile kanal içerisinde elde edilen sonuçların hassasiyeti, üst kapağı hareketli kare kesitli akış ve ısı tranferi içeren doğal konveksiyon problemleri çözülerek karşılaştırılmaktadır. Doğal konveksiyon akış problemi, dışarıdan uygulanan manyetik alan etkisi ele alınarak da çözülmektedir. Burada, küçük manyetik Reynolds sayısı varsayımı ve Boussinesq yaklaşımı ile magnetohidrodinamik sistem, enerji denklemi ile yer çekimi kuvveti kullanılarak birleştirilir.

Zamana bağlı, bir boyutlu magnetohidrodinamik akış ve ısı transferi, iki paralel plaka arasında Chebyshev spektral kollokasyon yöntemi ile çözülmektedir. Yöntemin, kolay uygulanabilirliği ve yüksek hassasiyetli çözüm verme özelliklerinden yararlanılmaktadır. Zaman integrasyonunda, koşulsuz kararlı olan geri farklar yöntemi kullanılmaktadır. Üst plakanın ve giriş/çıkış konveksiyon hareketlerinin akım üzerindeki etkileri incelenmektedir. İki paralel plaka arasındaki magnetohidrodinamik akış problemi, katı parçacık içeren akışkan için, ek denk-

lemler ile genişletilerek çözülmektedir. Burada, akışkanın ve katı parçacıkların hızları için Navier-slip koşulu uygulanır. Hartmann sayısı, viskozite parametresi ve Navier-slip parametresinin akış ve ısı transferi üzerindeki etkileri araştırılmakta ve sonuçlar grafiksel olarak yorumlarıyla birlikte verilmektedir.

Biyomanyetik akışkan (kan) akışı ve ısı transferi daralmalı ve daralmasız kanallar içerisinde modellenmektedir. Akışkan (kan) modeli, ferrohidrodinamik ve magnetohidrodinamik ilkelerine dayalı biyomanyetik akışkanlar dinamiği ile uyumlu olarak alınır. Newtonian olarak varsayılan biyomanyetik akışkanın elektrikçe iletken olduğu ve iletken olmadığı durumlar ayrıca incelenmektedir. Elektrikçe iletken olmayan akışkanın, zamandan bağımsız akış ve ısı transferi modeli sonlu elemanlar ve sınır elemanları yöntemleri kullanılarak çözülmektedir. Dışarıdan uygulanan manyetik alanın akış ve ısı dağılımı üzerindeki etkisi ayrıntılı olarak incelenmektedir. Sonlu elemanlar yöntemi, ayrıca, daralma içeren kanallar boyunca biyomanyetik akışkan akışı probleminin çözümünde kullanılmaktadır. Daralma profilinin, manyetik kaynağın yeri ve yoğunluğunun biyomanyetik akışkanın akış ve ısı transferi üzerindeki etkileri analiz edilmektedir.

Anahtar Kelimeler: Sonlu elemanlar yöntemi, Karşılıklı sınır elemanları yöntemi, Spektral yöntemi, Magnetohidrodinamik akış, Biyomanyetik akış

To the memory of my mother, Semire

ACKNOWLEDGMENTS

TABLE OF CONTENTS

LIST OF FIGURES

LIST OF TABLES

CHAPTER 1

INTRODUCTION

There are numerous problems in engineering, industrial and scientific disciplines that are described by partial differential equations (PDEs), and cannot be solved analytically. This is the ground for the massive demand on development of novel, efficient and accurate numerical techniques for solving PDEs. Computational fluid dynamics (CFD), is one of the major research areas which involves the applications of numerical analysis in fluid flows and heat transfer. CFD, basically aims to solve numerically complex problems of fluid dynamics arising in many fields such as aerodynamics, chemical process engineering, biomedical engineering and biological systems, ocean engineering, and air pollution modeling. It is an extensive field which utilizes scientific computation in conjunction with mathematical modeling to examine fluid behaviors in the interactive motion of a large number of individual particles. The fundamental aspects of CFD particularly model the physical process as a continuum of fluid particles and the equations which represent the continuum dynamics. The derivation of the principal equations of fluid dynamics is based on the fact that the dynamical behavior of a fluid is determined by the fundamental conservation laws, which are the conservation of mass, the conservation of momentum, and the conservation of energy. The conservation of a certain flow quantity means that its total variation inside an arbitrary volume can be expressed as the net effect of the amount of the quantity being transported across the boundary, of any internal forces and sources, and of external forces acting on the volume. The amount of the quantity crossing the boundary is called flux. The flux can be in general decomposed into two different parts. One is due to the convective transport and the other is due to the molecular motion present in the fluid at rest. This second contribution is of a diffusive nature, it is proportional to the gradient of the quantity considered, and hence, it will vanish for a homogeneous distribution [12, 20]. The discussion of the conservation laws leads to the idea of dividing the flow field into a number of volumes and to concentrate on the modeling of the behavior of the fluid in such a finite region. For this purpose, control volumes are defined, and the mathematical description of the physical properties is modeled on this control volume. The resulting partial differential equations are the continuity equation, the Navier-Stokes equations and the energy equation. According to the additional internal and external forces such as radiation and magnetic field effects, components of Navier-Stokes equations are supplied with additional terms.

Analytical methods are applicable only to some simplified flow problems in simple geometries. Thus, in majority of the flow configurations, numerical methods are used. There are several available CFD software tools, but still an extensive research is in need and ongoing to improve the numerical methods and the physical models. There exists a vast number of solution methodologies applied to solve flow problems. Finite difference method (FDM) is among the first and the most widespread approaches applied to the numerical solution of differential equations as well as CFD problems. The principle of FDM is to employ a Taylor series expansion for the discretization of the derivatives of the flow variables. The method is directly applied to the differential form of the governing equations. The partial differential equations are replaced by finite-divided differences, hence, the methods are generally referred as point-wise approximations. The solution domain is divided in a grid of discrete points (or nodes), and the differential form of the conservation equations are discretized. An important advantage of the finite difference methodology is its simplicity. Another advantage is the possibility of obtaining high-order approximations, and hence to achieve high-order accuracy of the spatial discretization. On the other hand, since the method requires a structured grid, the range of applications is restricted, and especially in complex geometries the method cannot be applied directly [12, 20].

Finite Volume Method (FVM) is another prevalent technique applied in numerical solutions of differential equations, also in CFD models. The method can be shown to be equivalent to the finite difference method under certain conditions. FVM is based on a discretization of the integral forms of the conversation laws. The finite volume method discretizes the governing equations by dividing the physical space into a number of arbitrary control volumes. The main advantage of the finite volume method is that the spatial discretization is carried out directly in the physical space, and the method is very flexible so that it can be rather easily implemented on structured as well as on unstructured grids [12, 20].

Spectral methods are a family of numerical approaches, which are also widely used for solving differential equations and flow simulations. The most characteristic property of spectral methods is the global approximation feature. The spatial derivatives of the solution are approximated by the derivatives of previously assigned polynomials. Periodic and non-periodic problems are treated with trigonometric and algebraic polynomials, respectively. Some of the spectral methods commonly used in the literature are the Fourier collocation methods for periodic domains and the Jacobi polynomials for non-periodic domains, with the Chebyshev and Legendre polynomials as special cases. The numerical solution is expressed as a finite expansion of some set of basis functions. When the PDE is written in terms of the coefficients of this expansion, the method is known as a Galerkin spectral method. Spectral collocation methods, also known as pseudospectral methods, are another subclass of spectral methods and are similar to finite difference methods due to direct use of a set of gridpoints, which are called collocation points. A third class is the Tau spectral methods. These methods are similar to the Galerkin spectral methods, however, the expanding basis is not obliged to satisfy boundary conditions. The coefficients related to the interpolating functions can be considered as a spectrum of the solution, which explains

the name for the method. The characteristic speciality of the spectral methods is the high accuracy resulting from the high order approximation compared to local methods where the solution at a particular node is affected by a limited number of points around it. Their main benefit is in the rate of convergence which depends on the smoothness of the solution, and the number of continuous derivatives that the solution admits. For infinitely smooth solution, the error in spectral method solution decreases exponentially. On the other hand, spectral methods are geometrically less flexible and the spectral representation of the solution is difficult to combine with sharp gradients, e.g. problems involving sharp variations and discontinuities [33].

The boundary element method (BEM) is a well-established numerical technique for solving boundary value problems arising in fluid dynamics. The basic idea of the technique is the transformation of the original differential equation describing the behavior of the unknown inside and on the boundary of the domain, into an equivalent integral equation only on the boundary. This boundary integral relates the boundary unknown solution values and their normal derivatives on the boundary. BEM requires only the boundary discretization, which reduces the dimensionality of the problem under consideration by one. Thus, a smaller system of equations is obtained in comparison with the numerical methods requiring domain discretization. Consequently, the solution is carried out very efficiently with substantial savings in computer time and storage. Another important advantage of the method is that it is also well suited for free and moving surface problems and for the problems defined on infinite regions for which the classical domain methods are not convenient [15]. A drawback of the method is the requirement of a fundamental solution to the original differential equation to avoid domain integrals in the boundary integral formulation. Moreover, the nonhomogeneous and nonlinear terms are incorporated in the BEM formulation by means of domain integrals. These domain integrals can usually be computed by cell integrations with internal discretization which considerably increases the computational cost. Thus, in such cases, to recover the avails of the boundary-only character of BEM, several techniques are introduced. Among these, the analytic integration, Fourier expansion, Galerkin vector technique, the multiple reciprocity method and the dual reciprocity method can be counted. The dual reciprocity method is one of the most widely used procedure for constructing solutions of nonlinear and time-dependent problems to represent any internal source distribution. In dual reciprocity BEM (DRBEM), the basic idea is to employ a fundamental solution corresponding to a simpler equation and to treat the remaining terms, as well as other nonhomogeneous terms in the original equation, through a procedure which involves a series expansion using global approximating functions and the application of reciprocity principles [16].

The finite element method is a well developed rigorous technique which is widely used in many fields as well as in CFD models to approximate solutions with high accuracy achievements. The method is accepted to be one of the most powerful methods, due to its crucial characteristics as a numerical method. One of the key features of the method is that the problem domain is represented by a collection of simple subdomains which are called finite elements. These

elements can be rectilinear or curved, also the grid itself need not be structured so that complex geometries can be handled easily. Depending on the element type and the required accuracy, a certain number of points at the boundary and/or inside an element is specified, where the solution of the flow problem is obtained. The so-called shape functions are defined, which represent the variation of the solution inside each element. Therefore, the representation of the solution is strongly linked to the geometric representation of the domain. In FEM, the governing equations are transformed from the differential form into an equivalent integral form. This can be accomplished in two different ways. The first one is based on the variational principle, where a physical solution is sought, for which a certain functional possesses an extremum. The second possibility is known as the method of weighted residuals or the weak formulation. Here, it is required that the weighted average of the residuals is identically zero over the physical domain. The weak formulation is preferred over the variational methodology, as it possesses the advantage of the conservation laws and allows the treatment of discontinuous solutions. The combination of the representation of the solution in a given function space, with the integral formulation treating rigorously the boundary conditions, gives the method an extremely strong and rigorous mathematical foundation [12, 59].

1.1 Incompressible Fluid Flows with Heat Transfer under a Magnetic Field

This section introduces the mathematical formulations for several flows of incompressible fluids and heat transfer. First, the Navier-Stokes (N-S) equations which constitute the basis of numerical fluid mechanics are introduced. Second, the natural convection flow equations obtained by the addition of the energy equation to the N-S equations is given. Next, an externally applied magnetic field effect is considered in the natural convection flow, and the momentum equations are extended so as to involve magnetohydrodynamic terms. Thus, the governing equations for MHD flow between parallel plates and heat transfer are presented under an external magnetic field effect. The MHD flow of a dusty fluid and heat transfer between parallel plates is also introduced in the sequel. Finally, in Section 1.2, the mathematical formulation of the biomagnetic fluid flow equations is presented.

1.1.1 The Navier-Stokes Equations

One of the most important sets of equations in analysing fluid flows mathematically, are the well known Navier-Stokes (N-S) equations. They can be used to describe the physics of a very large number of phenomena such as weather movements, ocean currents, fluid flows in pipes, aircraft designs, motion of stars in galaxies, blood flow studies and design of power stations. There are two equations namely, the continuity equation and the momentum equations, constituting

the N-S equations. The continuity equation comes from the law of conservation of mass for the fluid entering a control volume, that is, the mass is balanced over a control volume of infinitesimal size. The momentum equations which are derived from Newton's second law of motion, express the proportionality between the force applied and the resulting acceleration of a particle. When a two dimensional flow of an incompressible viscous fluid is considered, the N-S equations in vector form can be formulated as follows. The momentum equation

$$\bar{\rho}\frac{\partial \bar{\mathbf{u}}}{\partial \bar{t}} + \bar{\rho}\bar{\mathbf{u}} \cdot \nabla \bar{\mathbf{u}} = -\nabla \bar{p} + \bar{\mu}\nabla^2 \bar{\mathbf{u}} + \bar{\rho}\bar{\mathbf{f}} \tag{1.1}$$

and the continuity equation

$$\nabla \cdot \bar{\mathbf{u}} = 0 \tag{1.2}$$

where $\nabla^2 = \partial^2/\partial \bar{x}^2 + \partial^2/\partial \bar{y}^2$ is the two-dimensional Laplace operator, $\bar{p}$ is the pressure, $\bar{\rho}$ and $\bar{\mu}$ are the density and viscosity of the fluid, respectively. The vector $\bar{\mathbf{u}}$ is the velocity field and the vector $\bar{\mathbf{f}}$ represents the collection of body forces acting upon the fluid such as gravity.

The N-S equations for the two-dimensional, unsteady flow of an incompressible viscous fluid with a constant viscosity can be written as

$$\frac{\partial \bar{u}}{\partial \bar{t}} + \bar{u}\frac{\partial \bar{u}}{\partial \bar{x}} + \bar{v}\frac{\partial \bar{u}}{\partial \bar{y}} = \bar{f}_1 - \frac{1}{\bar{\rho}}\frac{\partial \bar{p}}{\partial \bar{x}} + \bar{\gamma}\left(\frac{\partial^2 \bar{u}}{\partial \bar{x}^2} + \frac{\partial^2 \bar{u}}{\partial \bar{y}^2}\right)$$

$$\frac{\partial \bar{v}}{\partial \bar{t}} + \bar{u}\frac{\partial \bar{v}}{\partial \bar{x}} + \bar{v}\frac{\partial \bar{v}}{\partial \bar{y}} = \bar{f}_2 - \frac{1}{\bar{\rho}}\frac{\partial \bar{p}}{\partial \bar{y}} + \bar{\gamma}\left(\frac{\partial^2 \bar{v}}{\partial \bar{x}^2} + \frac{\partial^2 \bar{v}}{\partial \bar{y}^2}\right) \tag{1.3}$$

for the momentum equations, and the continuity equation takes the form

$$\frac{\partial \bar{u}}{\partial \bar{x}} + \frac{\partial \bar{v}}{\partial \bar{y}} = 0 \tag{1.4}$$

in cartesian coordinates. Here, $\bar{u}$ and $\bar{v}$ are the velocity components which depend on the space variables x, y and the time variable t. The functions $\bar{f}_1$ and $\bar{f}_2$ are the x- and y- components of the body force vector, respectively, such that $\bar{\mathbf{f}} = (\bar{f}_1, \bar{f}_2)$. The constant $\bar{\gamma} = \bar{\mu}/\bar{\rho}$ is the kinematic viscosity.

Introducing a characteristic length $\bar{L}$ and a characteristic velocity $\bar{U}$, and defining dimensionless quantities

$$x = \frac{\bar{x}}{\bar{L}}, \quad y = \frac{\bar{y}}{\bar{L}}, \quad u = \frac{\bar{u}}{\bar{U}}, \quad t = \frac{\bar{t}}{(\bar{L}/\bar{U})}, \quad v = \frac{\bar{v}}{\bar{U}}, \quad p = \frac{\bar{p}}{\bar{U}^2\bar{\rho}}, \tag{1.5}$$

the momentum equations (1.3) can be written in non-dimensional form as

$$\frac{\partial u}{\partial t} + u\frac{\partial u}{\partial \bar{x}} + v\frac{\partial u}{\partial y} = f_1 - \frac{\partial p}{\partial x} + \frac{1}{Re}\left(\frac{\partial^2 u}{\partial x^2} + \frac{\partial^2 u}{\partial y^2}\right)$$

$$\frac{\partial v}{\partial t} + u\frac{\partial v}{\partial x} + v\frac{\partial v}{\partial y} = f_2 - \frac{\partial p}{\partial y} + \frac{1}{Re}\left(\frac{\partial^2 v}{\partial x^2} + \frac{\partial^2 v}{\partial y^2}\right) \tag{1.6}$$

and the continuity equation (1.4) in non-dimensional form becomes

$$\frac{\partial u}{\partial x} + \frac{\partial v}{\partial y} = 0. \tag{1.7}$$

Here, the Reynolds number Re is defined as

$$Re = \frac{\bar{U}\bar{L}}{\bar{\gamma}} \tag{1.8}$$

which gives the ratio of inertial forces to viscous forces. The Reynolds number distinguishes the relativity of these forces and hence, characterizes the regime of the flow. The flow under consideration is identified as laminar when $Re <\approx 2100$, and otherwise, the flow is said to be turbulent. The unsteady N-S equations (1.6)-(1.7) are usually supplied with essential boundary conditions for velocity as

$$u(x_b, y_b, t) = u_b, \qquad v(x_b, y_b, t) = v_b, \tag{1.9}$$

for $t > 0$, where the subscript b represents the boundary point. When $u_b = v_b = 0$ is taken, the no-slip velocity condition is imposed indicating that the fluid is at rest on the boundary of the flow region. An initial condition on the velocity components is also provided as

$$u(x, y, 0) = u_0, \qquad v(x, y, 0) = v_0. \tag{1.10}$$

The pressure physically has no boundary conditions. Thus, the pressure conditions are usually determined numerically. Equations in (1.6)-(1.7) constitute the fluid flow phenomena accurately, however, the direct solution to this system of equations has traditional difficulties due to the pressure term. Therefore, other alternative formulations have been introduced to represent the N-S equations and have been adopted very successfully by many researchers. One of these methodologies for the two-dimensional flows, is the well established stream function-vorticity formulation which is used extensively in the literature for solving incompressible viscous flow problems.

To obtain the stream function-vorticity formulation of the N-S equations (1.6) and (1.7), stream function ψ satisfying the continuity equation directly is defined as

$$\frac{\partial \psi}{\partial y} = u, \quad \frac{\partial \psi}{\partial x} = -v. \tag{1.11}$$

The pressure term is eliminated by subtracting the derivative of the first equation in (1.6) with respect to y from the derivative of the second equation with respect to x. The only nonzero component of the vorticity field in a two-dimensional flow is introduced as

$$w = \frac{\partial v}{\partial x} - \frac{\partial u}{\partial y} = -\left(\frac{\partial^2 \psi}{\partial x^2} + \frac{\partial^2 \psi}{\partial y^2}\right) = -\nabla^2 \psi \tag{1.12}$$

and the momentum equations provide a vorticity transport equation

$$\frac{1}{Re}\nabla^2 w = \frac{\partial w}{\partial t} + u\frac{\partial w}{\partial x} + v\frac{\partial w}{\partial y} + f \tag{1.13}$$

6

where $f = \dfrac{\partial f_1}{\partial y} - \dfrac{\partial f_2}{\partial x}$.

If the flow is at steady-state, that is, if the velocity field remains unchanged with respect to time, the term $\partial w/\partial t$ in equation (1.13) vanishes and thence, the steady N-S equations are obtained as

$$\nabla^2 \psi = -w \,, \tag{1.14}$$

$$\frac{1}{Re}\nabla^2 w + \frac{\partial \psi}{\partial x}\frac{\partial w}{\partial y} - \frac{\partial \psi}{\partial y}\frac{\partial w}{\partial x} = f \,. \tag{1.15}$$

In the stream function-vorticity formulation, the stream function has Dirichlet type boundary conditions as $\psi(x_b, y_b) = \psi_b$, since the boundaries are also streamlines. Moreover, the boundary conditions for velocity specify the Neumann type boundary conditions for stream function via Equation (1.11). On the other hand, the vorticity function has no physical boundary conditions. Thus, the derivative boundary conditions of stream function are usually made use of for computing the vorticity boundary values.

1.1.2 The Natural Convection Flow

The N-S equations which govern the isothermal flow of an incompressible viscous fluid are given in Section 1.1.1. If there are considerable changes in the temperature of the fluid, the heat flux occurs and consequently an additional equation is required. This equation results from the conservation of energy which states that the total energy of a system and its surroundings remains constant. The main effect of the temperature on the fluid is the change of fluid density due to the changes in temperature. Thus, Boussinesq approximation is used for relating the density changes to temperature changes. Therefore, the flow field and the temperature field are coupled, and the natural convection equations are obtained. The natural convection flow is an important heat transfer mechanism having numerous application areas such as nuclear reactor systems, energy storage and conservation, boilers, fire control and metallurgical industries [61].

The equations which govern the steady natural convection flow are obtained by coupling the vorticity transport equation to the energy equation through the buoyancy force term as [46, 61]

$$\frac{\partial \bar{u}}{\partial \bar{x}} + \frac{\partial \bar{v}}{\partial \bar{y}} = 0,$$

$$\bar{u}\frac{\partial \bar{u}}{\partial \bar{x}} + \bar{v}\frac{\partial \bar{u}}{\partial \bar{y}} = -\frac{1}{\bar{\rho}}\frac{\partial \bar{p}}{\partial \bar{x}} + \bar{\gamma}\left(\frac{\partial^2 \bar{u}}{\partial \bar{x}^2} + \frac{\partial^2 \bar{u}}{\partial \bar{y}^2}\right),$$

$$\bar{u}\frac{\partial \bar{v}}{\partial \bar{x}} + \bar{v}\frac{\partial \bar{v}}{\partial \bar{y}} = -\frac{1}{\bar{\rho}}\frac{\partial \bar{p}}{\partial \bar{y}} + \bar{\gamma}\left(\frac{\partial^2 \bar{v}}{\partial \bar{x}^2} + \frac{\partial^2 \bar{v}}{\partial \bar{y}^2}\right) + g\bar{\beta}(\bar{T} - \bar{T}_c),$$

$$\tag{1.16}$$

$$\bar{u}\frac{\partial \bar{T}}{\partial \bar{x}} + \bar{v}\frac{\partial \bar{T}}{\partial \bar{y}} = \bar{\alpha}\left(\frac{\partial^2 \bar{T}}{\partial \bar{x}^2} + \frac{\partial^2 \bar{T}}{\partial \bar{y}^2}\right),$$

where g is the gravitational acceleration, $\bar{\alpha}$ is the thermal diffusivity, and $\bar{\beta}$ is the coefficient of thermal expansion. The use of characteristic length $\bar{L}$ and characteristic velocity $\bar{U}$ gives dimensionless quantities

$$x = \frac{\bar{x}}{\bar{L}}, \quad y = \frac{\bar{y}}{\bar{L}}, \quad u = \frac{\bar{u}\bar{L}}{\bar{\alpha}}, \quad v = \frac{\bar{v}\bar{L}}{\bar{\alpha}}, \quad p = \frac{\bar{p}\bar{L}^2}{\bar{\alpha}^2\bar{\rho}}, \quad T = \frac{\bar{T} - \bar{T}_c}{\bar{T}_h - \bar{T}_c}, \qquad (1.17)$$

where T_c and T_h are the temperature of the hot and cold walls of the problem region, respectively. Then, Equations (1.16) are written in non-dimensional form as

$$\frac{\partial u}{\partial x} + \frac{\partial v}{\partial y} = 0,$$

$$u\frac{\partial u}{\partial x} + v\frac{\partial u}{\partial y} = -\frac{\partial p}{\partial x} + Pr\left(\frac{\partial^2 u}{\partial x^2} + \frac{\partial^2 u}{\partial y^2}\right),$$

$$u\frac{\partial v}{\partial x} + v\frac{\partial v}{\partial y} = -\frac{\partial p}{\partial y} + Pr\left(\frac{\partial^2 v}{\partial x^2} + \frac{\partial^2 v}{\partial y^2}\right) + RaPrT,$$

$$u\frac{\partial T}{\partial x} + v\frac{\partial T}{\partial y} = \frac{\partial^2 T}{\partial x^2} + \frac{\partial^2 T}{\partial y^2}.$$

$$(1.18)$$

The dimensionless parameters Pr and Ra, respectively denote the Prandtl number and Rayleigh number which are defined as

$$Pr = \frac{\bar{\gamma}}{\bar{\alpha}}, \quad Ra = \frac{g\bar{\beta}(\bar{T}_h - \bar{T}_c)\bar{L}^3}{\bar{\alpha}\bar{\gamma}}. \qquad (1.19)$$

A similar procedure described in the previous section is followed, and Equations (1.18) are transformed into stream function ψ, vorticity w, and temperature T form as

$$\nabla^2 \psi = -w$$

$$\frac{\partial \psi}{\partial y}\frac{\partial w}{\partial x} - \frac{\partial \psi}{\partial x}\frac{\partial w}{\partial y} = Pr\nabla^2 w + RaPr\frac{\partial T}{\partial x} \qquad (1.20)$$

$$\frac{\partial \psi}{\partial y}\frac{\partial T}{\partial x} - \frac{\partial \psi}{\partial x}\frac{\partial T}{\partial y} = \nabla^2 T \,.$$

The boundary conditions for temperature can be defined as Dirichlet type

$$T(x_b, y_b) = T_b,$$

or Neumann type

$$\frac{\partial T}{\partial n} = g(q)$$

where $g(q)$ denotes a function of heat flux q through the boundary of the problem domain. The condition $\partial T/\partial n = 0$ is imposed when the boundary is adiabatic which means that no heat is transferred through the boundary.

1.1.3   Natural Convection Flow under a Magnetic Field

The natural convection flow equations which govern the flow of an incompressible and viscous fluid with temperature flux are given in Section 1.1.2. In the case when an externally applied magnetic field occurs, the flow and the heat transfer are also influenced when the fluid inside the enclosure is electrically conducting. In such regimes, the flow is characterized by the two-dimensional incompressible Navier-Stokes and Maxwell equations (MHD equations). The MHD system is coupled with the temperature effect through gravitational force by means of the Boussinesq approximation. As a consequence, flow and temperature fields are adjusted by the application of external magnetic field. The induced magnetic field inside the fluid is neglected with the assumption of small magnetic Reynolds number. A common technique is to neglect the magnetic induction equations through the low magnetic Reynolds number (Rm) approximation, which represents the ratio of advection to diffusion in the magnetic field [66]. The Joule heating of the fluid and the effect of viscous dissipation are also considered to be negligible. Consequently, the non-dimensional equations governing the natural convection flow in enclosures (channels) under an externally applied magnetic field are given in vector form as [40]

$$\nabla \cdot \mathbf{u} = \mathbf{0}$$
$$\mathbf{u} \cdot \nabla \mathbf{u} = -\nabla p + RaPrT\mathbf{e_Z} + Pr\nabla^2\mathbf{u} + PrHa^2(\mathbf{J} \times \mathbf{e_B}) \qquad (1.21)$$
$$\mathbf{u} \cdot \nabla T = \nabla^2 T$$

where $\mathbf{e_Z}$, $\mathbf{e_B}$ are unit vectors in the axial direction (axis of the channel) and in the direction of the external magnetic field, respectively. $\mathbf{J}$ is the current density $\mathbf{J} = \mathbf{u} \times \mathbf{e_B}$. The velocity vector is in the direction of the axis of the channel (z-axis), and the induced magnetic field in z-direction is ignored. The only component of magnetic field is in the direction of $\mathbf{e_B}$ which is perpendicular to the axis of the duct, and with a constant intensity B_0. The dimenionless parameters Ra and Pr are as in Section 1.1.2 and the Hartmann number Ha, is defined as

$$Ha = \bar{L}B_0\sqrt{\frac{\bar{\sigma}}{\bar{\mu}}} \qquad (1.22)$$

where $\bar{\sigma}$ is the electrical conductivity of the fluid. With a magnetic field applied in the horizontal direction, Equations (1.21) are written in stream function-vorticity-

temperature form as

$$\nabla^2 \psi \quad = \quad -w$$

$$Pr\nabla^2 w \quad = \quad \frac{\partial \psi}{\partial y}\frac{\partial w}{\partial x} - \frac{\partial \psi}{\partial x}\frac{\partial w}{\partial y} - RaPr\frac{\partial T}{\partial x} - Ha^2 Pr\frac{\partial^2 \psi}{\partial x^2} \qquad (1.23)$$

$$\nabla^2 T \quad = \quad \frac{\partial \psi}{\partial y}\frac{\partial T}{\partial x} - \frac{\partial \psi}{\partial x}\frac{\partial T}{\partial y} \, .$$

If the external magnetic field is applied with an angle φ from the x-axis and the channel is inclined from horizontal with an angle ϕ measured in counterclockwise direction as shown in Figure 1.1, the governing equations in stream function,
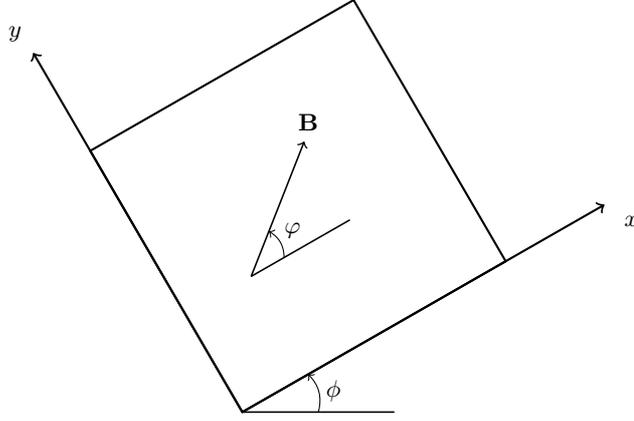
Figure 1.1: Problem geometry and the coordinate system for natural convection flow.

vorticity and temperature form are given as

$$\nabla^2 \psi \quad = \quad -w$$

$$Pr\nabla^2 w \quad = \quad \frac{\partial \psi}{\partial y}\frac{\partial w}{\partial x} - \frac{\partial \psi}{\partial x}\frac{\partial w}{\partial y} - RaPr\left(\cos\phi\frac{\partial T}{\partial x} - \sin\phi\frac{\partial T}{\partial y}\right)$$

$$- Ha^2 Pr\left[\cos\varphi\left(\sin\varphi\frac{\partial^2 \psi}{\partial x\partial y} + \cos\varphi\frac{\partial^2 \psi}{\partial x^2}\right)\right. \qquad (1.24)$$

$$\left. + \sin\varphi\left(\sin\varphi\frac{\partial^2 \psi}{\partial y^2} + \cos\varphi\frac{\partial^2 \psi}{\partial y\partial x}\right)\right]$$

$$\nabla^2 T \quad = \quad \frac{\partial \psi}{\partial y}\frac{\partial T}{\partial x} - \frac{\partial \psi}{\partial x}\frac{\partial T}{\partial y} \, .$$

10

1.1.4 MHD Flow and Heat Transfer between Parallel Plates

In this section, the one-dimensional flow of an unsteady, incompressible and electrically conducting fluid is considered. The flow is assumed to take place between two parallel electrically insulated plates located at the $y = \mp h$ planes. A cartesian frame is located on the rectangular channel with origin on the half-distance of the plates. The x-direction measures the distance along the channel and the y-direction is normal to it. Figure 1.2 visualizes the flow configuration. A constant pressure gradient is applied in the x- direction. The lower and upper plates are kept at constant temperatures T_1 and T_2, respectively, where $T_2 > T_1$. An external uniform magnetic field of intensity B_0 is directed along the y-axis, and it is assumed that the induced magnetic field and electric field can be neglected due to the assumption of very small magnetic Reynolds number [3, 24, 45]. The plates are infinite in the x- and z- directions implying no variation in these directions. Thus, the velocity and the temperature of the fluid are functions of y only. The governing equations are given as [3, 7, 45]

$$\bar{\rho}\frac{\partial \bar{u}}{\partial \bar{t}} + \bar{\rho}\bar{v}_w\frac{\partial \bar{u}}{\partial \bar{y}} = -\frac{\partial \bar{p}}{\partial \bar{x}} + \frac{\partial}{\partial \bar{y}}\left[\bar{\mu}(\bar{T})\frac{\partial \bar{u}}{\partial \bar{y}}\right] - \bar{\sigma}B_0^2\bar{u},$$

$$\bar{\rho}\bar{c}_p\frac{\partial \bar{T}}{\partial \bar{t}} + \bar{\rho}\bar{c}_p\bar{v}_w\frac{\partial \bar{T}}{\partial \bar{y}} = \bar{k}\frac{\partial^2 \bar{T}}{\partial \bar{y}^2} + \bar{\mu}(\bar{T})\left(\frac{\partial \bar{u}}{\partial \bar{y}}\right)^2 + \bar{\sigma}B_0^2\bar{u}^2 \tag{1.25}$$

where $\bar{c}_p$ is the specific heat, $\bar{k}$ is the thermal conductivity, $\bar{\mu}_0$ is the dynamic viscosity, $\bar{\nu}_0$ is the kinematic viscosity, and $\bar{\sigma}$ is the electrical conductivity. The last two terms of the second equation in Equations (1.25) represent the viscous dissipation and the Joule dissipation, respectively.
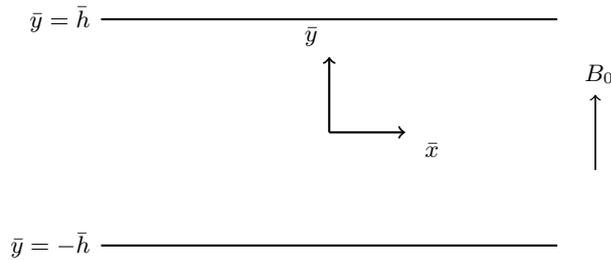
Figure 1.2: Problem configuration for MHD flow between parallel plates.

The following dimensionless variables are employed in Equations (1.25)

$$x = \frac{\bar{x}}{\bar{h}}, \quad y = \frac{\bar{y}}{\bar{h}}, \quad u = \frac{\bar{u}\bar{h}}{\bar{\nu}_0}, \quad t = \frac{\bar{t}\bar{\nu}_0}{\bar{h}^2}, \quad p = \frac{\bar{p}\bar{h}^2}{\bar{\nu}_0^2\bar{\rho}}, \quad T = \frac{\bar{T} - \bar{T}_1}{\bar{T}_2 - \bar{T}_1}, \quad \mu = \frac{\bar{\mu}}{\bar{\mu}_0},$$

and the governing equations in non-dimensional form are obtained as [45]

$$\frac{\partial u}{\partial t} + Rv \frac{\partial u}{\partial y} = G + \frac{\partial}{\partial y}\left[\mu(T)\frac{\partial u}{\partial y}\right] - Ha^2 u,$$

$$\frac{\partial T}{\partial t} + Rv \frac{\partial T}{\partial y} = \frac{1}{Pr}\frac{\partial^2 T}{\partial y^2} + Ec\ \mu(T)\left(\frac{\partial u}{\partial y}\right)^2 + Ec\ Ha^2\ u^2.$$

(1.26)

The dimensionless parameters are defined as

$$G = -\frac{\partial \bar{p}}{\partial \bar{x}}, \quad Pr = \frac{\bar{\mu}_0 \bar{c}_p}{\bar{k}}, \quad Ha = B_0 \bar{h}\sqrt{\bar{\sigma}/\bar{\mu}_0}, \quad Ec = \frac{\bar{\nu}_0^2}{\bar{h}^2 \bar{c}_p (\bar{T}_2 - \bar{T}_1)},$$

$Rv = \bar{v}_w \bar{h}/\bar{\nu}_0$ is the constant velocity component in the y- direction which may be considered as inflow/outflow parameter through the plates. $Rv = 0$ corresponds to the absence of inflow/outflow through plates at $y = \mp 1$.

The dynamic viscosity has exponential variation [4, 45]

$$\mu(T) = e^{-aT} \tag{1.27}$$

where a is the viscosity parameter defined as

$$a = \ln(\mu_1/\mu_2) \tag{1.28}$$

in which μ_1 and μ_2 are the dynamic viscosities evaluated at $T = T_1$ and $T = T_2$, respectively. Equations (1.26) are supplied with initial and boundary conditions which specify the initial values of the fluid velocity and temperature, and the essential conditions on lower and upper plates.

1.1.5 MHD Flow and Heat Transfer of a Dusty Fluid between Parallel Plates

In this section, the MHD flow of an unsteady, incompressible and electrically conducting fluid considered in the previous section, is extended in that, the fluid contains dust particles. The flow is one-dimensional and an external uniform magnetic field of density B_0 is directed along the y- axis, see Figure 1.3. The induced magnetic field is neglected due to the assumption of very small magnetic Reynolds number as in the previous section.

The dust particles are assumed to be spherical in shape and uniformly distributed throughout the fluid. The particle Reynolds number is assumed to be small. Both the fluid viscosity and the thermal conductivity are assumed to vary with temperature. The governing equations may be written in non-dimensional form as follows [50]
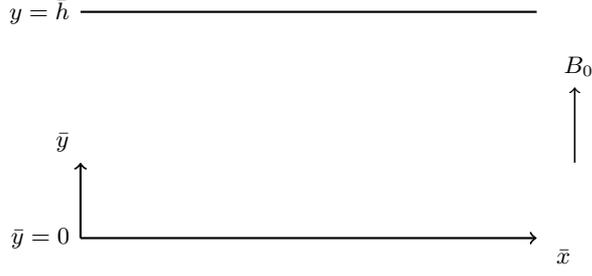
Figure 1.3: Problem configuration for MHD flow of a dusty fluid.

$$Re\frac{\partial u}{\partial t} = Re\ G + \frac{\partial}{\partial y}\left[\mu(T)\frac{\partial u}{\partial y}\right] - Ha^2 u - R(u - u_p),$$

$$\frac{\partial u_p}{\partial t} = \frac{1}{Re\ g}(u - u_p),$$

$$Re\frac{\partial T}{\partial t} = \frac{1}{Pr}\frac{\partial}{\partial y}\left(\kappa(T)\frac{\partial T}{\partial y}\right) + Ec\ \mu(T)\left(\frac{\partial u}{\partial y}\right)^2 + Ec\ Ha^2\ u^2 + \frac{2R}{3Pr}(T_p - T),$$

$$\frac{\partial T_p}{\partial t} = -L_T(T_p - T),$$

$$(1.29)$$

where $0 \le y \le 1,\ t > 0$.

In these equations, u denotes the velocity of the fluid which is fully developed in x-direction and varies parabolically with respect to y. u_p is the velocity of the particles, T is the temperature of the fluid and T_p is the temperature of the particles.

The following dimensionless variables are employed in the above equations

$$x = \frac{\bar{x}}{\bar{h}}, \quad y = \frac{\bar{y}}{\bar{h}}, \quad u = \frac{\bar{u}}{\bar{\nu}}, \quad u_p = \frac{\bar{u}_p}{\bar{\nu}}, \quad t = \frac{\bar{t}\bar{\nu}}{\bar{h}}, \quad T = \frac{\bar{T} - \bar{T}_1}{\bar{T}_2 - \bar{T}_1}, \quad T_p = \frac{\bar{T}_p - \bar{T}_1}{\bar{T}_2 - \bar{T}_1},$$

and the dimensionless parameters are given for the present case (channel flow) as

$$G = -\frac{\partial \bar{p}}{\partial \bar{x}} \quad Pr = \frac{\bar{\mu}_0 \bar{c}_p}{\bar{k}}, \quad Ha = B_0 \bar{h}\sqrt{\bar{\sigma}/\bar{\mu}_0}, \quad Ec = \frac{\bar{\nu}_0^2}{\bar{c}_p(\bar{T}_2 - \bar{T}_1)},$$

$$(1.30)$$

$$Re = \frac{\bar{\rho}\bar{\nu}_0\bar{h}}{\bar{\mu}_0}, \quad R = \frac{\bar{K}\bar{M}\bar{h}^2}{\bar{\mu}_0}, \quad g_p = \frac{\bar{\mu}_0}{\bar{M}\bar{h}^2}.$$

Here, $\bar{c}_p$ is the specific heat at constant pressure, $\bar{k}$ is the thermal conductivity at initial temperature, $\bar{\mu}_0$ is the dynamic viscosity at initial temperature, $\bar{\nu}_0$ is the fluid characteristic velocity, $\bar{\sigma}$ is the electrical conductivity, and $\bar{h}$ is the vertical

distance between the two plates. $\bar{p}$ is the pressure acting on the fluid, $\bar{\rho}$ is the density of the clean fluid. M is the number of dust particles per unit volume, K is the Stokes constant, $\bar{K} = 6\pi\bar{\mu}D$, D is the average radius of dust particles. g_p is the particle mass parameter. Ha, Re and R are the Hartmann number, Reynolds number and the particle concentration parameter, respectively. Pr and Ec are Prandtl and Eckert numbers, L_T is the temperature relaxation time parameter .

The dynamic viscosity and thermal conductivity have exponential variation as [50, 51]

$$\mu(T) = e^{-aT}, \quad \kappa(T) = e^{bT} \tag{1.31}$$

where the viscosity parameter a and the thermal conductivity parameter b contain the temperature difference $(T_2 - T_1)$ between the plates.

The initial and boundary conditions accompanying Equations (1.29) are

$$u(y,0) = u_p(y,0) = 0, \quad T(y,0) = T_p(y,0) = 0 \quad \text{on} \quad 0 \le y \le 1,$$

$$\beta\frac{\partial u}{\partial n} + \gamma u = 0 \quad \text{for} \quad y = 0, 1,$$

$$\beta\frac{\partial u_p}{\partial n} + \gamma u_p = 0 \quad \text{for} \quad y = 0, 1, \tag{1.32}$$

$$T(0,t) = T_p(0,t) = 0 \quad \text{and}$$

$$T(1,t) = T_p(1,t) = 1$$

where the Navier-slip parameters β and γ take several values resulting with Dirichlet, Neumann or mixed boundary conditions [51].

In this study, the Navier-slip boundary conditions are imposed on both the fluid velocity u and the particles velocity u_p which define the interaction between the constitutes of the flow and their interaction with solid boundaries [51]. The conventional boundary condition is the no-slip condition between the fluid and a solid. However, the boundary condition which corresponds to momentum transfer during the flow can vary from stick (no-slip) to slip, saving energy in response to physical chemical properties of the solid surface. The velocity of the fluid is completely zero on a solid boundary only if thermodynamic equilibrium is ensured near the boundary. But for systems where the collisions between the fluid and the solid surface is not high enough to have thermodynamic equilibrium, the tangential velocity slip is allowed. The slip velocity is assumed to be proportional to the tangential viscous stress [51]. Therefore, the Navier-slip boundary condition becomes at each plate

$$\beta\frac{\partial u}{\partial y} = +u \quad \text{at} \quad y = 0,$$

$$\beta\frac{\partial u}{\partial y} = -u \quad \text{at} \quad y = 1, \tag{1.33}$$

by taking the constant $\gamma = \mp 1$, and for various constant values of Navier-slip parameter β.

The same Navier-slip boundary condition is imposed to the particles velocity u_p assuming they have the same collision effect near the boundaries as in the fluid velocity case

$$\beta \frac{\partial u_p}{\partial y} = +u_p \quad \text{at} \quad y = 0,$$

$$\beta \frac{\partial u_p}{\partial y} = -u_p \quad \text{at} \quad y = 1.$$

(1.34)

1.2 Biomagnetic Fluid Flow and Heat Transfer in Channels

A biomagnetic fluid is a circulating fluid in the vascular system of humans and other vertebrates, which is influenced by the presence of a magnetic field. Blood is considered to be a typical biomagnetic fluid due to the interaction of intercellular proteins, membrane and the hemoglobin. Biomagnetic fluid dynamics (BFD) is a relatively new field which investigates the dynamics of biological fluids under the effect of magnetic fields. The BFD flow studies have been attracted many researchers in recent years due to their wide range of applications in bioengineering and medical sciences. Development of the magnetic devices for cell separation, use of magnetic fluids to produce blood flow stasis during surgeries, strengthening blood vessels by magnetic sedimentation, magnetic drug targeting, accelerating blood flow, measuring blood flow and provocation of occlusion of tumor feeding vessels tumors are among these applications [29, 35, 54, 60, 78]. In BFD formulations, in general, the mathematical models are based on the principles of Ferrohydrodynamics (FHD) also consistent with Magnetohydrodynamics (MHD) principles to include the effect of the electrical conductivity of blood under an applied magnetic field.

In this thesis, two-dimensional, unsteady, incompressible, laminar biomagnetic fluid (blood) flows are considered. The flows take place between two parallel plates of length $\bar{l}$, and separated at a distance $\bar{h}$, under the effect of an externally applied magnetic field. The flow at the entrance is assumed to be fully developed. The blood is considered as homogenous, electrically conducting biomagnetic fluid, and Newtonian behavior is assumed. The rotational forces acting on the erythrocytes when entering the magnetic field are discarded (equilibrium flow). The channel flow in terms of the dimensional velocity components $(\bar{u}, \bar{v})$, the pressure $\bar{p}$ and the temperature $\bar{T}$ is governed by the mass conservation, the fluid momentum equations at the $\bar{x}$-, $\bar{y}$- directions, and the energy equation, are given as [75, 76];

Continuity equation

$$\frac{\partial \bar{u}}{\partial \bar{x}} + \frac{\partial \bar{v}}{\partial \bar{y}} = 0.$$

(1.35)

15

Momentum equations

$$\bar{\rho}\left(\frac{\partial \bar{u}}{\partial \bar{t}} + \bar{u}\frac{\partial \bar{u}}{\partial \bar{x}} + \bar{v}\frac{\partial \bar{u}}{\partial \bar{y}}\right) = -\frac{\partial \bar{p}}{\partial \bar{x}} + \bar{\mu}_0 \bar{M}\frac{\partial \bar{H}}{\partial \bar{x}} - \bar{\sigma}\bar{B}^2\bar{u} + \bar{\mu}\nabla^2\bar{u},$$

$$\bar{\rho}\left(\frac{\partial \bar{v}}{\partial \bar{t}} + \bar{u}\frac{\partial \bar{v}}{\partial \bar{x}} + \bar{v}\frac{\partial \bar{v}}{\partial \bar{y}}\right) = -\frac{\partial \bar{p}}{\partial \bar{y}} + \bar{\mu}_0 \bar{M}\frac{\partial \bar{H}}{\partial \bar{y}} + \bar{\mu}\nabla^2\bar{v}.$$

$$(1.36)$$

Energy equation

$$\bar{\rho}\bar{c}_p\left(\frac{\partial \bar{T}}{\partial \bar{t}} + \bar{u}\frac{\partial \bar{T}}{\partial \bar{x}} + \bar{v}\frac{\partial \bar{T}}{\partial \bar{y}}\right) + \bar{\mu}_0\bar{T}\frac{\partial \bar{M}}{\partial \bar{T}}\left(\bar{u}\frac{\partial \bar{H}}{\partial \bar{x}} + \bar{v}\frac{\partial \bar{H}}{\partial \bar{y}}\right) - \bar{\sigma}\bar{B}^2\bar{u}^2$$

$$= \bar{k}\nabla^2\bar{T} + \bar{\mu}\left[2\left(\frac{\partial \bar{u}}{\partial \bar{x}}\right)^2 + 2\left(\frac{\partial \bar{v}}{\partial \bar{y}}\right)^2 + \left(\frac{\partial \bar{v}}{\partial \bar{x}} + \frac{\partial \bar{u}}{\partial \bar{y}}\right)^2\right].$$

$$(1.37)$$

In the above equations, as mentioned before, $\bar{u}$, $\bar{v}$ are the dimensional velocity components, and $\bar{T}$ is the dimensional temperature of the fluid, $\bar{p}$ is the pressure, $\bar{\rho}$, $\bar{\sigma}$ and $\bar{\mu}$ are density, electrical conductivity, and dynamic viscosity of the biomagnetic fluid, respectively. $\bar{\mu}_0$, $\bar{c}_p$ and $\bar{k}$ denote the magnetic permeability of vacuum, the specific heat at constant pressure and the thermal conductivity. $\bar{H}$ is the magnetic field intensity and $\bar{B} = \bar{\mu}_0\bar{H}$ is the magnetic induction where $\bar{M} = \bar{K}\bar{H}(\bar{T}_c - \bar{T})$, and $\bar{K}$ is a constant, $\bar{T}_c$ is the Curie temperature.

The suitable boundary conditions for the biomagnetic fluid flow are given as

Inflow, $\bar{x} = 0$, $0 \le \bar{y} \le \bar{h}$	:	$\bar{u} = \bar{u}(\bar{y})$, $\bar{v} = 0$, $\bar{T} = \bar{T}(\bar{y})$
Outflow, $\bar{x} = \bar{l}$, $0 \le \bar{y} \le \bar{h}$	:	$\partial \bar{R}/\partial \bar{x} = 0$
Lower plate, $\bar{y} = F(\bar{x})$, $0 \le \bar{x} \le \bar{l}$	:	$\bar{u} = 0$, $\bar{v} = 0$, $\bar{T} = \bar{T}_l$
Upper plate, $\bar{y} = G(\bar{x})$, $0 \le \bar{x} \le \bar{l}$	:	$\bar{u} = 0$, $\bar{v} = 0$, $\bar{T} = \bar{T}_u$.

$$(1.38)$$

Here, $\bar{u}(\bar{y})$, $\bar{T}(\bar{y})$ denote the velocity and temperature profiles respectively, at the entrance and $\bar{R}$ stands for ψ, w and T. Figure 1.4 visualizes the problem domain where the lower and upper plates are defined by functions $F(\bar{x})$ and $G(\bar{x})$, respectively.
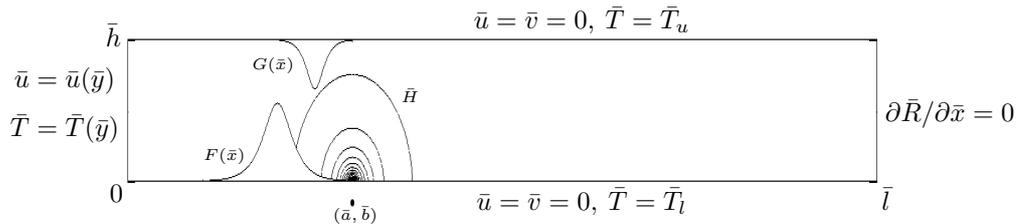
Figure 1.4: Problem configuration with constriction for biomagnetic fluid flow.

The $\bar{x}$ and $\bar{y}$ components of the magnetic field intensity, respectively $\bar{H}_x$ and $\bar{H}_y$, are given by

$$\bar{H}_x = \frac{\bar{\bar{\gamma}}}{2\pi} \frac{\bar{y} - \bar{b}}{(\bar{x} - \bar{a})^2 + (\bar{y} - \bar{b})^2}, \quad \bar{H}_y = -\frac{\bar{\bar{\gamma}}}{2\pi} \frac{\bar{x} - \bar{a}}{(\bar{x} - \bar{a})^2 + (\bar{y} - \bar{b})^2} \tag{1.39}$$

where $\vec{H} = (\bar{H}_x, \bar{H}_y)$, and $(\bar{a}, \bar{b})$ is the magnetic source point, and $\bar{\bar{\gamma}}$ is the magnetic field strength at this point $(x = \bar{a}, y = \bar{b})$. Thus, the magnetic field intensity $\bar{H}$ is given by

$$\bar{H} = (\bar{H}_x + \bar{H}_y)^{1/2} = \frac{\bar{\bar{\gamma}}}{2\pi} \frac{1}{\sqrt{(\bar{x} - \bar{a})^2 + (\bar{y} - \bar{b})^2}} \,. \tag{1.40}$$

The equations (1.35)-(1.37) are non-dimensionalized using

$$x = \frac{\bar{x}}{\bar{h}}, \, y = \frac{\bar{y}}{\bar{h}}, t = \frac{\bar{t}\bar{\mu}}{\bar{\rho}\bar{h}^2}, \, u = \frac{\bar{u}}{\bar{u}_r}, \, v = \frac{\bar{v}}{\bar{u}_r}, \, p = \frac{\bar{p}}{\bar{\rho}\bar{u}_r^2}, \, H = \frac{\bar{H}}{\bar{H}_r}, \, T = \frac{\bar{T} - \bar{T}_1}{\bar{T}_2 - \bar{T}_1}$$

where $\bar{u}_r$ is the maximum velocity of the fluid (blood) at the entrance of the channel, and $\bar{H}_r = \bar{H}(\bar{a}, \bar{b})$ is the magnetic field intensity at the magnetic source point, $(\bar{a}, \bar{b})$. In this configuration, $\bar{T}_1$ denote the temperature of the lower and upper plates, and $\bar{T}_2$ is the temperature of the fluid. As mentioned earlier, two-dimensional equations (1.35)-(1.37) can be transformed to non-dimensional form in terms of stream function ψ, vorticity w and temperature T as

$$\nabla^2 \psi = -w,$$

$$\frac{\partial w}{\partial t} = \nabla^2 w - Re \left\{ \frac{\partial w}{\partial x} \frac{\partial \psi}{\partial y} - \frac{\partial w}{\partial y} \frac{\partial \psi}{\partial x} \right\}$$

$$+ Mn_F ReH \left\{ \frac{\partial H}{\partial x} \frac{\partial T}{\partial y} - \frac{\partial H}{\partial y} \frac{\partial T}{\partial x} \right\} + Mn_M \frac{\partial}{\partial y} \left(H^2 \frac{\partial \psi}{\partial y} \right), \tag{1.41}$$

$$\frac{\partial T}{\partial t} = \frac{1}{Pr} \nabla^2 T - Re \left\{ \frac{\partial T}{\partial x} \frac{\partial \psi}{\partial y} - \frac{\partial T}{\partial y} \frac{\partial \psi}{\partial x} \right\}$$

$$+ Mn_F ReEcH(\varepsilon + T) \left\{ \frac{\partial H}{\partial x} \frac{\partial \psi}{\partial y} - \frac{\partial H}{\partial y} \frac{\partial \psi}{\partial x} \right\}$$

$$+ Mn_M EcH^2 \left(\frac{\partial \psi}{\partial y} \right)^2 + Ec \left\{ \left(\frac{\partial^2 \psi}{\partial y^2} - \frac{\partial^2 \psi}{\partial x^2} \right)^2 + 4 \left(\frac{\partial^2 \psi}{\partial x \partial y} \right)^2 \right\} \,.$$

The dimensionless parameters Reynolds number Re, Prandtl number Pr, Eckert number Ec and temperature number ε, are given as

$$Re = \frac{\bar{h}\bar{\rho}\bar{u}_r}{\bar{\mu}}, \quad Pr = \frac{\bar{c}_p \bar{\mu}}{\bar{k}}, \quad Ec = \frac{\bar{u}_r^2}{\bar{c}_p(\bar{T}_2 - \bar{T}_1)}, \quad \varepsilon = \frac{\bar{T}_1}{\bar{T}_2 - \bar{T}_1} \,. \tag{1.42}$$

The non-dimensional magnetic numbers arising from FHD, Mn_F and arising from MHD, Mn_M are defined as [75]

$$Mn_F = \frac{\bar{\mu}_0 \bar{H}_r^2 \bar{K}(\bar{T}_2 - \bar{T}_1)}{\bar{\rho}\bar{u}_r^2}, \qquad Mn_M = \frac{\bar{\mu}_0^2 \bar{H}_r^2 \bar{h}^2 \bar{\sigma}}{\bar{\mu}} = Ha^2. \qquad (1.43)$$

In the above equations, Ha is the Hartmann number. The magnitude of the magnetic field intensity at the point (a, b) in non-dimensional form is given by

$$H(x, y) = \frac{|b|}{\sqrt{(x-a)^2 + (y-b)^2}}. \qquad (1.44)$$

In BFD models where the effect of polarization and magnetization is considered as small, the Lorentz force is much smaller in comparison to the magnetization force, and accordingly blood is considered as a poor conductor. Thus, in these models, the fluid is taken as electrically non-conducting biomagnetic fluid, and the flow is affected only by the magnetization of the fluid due to the externally applied magnetic field. When the electrically non-conducting biomagnetic fluid flow is time independent, and moreover, when the temperatures of the parallel plates are different,

$$T = \frac{\bar{T}_u - \bar{T}}{\bar{T}_u - \bar{T}_l}$$

is employed in the non-dimensionalization so that $\bar{T}_1 = \bar{T}_l$ and $\bar{T}_2 = \bar{T}_u$ are taken in the parameters given in (1.42). As a consequence, the steady flow of an electrically non-conducting fluid takes the form [47]

$$\frac{\partial u}{\partial x} + \frac{\partial v}{\partial y} = 0, \qquad (1.45)$$

$$\frac{1}{Re}\nabla^2 u = \frac{\partial p}{\partial x} + u\frac{\partial u}{\partial x} + v\frac{\partial u}{\partial y} - Mn_F T H \frac{\partial H}{\partial x},$$
$$\qquad (1.46)$$
$$\frac{1}{Re}\nabla^2 v = \frac{\partial p}{\partial y} + u\frac{\partial v}{\partial x} + v\frac{\partial v}{\partial y} - Mn_F T H \frac{\partial H}{\partial y},$$

$$\nabla^2 T = PrRe(u\frac{\partial T}{\partial x} + v\frac{\partial T}{\partial y}) + PrEc[2(\frac{\partial u}{\partial x})^2 + 2(\frac{\partial v}{\partial x})^2 + (\frac{\partial v}{\partial x} + \frac{\partial u}{\partial y})^2]$$
$$\qquad (1.47)$$
$$+ Mn_F PrReEcH(\varepsilon - T)(u\frac{\partial H}{\partial x} + v\frac{\partial H}{\partial y}).$$

Equations (1.45)-(1.47) are written in terms of stream function ψ, vorticity w,

and temperature T as

$$\nabla^2 \psi = -w$$

$$\nabla^2 w = Re\left\{\frac{\partial w}{\partial x}\frac{\partial \psi}{\partial y} - \frac{\partial w}{\partial y}\frac{\partial \psi}{\partial x}\right\} + MnReH\left\{\frac{\partial H}{\partial x}\frac{\partial T}{\partial y} - \frac{\partial H}{\partial y}\frac{\partial T}{\partial x}\right\}$$

$$\nabla^2 T = PrRe\left\{\frac{\partial T}{\partial x}\frac{\partial \psi}{\partial y} - \frac{\partial T}{\partial y}\frac{\partial \psi}{\partial x}\right\} \qquad (1.48)$$

$$+ MnPrReEcH(\varepsilon - T)\left\{\frac{\partial H}{\partial x}\frac{\partial \psi}{\partial y} - \frac{\partial H}{\partial y}\frac{\partial \psi}{\partial x}\right\}$$

$$+ PrEc\left\{\left(\frac{\partial^2 \psi}{\partial y^2} - \frac{\partial^2 \psi}{\partial x^2}\right)^2 + 4\left(\frac{\partial^2 \psi}{\partial x \partial y}\right)^2\right\}$$

where Mn denote the remaining magnetic number Mn_F.

1.3 Literature Survey

The lid-driven cavity flow problem which is governed by N-S equations, has been studied extensively in the literature as a validation problem for 2-D incompressible flow algorithms. Results are available for finite difference, finite volume, boundary element, finite element and spectral methods. Burggraf [17] is one of the earliest scientists who studied the problem. His work provided analytical solutions for an eddy bounded by a circular streamline. Besides, Burggraf presented results for Reynolds numbers up to 1000, for the solutions of N-S equations for an eddy in a square cavity driven by a moving top lid by using a second order finite difference approximation. Ghia *et al.* [32] were among the first to provide detailed solutions of the lid-driven cavity problem for Reynolds numbers up to 10000. They employed a coupled strongly implicit multigrid (CSI-MG) method. Barragy and Carey [9] presented p-type finite element formulation combined with a strongly graded and refined element mesh providing a highly accurate calculation. The results are obtained in terms of streamlines and vorticity contours for Reynods number values up to 12500. New tertiary and quaternary corner vortex features in the flow field are reported. Botella and Peyret [13] applied Chebyshev collocation method to solve the lid-driven cavity problem, and achieved accurate results by using the leading term of the asymptotic expansion of the solution in the vicinity of the corner where there is a discontinuity of velocity. Critical comparison with former numerical experiments for the flow at Reynolds number value 1000 is provided in their study. Auteri *et al.* [8] have shown singularity subtraction scheme based on a split approach to the vorticity and stream function equations. A Galerkin-Legendre approximation of the problem for the perturbation, and an evaluation of the nonlinear terms by Gauss-Legendre numerical integration have been used. Results for Re=0, 100, and 1000 compare well with

the benchmark steady solutions provided by the collocation-Chebyshev projection method. An implicit finite volume method has been used to obtain the solution of the Navier-Stokes equations by Sahin and Owens [64] in a lid-driven cavity for Re values up to 10000. Erturk et $al.$ [27], presented a finite difference formulation of the Navier-Stokes equations in stream function and vorticity formulation and obtained steady solutions using a uniform mesh of 601×601 for Reynolds number values up to 21000.

Natural convection flows in enclosures have also been investigated by many researchers. De Vahl Davis [22] obtained an accurate solution of the equations governing the two-dimensional natural convection in a square cavity with differentially heated walls. The equations are modified to involve time derivatives, and the results are obtained for Rayleigh number values between 10^3, and 10^6, using finite difference method (forward differences for the time derivatives and second-order central difference for spatial derivatives). Rasoul and Prinos [58], showed that the flow and the temperature fields in a square enclosure are greatly affected by the inclination of the enclosure. Ding et $al.$ [23] presented a mesh free finite difference scheme based on the weighted least-square approximation procedure together with a Taylor series expansion of the unknown function to solve the natural convection equations in terms of stream function vorticity and temperature. In their study, the streamlines and isotherms are visualized for $Ra = 10^4$ and 10^5. Roy and Basak [61], have solved natural convection flow in a square cavity with a sinusoidal temperature variation by using Galerkin FEM. They observed that for the case of this non-uniform heating, the heat transfer rate is maximum at the center of the heated wall. Bilgen and Yedder [11], also analyzed sinusoidal temperature boundary conditions for natural convection flow in enclosures using SIMPLER algorithm. Lo et $al.$ [46] also considered the natural convection problem in differentially heated enclosures for Ra values up to 10^7. In this study, velocity-vorticity formulation of the governing equations are considered using differential quadrature method, and the coupled equations are solved simultaneously by imposing the vorticity definition at boundary without any iterative procedure.

An externally applied magnetic field also influences the flow and heat transfer in natural convection flow when the fluid inside the enclosure is electrically conducting. Karcher et $al.$ [41] and Kakarantzas et $al.$ [40] investigated the effect of a vertical magnetic field on the convective heat transfer in a cylindrical container filled by a liquid metal heated locally from above. Studies of natural convection flow in rectangular enclosures with transverse magnetic fields have been reported in [66, 30] and with vertical magnetic fields in [62]. Effect of magnetic field on the natural convection flow in a liquid gallium filled square cavity for linearly heated side walls is given in [67]. They obtained results by using penalty finite element method up to $Ha = 100$ and $Ra = 10^5$. Mahmud and Fraser [48], investigated the MHD free convection and entropy generation for a square cavity for low Hartmann numbers indicating that higher values of Hartmann number retard the fluid motion in the cavity. Hady et $al.$ [34], solved MHD free convection flow along a vertical wavy surface with heat generation or absorbtion. Chamkha [19], solved numerically the MHD flow in a vertical lid-driven cavity considering

heat generation or absorption. Ece and Buyuk [25], give differential quadrature solutions of natural convection flow under a magnetic field in an inclined rectangular enclosure heated or cooled on adjacent walls, and with isothermal vertical or adiabatic horizontal walls. They showed that convection becomes stronger as Ra increases while the magnetic field suppresses the convective flow and the heat transfer rate. Oztop *et al.* [56], have analyzed MHD buoyancy-induced flow in an non-isothermally heated square enclosure by using finite volume method.

The magnetohydrodynamic flow and heat transfer of a viscous, electrically conducting, incompressible fluid between two parallel plates has been studied by many researchers due to the important applications. Nigam and Singh [55] and Alpher [2] considered thermally developed MHD flow between parallel plates by adopting small temperature differences and constant viscosity parameter. Some exact and numerical solutions for the MHD heat transfer problems are found in [7] and [55]. Attia and Kotb [7], studied the steady MHD flow and heat transfer by considering an exponential temperature variation of the viscosity in a channel between parallel plates. More accurate behavior of the flow and heat transfer is captured by taking temperature dependent viscosity especially under the effect of externally applied magnetic field. Attia extended the analysis in [7] including the time derivatives for the MHD flow and heat transfer in [3]. Attia in [4], studied the influence of variation in physical variables on the steady Hartmann flow with heat transfer. He has used finite difference method in all of his studies for discretizing the governing equations and obtaining numerical solutions. A hybrid solution technique (generalized integral transform) has been used by Lima *et al.* [45] for the MHD flow and heat transfer of a Newtonian fluid in parallel-plates channels. In their work, both the stationary plates and moving upper plate cases, and the inflow/outflow through plates are considered with the assumption of variable viscosity. In the above mentioned studies the plates are oriented in two directions by taking infinite lengths and thus the flow can be considered as one-dimensional. The effect of variable properties on the unsteady Couette flow with heat transfer under a magnetic field is given in [5] by taking into account two components of the velocity field, and the variation is again in one dimension. In the papers of Sweet *et al.* [71] and Maikap [49], MHD flow of a viscous fluid between moving parallel plates and plates with smooth expansion are given respectively. In these papers, the homotopy analysis and finite difference methods have been used, respectively. A series solution has been constructed using homotopy analysis method (HAM) for the MHD flow of an incompressible second grade fluid past a semi-infinite fixed plate in [37]. Influence of thermal radiation on the MHD flow has been also examined including coupled energy equation in the solution procedure. Later, Hayat and Qasim have applied HAM to obtain analytical solution for heat and mass transfer over a stretching sheet in the presence of Joule heating and thermophoresis in Darcian porous medium [38].

Singh [68] considered the flow of a conducting viscous incompressible fluid with embedded non-conducting identical spherical particles through a long rectangular channel under the influence of a uniform magnetic field with a time varying several cases for pressure gradient. The governing equations in this study are solved using finite cosine transforms. Chamkha [18] used two-phase continuum model to

formulate the problem of unsteady laminar flow and heat transfer of a particulate suspension in an electrically conducting fluid through channels and also circular pipes in the presence of a uniform transverse magnetic field. Numerical solutions are obtained based on finite difference methods. Attia in [6] studied the unsteady Couette flow and heat transfer of a dusty conducting fluid between two parallel plates with temperature dependent viscosity and thermal conductivity, under the assumption of constant pressure gradient and an external uniform magnetic field. The governing coupled momentum and energy equations in his study are solved numerically using finite differences. Sreeharireddy *et al.* [70] considered the flow of a viscous conducting liquid with uniform distribution of dust particles in a channel under the influence of a uniform transverse magnetic field with linearly varying time dependent pressure gradient. The unsteady flow and heat transfer of a dusty fluid between two parallel plates with variable viscosity and electrical conductivity is studied by Makinde and Chinyoka in [50]. In their study, the fluid is driven by a constant pressure gradient, and an external uniform magnetic field is applied perpendicular to the plates with a Navier-slip boundary condition. A semi-implicit finite difference scheme is used, and the effects of the wall slip parameter, viscosity, electrical conductivity variation, and the uniform magnetic field on the velocity and temperature fields for both the fluid and dust particles are discussed. Saidu *et al.* [65] studied laminar convective flow of an incompressible, conducting, viscous fluid embedded with non-conducting dust particles through a porous medium in the presence of uniform magnetic field. Constant pressure gradient and volume fraction of a dust particle are taken into account when one plate of the channel is fixed and the other is oscillating in time. Eguía *et al.* [26] investigated the effects of dependence on temperature of the viscosity, electric conductivity, Reynolds number and particle concentration on the unsteady MHD flow. In their study, the velocity and the temperature of a dusty, electrically conducting fluid are obtained between parallel plates in the presence of an external uniform magnetic field using the network simulation method (NSM) with the electric circuit simulation program Pspice.

Many numerical methods have been introduced for approximate solutions of blood flow problems under the imposition of a magnetic field. Haik *et al.* developed a mathematical model of biomagnetic fluid flow, and studied the apparent viscosity due to magnetic field effects on human body in [36]. They showed experimentally that blood flow rate under gravity is reduced by %30 under the action of a high intensity magnetic field ($10T$). Loukopoulos and Tzirtzilakis [47] investigated numerically by using FDM, the influence of spatially-varying magnetic field on biomagnetic flow and heat transfer between two parallel plates. Tzirtzilakis [74] analyzed the laminar biomagnetic blood flow in a 3-D conduit using FDM. Time-dependent biomagnetic fluid flow equations in a 2-D rectangular channel were solved with a pseudo-transient technique in the work of Tzirtzilakis [76]. A grid stretching was used to be dense at the area where the major disturbances of the flow are expected. Tzirtzilakis [75] has also studied biomagnetic fluid flow in a channel with stenosis under the influence of a steady localized magnetic field by using finite difference method with a semi-implicit pseudo-transient numerical methodology. Time variable played the role of iteration between the equations, and again stretching of the grid was used. Neofytou and Drikasis [53] investigated

Newtonian and non-Newtonian modeling effects on the unsteady flow through a stenosis using the most well-documented blood constitutive equations with FVM. Their computations reveal that the results for the vortex formation and wall shear stress distribution are dependent on the non-Newtonian model. Krashan and Haik [43] studied laminar blood flow over a 2-D eccentric stenotic orifice subjected to a permanent magnet with FVM. Lorentz force was neglected and they found that the location of reattachment point downstream the orifice is altered according to the place and strength of the magnet. Numerical studies of blood flow in healthy, stenosed and stented carotid arteries were carried by Gay and Zhang [31] by using immersed FEM. They did not consider the magnetic field effect since the main aim of the study was to show the flexibilities in handling varying shapes of embedded structures of the blood flow. Li and Huang [44] have considered solutions to non-Newtonian, electrically conducting biomagnetic fluid flow and heat transfer using FVM. Effect of magnetic field has been shown in the presence of stenosis. A fully closed systems of momentum and magnetic field equations are solved with FVM accounting for the Lorentz force and magnetization force in the study of Kenjeres [42]. A modified finite difference algorithm was introduced in [63] for solving biomagnetic fluid flow in a channel in the absence of energy equation. In this study, dual time stepping scheme and point-implicit five-stage Runge-Kutta (RK5) method were implemented to enhance the efficiency and the stability in the iterative solution procedure. Bhargava *et al.* [10] used FEM for solving 2-D biomagnetic micropolar flow in a square geometry. The effect of magnetization of the fluid is added in momentum equations. They showed that increasing the biomagnetic parameter decreases translational velocities, whereas they are increased with a rise in microinertia parameter. Ikbal [39] obtained numerical solutions for blood flow considering a viscoelastic fluid having shear-thinning rheology which was characterized by generalized Oldroyd-B model, using a control volume-based finite difference method known as MAC (Marker and Cell). Recently, Tzirakis *et al.* [73] presented a mathematical model for the description of biomagnetic Newtonian fluid flow for investigating the effects of magnetic field produced by a constant current carrying infinite wire, and a dipole like field. The results are obtained on straight and symmetrically stenosed channels. They used an open source adaptive mesh refinement solver (gnuid) which is based on a pressure correction scheme combining continuous Galerkin (for pressure) and discontinuous Galerkin (for velocity) methods. It was shown that a time invariant and irrotational magnetic field does not alter the velocity field, however, rotational magnetization forces alters the flow field. In another recent study, [77], Tzirtzilakis and Xenos studied the biomagnetic fluid flow in a lid-driven cavity under the influence of a steady localized magnetic field. In their study, finite volume method on a staggered grid was used for discretizing the non linear systems in the equations, and numerical solutions are obtained by the SIMPLE algorithm. It was shown that the application of the magnetic field below the bottom plate of the cavity, breaks characteristic primary vortex of the pure hydrodynamic flow. Also, the strength of the magnetic field influences the flow in terms of number of vortices reducing the velocities of the flow close to the bottom plate.

1.4 Plan of the Thesis

In the next chapter, the FEM analysis of two-dimensional flows of incompressible viscous fluids is presented. The FEM derivation of the N-S equations is introduced by demonstrating the fundamental steps of the method. The FEM formulation of N-S equations is extended through the additional steps for solving the natural convection flow equations. Next, FEM application to the natural convection flow equations involving magnetic field effect is given. Lastly, the numerical results and discussions are presented for several incompressible fluid flow problems.

In Chapter 3, Chebyshev spectral collocation method is developed for MHD flow and heat transfer problems. Both one-dimensional and two-dimensional laminar flows of incompressible viscous fluids are considered in various physical configurations. In particular, the Navier-Stokes equations, and natural convection flow under magnetic field equations are resolved, and both quantitative and qualitative comparison with the FEM results of Chapter 2 are presented. The CSCM solution to the problems of unsteady, one-dimensional MHD flow and heat transfer between parallel plates is presented. For the time discretization, an implicit backward finite difference scheme is made use of.

Chapter 4 presents the biomagnetic fluid flow (blood flow) and heat transfer in channels with various physical configurations. A BFD model consistent with both MHD and FHD principles is considered. Both steady and unsteady flows and heat transfer of a biomagnetic fluid are considered in channels without and with stenosis. The fluid is assumed as Newtonian, and both electrically conducting and nonconducting fluid flows are considered. The FEM and DRBEM applications are introduced for the steady biomagnetic fluid flow model where the fluid is considered as electrically non-conducting. FEM applications are presented for the solution of the problem for biomagnetic fluid flow through irregularly and multiply-stenosed channels.

Finally, Chapter 5 summarizes the work carried in the thesis, and discusses ideas for future research.

1.5 Contributions in the Thesis

In this thesis, numerical solutions to the problems of laminar, steady and/or unsteady flows of incompressible, viscous fluids are presented. Considered problems are mainly combined in three groups according to the numerical methods used or the physical configuration of the problems.

First, the incompressible fluid flow equations are solved in channels in terms of stream function and vorticity for laminar regime ($Re \leq 2000$) by using both FEM and CSCM. FEM with quadratic triangular elements gives more accurate results and solutions can be even obtained for Re values up to 10000 proving the capability of the FEM code prepared. CSCM gives results for up to $Re = 1000$

with considerably small number of collocation points and computational cost. Applications of both methods are extended to natural convection flow in enclosures and natural convection flow under a magnetic field in inclined enclosures for high values of Rayleigh number, $Ra = 10^6$, and Hartmann number values up to $Ha = 100$. In this part, high accuracy and efficiency of FEM using quadratic triangular elements have been shown comparing the solutions with the results obtained from CSCM which has the advantage of giving the same behavior of the flow with relatively small computational cost and work. This is the first contribution in the thesis.

In the second group of the problems, the simplicity and efficiency of CSCM in the computations has been made use of in solving unsteady one-dimensional MHD flow problems between parallel plates. The movement of one of the plates, additional equations due to the dust particles, variations of viscosity of the fluid, Navier-slip boundary conditions, and the intensity of the applied magnetic field are all considered as different physical situations and the solutions are simulated. This study constitutes the second major contribution of the thesis.

Finally, the biomagnetic fluid flow (blood flow) and heat transfer in channels between parallel plates imposed to a magnetic source below the channels, are simulated even when the channels have stenoses. Both electrically conducting and nonconducting fluid cases are considered, and for a poor conducting fluid, steady biomagnetic fluid flow equations are solved by using both FEM and DRBEM. Boundary only nature of BEM resulted in small algebraic systems giving the behavior of the flow and temperature at a small expense. However, FEM is more powerful for obtaining solutions for electrically conducting biomagnetic fluid flows for high values of problem parameters. By modifying the mesh generation (with quadratic triangular elements) which uses quite fine elements wherever required, it was possible to solve the biomagnetic fluid flow in irregularly-multiply-stenosed channels. A FEM based procedure was also derived for obtaining unknown vorticity boundary values in channels containing irregular stenoses. These are the most important original contributions obtained in the thesis in solving biomagnetic fluid flows.

CHAPTER 2

FEM Solution of Incompressible Fluid Flow Problems

In this chapter, the finite element method (FEM) analysis of two-dimensional flows of incompressible viscous fluids in laminar regimes is presented. The flow problems under consideration are governed by a set of coupled partial differential equations (PDEs), namely the continuity, momentum and energy equations which are the fundamental governing equations of fluid dynamics. The FEM analysis is widely used in computational fluid dynamics due to the considerable advantages such as the treatment of complex geometries, the consistent treatment of differential boundary conditions, the flexibility in program design for solving algebraic, differential and integral equations and obtaining higher order accuracy in solutions compared to the other numerical techniques. The analysis is first introduced by the FEM derivation of the Navier-Stokes (N-S) equations which constitute the fundamental equations in modeling fluid flow problems, and the basic steps of the method in details are presented in Section 2.1. The FEM formulation of N-S equations is extended through the additional steps for solving the natural convection flow equations in Section 2.2. The FEM formulations are finalized with the application to the natural convection flow equations involving magnetic field effect, and are presented in Section 2.3. The numerical results and discussions to selected incompressible fluid flow problems are provided in Section 2.4. The FEM formulations given in this chapter for the incompressible fluid flow problems involving temperature variations and external magnetic source effects constitute a basis for the FEM analysis of the biomagnetic fluid flow problems in Chapter 4.

The finite element method, basically seeks an approximation Φ_h to the solution Φ of a boundary value problem,

$$\mathcal{L}\Phi = g(x, y)$$

$$\mathcal{B}\Phi = s(x, y)$$

$$(2.1)$$

in the form

$$\Phi \approx \Phi_h = \sum_{j=1}^{n} \Phi_j N_j \qquad (2.2)$$

where Φ_j are the nodal values of Φ_h, N_j are the interpolation functions and n is the number of nodes in the problem domain. In the boundary problem (2.1), $\mathcal{L}$ is

the differential operator, $\mathcal{B}$ is the boundary operator which can involve Dirichlet, Neumann or mixed type of boundary conditions, g and s are known functions in the problem domain and on the boundary, respectively. Generally, substituting these approximations does not result in necessary and sufficient number of equations to determine the unknown coefficients Φ_j. Hence, weighted integral form of the governing equations are used to obtain the necessary and sufficient equations. The fundamental steps of FEM usually start with the discretization of the problem domain into a set of elements which are called finite elements. Next, the weak or weighted integral equations of the governing differential equations are obtained. Interpolating functions are derived and the discretized FEM equations are obtained via the weak form. The assembly of the finite elements and the imposition of the boundary conditions follows. Finally, the system of algebraic equations is solved to obtain all unknowns through the problem domain. This general concept of finite element method is detailed with its application to the Navier-Stokes equations defined in a closed domain together with Dirichlet or Neumann type boundary conditions.

2.1 FEM analysis of Navier-Stokes Equations

The FEM formulation of Navier-Stokes equations starts with considering steady, laminar flow of an incompressible fluid in a domain Ω, and taking them in terms of stream function ψ and vorticity w which are introduced in Section 1.1.1 as

$$\nabla^2 \psi = -w \, , \tag{2.3}$$

$$\frac{1}{Re}\nabla^2 w + \frac{\partial \psi}{\partial x}\frac{\partial w}{\partial y} - \frac{\partial \psi}{\partial y}\frac{\partial w}{\partial x} = f \, . \tag{2.4}$$

The equations are given in non-dimensional form, ∇^2 is the Laplace operator, Re is the dimensionless parameter Reynolds number and f is the forcing function. The equations are accompanied by the no-slip wall conditions for the velocity which are converted into Dirichlet type boundary conditions for stream function and vorticity, on the boundary $\partial\Omega$. The derivation of unknown boundary conditions for the vorticity transport equation is given in Section 2.1.1.

A weak form is a weighted integral statement of a differential equation where the differentiation is distributed among the dependent variable and the weight function, and also includes the natural boundary conditions of the problem. The weak form of the N-S equations, (2.3) and (2.4), is developed by first multiplying the equations with the weight functions ω_1 and ω_2, respectively. The weight functions are taken from the space of admissible functions that satisfy the homogeneous Dirichlet boundary conditions and are assumed to be differentiable twice with respect to the space variables x and y, for the integrals appearing in the variational problem to be well defined, [52, 59]. Integrating over the problem

domain, the resulting weighted averages are set equal to zero

$$\int_\Omega \omega_1 \left(\nabla^2 \psi + w \right) d\Omega = 0 \tag{2.5}$$

$$\int_\Omega \omega_2 \left(\frac{1}{Re} \nabla^2 w + \frac{\partial \psi}{\partial x} \frac{\partial w}{\partial y} - \frac{\partial \psi}{\partial y} \frac{\partial w}{\partial x} - f \right) d\Omega = 0 \, . \tag{2.6}$$

Applying the divergence theorem to the weighted residual formulations, the weak form of the equations (2.3) and (2.4) is obtained as

$$-\int_\Omega \left(\frac{\partial \omega_1}{\partial x} \frac{\partial \psi}{\partial x} + \frac{\partial \omega_1}{\partial y} \frac{\partial \psi}{\partial y} \right) d\Omega + \int_\Omega \omega_1 w d\Omega + \int_{\partial\Omega} \omega_1 \frac{\partial \psi}{\partial n} ds = 0 \tag{2.7}$$

$$-\frac{1}{Re} \int_\Omega \left(\frac{\partial \omega_2}{\partial x} \frac{\partial w}{\partial x} + \frac{\partial \omega_2}{\partial y} \frac{\partial w}{\partial y} \right) d\Omega + \int_\Omega \omega_2 \left(\frac{\partial \psi}{\partial x} \frac{\partial w}{\partial y} - \frac{\partial \psi}{\partial y} \frac{\partial w}{\partial x} \right) d\Omega$$

$$-\int_\Omega \omega_2 f d\Omega + \frac{1}{Re} \int_{\partial\Omega} \omega_2 \frac{\partial w}{\partial n} ds = 0 \tag{2.8}$$

where $\mathbf{n} = (n_x, n_y)$ is the unit normal vector pointing outward on the boundary $\partial\Omega$. The region Ω is divided into finite elements to reduce the approximate solution to each element. These elements can be triangles or quadrilaterals or any flat planar geometric shapes in 2-D. In this study, quadratic type triangular elements having six nodes which are located at the vertices and on midpoints of each edge are used to discretize the problem domain. It is assumed that the unknowns ψ and w, and the source function f can be approximated over an element e by using quadratic shape functions,

$$\psi^e(x, y) \approx \sum_{j=1}^6 \psi_j^e N_j^e(x, y),$$

$$w^e(x, y) \approx \sum_{j=1}^6 w_j^e N_j^e(x, y), \tag{2.9}$$

$$f^e(x, y) \approx \sum_{j=1}^6 f_j^e N_j^e(x, y) \, .$$

The quadratic shape functions N_j^e's are given in area coordinates [28, 52], as

$$\begin{array}{lll} N_1^e = \xi_1(2\xi_1 - 1), & N_2^e = \xi_2(2\xi_2 - 1), & N_3^e = \xi_3(2\xi_3 - 1) \\ N_4^e = 4\xi_1\xi_2, & N_5^e = 4\xi_2\xi_3, & N_6^e = 4\xi_1\xi_3 \end{array} \tag{2.10}$$

and $\xi_i = A_i/A_e$, $(i = 1, 2, 3)$ are linear shape functions given in local area coordinates for each element. ψ_i^e, w_i^e and f_i^e are the nodal values of ψ, w and f over an element e, respectively. Here, A_e is the area of the triangle, and A_i's are

the areas of the subtriangles formed by using vertices with the centroid of the triangle as shown in Figure 2.1. The quadratic interpolation functions N_i^e satisfy the cardinal property that $N_i^e = 1$ at the i-th node, and $N_i^e = 0$ at other nodes of the element e, that is,

$$N_i^e(x_j, y_j) = \delta_{ij}$$

where δ_{ij} is the Kronecker's delta function.
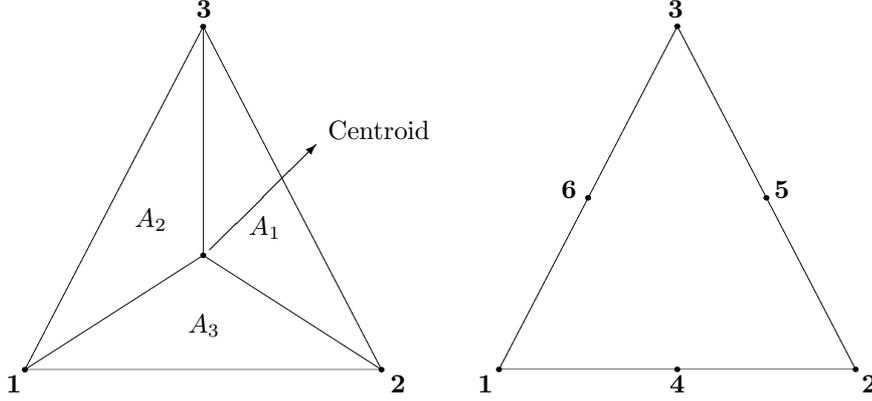
Figure 2.1: Three-nodal (linear) and six-nodal (quadratic) triangular elements.

In Galerkin method which is a weighted residual method, weight function ω_i is taken as equal to the shape function used in the approximation of the solution. Substituting the approximations (2.9) into the equations (2.7) and (2.8), and dropping the boundary integrals due to the property of shape functions to be vanished for Dirichlet type boundary conditions, the integral equations for any six-nodal triangular element Ω_e are written as

$$-\int_{\Omega_e} \left(\frac{\partial N_i^e}{\partial x} \sum_{j=1}^{6} \frac{\partial N_j^e}{\partial x} + \frac{\partial N_i^e}{\partial y} \sum_{j=1}^{6} \frac{\partial N_j^e}{\partial y} \right) \psi_j^e d\Omega_e + \int_{\Omega_e} N_i^e \sum_{j=1}^{6} N_j^e w_j^e d\Omega_e = 0$$

(2.11)

$$-\frac{1}{Re} \int_{\Omega_e} \left(\frac{\partial N_i^e}{\partial x} \sum_{j=1}^{6} \frac{\partial N_j^e}{\partial x} + \frac{\partial N_i^e}{\partial y} \sum_{j=1}^{6} \frac{\partial N_j^e}{\partial y} \right) w_j^e d\Omega_e - \int_{\Omega_e} N_i^e \sum_{j=1}^{6} N_j^e f_j^e d\Omega_e$$

$$-\int_{\Omega_e} N_i^e \left[\left(\sum_{k=1}^{6} \frac{\partial N_k^e}{\partial y} \psi_k^e \right) \sum_{j=1}^{6} \frac{\partial N_j^e}{\partial x} - \left(\sum_{k=1}^{6} \frac{\partial N_k^e}{\partial x} \psi_k^e \right) \sum_{j=1}^{6} \frac{\partial N_j^e}{\partial y} \right] w_j^e d\Omega_e = 0 \,,$$

(2.12)

where $i = 1, ..., 6$.

After the integrals are evaluated over the element e by using the area coordinates ξ_i, where $i = 1, 2, 3$, these equations can be written as 6×6 matrix-vector equations as

$$[K^e]\{\psi^e\} = [M^e]\{w^e\} \tag{2.13}$$

$$-\frac{1}{Re}[K^e]\{w^e\} - [A^e]\{w^e\} = [M^e]\{f^e\} \tag{2.14}$$

for each element e, in which the element-level matrices are defined as

$$K_{ij}^e = \int_{\Omega_e} \left(\frac{\partial N_i^e}{\partial x}\frac{\partial N_j^e}{\partial x} + \frac{\partial N_i^e}{\partial y}\frac{\partial N_j^e}{\partial y} \right) d\Omega_e$$

$$A_{ij}^e = \int_{\Omega_e} N_i^e \left[\left(\sum_{k=1}^{6} \frac{\partial N_k^e}{\partial y}\psi_k^e \right) \frac{\partial N_j^e}{\partial x} - \left(\sum_{k=1}^{6} \frac{\partial N_k^e}{\partial x}\psi_k^e \right) \frac{\partial N_j^e}{\partial y} \right] d\Omega_e$$

$$M_{ij}^e = \int_{\Omega_e} N_i^e N_j^e d\Omega_e \, .$$

After performing the assembly procedure which connects all local element equations to the global equation system over the whole problem domain, the global matrix-vector systems are obtained

$$[K]\{\psi\} = [M]\{w\} \tag{2.15}$$

$$-\frac{1}{Re}[K]\{w\} - [A]\{w\} = [M]\{f\} \tag{2.16}$$

where the global matrices and force vector are

$$[K] = \sum_{e=1}^{M_e} \int_{\Omega_e} \left(\frac{\partial N_i^e}{\partial x}\frac{\partial N_j^e}{\partial x} + \frac{\partial N_i^e}{\partial y}\frac{\partial N_j^e}{\partial y} \right) d\Omega_e$$

$$[A] = \sum_{e=1}^{M_e} \int_{\Omega_e} N_i^e \left[\left(\sum_{k=1}^{6} \frac{\partial N_k^e}{\partial y}\psi_k^e \right) \frac{\partial N_j^e}{\partial x} - \left(\sum_{k=1}^{6} \frac{\partial N_k^e}{\partial x}\psi_k^e \right) \frac{\partial N_j^e}{\partial y} \right] d\Omega_e$$

$$[M] = \sum_{e=1}^{M_e} \int_{\Omega_e} N_i^e N_j^e d\Omega_e$$

$$\{f\} = \sum_{e=1}^{M_e} f_j^e \, .$$

Here, $i, j = 1, ..., 6$ refer to nodes for the element e, and the summation $\sum_{e=1}^{M_e}$ addresses the assembly procedure, which results in a system of equations of size equal to the number of total nodes in the solution domain. The matrices $[K]$, $[A]$, $[M]$ are generally referred as the stiffness, advection and mass matrices, respectively. The integrations are carried out using an isoparametric interpolation

in which an arbitrary triangular element on the physical xy-plane of the problem is mapped to the standard right isosceles triangle in the parametric $\zeta\eta$-plane as shown in Figure 2.2 by a coordinate transformation

$$x = \sum_{j=1}^{6} x_j^e N_j^e \qquad y = \sum_{j=1}^{6} y_j^e N_j^e$$

where N_j^e are the shape functions given in (2.10). The integrands are transformed from six-nodal physical triangle to the standard triangle, and the integrals are approximated using six-point Gauss triangle quadrature [57, 59]. If the boundary conditions are given in terms of normal derivatives (Neumann type), the boundary integrals in (2.7) and (2.8) are also evaluated for each element e and then go through the assembly procedure for the whole domain. Since these boundary integrals contain the unknowns stream function ψ and vorticity w, the stiffness matrix $[K]$ will include extra terms corresponding to these integrals.
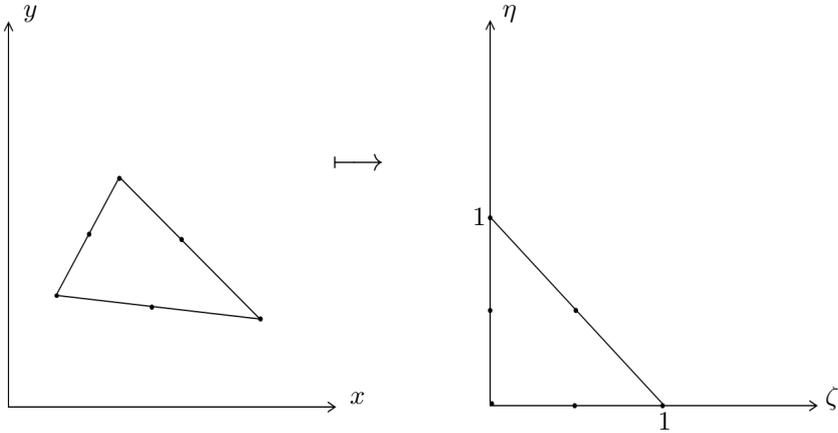
Figure 2.2: Mapping from physical (x, y) plane to the parametric (ζ, η) plane.

2.1.1   Vorticity Boundary Conditions

As the equations are given in terms of stream function and vorticity, the boundary conditions for vorticity are physically unavailable. However, for the incompressible fluid flow problem to be well defined, appropriate boundary conditions for vorticity must be introduced. There are several approaches which can be considered to obtain the required boundary conditions. Throughout this chapter, a Taylor series approximation of the stream function equation (2.3) on the boundary is considered. The relation

$$w_{i,j} = \nabla^2 \psi_{i,j} \tag{2.17}$$

is used to calculate the missing vorticity boundary conditions where (i, j) is a boundary node. In this approach, $\dfrac{\partial^2 \psi}{\partial n^2}$ is approximated on a boundary node 0 as

$$\psi_{nn}|_0 = a_0 \psi_0 + a_1 \psi_p + a_2 \psi_q + a_3 \psi_n \tag{2.18}$$

32

where 0, p and q subscripts indicate ψ values on the boundary node, and ph and qh distance away nodes along the normal direction **n**. The Taylor series approximation of ψ_p and ψ_q about the node 0 are written and reorganizing,

$$\psi_{nn}|_0 = \psi_0(a_0 + a_1 + a_2) + \psi_n|_0 \left(pha_1 + qha_2 + a_3\right) + \psi_{nn}|_0 \left(p^2 h^2 a_1/2 + q^2 h^2 a_2/2\right)$$

is obtained. By equating the coefficients of the same derivative terms on both sides, the coefficients a_0, a_1, a_2 and a_3 are obtained as follows

$$a_0 = \frac{-2(p^3 - q^3)}{h^2 p^2 q^2 (p-q)}, \quad a_1 = \frac{-2q}{h^2 p^2 (p-q)}, \quad a_2 = \frac{2p}{h^2 q^2 (p-q)}, \quad a_3 = \frac{-2(p+q)}{hpq}$$

where $p \neq q$ are positive integers. Consequently, the boundary approximation for the vorticity w_0 can be written as

$$w_0 = -\left(a_0 \psi_0 + a_1 \psi_p + a_2 \psi_q + a_3 \psi_n\right). \tag{2.19}$$

The Equation (2.19), involves the stream function values at distances ph and qh from the boundary, which are assumed to be known. In addition, when the boundary values of ψ, ψ_n are prescribed, Equation (2.19) can be used to approximate the unknown vorticity boundary condition with a truncation error of order $O(h^2)$.

2.1.2 Iterative Solution Procedure

Finite element application to N-S equations using Galerkin approach results in two coupled nonlinear matrix-vector equations (2.15) and (2.16) for stream function and vorticity, respectively. Due to the nonlinearity, the coupled system of equations is solved iteratively so that the system of equations is reduced to a set of two linear algebraic equations in every iteration. The algebraic equations are solved imposing the Dirichlet type boundary conditions for stream function and the calculated boundary conditions for vorticity. In the iterative procedure, first the stream function equation (2.15) is solved by using an initial estimate for vorticity. Next, the calculated stream function values are used to obtain the boundary conditions for vorticity. In the calculation of vorticity boundary conditions, an experimentally determined smoothing parameter λ is made use of for increasing the convergence rate of the iterative procedure. The vorticity boundary values w_B, at the $(m+1)$-th iteration level are averaged by the corresponding values from the m-th level via the relation $w_B^{(m+1)} = \lambda w_B^{(m+1)} + (1-\lambda) w_B^{(m)}$ where $0 < \lambda < 1$. The final step of each iteration is to solve the vorticity equation (2.16) to obtain the vorticity values over the whole domain by using the newly obtained stream function values in the matrix $[A]$ and the derived boundary conditions of vorticity. These steps are repeated until a preassigned convergence criteria is met for both the stream function and the vorticity values on the whole computational domain with a given tolerance,

$$\left|\psi_{ij}^{(m+1)} - \psi_{ij}^{(m)}\right| \leq \varepsilon, \quad \left|w_{ij}^{(m+1)} - w_{ij}^{(m)}\right| \leq \varepsilon$$

where ij denotes the ij-th node varying from 1 to the total number of nodes in the domain.

2.2   Natural Convection Flow

This section extends the FEM analysis to natural convection flow equations which are resulting from the addition of energy equation to the Navier-Stokes equations. The natural convection flow which corresponds to the physical situation in which the heat flux occurs inside the fluid due to the interaction of the flow and the temperature difference of the fluid, is introduced in Section 1.1.2. The governing continuity, momentum and energy equations in terms of stream function ψ, vorticity w and temperature T are given in non-dimensional form as

$$\nabla^2 \psi = -w$$

$$\frac{\partial \psi}{\partial y}\frac{\partial w}{\partial x} - \frac{\partial \psi}{\partial x}\frac{\partial w}{\partial y} = Pr\nabla^2 w + RaPr\frac{\partial T}{\partial x} \qquad (2.20)$$

$$\frac{\partial \psi}{\partial y}\frac{\partial T}{\partial x} - \frac{\partial \psi}{\partial x}\frac{\partial T}{\partial y} = \nabla^2 T \ .$$

The dimensionless parameters Pr, Ra and Ha denote the Prandtl number, the Rayleigh number and the Hartmann number, respectively. The problem domain is usually taken as an enclousre $[0,1] \times [0,1]$ and the no-slip boundary conditions for the velocity are accompanied with Dirichlet type conditions for stream function and vorticity and/or homogenous Neumann type boundary conditions for the temperature as discussed in Section 1.1.2. The FEM formulation is analogous to that presented in the previous section for N-S equations, and starts with the development of the weak form of the equations in (2.20). The weak form is obtained by multiplying each equation in (2.20) with the corresponding weight functions ω_1, ω_2 and ω_3 for the stream function, vorticity and temperature, respectively. The weight functions ω_1, ω_2 and ω_3 are similarly taken from the space of admissible functions that satisfy the homogenous Dirichlet type boundary conditions and assumed to be twice differentiable with respect to the spatial variables. Then, integrating the weighted equations over the problem domain and setting equal to zero gives

$$\int_\Omega \omega_1 \left(\nabla^2 \psi + w \right) d\Omega = 0 \qquad (2.21)$$

$$\int_\Omega \omega_2 \left(Pr\nabla^2 w + RaPr\frac{\partial T}{\partial x} + \frac{\partial \psi}{\partial x}\frac{\partial w}{\partial y} - \frac{\partial \psi}{\partial y}\frac{\partial w}{\partial x} \right) d\Omega = 0 \qquad (2.22)$$

$$\int_\Omega \omega_3 \left(\nabla^2 T + \frac{\partial \psi}{\partial x}\frac{\partial T}{\partial y} - \frac{\partial \psi}{\partial y}\frac{\partial T}{\partial x} \right) d\Omega = 0 \qquad (2.23)$$

Applying the divergence theorem to reduce the derivative orders in Laplace terms, the weak form of the equations in (2.20) is obtained as follows,

$$-\int_\Omega \left(\frac{\partial \omega_1}{\partial x}\frac{\partial \psi}{\partial x} + \frac{\partial \omega_1}{\partial y}\frac{\partial \psi}{\partial y} \right) d\Omega + \int_\Omega \omega_1 w d\Omega + \int_{\partial\Omega} \omega_1 \frac{\partial \psi}{\partial n} ds = 0 \qquad (2.24)$$

$$-Pr \int_\Omega \left(\frac{\partial \omega_2}{\partial x} \frac{\partial w}{\partial x} + \frac{\partial \omega_2}{\partial y} \frac{\partial w}{\partial y} \right) d\Omega + \int_\Omega \omega_2 \left(\frac{\partial \psi}{\partial x} \frac{\partial w}{\partial y} - \frac{\partial \psi}{\partial y} \frac{\partial w}{\partial x} \right) d\Omega$$

$$+RaPr \int_\Omega \omega_2 \frac{\partial T}{\partial x} d\Omega + Pr \int_{\partial\Omega} \omega_2 \frac{\partial w}{\partial n} ds = 0 \tag{2.25}$$

$$-\int_\Omega \left(\frac{\partial \omega_3}{\partial x} \frac{\partial T}{\partial x} + \frac{\partial \omega_3}{\partial y} \frac{\partial T}{\partial y} \right) d\Omega + \int_\Omega \omega_3 \left(\frac{\partial \psi}{\partial x} \frac{\partial T}{\partial y} - \frac{\partial \psi}{\partial y} \frac{\partial T}{\partial x} \right) d\Omega$$

$$+ \int_{\partial\Omega} \omega_3 \frac{\partial T}{\partial n} ds = 0 . \tag{2.26}$$

The unknowns ψ, w and T are approximated over an element by using quadratic shape functions N_j^e's given in (2.10) as follows

$$\psi^e(x,y) \approx \sum_{j=1}^{6} \psi_j^e N_j^e(x,y), \quad w^e(x,y) \approx \sum_{j=1}^{6} w_j^e N_j^e(x,y),$$

$$T^e(x,y) \approx \sum_{j=1}^{6} T_j^e N_j^e(x,y). \tag{2.27}$$

Following the steps of the previous section, the integral equations (2.24)-(2.26) for each element e are written by dropping the boundary integrals as the shape functions ω_1 and ω_2 vanish due to the Dirichlet boundary conditions for stream function and vorticity, respectively. For the temperature equation, the walls are either heated or cooled (Dirichlet type boundary condition) or adiabatic (normal derivatives are zero). Thus, in both cases the boundary integral in (2.26) drops. Discretizing the domain by using six-nodal triangular elements and evaluating the integrals over each element results in 6×6 systems of matrix-vector equations for stream function, vorticity and temperature equations. The assembly procedure results in the algebraic systems of equations with the size equals to the number of total nodes for each system

$$[K]\{\psi\} = [M]\{w\} \tag{2.28}$$

$$Pr[K]\{w\} + [A]\{w\} = RaPr\{F_1\} \tag{2.29}$$

$$[K]\{T\} + [A]\{T\} = 0 \tag{2.30}$$

where the matrices $[K]$, $[A]$ and $[M]$ are defined in the previous section, and the vector $\{F_1\}$ is given as

$$\{F_1\} = \sum_{e=1}^{M_e} \int_{\Omega_e} N_i^e \left(\sum_{j=1}^{6} \frac{\partial N_j^e}{\partial x} T_j^e \right) d\Omega_e$$

where $i = 1, ..., 6$ and as before, the summation $\sum_{e=1}^{M_e}$ indicates the assembly procedure over all elements. The existence of the nonlinear terms in the coupled Equations (2.28)-(2.30) necessitates an iterative solution procedure. The scheme described in Section 2.1.2 is extended so as to include the temperature equation (2.30). In each iteration, the stream function equation (2.28) is first solved using an initial guess for vorticity. Next, the boundary conditions for vorticity are obtained via Equation (2.19) derived in Section 2.1.1. A smoothing parameter, λ, for vorticity boundary values is made use of to accelerate the convergence of the solution (see Section 2.1.1). Having the vorticity boundary conditions computed, the vorticity equation (2.29) is solved to obtain the vorticity values on the whole computational domain. The final step of each iteration is to solve the temperature equation (2.30) using the newly calculated stream function and vorticity values. This iterative procedure is terminated when the convergence criteria between two successive iterations for all unknowns is satisfied so that,

$$\left| \psi_{ij}^{(m+1)} - \psi_{ij}^{(m)} \right| \le \varepsilon, \quad \left| w_{ij}^{(m+1)} - w_{ij}^{(m)} \right| \le \varepsilon, \quad \left| T_{ij}^{(m+1)} - T_{ij}^{(m)} \right| \le \varepsilon$$

where ε is the convergence tolerance and ij denotes the ij-th node varying from 1 to the total number of nodes in the domain as in Section 2.1.2.

2.3   Natural Convection Flow in Enclosures under a Magnetic Field

The FEM discretization of natural convection flow equations is extended to the case where an externally applied magnetic field is involved, in this section. The induced magnetic field inside the fluid is neglected. In the case where the external magnetic field is applied with an angle φ from the x-axis and the square cavity is inclined from horizontal with an angle ϕ (see Figure 2.3), the governing equations in stream function, vorticity and temperature are given as in Section 1.1.3,

$$\nabla^2 \psi = -w$$

$$Pr\nabla^2 w = \frac{\partial \psi}{\partial y}\frac{\partial w}{\partial x} - \frac{\partial \psi}{\partial x}\frac{\partial w}{\partial y} - RaPr\left(\cos\phi\frac{\partial T}{\partial x} - \sin\phi\frac{\partial T}{\partial y}\right)$$

$$-Ha^2 Pr\left[\cos\varphi\left(\sin\varphi\frac{\partial^2\psi}{\partial x\partial y} + \cos\varphi\frac{\partial^2\psi}{\partial x^2}\right)\right. \tag{2.31}$$

$$\left. +\sin\varphi\left(\sin\varphi\frac{\partial^2\psi}{\partial y^2} + \cos\varphi\frac{\partial^2\psi}{\partial y\partial x}\right)\right]$$

$$\nabla^2 T = \frac{\partial \psi}{\partial y}\frac{\partial T}{\partial x} - \frac{\partial \psi}{\partial x}\frac{\partial T}{\partial y}.$$

The no-slip boundary conditions for the velocity are converted into stream function boundary conditions so that the stream function is specified on the walls of the cavity, and the normal derivatives of stream function are made use of in calculating the vorticity wall conditions. Thus, the stream function equation and vorticity equation are accompanied by Dirichlet type boundary conditions. For the temperature equation, both Dirichlet type boundary conditions and homogenous Neumann type boundary conditions are taken into consideration since heated and/or adiabatic walls may physically be given.
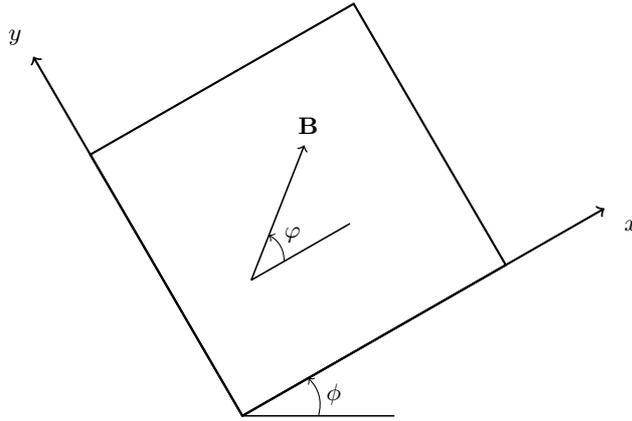
Figure 2.3: Problem configuration for MHD natural convection flow.

Comparing Equations (2.20) and (2.31) it can be seen that the effect of heat exchange appears as temperature convection terms through the inclination angle ϕ. The external magnetic field effect is introduced as multiplication of velocity variations by Ha^2 and Pr in the last term on the right hand side of the vorticity transport equation. The stream function and temperature equations remain unchanged. Therefore, the FEM methodology described for Equations (2.20) will only differ in the second and third terms of the right hand side of the vorticity equation. The FEM discretized systems for Equations (2.31) can then be written as follows

$$[K]\{\psi\} = [M]\{w\} \tag{2.32}$$

$$Pr\,[K]\{w\} + [A]\{w\} = RaPr\,\{F_2\} + Ha^2 Pr\,\{F_3\} \tag{2.33}$$

$$[K]\{T\} + [A]\{T\} = 0\,. \tag{2.34}$$

The matrices $[K]$, $[A]$ and $[M]$ are defined in Section 2.1, the vectors $\{F_2\}$ and $\{F_3\}$ are defined as,

$$\{F_2\} = \sum_{e=1}^{M_e} \int_{\Omega_e} N_i^e \left(\cos\phi \sum_{j=1}^{6} \frac{\partial N_j^e}{\partial x} T_j^e - \sin\phi \sum_{j=1}^{6} \frac{\partial N_j^e}{\partial y} T_j^e \right) d\Omega_e$$

37

$$\{F_3\} = \sum_{e=1}^{M_e} \int_{\Omega_e} N_i^e \left[\cos\varphi \left(\sin\varphi \sum_{j=1}^{6} \frac{\partial^2 N_j^e}{\partial x \partial y} \psi_j^e + \cos\varphi \sum_{j=1}^{6} \frac{\partial^2 N_j^e}{\partial x^2} \psi_j^e \right) \right.$$

$$\left. + \sin\varphi \left(\sin\varphi \sum_{j=1}^{6} \frac{\partial^2 N_j^e}{\partial y^2} \psi_j^e + \cos\varphi \sum_{j=1}^{6} \frac{\partial^2 N_j^e}{\partial x \partial y} \psi_j^e \right) \right] d\Omega_e \ .$$

Here, $i = 1, ..., 6$ and the $\sum_{e=1}^{M_e}$ as mentioned earlier, represents the assembly procedure. The iterative procedure given in the previous section is followed in solving the coupled equations (2.32)-(2.34). Each iteration starts with solving the stream function equation (2.32), and then, the vorticity wall conditions are approximated as given in Section 2.1.1. Henceforth, the vorticity equation (2.33) is solved to obtain all nodal values of the vorticity in the whole problem domain. As the final step of each iteration, the temperature equation (2.34) is solved. These iterations are carried on until the preassigned convergence tolerance is reached between two successive iterations for stream function, vorticity and temperature.

2.4 Numerical Results

This section presents FEM solutions to steady, two-dimensional, laminar flow problems of incompressible Newtonian fluids in square enclosures. First, in Section 2.4.1, the efficiency of the numerical method is tested through a problem defined by the Navier-Stokes equations where the exact solution is available. Second, solution to the flow in a lid-driven square cavity, the benchmark problem, is given in Section 2.4.2. Next, Section 2.4.3 presents the solution of natural convection flow in a square cavity. The natural convection flow is extended to the case where an external magnetic field takes place outside the enclosures, and two applications with different sets of boundary conditions reflecting different physical configurations are provided in Section 2.4.4. The numerical solutions are obtained using the iterative procedure discussed in Section 2.1.2. For the problems involving heat transfer, the iterative procedure is extended and the temperature equation is involved as explained in Section 2.2. The problem regions are discretized using quadratic triangular elements. A sample discretization using $M_e = 18$ elements and the local-global node numbering system are shown in Figure 2.4. The number of elements, M_e, used in the computations is specified in each problem. In the simulations, the iterations are initialized with zero estimates (for vorticity or temperature), and the converged results obtained for lower parameter values are used as starting vectors in the iterative procedures for higher parameters provided that the number of elements are equal. The systems of equations in each iteration, are solved using a MATLAB code involving a sparse system solver function, and the convergence tolerance in all test problems for all cases is taken as 10^{-6}.
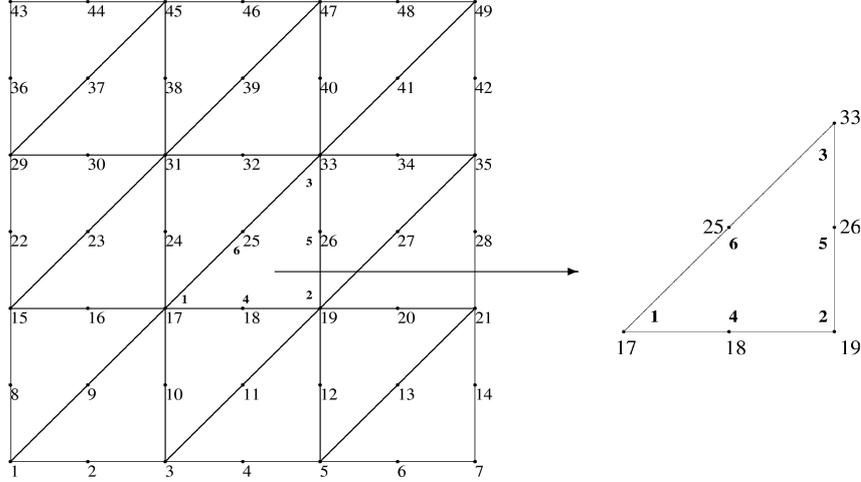
Figure 2.4: Sample discretization of a square region using $M_e = 18$ elements.

2.4.1 Navier-Stokes Equations with Exact Solution

A test problem with known solution is first solved to verify the accuracy of the FEM procedure given in Section 2.1. The N-S equations including an additional non-dimensional force term f which are given as

$$\nabla^2 \psi = -w, \tag{2.35}$$

$$\nabla^2 w + Re \left(\frac{\partial \psi}{\partial x} \frac{\partial w}{\partial y} - \frac{\partial \psi}{\partial y} \frac{\partial w}{\partial x} \right) = f, \tag{2.36}$$

are considered in a square domain where $0 \leq x, y \leq 1$. The problem constructed in [69] is designed so as to satisfy the no-slip boundary conditions ($u = v = 0$) and consequently the exact stream function is taken as

$$\psi_e = -8(x - x^2)^2(y - y^2)^2 . \tag{2.37}$$

The corresponding exact vorticity function is easily obtained from (2.35) as

$$w_e = 16[(6x^2 - 6x + 1)(y - y^2)^2 + (x - x^2)^2(6y^2 - 6y + 1)] . \tag{2.38}$$

The Dirichlet type boundary conditions for both stream function and vorticity are obtained directly from the exact solutions (2.37) and (2.38), respectively. The problem geometry and the boundary conditions are shown in Figure 2.5. The forcing function f is derived by substituting (2.37) and (2.38) into (2.36). Numerical calculations are performed for several values of Reynolds numbers, $Re = 0$, 10^3, 10^4 and 10^6. The $Re = 0$ case corresponds to the elimination of convective terms in the vorticity transport equation (Stoke's flow), whereas, $Re = 10^6$, is a case where the convective terms are highly dominating. The numerical solutions are obtained using $M_e = 800$ quadratic triangular elements for the cases
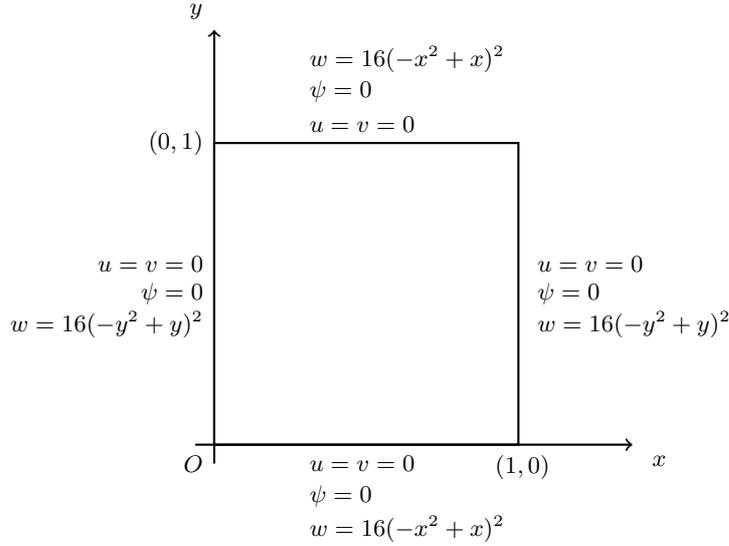
Figure 2.5: Domain and boundary conditions of Problem 2.4.1.

where $Re = 0$ and $Re = 10^3$, however, the solutions for higher values, $Re = 10^4$ and $Re = 10^6$, are obtained using $M_e = 1250$ elements. In order to investigate the efficiency of the numerical procedure quantitatively, the maximum absolute errors ϵ_ψ and ϵ_w are calculated for stream function and vorticity, respectively, which are defined as

$$\epsilon_\psi = \max_{ij} |\psi_{ij} - \psi_e(x_i, y_j)|, \quad \epsilon_w = \max_{ij} |w_{ij} - w_e(x_i, y_j)|$$

where the point (x_i, y_j) goes through all the nodes. It is obvious from the definitions of the exact stream function (2.37) and the exact vorticity function (2.38) that the solutions are independent of the Reynolds number. Figure 2.6 shows the streamlines and the vorticity contours for (a) $Re = 0$, (b) $Re = 10^3$, (c) $Re = 10^4$ and (d) $Re = 10^6$. The perfect agreement between the exact solution and the numerical solution guarantees the efficiency of the FEM for these types of flow problems even for high Re governing the flow. Moreover, Figure 2.6 presents the maximum error values for both the stream function and vorticity on the top of each plot. It is observed that the differences between the numerical solutions and the exact solutions are significantly small especially in the stream function. The error values increase with an increase in Re, particularly for vorticity, this increase is more pronounced which is an expected result due to the dependency of the vorticity equation on Re. Furthermore, the numerical tests performed using number of elements in the range $M_e = 32$ to $M_e = 5000$, for a fixed Reynolds number, $Re = 10^3$, to examine the dependence of M_e on ϵ_ψ and ϵ_w for stream function and vorticity, and the results are listed in Table 2.1. It is observed that, increasing M_e results in a continuous decrease in the error values for both the stream function and vorticity. The ϵ_ψ value is smaller compared to the ϵ_w value in each case, and this is an expected result due to the existence of nonlinear terms in the vorticity equation.

40
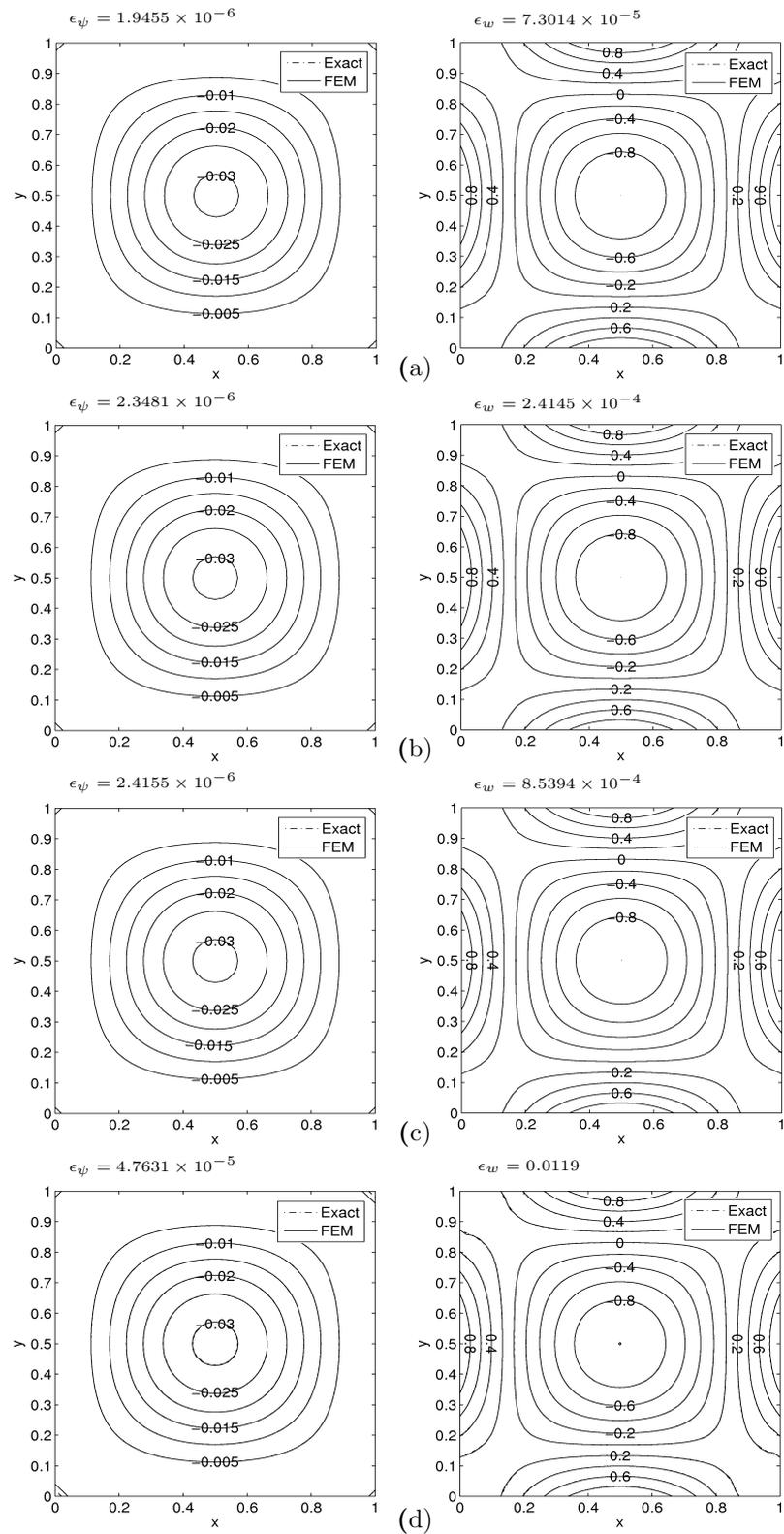
Figure 2.6: Problem 2.4.1: Streamlines (L) and vorticity contours (R) for (**a**) $Re = 0$, (**b**) $Re = 10^3$, (**c**) $Re = 10^4$, (**d**) $Re = 10^6$.

Table 2.1: Maximum absolute errors of Problem 2.4.1 for $Re = 10^3$ with various M_e values.

M_e	ϵ_ψ	ϵ_w
32	0.0016	0.0630
128	7.9709×10^{-5}	0.0063
288	1.7226×10^{-5}	0.0014
512	5.6069×10^{-6}	5.3324×10^{-4}
800	2.3481×10^{-6}	2.4145×10^{-4}
1152	1.1353×10^{-6}	1.2390×10^{-4}
1568	6.0716×10^{-7}	6.9724×10^{-5}
2048	3.4906×10^{-7}	4.2099×10^{-5}
2592	2.1137×10^{-7}	2.6862×10^{-5}
3200	1.3268×10^{-7}	1.7918×10^{-5}
5000	4.4948×10^{-8}	7.5455×10^{-6}

2.4.2 Lid-driven Square Cavity Flow

Having put forth the efficiency of FEM in the previous section, the lid-driven cavity flow problem is taken into consideration. This benchmark problem has been investigated extensively by many researchers and used to test computational fluid dynamics numerical schemes. The governing equations are given as before (Section 1.1.1)

$$\nabla^2 \psi = -w, \tag{2.39}$$

$$\frac{1}{Re}\nabla^2 w + \frac{\partial \psi}{\partial x}\frac{\partial w}{\partial y} - \frac{\partial \psi}{\partial y}\frac{\partial w}{\partial x} = 0\,. \tag{2.40}$$

The no-slip boundary conditions, $u = v = 0$, on the three solid walls of the square cavity are assigned, and the top wall is moving in its plane to the right with a velocity $u = 1$, $v = 0$. These conditions are imposed in terms of the stream function as visualized in Figure 2.7 that

$$\psi = 0 \qquad \text{on } x = y = 0 \text{ and } x = y = 1,$$

$$\frac{\partial \psi}{\partial x} = 0 \qquad \text{on } x = y = 0 \text{ and } x = y = 1,$$

$$\frac{\partial \psi}{\partial y} = 0 \qquad \text{on } x = y = 0 \text{ and } x = 1, \tag{2.41}$$

$$\frac{\partial \psi}{\partial y} = 1 \qquad \text{on } y = 1.$$
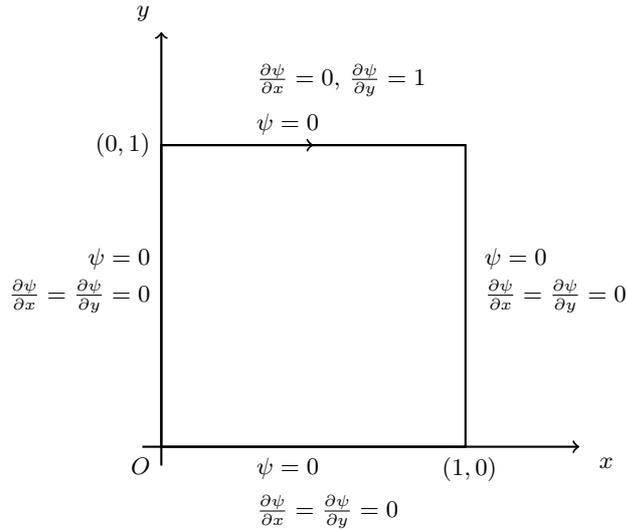
Figure 2.7: Domain and boundary conditions of Problem 2.4.2.

The FEM procedure given in Section 2.2 is followed and the final algebraic equations (2.15) and (2.16) are solved iteratively for Reynolds number $Re = 100$, 500, 1000, 1500 and 2000. It is important to note that when laminar flows are under consideration, the Reynolds number is generally less then the accepted critical value which is approximately 2100. However, it is a widely used practice to test the efficiency of the numerical method for higher values of Re, as in [32, 64]. Henceforth, the numerical tests with $Re = 5000$ and 10000 are also conducted in the present study to enlighten the efficiency of the procedure. In the computations, $M_e = 1250$ quadratic triangular elements are used for Re values up to 2000, whereas the number of elements used for the cases $Re = 5000$ and 10000 is $M_e = 5000$. The numerical solutions are illustrated in terms of streamlines and vorticity contours in Figure 2.8 and Figure 2.9, respectively. Figure 2.8 depicts the effect of the increase of Re in streamlines. It is observed that, when Reynolds number is 100, there is a primary vortex formation through the right upper corner, and a secondary eddy (downstream) is also observed close to the right lower corner of the cavity. Increasing Reynolds number, causes the primary vortex to move to the center of the cavity. Another secondary eddy (upstream) formation is observed close to the left lower corner of the cavity when $Re = 500$. These secondary eddies are growing as Reynolds number increases. Existence of a third eddy close to the left wall is noticed when Re is close to 1000, and this eddy is growing as Reynolds number increased to 1500 and 2000. Further formation of new vortices and growth in the secondary eddies can be seen for high values of Reynolds number ($Re = 5000$ and 10000) in Figure 2.10. It can be observed from Figure 2.9 that the vorticity contours are slightly disturbed from being symmetric with respect to vertical centerline of the cavity starting from $Re = 100$ due to the movement of the upper lid. As Reynolds number increases, however, the vorticity contours move away from the cavity center towards the walls of the cavity. The dominance of the convective terms becomes more evident starting from $Re = 500$ up to 2000. There is a very strong vorticity gradient development observed on the moving lid when Reynolds number is high. On the other hand, the center of

the cavity is stagnant, and the fluid forms boundary layers close to the walls of the cavity. The stagnant region and the formation of boundary layers are more pronounced with a further increase in Re to 5000 and 10000 as can be seen in Figure 2.10. The boundary layer formation, the behavior of the fluid and vortex developments perfectly agree with the results provided in the literature [32, 64].
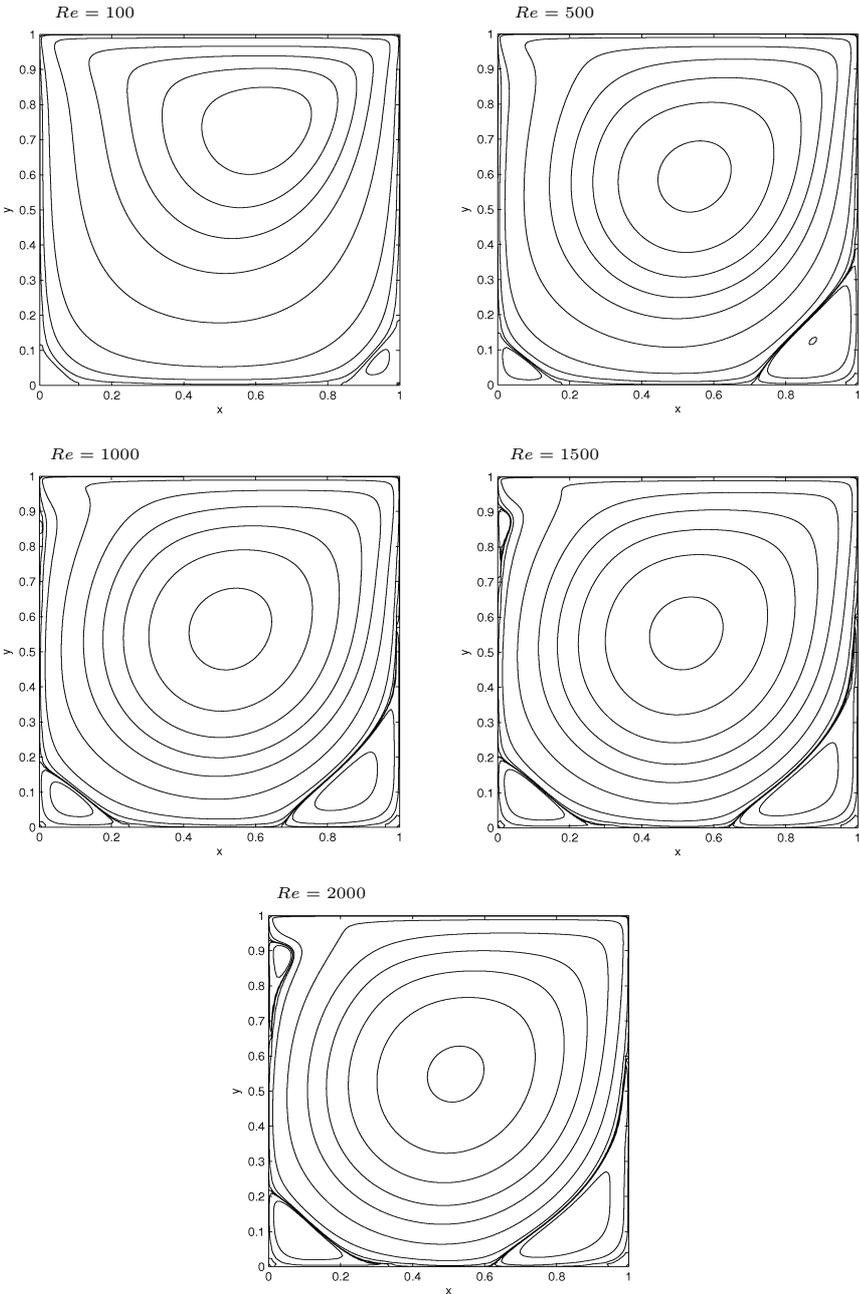
Figure 2.8: Problem 2.4.2: Streamlines for $Re = 100$, 500, 1000, 1500 and 2000.
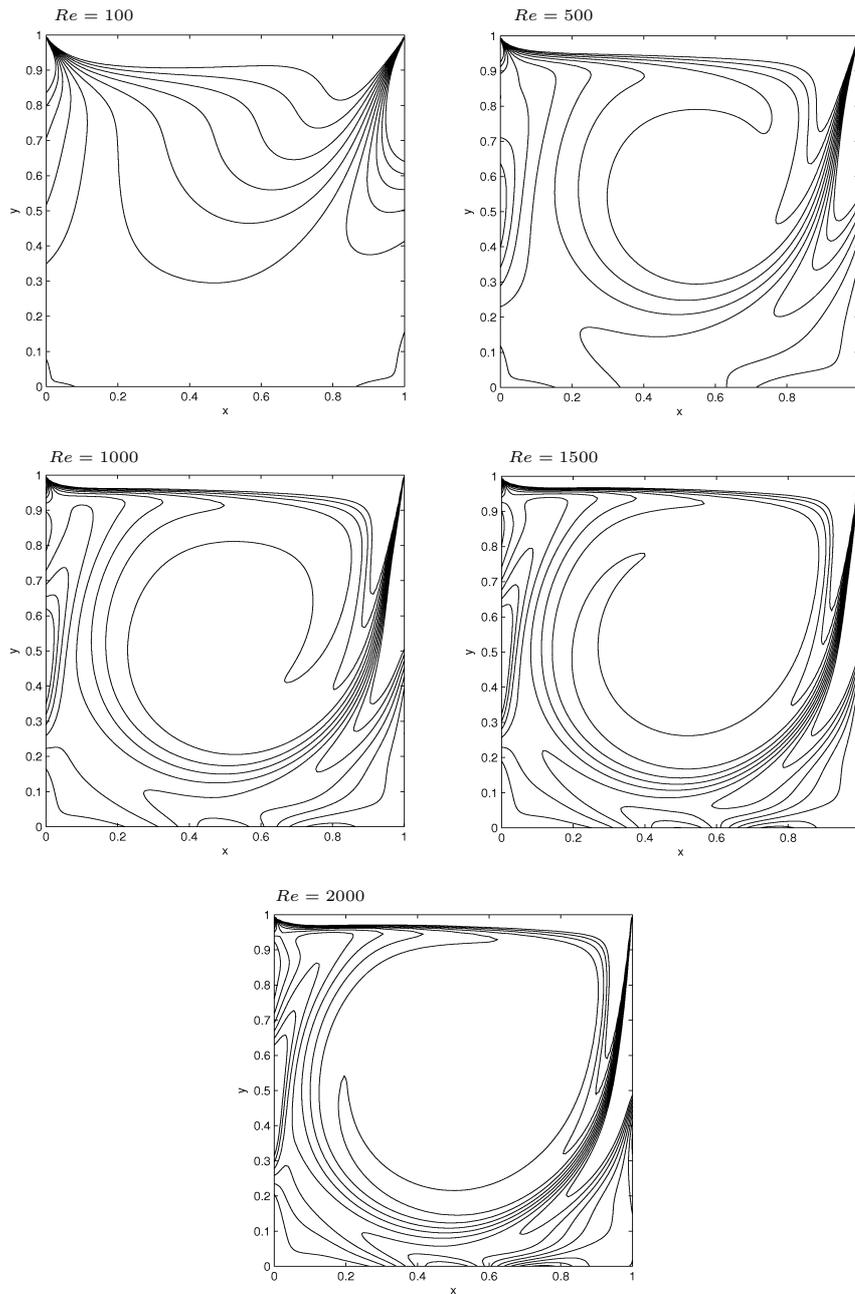
Figure 2.9: Problem 2.4.2: Vorticity contours for $Re = 100, 500, 1000, 1500$ and 2000.
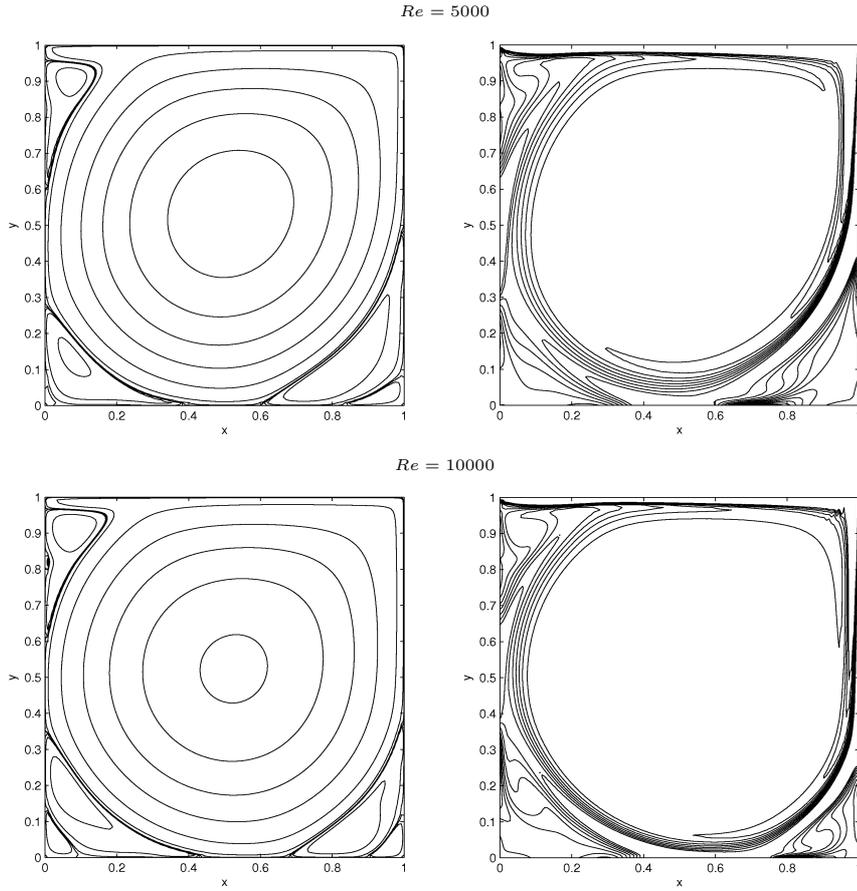
Figure 2.10: Problem 2.4.2: Streamlines (L) and vorticity contours (R) for $Re = 5000$ and 10000.

2.4.3 Natural Convection Flow

In this section, numerical solution to the natural convection flow in enclosures is given. The governing equations given in (2.20) as

$$\nabla^2 \psi = -w$$

$$\frac{\partial \psi}{\partial y}\frac{\partial w}{\partial x} - \frac{\partial \psi}{\partial x}\frac{\partial w}{\partial y} = Pr\nabla^2 w + RaPr\frac{\partial T}{\partial x} \qquad (2.42)$$

$$\frac{\partial \psi}{\partial y}\frac{\partial T}{\partial x} - \frac{\partial \psi}{\partial x}\frac{\partial T}{\partial y} = \nabla^2 T$$

are solved using the iterative procedure described in Section 2.2. The no-slip boundary conditions for the velocity are assumed, and accordingly the boundary conditions of stream function are taken as zero on all the walls of the cavity. The

46

vorticity boundary conditions are derived from Taylor series expansion of stream function as given in Section 2.1.1. Temperature has Dirichlet type wall conditions as $T = 1$ and $T = 0$ at the left and right walls of the cavity, respectively, whereas adiabatic conditions $\partial T / \partial y = 0$ are imposed on the top and bottom walls (Figure 2.11).
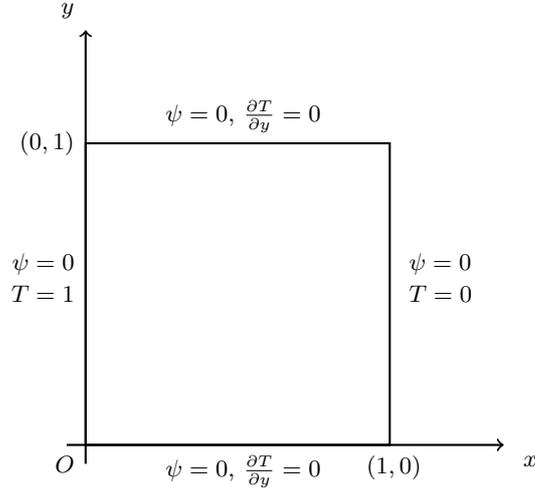
Figure 2.11: Domain and boundary conditions of Problem 2.4.3.

The Prandtl number is taken as 0.7 in the numerical simulations, and the streamlines, vorticity contours and isotherms are obtained for Rayleigh number values, $Ra = 10^3$, 10^4, 10^5 and 10^6. The problem domain is discretized using $M_e = 1250$ elements.

Figure 2.12 shows the streamlines, vorticity contours and isotherms for the corresponding Rayleigh numbers. For $Ra = 10^3$, it is observed that the viscous forces dominate the flow. The lenient convection effect is observed as the streamlines have a circular pattern, the vorticity contours take place mostly at the center of the cavity, and the isotherms are in regular behavior which are nearly vertical. As Rayleigh number increases, natural convection dominates the flow pattern. The increase in Rayleigh number corresponds to the increase in Buoyancy forces which results in significant convection in the flow. The streamlines gain an elliptic profile, the vorticity contours get separated into two major vortices towards the main diagonal of the cavity. The isotherms are distorted from vertical profile into horizontal behavior through the center of the cavity. For all unknowns it is noted that as Rayleigh number gets higher values, boundary layer formation occurs along the vertical walls. These behaviors are in excellent agreement with the previously published results [22, 46].
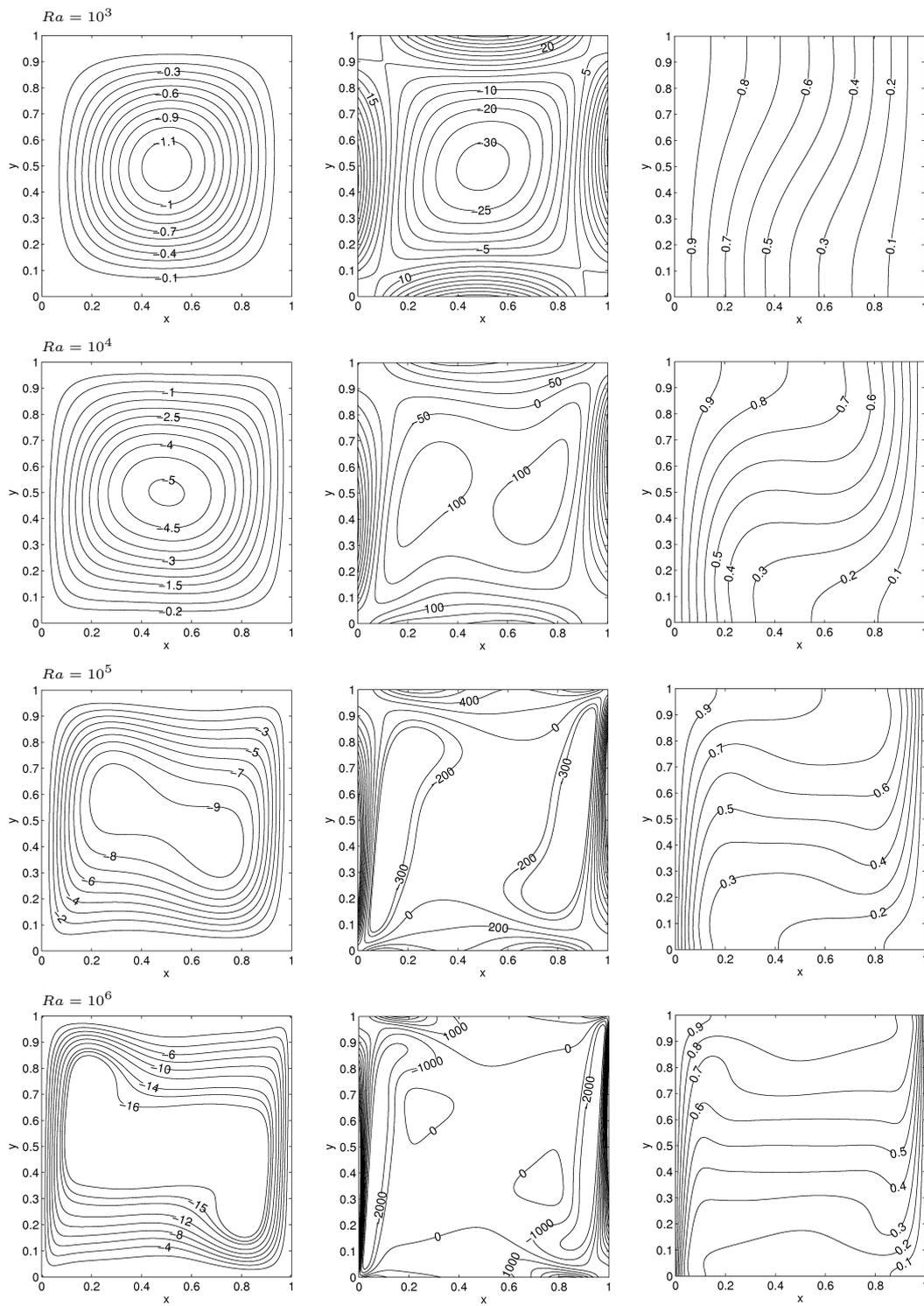
Figure 2.12: Problem 2.4.3: Streamlines (L), vorticity contours (M) and isotherms (R) for $Ra = 10^3$, 10^4, 10^5 and 10^6.

2.4.4   Natural Convection Flow in Enclosures under a Magnetic Field

This section presents two natural convection flow problems under an externally applied magnetic field in square enclosures. The governing equations are given in Equations (2.31) as

$$\nabla^2\psi \;=\; -w$$

$$Pr\nabla^2 w \;=\; \frac{\partial\psi}{\partial y}\frac{\partial w}{\partial x} - \frac{\partial\psi}{\partial x}\frac{\partial w}{\partial y} - RaPr\left(\cos\phi\frac{\partial T}{\partial x} - \sin\phi\frac{\partial T}{\partial y}\right)$$

$$-Ha^2 Pr\left[\cos\varphi\left(\sin\varphi\frac{\partial^2\psi}{\partial x\partial y} + \cos\varphi\frac{\partial^2\psi}{\partial x^2}\right)\right.$$

$$\left.+\sin\varphi\left(\sin\varphi\frac{\partial^2\psi}{\partial y^2} + \cos\varphi\frac{\partial^2\psi}{\partial y\partial x}\right)\right] \tag{2.43}$$

$$\nabla^2 T \;=\; \frac{\partial\psi}{\partial y}\frac{\partial T}{\partial x} - \frac{\partial\psi}{\partial x}\frac{\partial T}{\partial y}\,.$$

The FEM discretized system of Equations (2.32)-(2.34) are given in Section 2.3. The angles in Equations (2.43), ϕ and φ are measured in degrees as counterclockwise direction (positive), and clockwise direction (negative). The test cases are taken with different temperature boundary conditions which reflect the physical setup of the problems. In the first problem, the bottom wall of the cavity is sinusoidally heated and the effect of the temperature variation in the cavity is investigated. The second problem of natural convection flow is considered with two linearly heated walls. Both problems are initially solved under the assumption that the inclination of the cavity is absent and the direction of the external magnetic field is horizontal. Accordingly, setting $\phi = 0$ and $\varphi = 0$, Equations (2.43) take the form

$$\nabla^2\psi \;=\; -w$$

$$Pr\nabla^2 w \;=\; \frac{\partial\psi}{\partial y}\frac{\partial w}{\partial x} - \frac{\partial\psi}{\partial x}\frac{\partial w}{\partial y} - RaPr\frac{\partial T}{\partial x} - Ha^2 Pr\frac{\partial^2\psi}{\partial x^2} \tag{2.44}$$

$$\nabla^2 T \;=\; \frac{\partial\psi}{\partial y}\frac{\partial T}{\partial x} - \frac{\partial\psi}{\partial x}\frac{\partial T}{\partial y}\,.$$

The numerical investigation is carried on by several inclination and magnetic field direction angle variations. In the numerical computations for both of the problems, the Prantdl number is taken as 1. Numerical solutions are obtained for Hartmann number values up to 100 and Rayleigh number values up to 10^6. $M_e = 5000$ elements are used in the computations.

2.4.4.1 Sinusoidal bottom wall temperature

In this problem, natural convection flow in a square enclosure (cavity) under an externally applied magnetic field is considered. The cavity is fixed in the horizontal direction where the inclination angle is $\phi = 0$ as shown in Figure 2.13. No-slip boundary conditions are imposed for velocity implying zero stream function and its normal derivatives on the walls. The vertical walls of the cavity are thermally insulated (adiabatic) whereas the bottom wall is sinusoidally heated and the top is isothermally cooled. The boundary conditions are given as [56]
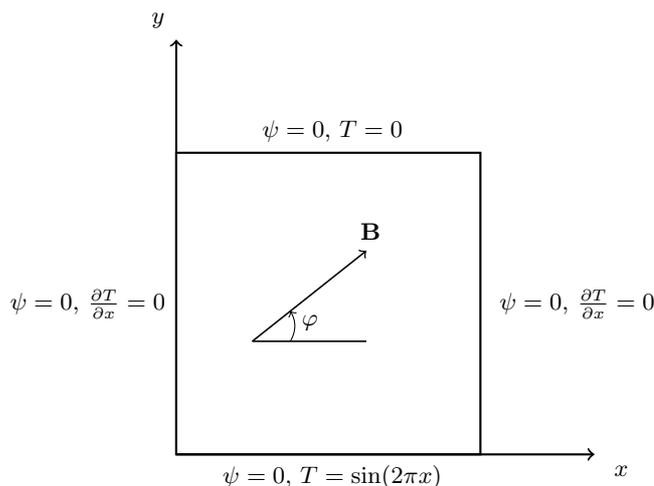
Figure 2.13: The geometry and boundary conditions of Problem 2.4.4.1.

$$u(x,0) = 0, \quad v(x,0) = 0, \quad u(x,1) = 0, \quad v(x,1) = 0,$$

$$u(0,y) = 0, \quad v(0,y) = 0, \quad u(1,y) = 0, \quad v(1,y) = 0,$$

$$\left.\frac{\partial T}{\partial x}\right|_{x=0} = 0, \quad \left.\frac{\partial T}{\partial x}\right|_{x=1} = 0, \quad T(x,1) = 0, \quad T(x,0) = \sin(2\pi x),$$

$$\psi(x,0) = 0, \quad \psi(0,y) = 0, \quad \psi(x,1) = 0, \quad \psi(1,y) = 0,$$

$$\left.\frac{\partial \psi}{\partial y}\right|_{y=0} = 0, \quad \left.\frac{\partial \psi}{\partial y}\right|_{y=1} = 0, \quad \left.\frac{\partial \psi}{\partial x}\right|_{x=0} = 0, \quad \left.\frac{\partial \psi}{\partial x}\right|_{x=1} = 0 \,.$$

This physical configuration has important implications especially for shallow enclosures in which thermal penetration has certain importance in industrial processes and furnaces. The spatial sinusoidal temperature variations occur when an array of cylindrical heaters is used to heat one of the walls of the cavity. In these cases, the temperature of the wall attains its maximum value at the contact point of the circular cross-section of each heater. The temperatures before and after the contact region decreases as the distance from the heater surface of the wall is increasing. The numerical results are presented in terms of non-dimensional stream function, vorticity and temperature contour values in the figures, from left to right, respectively.
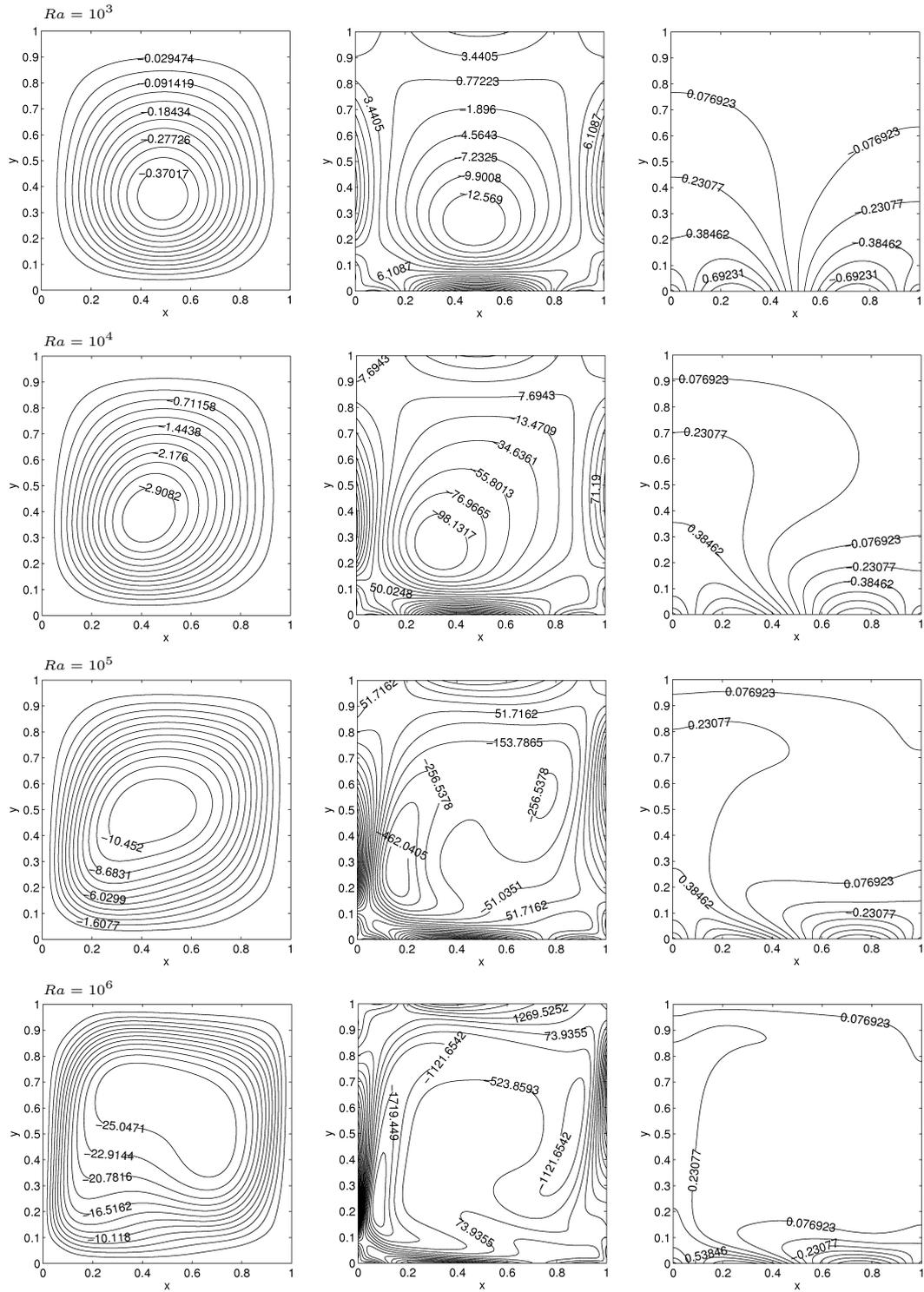
Figure 2.14: Problem 2.4.4.1: Streamlines (L), vorticity contours (M) and isotherms (R) for $Ha = 10$, $Ra = 10^3$, 10^4, 10^5 and 10^6.

Figures 2.14 and 2.15 present the streamlines, vorticity contours and isotherms at fixed Hartmann numbers $Ha = 10$ and $Ha = 50$, respectively, for the values of
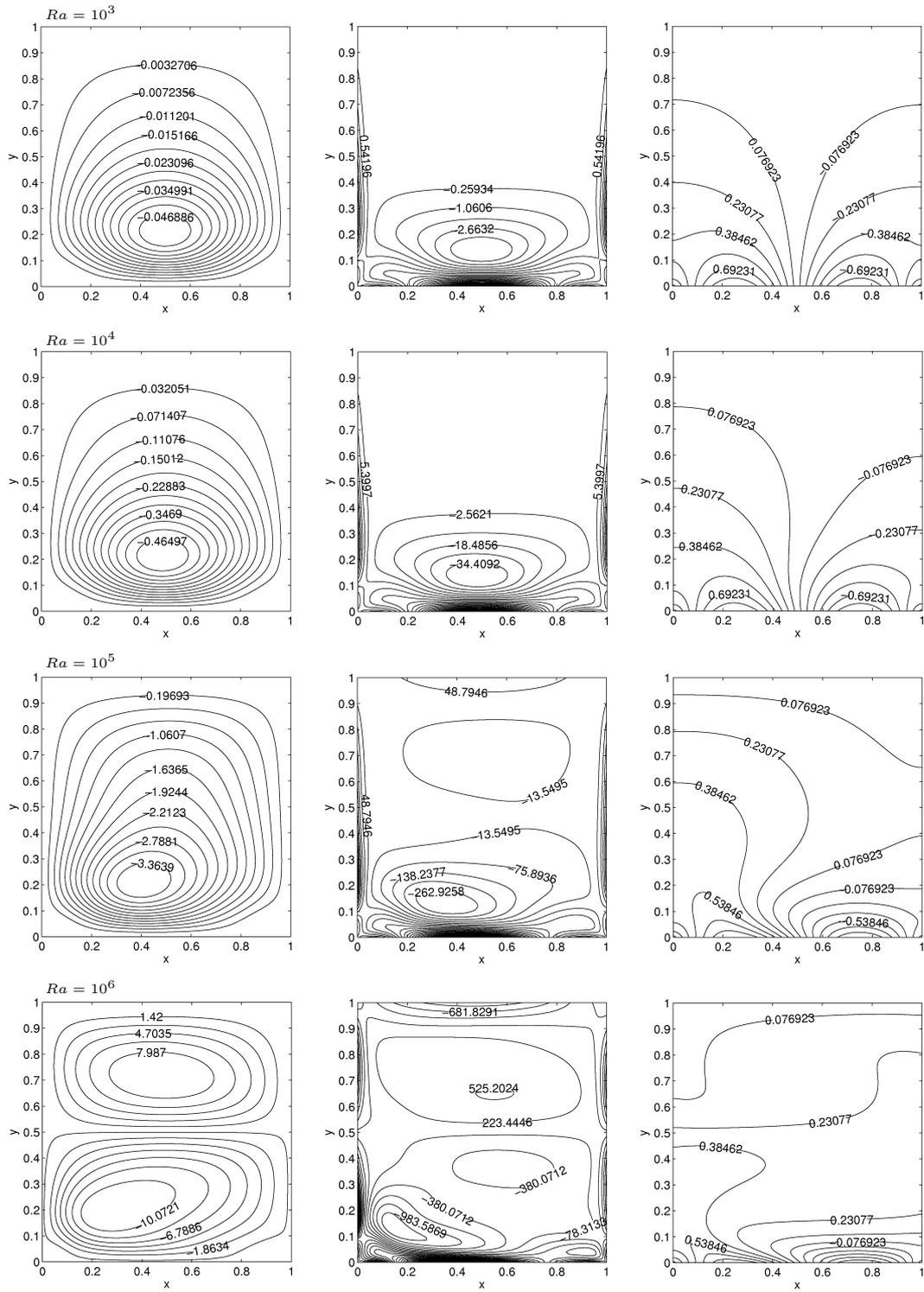
Figure 2.15: Problem 2.4.4.1: Streamlines (L), vorticity contours (M) and isotherms (R) for $Ha = 50$, $Ra = 10^3$, 10^4, 10^5 and 10^6.

Rayleigh number, $Ra = 10^3$, 10^4, 10^5 and 10^6. Increasing Rayleigh number when Hartmann number is fixed (Figure 2.14 when $Ha = 10$ and Figure 2.15 when
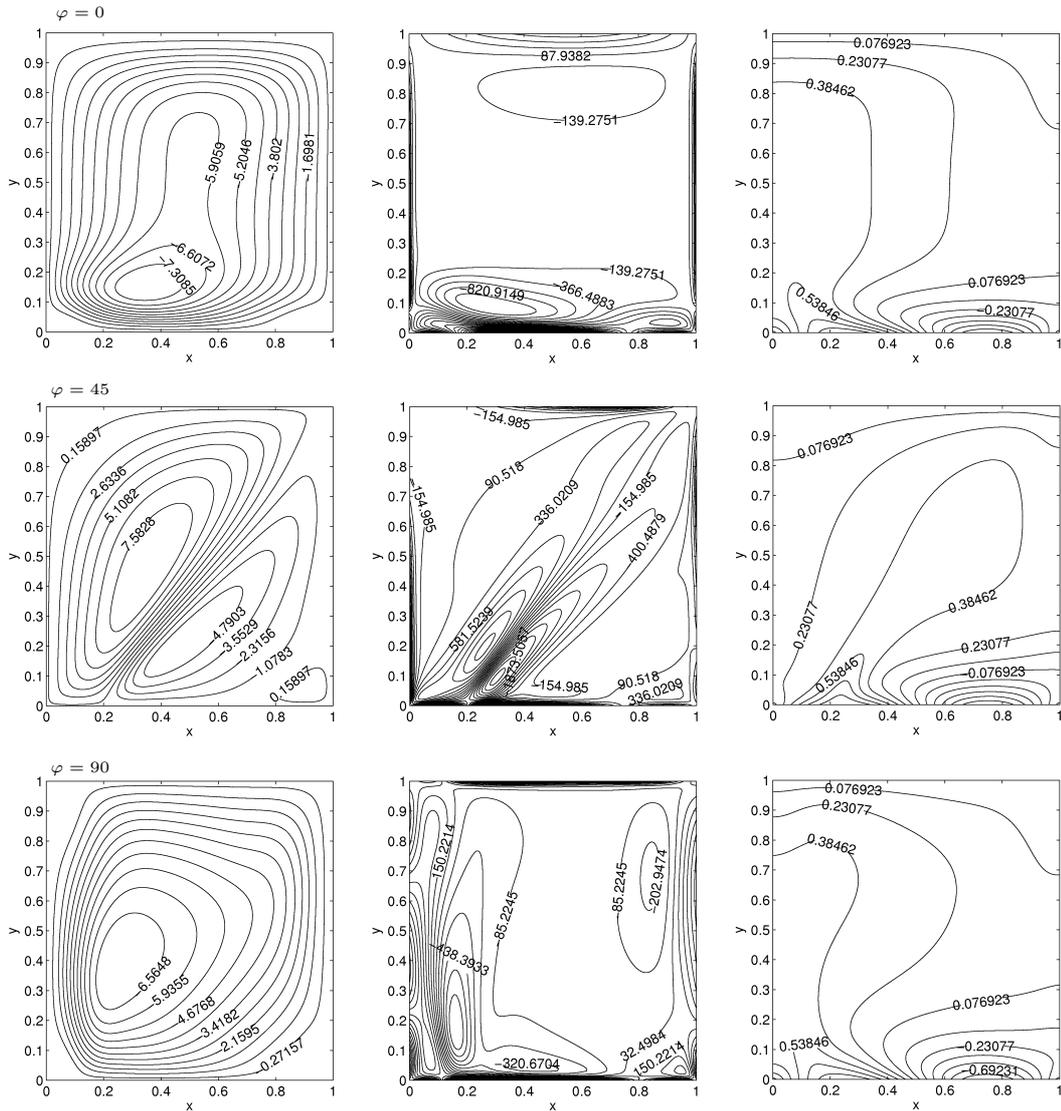
Figure 2.16: Problem 2.4.4.1: Streamlines (L), vorticity contours (M) and isotherms (R) when $Ra = 10^6$ and $Ha = 100$ for $\phi = 0$, $\varphi = 0$, 45 and 90.

$Ha = 50$), causes the streamlines and vorticity contours to be increased in magnitudes. The flow starts to develop boundary layers close to heated bottom wall and then on adjacent adiabatic walls. The isotherms are deformed and start getting pushed towards the heated wall. This shows that the sinusoidally heated bottom wall controls the flow and temperature behavior mostly. Higher values of Ra cause a deformation on streamlines from heated bottom wall through cooled top wall. In terms of streamlines and vorticity contours, increasing Rayleigh number from $Ra = 10^3$ to $Ra = 10^4$ does not have a major effect for both $Ha = 10$ and $Ha = 50$ cases. However, higher Ra values cause significant alteration on streamlines and vorticity contours. This effect is more pronounced when Rayleigh number is increased to 10^6. Also, higher values of both Ha and Ra as $Ha = 50$ and $Ra = 10^6$ separate the flow along the horizontal centerline of the cavity into two vortices. This means that the external magnetic field is more powerful

controlling the flow. The increase in Ra increases the vortex moves in vorticity through the bottom of the cavity and boundary layer formation starts near the bottom wall especially for high value of Ha (Figure 2.15). Increasing Ha has not much effect on isotherms.

Figure 2.16 depicts the streamlines, vorticity contours and isotherms for $Ra = 10^6$ and $Ha = 100$ when the magnetic field is applied with angles $\varphi = 0°$, $45°$ and $90°$. When the magnetic field is applied horizontally ($\varphi = 0°$), a further increase in Ha ($Ha = 100$) for a fixed $Ra = 10^6$ shows a concentration of the flow to the heated bottom wall in terms of boundary layer for both streamlines and vorticity. These results show a reasonable agreement with the results presented in [56] which considers only the case of magnetic field parallel to the x-axis. When the magnetic field is applied at an angle of $\varphi = 45°$, formation of two loops along the diagonal of the cavity and development of boundary layers in the direction of the magnetic field are observed in streamlines. In addition to the boundary layers close to the bottom wall, layers are observed along the diagonal in vorticity contours forming vortices with opposite circulations. The deformation is also observed in isotherms in the direction of the applied magnetic field, however, the boundary layers near the heated bottom wall show a relatively small alteration. When the magnetic field applies with an angle of $\varphi = 90°$, formation of boundary layers in both stream function and vorticity contours is observed close to the left wall. A major vortex in streamlines near the left wall of the cavity, and multiple eddies in vorticity contours indicating the retarding effect of the magnetic field are seen vertically. The isotherms seem to be not much affected when compared with the horizontally applied magnetic field case.

2.4.4.2 Linearly heated left and bottom walls

In this problem, a physical configuration of natural convection flow under magnetic field is considered where the non-dimensional temperature is zero on the right and top walls, and on the left and bottom walls it varies linearly. No-slip boundary conditions for velocity are converted into the stream function boundary conditions where the stream function and its normal derivatives are zero on the walls. The boundary conditions are described as in [25]

$$u(x,0) = 0, \ \ v(x,0) = 0, \ \ u(x,1) = 0, \ \ v(x,1) = 0,$$

$$u(0,y) = 0, \ \ v(0,y) = 0, \ \ u(1,y) = 0, \ \ v(1,y) = 0,$$

$$T(x,1) = 0, \ \ T(1,y) = 0, \ \ T(x,0) = 1 - x, \ \ T(0,y) = 1 - y,$$

$$\psi(x,0) = 0, \ \ \psi(0,y) = 0, \ \ \psi(x,1) = 0, \ \ \psi(1,y) = 0,$$

$$\left.\frac{\partial \psi}{\partial y}\right|_{y=0} = 0, \ \ \left.\frac{\partial \psi}{\partial y}\right|_{y=1} = 0, \ \ \left.\frac{\partial \psi}{\partial x}\right|_{x=0} = 0, \ \ \left.\frac{\partial \psi}{\partial x}\right|_{x=1} = 0 \, .$$

The boundary conditions for stream function and temperature are shown on the problem domain in Figure 2.17. In this problem, in addition to the effects of Rayleigh number, Hartmann number and magnetic field direction on the flow

behavior, several cavity inclination angle tests are carried, and the results are given in terms of streamlines, vorticity contours and isotherms.
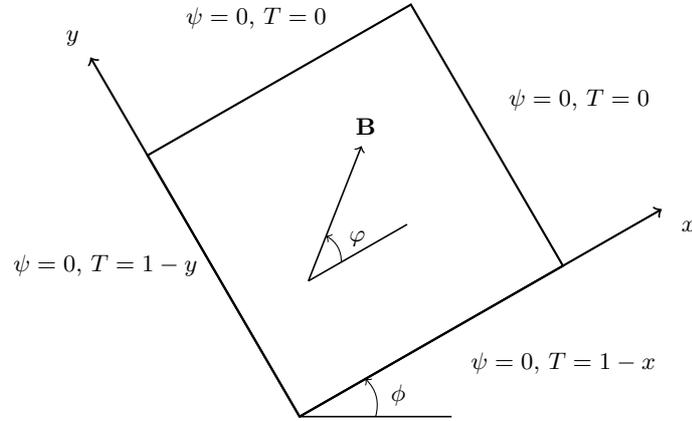
Figure 2.17: The geometry and boundary conditions of Problem 2.4.4.2.

Figures 2.18, 2.19 and 2.20 show the streamlines, vorticity contours and isotherms for Rayleigh number values $Ra = 10^3$, 10^4 and 10^5 when $Ha = 0$, $Ha = 30$ and $Ha = 80$, respectively. Inclination angle ϕ and magnetic field direction angle φ are taken as zero. As can be seen from these figures that, increasing Rayleigh number causes an increase in the magnitudes of the streamlines and vorticity contours for a fixed Hartmann number. The central vortex in vorticity is destroyed and concentrates through the bottom and side walls as Ra increases, and as Ha increases boundary layers are formed completely close to these walls. The isotherms circulate in the cavity as Ra increases, and this circulation is especially prominent in the absence of magnetic effect ($Ha = 0$) when Ra is high ($Ra = 10^5$). As Ha increases, however, the magnetic force dominates the buoyancy effect and the circulation of the isotherms is reduced. The contours of the stream function, vorticity and temperature are drawn for the highest set of Rayleigh number 10^6 and Hartmann number 100 in Figures 2.21-2.23 with several combinations of cavity inclination angle and magnetic field direction angle values. The effect of the magnetic field direction is investigated by considering $\varphi = 0°$, 45° and 90° values, where the inclination angle of the cavity is taken as $\phi = 0$ in Figure 2.21, $\phi = 45°$ in Figure 2.22 and $\phi = -45°$ in Figure 2.23. It is seen from these figures that the streamlines, vorticity contours and also the isotherms are changed in the same direction with the magnetic field. Especially streamlines form boundary layers close to the walls which are parallel to the applied magnetic field. Secondary flows in opposite directions are developing along the magnetic field direction for 0° and 45° inclinations of the cavity, but −45° inclination does not cause secondary flows. The boundary layers and vortices are also observed in the vorticity contours. Because of the domination in the convection, the isotherms are shifted towards the cold (upper right) corner. The significant variations in stream function, vorticity and temperature are observed with respect to the inclination of the cavity only when the inclination angle is negative. Isotherms do not alter for $\phi = 0°$ and $\phi = 45°$, but for $\phi = -45°$ they expand vertically compared to other cases. Streamlines and vorticity behaviors are almost the same which were

Figure 2.18: Problem 2.4.4.2: Streamlines (L), vorticity contours (M) and isotherms (R) when $Ha = 0$ for $Ra = 10^3$, 10^4 and 10^5, $\phi = 0$, $\varphi = 0$.

observed for changing values of φ (magnetic field direction) in the cases $\phi = 0°$ and $\phi = 45°$. As the cavity is inclined $45°$ in clockwise direction ($\phi = -45°$), a single circulation eddy is observed in all applied magnetic field directions (Figure 2.23). In both streamlines and vorticity contours, boundary layers along the horizontal walls are observed in the case where $\varphi = -45°$.

It can be inferred from these figures that the flow pattern and heat convection in the square cavity is strongly affected by the variations of Ra and Ha in terms of magnitudes and boundary layers. The inclination of the enclosure with respect to the horizontal direction and the direction of the externally applied magnetic field have also significant influence on the flow. The flow action and boundary layer formation take place along the direction of the magnetic field. The behaviors of the streamlines and isotherms show a good agreement with the results observed

56
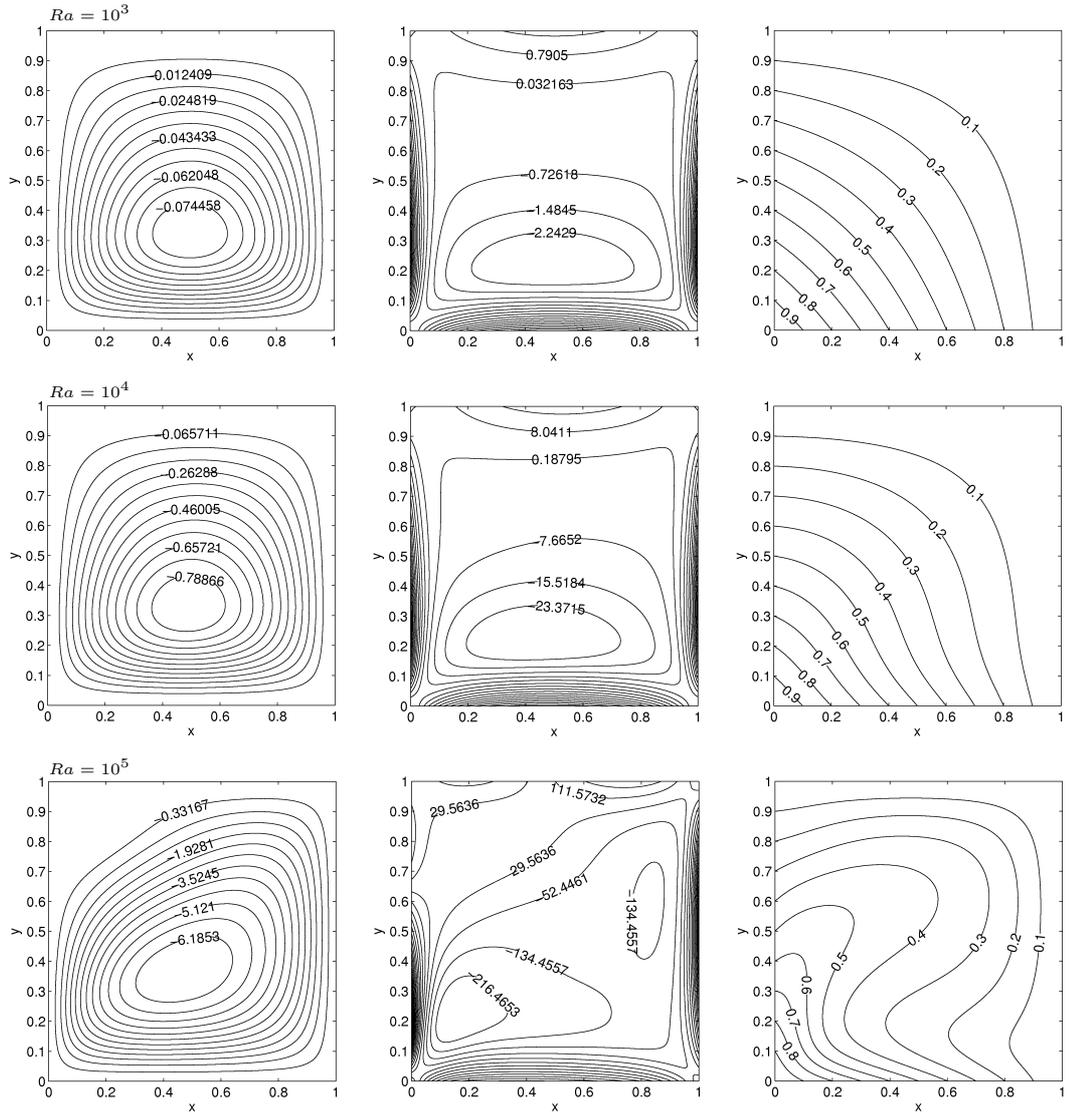
Figure 2.19: Problem 2.4.4.2: Streamlines (L), vorticity contours (M) and isotherms (R) when $Ha = 30$ for $Ra = 10^3$, 10^4 and 10^5, $\phi = 0$, $\varphi = 0$.

in [25]. In addition, in this thesis, vorticity behaviors are supplied for all the variations of Ra, Ha and the angles, ϕ and φ.

As a conclusion, in this chapter, the fundamental steps of FEM application to incompressible fluid flow and natural convection flow equations in terms of stream function, vorticity and temperature are demonstrated. Numerical solutions for several problems including lid-driven cavity flow and natural convection flow under a magnetic field in inclined enclosures are presented. In FEM discretizations, quadratic triangular elements are used to ensure accurate approximation for the second order derivatives of stream function in the vorticity equation. The efficiency of the method is proved through a test problem for which the exact solution is available. Solutions to the lid-driven cavity flow problem are provided for laminar flow regimes up to Reynolds number value $Re = 2000$, and furthermore,
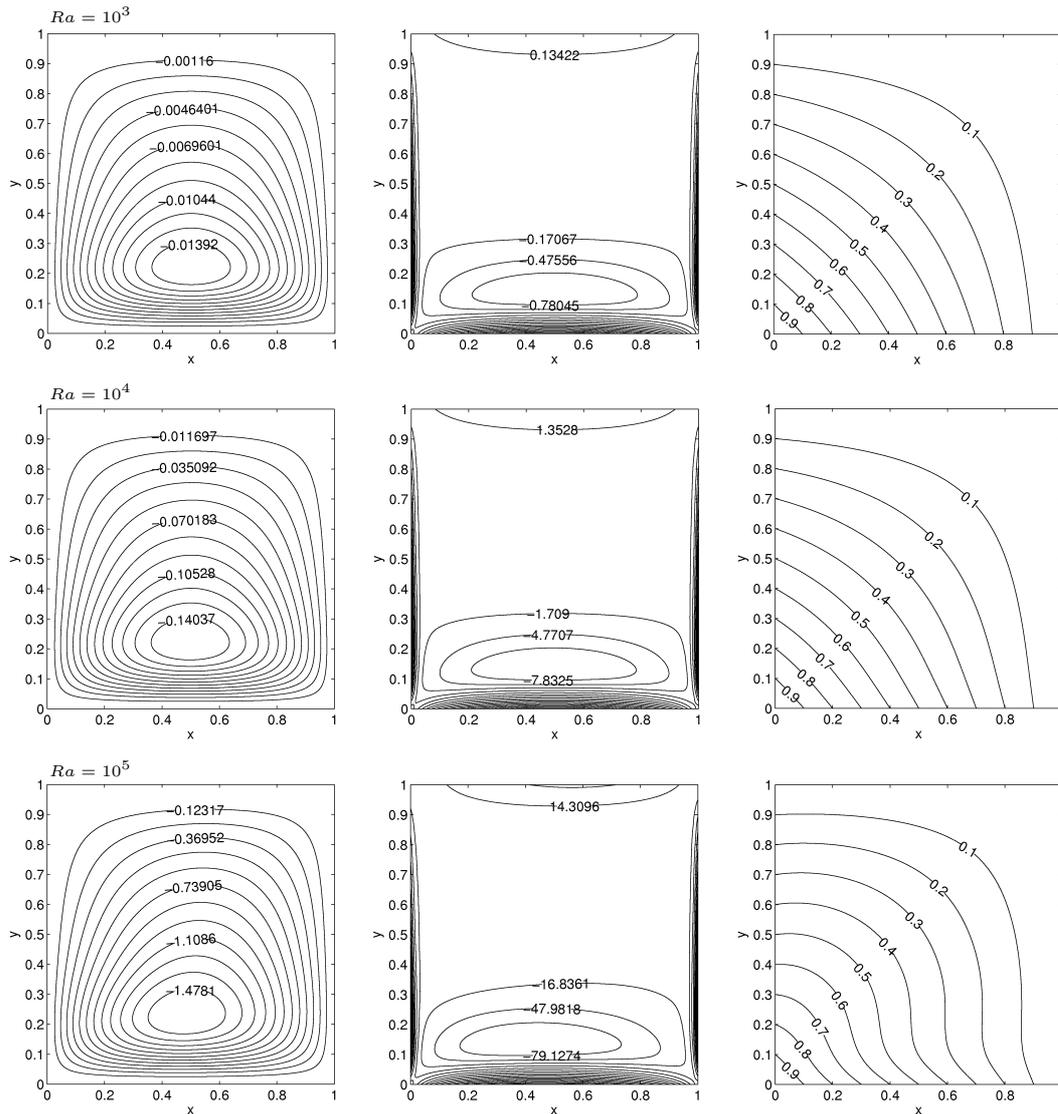
Figure 2.20: Problem 2.4.4.2: Streamlines (L), vorticity contours (M) and isotherms (R) when $Ha = 80$ for $Ra = 10^3$, 10^4 and 10^5, $\phi = 0$, $\varphi = 0$.

the numerical solutions are presented for higher Re values as 5000 and 10000 for showing the efficiency of the FEM algorithm and capability of the code prepared in the thesis. FEM solutions of natural convection flow in inclined enclosures in the presence of an oblique magnetic field are presented. The application of FEM with quadratic elements for solving natural convection flow problems under the influence of an external magnetic field, constitutes the original core part of this chapter in the sense that the results are obtained for large values of Rayleigh and Hartmann numbers up to $Ra = 10^6$ and $Ha = 100$. The increase in Re for the lid-driven cavity flow and the increase in Ra in natural convection flow have the common effect as the development of stagnant regions at the center of the enclosure for the flow, and formation of boundary layers for all unknowns. It is found that, external magnetic field is more powerful controlling the flow than the buoyancy force in natural convection flow.
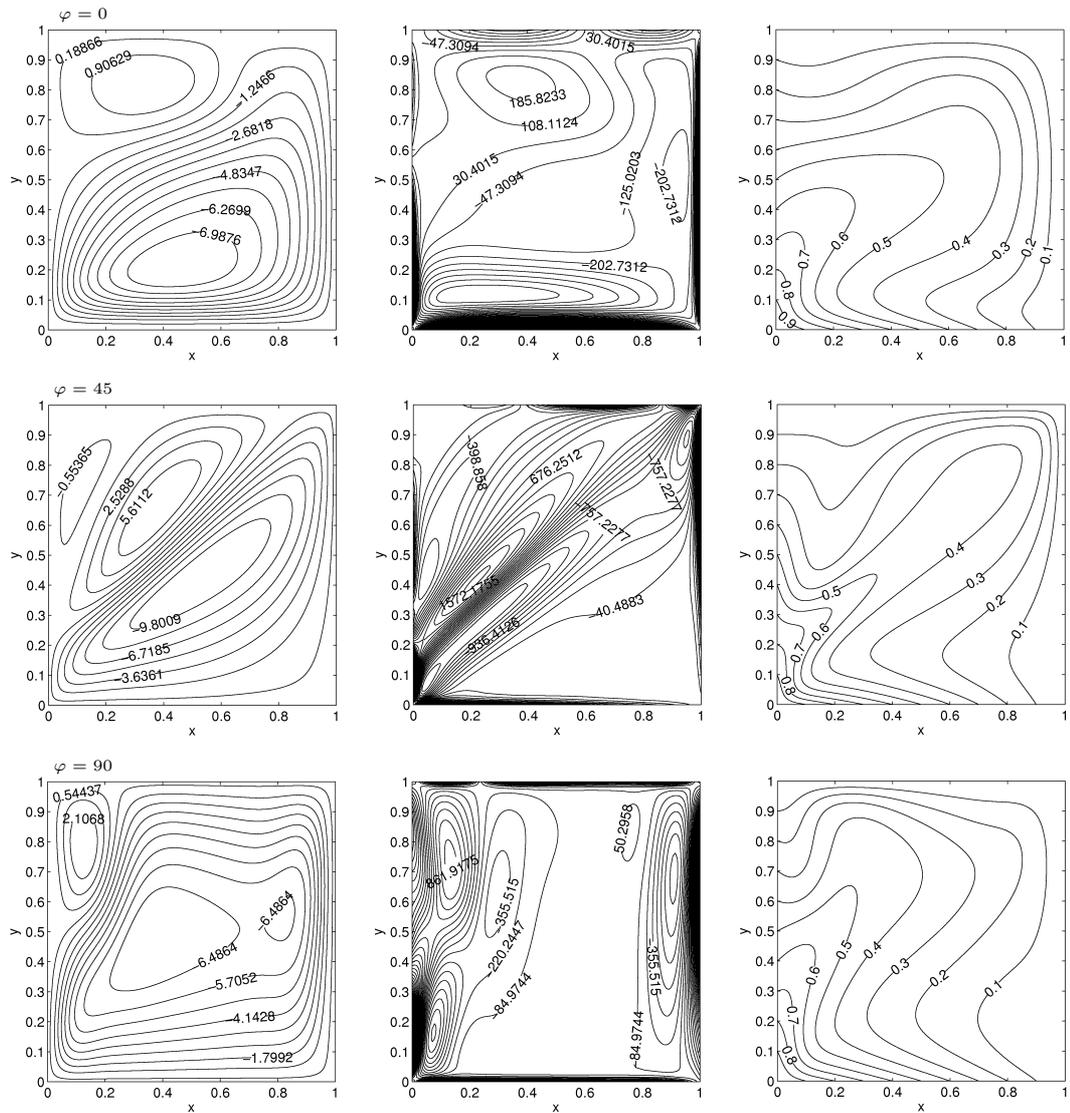
Figure 2.21: Problem 2.4.4.2: Streamlines (L), vorticity contours (M) and isotherms (R) when $Ra = 10^6$ and $Ha = 100$ for $\phi = 0$, $\varphi = 0$, 45 and 90.
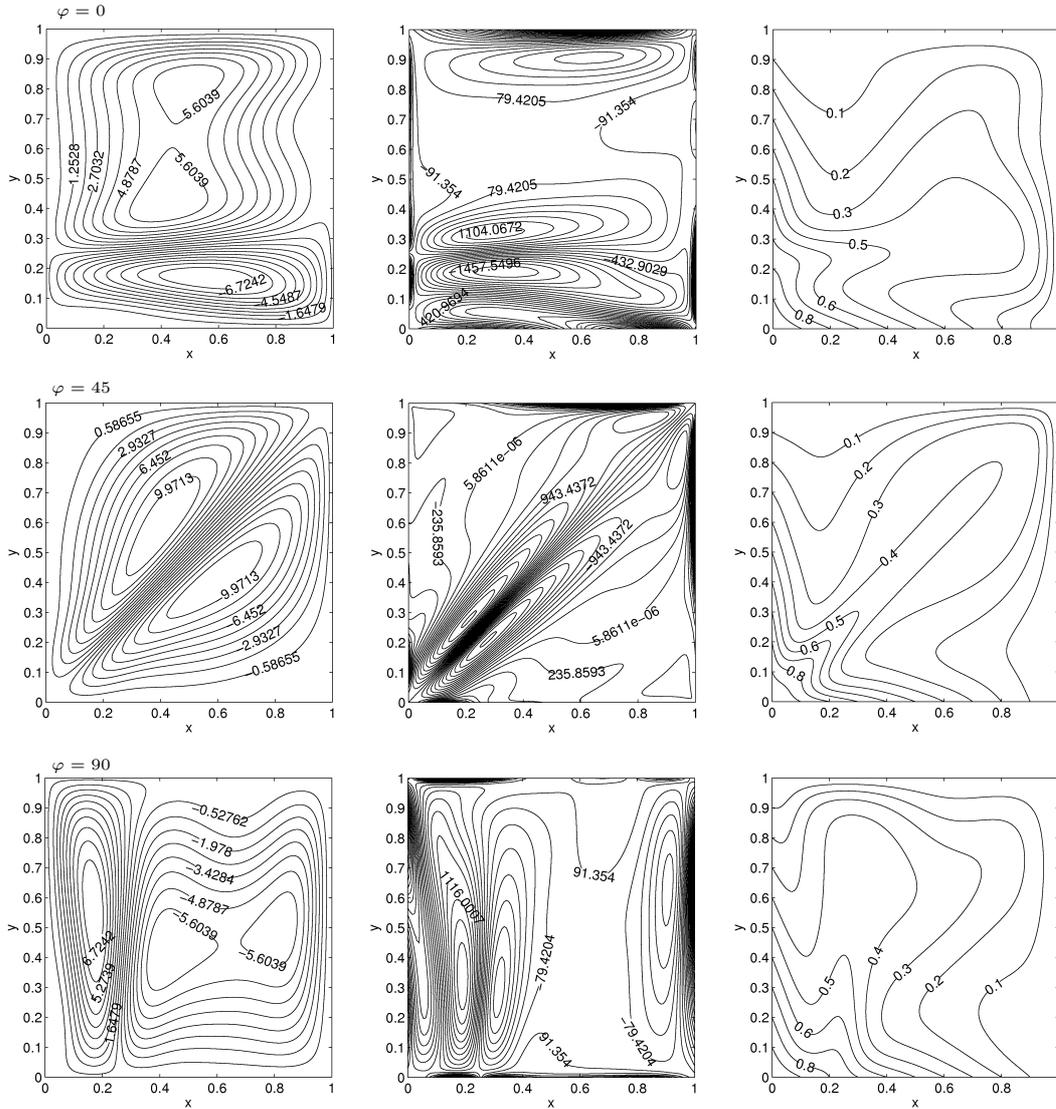
Figure 2.22: Problem 2.4.4.2: Streamlines (L), vorticity contours (M) and isotherms (R) when $Ra = 10^6$ and $Ha = 100$ for $\phi = 45$, $\varphi = 0$, 45 and 90.
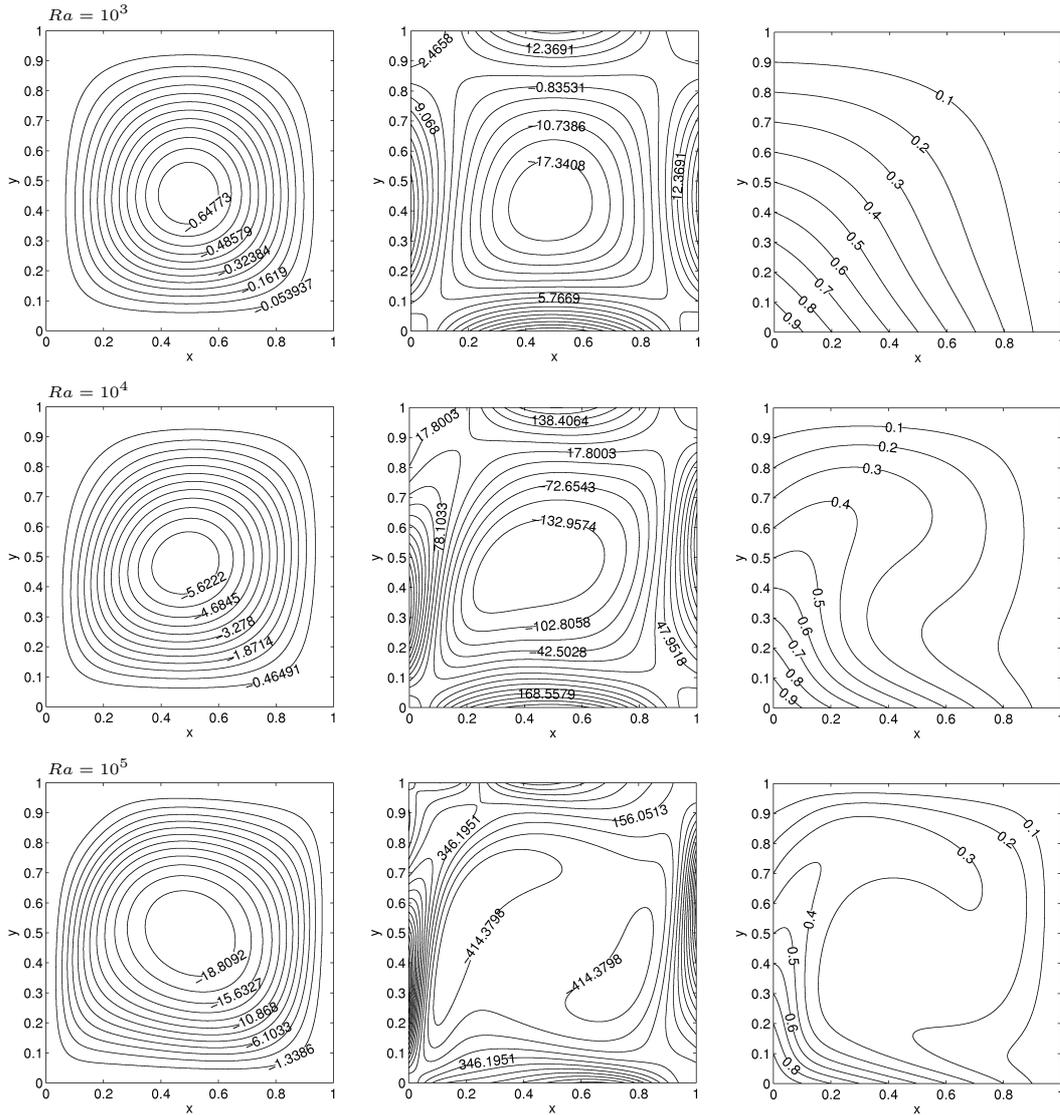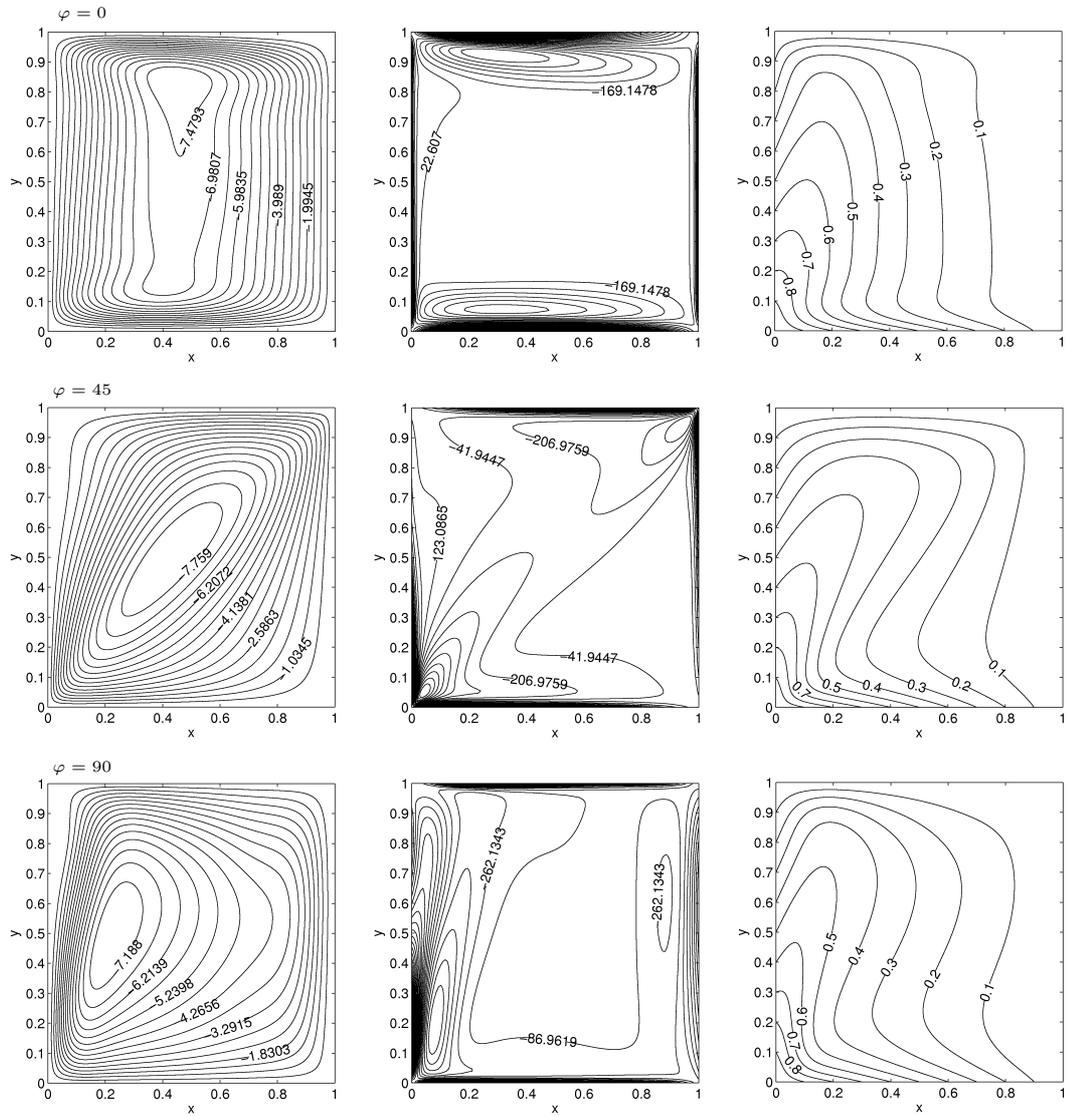
Figure 2.23: Problem 2.4.4.2: Streamlines (L), vorticity contours (M) and isotherms (R) when $Ra = 10^6$ and $Ha = 100$ for $\phi = -45$, $\varphi = 0$, 45 and 90.

CHAPTER 3

Numerical Solutions of MHD Natural Convection Flow using Chebyshev Spectral Collocation Method

This chapter presents the numerical solutions of MHD flow and heat transfer problems using Chebyshev spectral collocation method (CSCM). In general, spectral methods are a family of numerical methods in which a function is approximated globally by representing it as a finite sum of preassigned orthogonal functions. In spectral methods, each function spans the whole domain under consideration, and therefore, the derivatives of the function depend on the entire discretization. When the interpolating polynomials for approximating the unknown functions are defined on a set of clustered Chebyshev-Gauss-Lobatto (CGL) points in which the differential equations are discretized, the method is referred as Chebyshev spectral collocation method. The polynomials are differentiated analytically and a differentiation matrix is constructed for derivative approximation. The higher order derivatives can easily be obtained by multiplying these differentiation matrices. This makes the procedure computationally cheap and a high order accuracy is achieved, hence, the method is frequently used especially in simple geometries. The primary objective of this chapter is to utilize the ease of implementation and the convenience of CSCM with high order accuracy to especially one-dimensional problems. Additionally, for the integrity of the whole thesis, the two-dimensional flows studied in Chapter 2 are reconsidered. Thus, the present chapter presents the CSCM applications to both one-dimensional and two-dimensional laminar flows of incompressible viscous fluids for various physical configurations. The method of obtaining the differentiation matrices and the details of the collocation approach using CGL points are described in Section 3.1. The two-dimensional extension is described in Section 3.2 where the CSCM applications to Navier-Stokes and natural convection flow under magnetic field equations are provided. In particular, solution to N-S equations with exact solution is provided in Section 3.2.1, the lid-driven square cavity problem is solved in Section 3.2.2, and Section 3.2.3 deals with the solutions of natural convection flow problem. Sections 3.3 and 3.4 present the CSCM solutions to one-dimensional MHD flows with heat transfer between parallel plates, where the fluid contain particles (dusty fluid) in the latter case. In each problem section, the problem definition, the CSCM application and the numerical results are presented individually.

3.1 Chebyshev Spectral Collocation Method

In collocation methods, the fundamental idea is to require the numerical approximation Φ_N of a solution Φ to boundary value problem

$$\mathcal{L}\Phi = g$$

$$\mathcal{B}\Phi = s \tag{3.1}$$

to be exactly satisfied on a set of previously defined points which are called the collocation points. $\mathcal{L}$ is the differential operator, $\mathcal{B}$ is the boundary operator, g and s are known functions in the problem domain and on the boundary, respectively. In general, the solution Φ is interpolated at the collocation points, and the derivatives of the solution are approximated by the derivatives of the interpolating polynomial. In CSCM, the collocation points are taken as the Chebyshev-Gauss-Lobatto (CGL) points which are the nodes of the Gauss-Lobatto quadrature formula for the Chebyshev polynomials and also the extreme points of the Chebyshev polynomials (in $[-1, 1]$). The CGL points are widely used in interpolation due to the desired property of uneven distribution in the standard interval, where the majority of them are gathered near the endpoints of the interval.

The Chebyshev polynomial of the first kind $T_n(x)$ is a polynomial of degree n defined for the interval $[-1, 1]$ by

$$T_n(x) = \cos(n \arccos x), \ \ n = 0, 1..., N. \tag{3.2}$$

The trigonometric relation

$$\cos(n+1)\theta + \cos(n-1)\theta = 2\cos\theta\sin\theta \tag{3.3}$$

gives the recurrence relation [1]

$$T_{n+1}(x) - 2xT_n(x) + T_{n-1}(x) = 0, \ n \geq 1 \tag{3.4}$$

with $T_0(x) = 1$ and $T_1(x) = x$. The recurrence relation on the derivative is

$$\frac{T'_{n+1}(x)}{n+1} - \frac{T'_{n-1}(x)}{n-1} = 2T_n(x), \ \ n > 1. \tag{3.5}$$

A function $\Phi(x)$ defined in $[-1, 1]$ is interpolated by the polynomial $\Phi_N(x)$ of degree at most N of the form [14, 72]

$$\Phi_N(x) = \sum_{j=0}^{N} C_j(x)\Phi(x_j) \tag{3.6}$$

with $\Phi_N(x_j) = \Phi(x_j)$, and $C_j(x)$ is a Cardinal function of degree N defined by

$$C_j(x) \ \ = \ \ (-1)^{i+j}\frac{(1-x^2)T'_N(x)}{c_j N^2(x-x_j)}, \ \ \ j = 0, 1, ..., N$$

$$\tag{3.7}$$

$$= \ \ \frac{2}{N\xi_j}\sum_{m=0}^{N}\frac{1}{\xi_m}T_m(x_j)T_m(x).$$

64

The collocation points are the CGL points which are defined on the standard interval as

$$x_j = \cos(\frac{j\pi}{N}) \qquad (3.8)$$

and $c_0 = c_N = 2$, and $c_j = 1$ for $j = 1, ..., N-1$.

$$C_j(x_k) = \delta_{jk}, \quad j, k = 0, 1..., N \qquad (3.9)$$

and $\xi_j = 2$ for $j = 0, N, \quad \xi_j = 1$ if $j = 1, ..., N-1$. The $n-$th derivative of $\Phi(x)$ is then approximated by

$$\Phi_N^{(n)}(x) = \sum_{j=0}^{N} C_j^{(n)}(x)\Phi(x_j). \qquad (3.10)$$

The first derivative at the CGL points satisfy $C_j^{(1)}(x_i) = d_{ij}$ where

$$d_{00} = \frac{2N^2 + 1}{6}$$

$$d_{NN} = -d_{00} \qquad (3.11)$$

$$d_{ij} = \frac{\xi_i}{\xi_j} \frac{(-1)^{i+j}}{x_i - x_j} \quad j \neq i, \quad j, i = 1, ..., N-1.$$

Now, the discrete values of the first derivative of the function $\Phi_N(x)$ can be obtained as

$$\Phi_N^{(1)}(x_i) = \sum_{j=0}^{N} d_{ij}\Phi_N(x_j). \qquad (3.12)$$

This equation can be written in matrix-vector form as

$$\frac{d}{dx}\{\Phi_N\} = [D_N^{(1)}]\{\Phi_N\} \qquad (3.13)$$

where $[D_N^{(1)}] = [d_{ij}]$ is called the first order Chebyshev spectral differentiation matrix which is of size $(N+1) \times (N+1)$, [14, 72]. In order to minimize the roundoff errors for the calculation of the first derivatives, the diagonal entries d_{ii} are computed by [72]

$$d_{ii} = -\sum_{j=0, j\neq i}^{N} d_{ij}. \qquad (3.14)$$

The $n-$th order derivative of the function $\Phi(x)$ is approximated now by

$$\frac{d^n}{dx^n}\{\Phi_N\} = [D_N^{(n)}]\{\Phi_N\} \qquad (3.15)$$

where $[D_N^{(n)}] = [D_N^{(1)}]^n$ and n denotes the usual matrix multiplication n-times. $[D_N^{(n)}]$ is referred as the n-th order Chebyshev spectral differentiation matrix.

The use of matrix multiplication for higher order derivatives and the use of equation (3.14) for obtaining diagonal entries lead to significantly greater accuracy in the computation of second and higher order derivatives for a wide range of functions. The Chebyshev spectral differentiation matrix for functions defined on an arbitrary interval $[a, b]$ can be constructed by a linear transformation

$$x_j = \frac{b - a}{2}x + \frac{a + b}{2} \tag{3.16}$$

which maps the standard interval $[-1, 1]$ to any finite interval $[a, b]$. Thus, the CGL points over the interval $[a, b]$ can be taken as

$$x_j = \frac{b - a}{2}\cos(\frac{j\pi}{N}) + \frac{a + b}{2} \tag{3.17}$$

where $j = 0, 1, ..., N$.

3.2 Applications of CSCM to Navier-Stokes Equations and Natural Convection Flow under a Magnetic Field

The applications of the Chebyshev spectral collocation method to two-dimensional flow problems of incompressible fluids are presented in this section. First, in Section 3.2.1, the efficiency of the method is investigated by means of the Navier-Stokes equations with exact solution. Next, the CSCM application to lid-driven square cavity problem is provided in Section 3.2.2. Natural convection flow problem in inclined enclosures under the magnetic field effect is the third application which is considered in Section 3.2.3. The derivation of CSCM equations, solution procedure, numerical results and also a comparison with the previously obtained FEM results are discussed separately for each problem.

3.2.1 Navier-Stokes Equations with Exact Solution

The problem of N-S equations with known solution which is solved in Section 2.4.1 of Chapter 2 using FEM, is reconsidered in this section as the first numerical test. The application of CSCM to the given problem, tests the efficiency of the method and moreover, provides a comparison with previously obtained FEM results. The N-S equations including an additional non-dimensional force term f, are given as

$$\nabla^2\psi = -w, \tag{3.18}$$

$$\nabla^2 w + Re\left(\frac{\partial\psi}{\partial x}\frac{\partial w}{\partial y} - \frac{\partial\psi}{\partial y}\frac{\partial w}{\partial x}\right) = f, \tag{3.19}$$

in a square domain where $0 \leq x, y \leq 1$. The no-slip boundary conditions are imposed, and the exact solutions for the stream function and vorticity are

$$\psi_e = -8(x - x^2)^2(y - y^2)^2, \tag{3.20}$$

and

$$w_e = 16[(6x^2 - 6x + 1)(y - y^2)^2 + (x - x^2)^2(6y^2 - 6y + 1)] \,. \qquad (3.21)$$

The boundary conditions for stream function and vorticity are obtained directly from (3.20) and (3.21) as (see Figure 3.1)

$$\psi = 0 \qquad \text{on } x = y = 0 \text{ and } x = y = 1,$$

$$w = 16(-y^2 + y)^2 \qquad \text{on } x = 0 \text{ and } x = 1, \qquad (3.22)$$

$$w = 16(-x^2 + x)^2 \qquad \text{on } y = 0 \text{ and } y = 1 \,.$$

The forcing function f is derived by substituting (3.20) and (3.21) into (3.19).
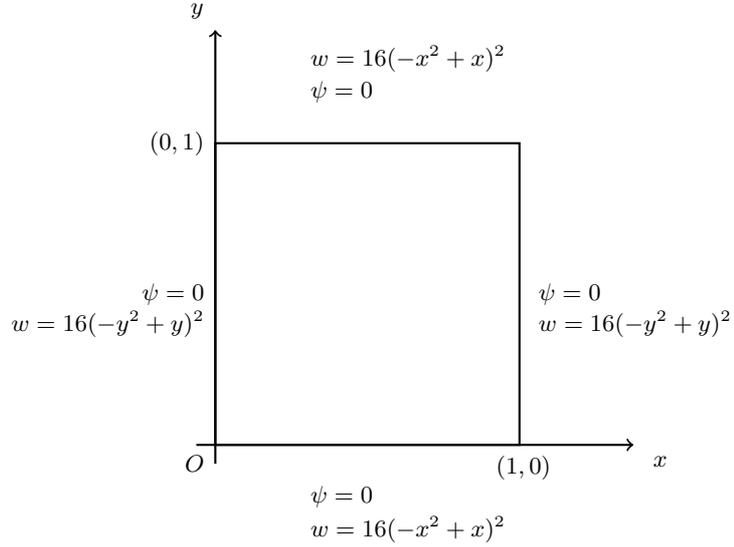
Figure 3.1: Domain and boundary conditions of Problem 3.2.1.

The CSCM introduced in Section 3.1 is applied to the two-dimensional N-S equations given in (3.18)-(3.19). The CGL points are taken independently in x- and y- directions to discretize the problem domain. That is, the number of points on which the problem region is discretized and the differentiation matrices are based on, can be different. In this study, however, equal number of points in each direction are taken. As the problem is defined on $0 \le x, y \le 1$, the CGL points in the interval $[0, 1]$ in x- direction are taken as

$$x_i = \frac{1}{2} \cos(\frac{i\pi}{N}) + \frac{1}{2} \,,$$

and similarly in y- direction as

$$y_j = \frac{1}{2} \cos(\frac{j\pi}{N}) + \frac{1}{2}$$
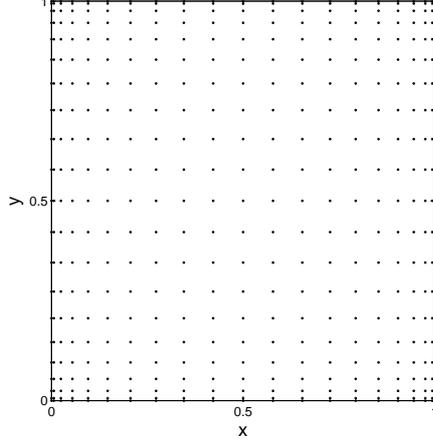
Figure 3.2: A sample CGL node distribution of a square region using $N = 20$.

where $i, j = 0, 1, ..., N$. The collocation points in this case, gather through the boundaries as can be seen from Figure 3.2, where a sample distribution of collocation points on a 21×21 grid in a square domain is illustrated.

Following the steps of Section 3.1, the first order Chebyshev differentiation matrix $[D_N^{(1)}] = [d_{ij}^{(1)}]$ in x- direction is derived, where $d_{ij}^{(1)}$ are computed using (3.11). Similarly, the first order differentiation matrix in y- direction, $[E_N^{(1)}] = [e_{ij}^{(1)}]$, is computed in the same way replacing x_j by y_j in (3.11). As mentioned in Section 3.1, the diagonal entries $d_{ii}^{(1)}$ and $e_{ii}^{(1)}$, where $i = 0, 1, ..., N$, are calculated using (3.14) and the second order differentiation matrices are obtained by squaring the first order matrices. Hence, the second order Chebyshev differentiation matrix in x-direction $[D_N^{(2)}]$ is computed as

$$[D_N^{(2)}] = [D_N^{(1)}]^2$$

and similarly the second order Chebyshev differentiation matrix in y-direction $[E_N^{(2)}]$ is computed as

$$[E_N^{(2)}] = [E_N^{(1)}]^2 .$$

Having constructed the differentiation matrices, the approximations ψ_N to stream function and w_N to vorticity are substituted into the equations (3.18) and (3.19)

$$d_{ij}^{(2)}(\psi_N)_{ij} + e_{ij}^{(2)}(\psi_N)_{ij} = -(w_N)_{ij},$$

$$d_{ij}^{(2)}(w_N)_{ij} + e_{ij}^{(2)}(w_N)_{ij} = \qquad (3.23)$$

$$-Re \left[d_{ij}^{(1)}(\psi_N)_{ij} \; e_{ij}^{(1)}(w_N)_{ij} - e_{ij}^{(1)}(\psi_N)_{ij} \; d_{ij}^{(1)}(w_N)_{ij} \right] + f_{ij}$$

where $i, j = 0, 1, ..., N$, and $d_{ij}^{(n)}$ and $e_{ij}^{(n)}$ are Chebyshev spectral $n-$th derivative coefficients in $x-$ and $y-$ directions, respectively. The discretized equations in

(3.23) can be written in matrix-vector form by using the Kronecker product $\otimes$. The Kronecker product of an $m_1 \times n_1$ matrix P and an $m_2 \times n_2$ matrix S is defined as the $m_1 m_2 \times n_1 n_2$ matrix $P \otimes S$, which is an $m_1 \times n_1$ block matrix with ij-th block is the $m_2 \times n_2$ matrix $p_{ij} S$. Then, equations in (3.23) are written in matrix-vector notation as

$$[\tilde{A}]\{\psi_N\} = -\{w_N\}$$

$$[\tilde{A}]\{w_N\} + Re[\tilde{B}]\{w_N\} = \{\tilde{F}_1\} \ .$$

(3.24)

The $(N+1)^2 \times (N+1)^2$ matrices $[\tilde{A}]$ and $[\tilde{B}]$ are defined as

$$[\tilde{A}] = [I_N] \otimes [D_N^{(2)}] + [E_N^{(2)}] \otimes [I_N]$$

and

$$[\tilde{B}] = \left([I_N] \otimes [D_N^{(1)}]\right)\{\psi_N\} \ \left([E_N^{(1)}] \otimes [I_N]\right)$$

$$- \left([E_N^{(1)}] \otimes [I_N]\right)\{\psi_N\} \ \left([I_N] \otimes [D_N^{(1)}]\right) \ .$$

The right hand side vector $\{\tilde{F}_1\}$ is of size $(N+1)^2$ and computed in the following pattern

$$\{\tilde{F}_1\} = [f(x_0, y_0), ..., f(x_N, y_0), ..., f(x_0, y_N), ..., f(x_N, y_N)]^{\mathrm{T}} \ .$$

The approximation vectors $\{\psi_N\}$ and $\{w_N\}$ have the same ordering as $\{\tilde{F}_1\}$. Application of CSCM to the N-S equations (3.18) and (3.19) results in two coupled and nonlinear equations given in (3.24). In order to solve the resulting equations, an iterative procedure is introduced which reduces the equations into a set of linear algebraic equations in each iteration. The algebraic equations are solved by imposing the given boundary conditions. For the present problem, boundary conditions for both stream function and vorticity are supplied as of Dirichlet type. These boundary conditions are imposed by modifying the left hand side matrices of the systems and inserting the corresponding values on the right hand side vectors. In general, Neumann or mixed types of boundary conditions can be imposed by a similar modification of the left hand side matrices and right hand side vectors. The iterative process for CSCM Equations (3.24) starts with a given initial estimate for vorticity. The first equation in (3.24) is solved and the stream function values are obtained on the whole problem domain. The second equation in (3.24), is next solved to obtain the new values of the vorticity on the computational domain. These steps are repeated until the convergence criteria

$$\left|(\psi_N)_k^{(m+1)} - (\psi_N)_k^{(m)}\right| \le \varepsilon, \quad \left|(w_N)_k^{(m+1)} - (w_N)_k^{(m)}\right| \le \varepsilon$$

is met, where the superscript m is the iteration level, k denotes the k-th node, and $k = 1, ..., (N+1)^2$.

3.2.1.1 Numerical results

The solution procedure is carried out by means of a MATLAB code, and the iterations are terminated when the convergence tolerance is $\varepsilon = 10^{-6}$. Numerical tests are performed for Reynolds numbers, $Re = 0$, 10^3 and 10^4. Figure 3.3 presents the streamlines and vorticity contours of the numerical solutions obtained by taking $N = 24$, and the exact solutions. It is observed in all cases that the numerical solutions perfectly agree with the exact solutions for both stream function and vorticity . The results indicate that CSCM can successively be used to capture the behavior of the flow defined by the N-S equations with considerably small computational cost compared to FEM.

Figure 3.3: Problem 3.2.1: Streamlines (L) and vorticity contours (R) when $N = 24$ for (**a**) $Re = 0$, (**b**) $Re = 10^3$, (**c**) $Re = 10^4$.

The maximum absolute error values ψ_e for stream function and w_e for vorticity which are defined as

$$\epsilon_\psi = \max_{ij} |(\psi_N)_{ij} - \psi_e(x_i, y_j)|, \quad \epsilon_w = \max_{ij} |(w_N)_{ij} - w_e(x_i, y_j)|$$

are also calculated for an efficiency investigation of the numerical procedure and a comparison with FEM solutions quantitatively. The numerical results of FEM

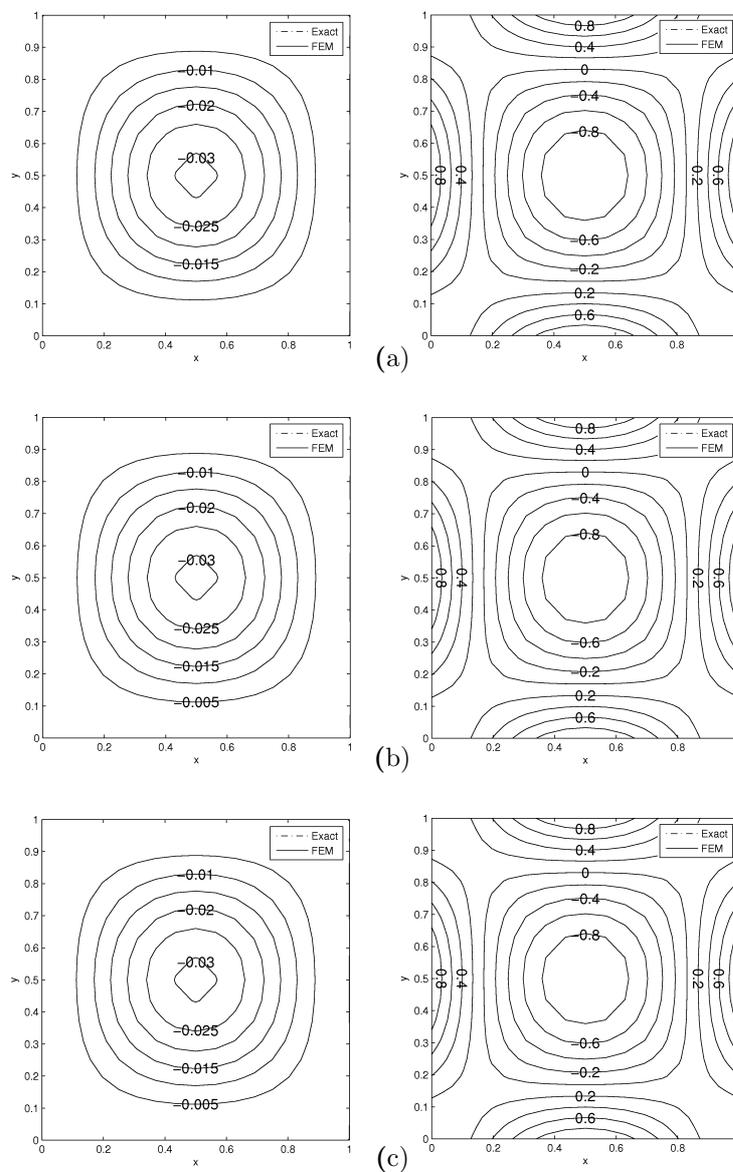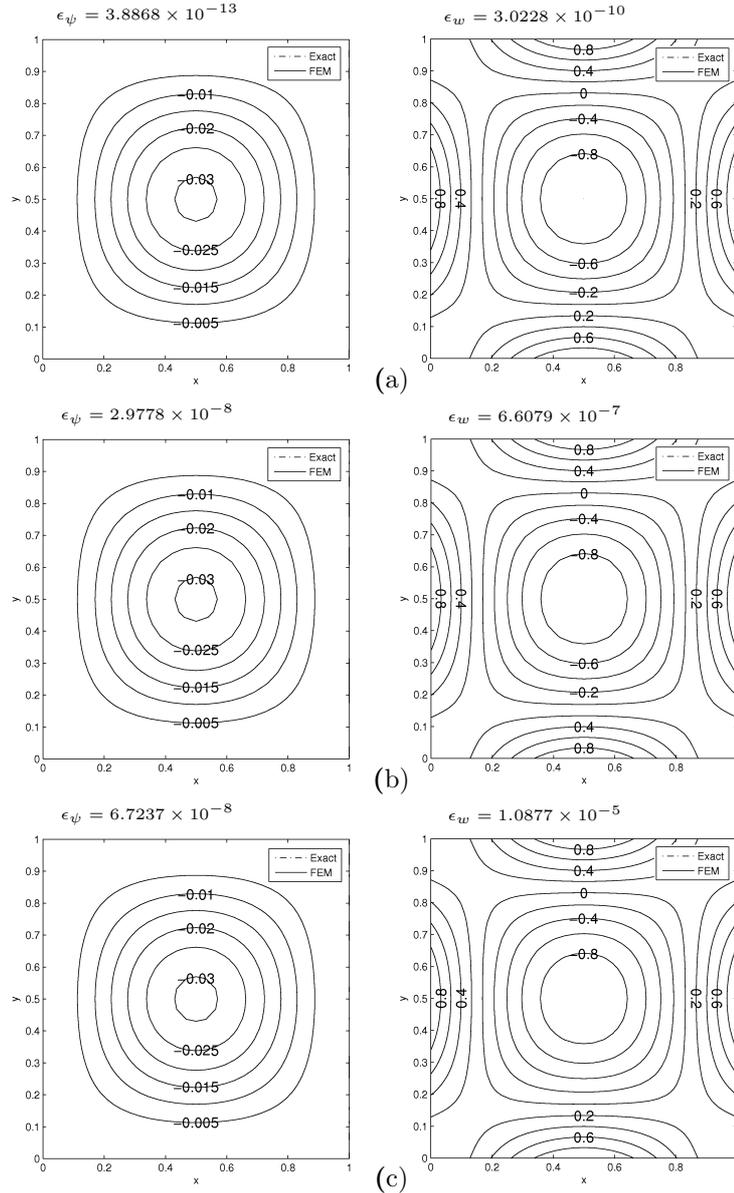
Figure 3.4: Problem 3.2.1: Streamlines (L) and vorticity contours (R) for (a) $Re = 0$, (b) $Re = 10^3$, (c) $Re = 10^4$.

application to Problem 3.2.1 are presented in Section 2.4.1 of Chapter 2. In FEM solutions, when $Re = 0$ and $Re = 10^3$, $M_e = 800$ quadratic triangular elements are used to discretize the problem domain which results in solving a system of

size 1521×1521, reduced after the imposition of the Dirichlet type boundary conditions in every iteration for each equation. For higher Reynolds number case where $Re = 10^4$, $M_e = 1250$ elements are used in discretization, and the resulting reduced system is of size 2401×2401. For a quantitative comparison in terms of maximum absolute errors, the number of collocation points are taken so as to result in equal degrees of freedom, for the two methods. Thus, the numerical results in CSCM solutions are obtained by taking $N = 40$ for the cases where $Re = 0$ and $Re = 10^3$, and $N = 50$ for the case where $Re = 10^4$. Figure 3.4 presents the streamlines and vorticity contours for Reynolds number values $Re = 0$, 10^3 and 10^4. The error values ϵ_ψ and ϵ_ψ are also provided in Figure 3.4 on the top of each plot. It is observed that the values ϵ_ψ and ϵ_ψ obtained from CSCM solutions are less than those obtained from FEM for the tested Re values $Re = 0$, 10^3 and 10^4. Especially the $Re = 0$ case which lacks the convective terms in the vorticity transport equation has very small error values in magnitude for both stream function and vorticity solutions. In the case where the convective terms are dominant, namely $Re = 10^4$, the differences between the corresponding ϵ_ψ and ϵ_ψ values obtained from CSCM and FEM are diminishing. For Reynolds number values up to 10^4, CSCM solutions are closer to the exact solutions compared to FEM solutions, although both numerical methods provide sufficient efficiency in solving these types of flow problems. These results put forward the high accuracy achievement of CSCM which is the well known advantage of spectral methods. However, the crucial point is that the CSCM for Reynolds numbers higher than $Re = 10^4$ produces oscillations and the method fails to produce convergent results. The Galerkin finite element method approach, achieves an excellent agreement with the exact solutions up to $Re = 10^6$ which is the highest value for these type of problems used in the literature to test numerical procedures. FEM possess the superiority to CSCM (although the computation complexity is high) when there is a convection dominance as in the cases $Re = 10^5$ and $Re = 10^6$ for the present problem.

3.2.2 Lid-driven Square Cavity Flow

The results of the previous section have put forward that the Chebyshev spectral collocation method can successively be applied to solve Navier-Stokes equations. In this section, the application of CSCM is extended to the lid-driven flow in square cavities. The lid-driven cavity problem is solved in Section 2.4.2 of Chapter 2 by using FEM, and the results for Reynolds number up to $Re = 10000$ are presented in the same section. This benchmark problem is reconsidered in this section to investigate the efficiency of the method and exhibit a comparison with previously obtained results. The governing equations are given as in Section 2.4.2

$$\nabla^2 \psi = -w, \tag{3.25}$$

$$\frac{1}{Re}\nabla^2 w + \frac{\partial \psi}{\partial x}\frac{\partial w}{\partial y} - \frac{\partial \psi}{\partial y}\frac{\partial w}{\partial x} = 0 \,. \tag{3.26}$$

As before, the no-slip boundary conditions, $u = v = 0$, on the three solid walls of the square cavity are assigned, and the top wall is moving in its plane to the right with a velocity $u = 1$, $v = 0$, see Figure 3.5.
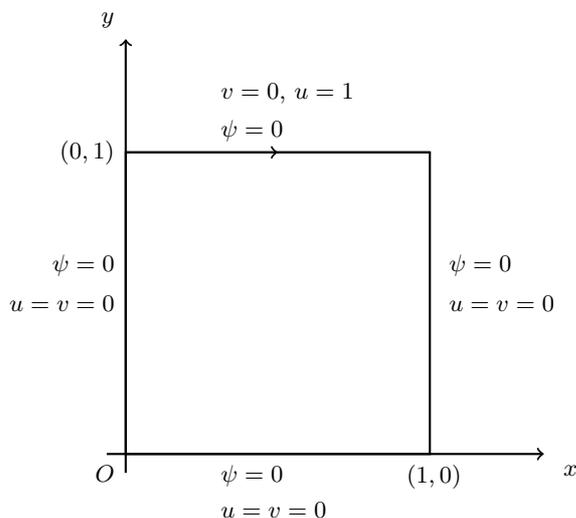
Figure 3.5: Domain and boundary conditions of Problem 3.2.2.

The lid-driven cavity problem is arduous because of the singularities at the moving wall where the velocity is discontinuous. It is well known that in spectral methods, as the approximation and derivatives of the unknown function depend on the entire discretization, the difficulties arising from the discontinuity at the boundaries are more pronounced. There are several approaches used by researchers to overcome the issue, such as smoothing the velocity on the upper lid so as that it vanishes at the corners and the continuity of the boundary conditions is assured. Another method as proposed in [13] is to use substraction of the leading part of the singularity in asymptotic expansion of the solution. In this study however, the essential intention of using the Chebyshev spectral collocation method is to benefit the simple formulation and low computational cost with high accuracy in one-dimensional problems as mentioned earlier. As the lid-driven cavity problem is reconsidered in this section to provide a basis for a comparison with finite element methodology, the governing equations (3.25) and (3.26) are discretized using CSCM, and the solutions are obtained by using a similar approach applied in Chapter 2. The basic steps of the previous section are followed to obtain the CSCM discretized form of the Equations (3.25)-(3.26). The number of CGL points is taken equal in both x- and y- directions as

$$x_i = \frac{1}{2}\cos(\frac{i\pi}{N}) + \frac{1}{2}, \qquad y_j = \frac{1}{2}\cos(\frac{j\pi}{N}) + \frac{1}{2}$$

where $i, j = 0, 1, ..., N$. The first order Chebyshev differentiation matrix $[D_N^{(1)}] = [d_{ij}^{(1)}]$ in x- direction and the first order differentiation matrix in y- direction, $[E_N^{(1)}] = [e_{ij}^{(1)}]$, are computed as in Section 3.1. Similarly, the second order Chebyshev differentiation matrices $[D_N^{(2)}]$ and $[E_N^{(2)}]$ are computed in x- and y- directions,

73

respectively. The approximations ψ_N for stream function and w_N for vorticity are substituted in equations (3.25) and (3.26)

$$d_{ij}^{(2)}(\psi_N)_{ij} + e_{ij}^{(2)}(\psi_N)_{ij} = -(w_N)_{ij},$$

$$\frac{1}{Re}\left(d_{ij}^{(2)}(w_N)_{ij} + e_{ij}^{(2)}(w_N)_{ij}\right) = \tag{3.27}$$

$$-\left[d_{ij}^{(1)}(\psi_N)_{ij}\; e_{ij}^{(1)}(w_N)_{ij} - e_{ij}^{(1)}(\psi_N)_{ij}\; d_{ij}^{(1)}(w_N)_{ij}\right]$$

where $i, j = 0, 1, ..., N$, and $d_{ij}^{(n)}$ and $e_{ij}^{(n)}$, are the Chebyshev spectral n-th derivative coefficients in x- and y- directions, respectively. The CSCM discretized equations can be written in matrix-vector form as

$$[\tilde{A}]\{\psi_N\} = -\{w_N\}$$

$$\frac{1}{Re}[\tilde{A}]\{w_N\} + [\tilde{B}]\{w_N\} = 0 \,. \tag{3.28}$$

The $(N+1)^2 \times (N+1)^2$ matrices $[\tilde{A}]$ and $[\tilde{B}]$ are defined in Section 3.2.1. The coupled and nonlinear discretized Equations (3.28) are solved using an iterative procedure. The boundary conditions of vorticity are computed in this iterative process. Given an initial nonzero estimate for vorticity, the stream function equation in (3.28) is solved with the imposition of the given boundary conditions. The newly obtained stream function values ($\{\psi_N\}^{(m+1)}$) are used to compute the velocity components $\{u_N\}$ and $\{v_N\}$ as follows

$$\{u_N\}^{(m+1)} = \left([I_N] \otimes [D_N^{(1)}]\right)\{\psi_N\}^{(m+1)}$$

$$\{v_N\}^{(m+1)} = -\left([E_N^{(1)}] \otimes [I_N]\right)\{\psi_N\}^{(m+1)} \tag{3.29}$$

by imposing the boundary conditions for velocity so that $\{u_N\}^{(m+1)} = 1$ and $\{v_N\}^{(m+1)} = 0$ on the upper wall ($y = 1$) and $\{u_N\}^{(m+1)} = \{v_N\}^{(m+1)} = 0$ on the three solid walls of the cavity where the superscript m is the iteration level. Having obtained the velocity components which satisfy the given boundary conditions properly, the vorticity boundary conditions are calculated through

$$\left[\{w_N\}^{(m+1)}\right]\Big|_l = \left[\left([I_N] \otimes [D_N^{(1)}]\right)\{v_N\}^{(m+1)}\right]\Big|_l$$

$$- \left[\left([E_N^{(1)}] \otimes [I_N]\right)\{u_N\}^{(m+1)}\right]\Big|_l \tag{3.30}$$

where l denotes the l-th boundary node, varying from 1 to the total number of boundary nodes. Imposing the calculated boundary conditions, the vorticity equation in (3.28) is solved, and the vorticity values on the whole domain are obtained for the next iterative level ($m + 1$). In the calculation of vorticity boundary conditions, an experimentally determined parameter λ is employed to

increase the rate of convergence of the iterative procedure. Thus, the vorticity boundary values $[\{w_N\}|_l]^{(m+1)}$, at the $(m+1)$-th iteration level are averaged by the corresponding values from the m-th level via the relation

$$\left[\{w_N\}^{(m+1)}\right]\big|_l = \lambda\left[\{w_N\}^{(m+1)}\right]\big|_l + (1-\lambda)\left[\{w_N\}^{(m)}\right]\big|_l \qquad (3.31)$$

where $0 < \lambda < 1$. The iterations stop when the convergence criteria

$$\left|(\psi_N)_k^{(m+1)} - (\psi_N)_k^{(m)}\right| \leq \varepsilon, \quad \left|(w_N)_k^{(m+1)} - (w_N)_k^{(m)}\right| \leq \varepsilon$$

is satisfied, where k denotes the k-th node ($k = 1, ..., (N+1)^2$).

3.2.2.1 Numerical results

The CSCM equations (3.28) are solved iteratively by the procedure described above. The vorticity boundary conditions are calculated from (3.30) using spectral derivative matrices via the velocity components (3.29) where the specified boundary conditions are imposed. In the computations, $N = 50$ is taken and the convergence tolerance is set to be $\varepsilon = 10^{-6}$. The numerical results are obtained for $Re = 500$ and $Re = 1000$, and the streamlines and vorticity contours are presented in Figure 3.6. It can be observed that the streamlines and vorticity contours show a reasonable agreement with the FEM results. The similar flow pattern in terms of vortices and boundary layers for when $Re = 500$ and $Re = 1000$ proves that CSCM with the presented approach grants capturing the flow behavior. However, it was not possible to obtain the results for Reynolds number higher than 1000 as the iterative procedure fails to converge. The main reason for the failure may be the strong singularity of the velocity wall conditions as Reynolds number increases (convection dominance). Moreover, the presented solutions obtained with $N = 50$ which results in a (reduced) system of size 2601×2601 for $Re = 1000$, correspond to the equal system sized FEM results ($M_e = 1250$) obtained in Section 2.4.2 of Chapter 2. The full structure of the collocation matrices does not show a band matrix form. The structures of the stiffness matrix $[K]$ in FEM where $M_e = 1250$ (see Section 2.1 of Chapter 2) and the collocation matrix $[\tilde{A}]$ corresponding to the Laplacian term where $N = 50$, are visualized in Figure 3.7. The number of the nonzero entries in $[K]$ and $[\tilde{A}]$ are 29103 and 262701, respectively, where the total number of entries in both matrices is 6765201. It can be concluded that the full structure of the collocation matrices put forward a drawback of CSCM compared to FEM in which the global matrices are sparse. This may be the reason that high Re can not be treated by CSCM which gives convection dominant flow and needs fine discretization.
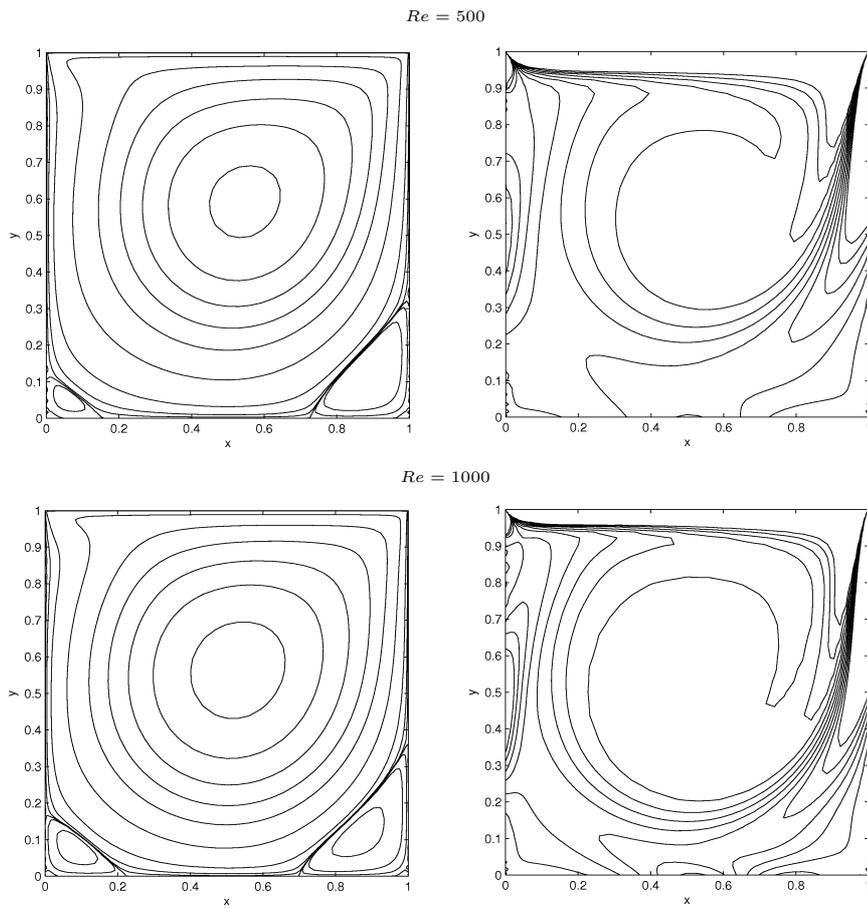
Figure 3.6: Problem 3.2.2: Streamlines (L) and vorticity contours (R) for $Re =$ 500 and 1000.
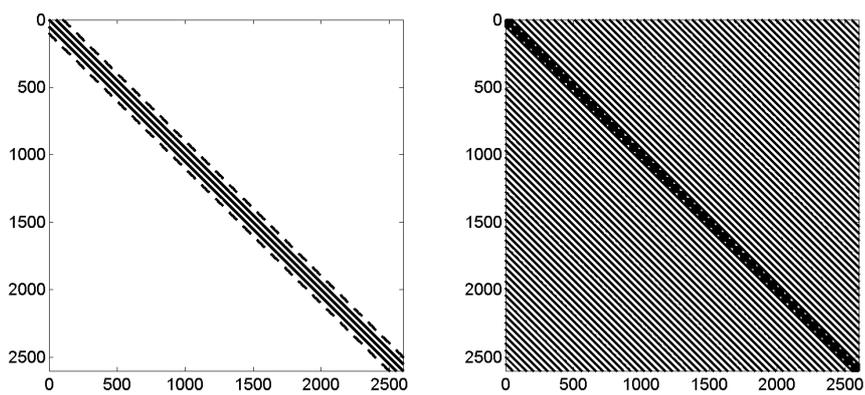
Figure 3.7: Sparsity patterns of FEM matrix $[K]$ (left) and CSCM matrix $[\tilde{A}]$ (right).

3.2.3 Natural Convection Flow under a Magnetic Field

In this section, the CSCM solution to the problem of natural convection flow under externally applied magnetic field in a square enclosure is presented. The governing equations in stream function ψ, vorticity w and temperature T are given as in Section 2.3,

$$\nabla^2 \psi = -w$$

$$
\begin{aligned}
Pr\nabla^2 w = \ & \frac{\partial \psi}{\partial y}\frac{\partial w}{\partial x} - \frac{\partial \psi}{\partial x}\frac{\partial w}{\partial y} - RaPr\left(\cos\phi\frac{\partial T}{\partial x} - \sin\phi\frac{\partial T}{\partial y}\right) \\
& -Ha^2Pr\left[\cos\varphi\left(\sin\varphi\frac{\partial^2\psi}{\partial x\partial y} + \cos\varphi\frac{\partial^2\psi}{\partial x^2}\right)\right. \\
& \left. +\sin\varphi\left(\sin\varphi\frac{\partial^2\psi}{\partial y^2} + \cos\varphi\frac{\partial^2\psi}{\partial y\partial x}\right)\right]
\end{aligned}
\tag{3.32}
$$

$$\nabla^2 T = \frac{\partial \psi}{\partial y}\frac{\partial T}{\partial x} - \frac{\partial \psi}{\partial x}\frac{\partial T}{\partial y}.$$

The angles φ and ϕ are the angles of the externally applied magnetic field direction and the inclination of the cavity. The Dirichlet type boundary conditions of stream function and temperature are specified as

$$\psi(x,0) = 0, \ \ \psi(0,y) = 0, \ \ \psi(x,1) = 0, \ \ \psi(1,y) = 0, \tag{3.33}$$

$$T(x,1) = 0, \ \ T(1,y) = 0, \ \ T(x,0) = 1 - x, \ \ T(0,y) = 1 - y. \tag{3.34}$$

These boundary conditions and the problem configuration are shown in Figure 3.8. The physically unknown boundary conditions of vorticity are calculated by an approach based on CSCM treatment of the stream function equation as in the previous section.
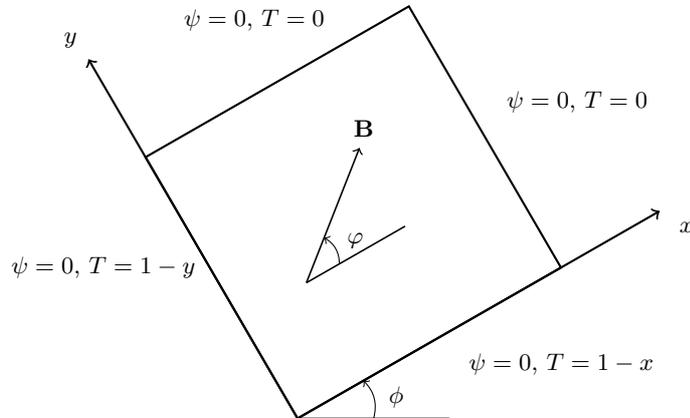
Figure 3.8: The geometry and boundary conditions of Problem 3.2.3.

The procedure given in Section 3.2.3 is followed to develop the Chebyshev spectral collocation method to the natural convection flow equations given in (3.32). Equal number of CGL points are taken in both x- and y- directions as

$$x_i = \frac{1}{2}\cos(\frac{i\pi}{N}) + \frac{1}{2}, \qquad y_j = \frac{1}{2}\cos(\frac{j\pi}{N}) + \frac{1}{2}$$

where $i, j = 0, 1, ..., N$. The first order Chebyshev differentiation matrix $[D_N^{(1)}] = [d_{ij}^{(1)}]$ in x-direction and the first order differentiation matrix in y-direction, $[E_N^{(1)}] = [e_{ij}^{(1)}]$, are computed as in Section 3.1. Similarly, the second order Chebyshev differentiation matrices $[D_N^{(2)}]$ and $[E_N^{(2)}]$ are computed in x- and y- directions, respectively. The approximations ψ_N, w_N and T_N for stream function, vorticity and temperature, respectively, are substituted into the equations in (3.32)

$$d_{ij}^{(2)}(\psi_N)_{ij} + e_{ij}^{(2)}(\psi_N)_{ij} = -(w_N)_{ij},$$

$$Pr\left(d_{ij}^{(2)}(w_N)_{ij} + e_{ij}^{(2)}(w_N)_{ij}\right) = e_{ij}^{(1)}(\psi_N)_{ij}d_{ij}^{(1)}(w_N)_{ij} - d_{ij}^{(1)}(\psi_N)_{ij}e_{ij}^{(1)}(w_N)_{ij}$$

$$-RaPr\left(\cos\phi\, d_{ij}^{(1)}(T_N)_{ij} - \sin\phi\, e_{ij}^{(1)}(T_N)_{ij}\right)$$

$$-Ha^2Pr\,\cos\varphi\left(\sin\varphi\, d_{ij}^{(1)}e_{ij}^{(1)}(\psi_N)_{ij} + \cos\varphi\, d_{ij}^{(2)}(\psi_N)_{ij}\right)$$

$$-Ha^2Pr\,\sin\varphi\left(\sin\varphi\, e_{ij}^{(2)}(\psi_N)_{ij} + \cos\varphi\, e_{ij}^{(1)}d_{ij}^{(1)}(\psi_N)_{ij}\right)$$

$$d_{ij}^{(2)}(T_N)_{ij} + e_{ij}^{(2)}(T_N)_{ij} = e_{ij}^{(1)}(\psi_N)_{ij}d_{ij}^{(1)}(T_N)_{ij} - d_{ij}^{(1)}(\psi_N)_{ij}e_{ij}^{(1)}(T_N)_{ij}\,.$$

$$(3.35)$$

where $i, j = 0, 1, ..., N$, and $d_{ij}^{(n)}$ and $e_{ij}^{(n)}$, are the Chebyshev spectral $n-$th derivative coefficients in x- and y- directions, respectively. The CSCM discretizated equations can be written in matrix-vector form as

$$[\tilde{A}]\{\psi_N\} = -\{w_N\} \tag{3.36}$$

$$Pr[\tilde{A}]\{w_N\} + [\tilde{B}]\{w_N\} = \{\tilde{F}_2\} \tag{3.37}$$

$$[\tilde{A}]\{T_N\} + [\tilde{B}]\{T_N\} = 0 \tag{3.38}$$

where the $(N+1)^2 \times (N+1)^2$ matrices $[\tilde{A}]$ and $[\tilde{B}]$ are defined in Section 3.2.1,

78

and the $(N+1)^2 \times 1$ vector $\{\tilde{F}_2\}$ is defined as

$$\{\tilde{F}_2\} = -RaPr \left[\cos\phi \left([I_N] \otimes [D_N^{(1)}] \right) \{T_N\} - \sin\phi \left([E_N^{(1)}] \otimes [I_N] \right) \{T_N\} \right]$$

$$-Ha^2 Pr \left[\cos\varphi \left(\sin\varphi \left([I_N] \otimes [D_N^{(1)}] \right) \left([E_N^{(1)}] \otimes [I_N] \right) \{\psi_N\} \right. \right.$$

$$+ \cos\varphi \left([I_N] \otimes [D_N^{(2)}] \right) \{\psi_N\} \right)$$

$$+ \sin\varphi \left(\sin\varphi \left([E_N^{(2)}] \otimes [I_N] \right) \{\psi_N\} \right.$$

$$\left. \left. + \cos\varphi \left([E_N^{(1)}] \otimes [I_N] \right) \left([I_N] \otimes [D_N^{(1)}] \right) \{\psi_N\} \right) \right].$$

Equations (3.36)-(3.38) are coupled and nonlinear and hence an iterative procedure similar to the one given the previous section is implemented. Given an initial nonzero estimate for vorticity, the stream function equation (3.36) is solved with the imposition of the given boundary conditions. Having obtained the stream function values on the whole domain, the vorticity boundary conditions are calculated from (3.30) through the velocity components in the same way as given in Section 3.2.2. Imposing the calculated boundary conditions, the vorticity equation (3.37) is solved (an initial estimate for temperature is used for the first iteration). The procedure carries on by solving the temperature equation (3.38) with the imposition of given boundary conditions, as the final step of each iteration. The iterations stop when the convergence criteria

$$\left| (\psi_N)_k^{(m+1)} - (\psi_N)_k^{(m)} \right| \leq \varepsilon$$

$$\left| (w_N)_k^{(m+1)} - (w_N)_k^{(m)} \right| \leq \varepsilon$$

$$\left| (T_N)_k^{(m+1)} - (T_N)_k^{(m)} \right| \leq \varepsilon$$

is met, where as before, the superscript m is the iteration level and k denotes the k-th node, $k = 1, ..., (N+1)^2$.

3.2.3.1 Numerical results

Numerical solutions to Problem 3.2.3 are obtained in Chapter 2 using FEM, and the numerical results with discussions are presented in Section 2.4.4.2 of the same chapter for various values of Ra, Ha, ϕ and φ. Thus, in this section, the numerical results obtained by the application of CSCM to the natural convection flow under magnetic field, are presented for the highest set of Rayleigh number and Hartmann number values, namely, $Ra = 10^6$ and $Ha = 100$. The CSCM equations (3.36)-(3.38) are solved following the iterative procedure described above and, $N = 50$ is taken in the computations. Prandtl number is taken as $Pr = 1$,

and the convergence tolerance is set to be $\varepsilon = 10^{-6}$. The numerical tests are carried out for various values of ϕ and φ, and the results are illustrated in terms of the contours of the unknowns. Figures 3.9, 3.10 and 3.11 present the streamlines, vorticity contours and isotherms for the sets of cavity inclination and magnetic field direction angles, $\phi = 0$, $\varphi = 0$; $\phi = 45$, $\varphi = 45$ and $\phi = -45$, $\varphi = 45$, respectively. It is observed that the CSCM solutions agree very well with the previously obtained FEM results for the given sets of angles. The contours possess the same behaviors especially for the streamlines and isotherms, in terms of contour magnitudes and boundary layers, although the contours are drawn on different grids based on the discretization of each method. There are slight discrepancies between the solutions obtained from CSCM and FEM, especially in vorticity magnitudes. The difference in magnitudes is mainly due to the different locations of the discretization points of CSCM and FEM. Another distinctive feature of the two methods is the computations of the vorticity wall conditions.

Figure 3.9: Problem 3.2.3: Streamlines (L), vorticity (M) and temperature (R) contours for $Ra = 10^6$ and $Ha = 100$, $\phi = 0$, $\varphi = 0$.

In CSCM, the vorticity wall values are computed based on the stream function values on the entire domain, whereas in FEM, the vorticity boundary values are calculated using two inner values of stream function by means of a second order Taylor series approximation. On the other hand, the tendency of vorticity contours and the magnitudes show an excellent agreement in both methods for all cases considered, noting unequal points where the solutions and the contour level calculations are based on. In the present problem, the continuity of the
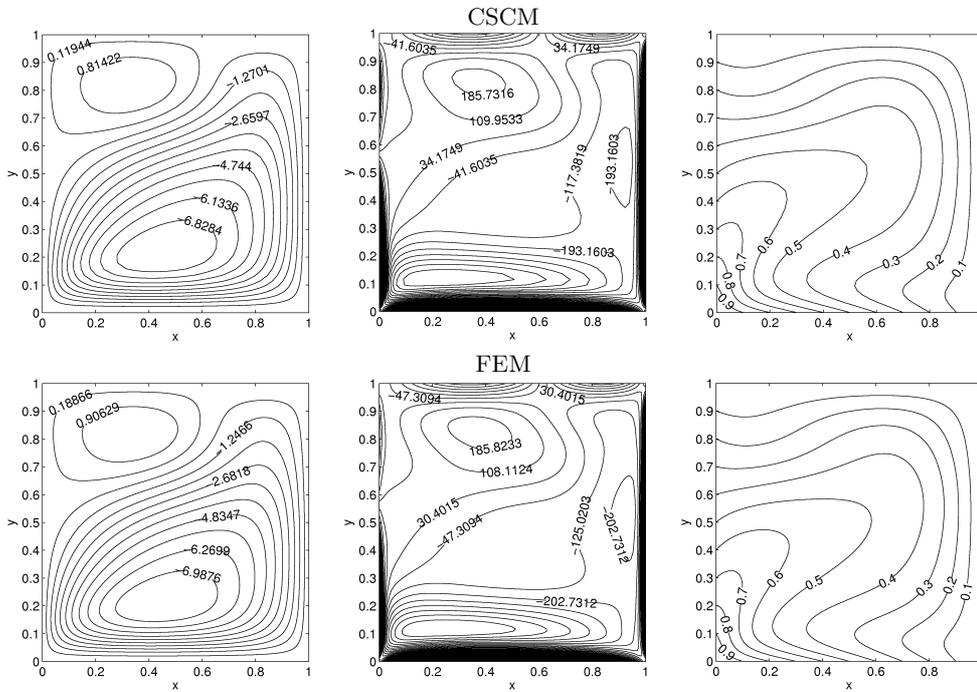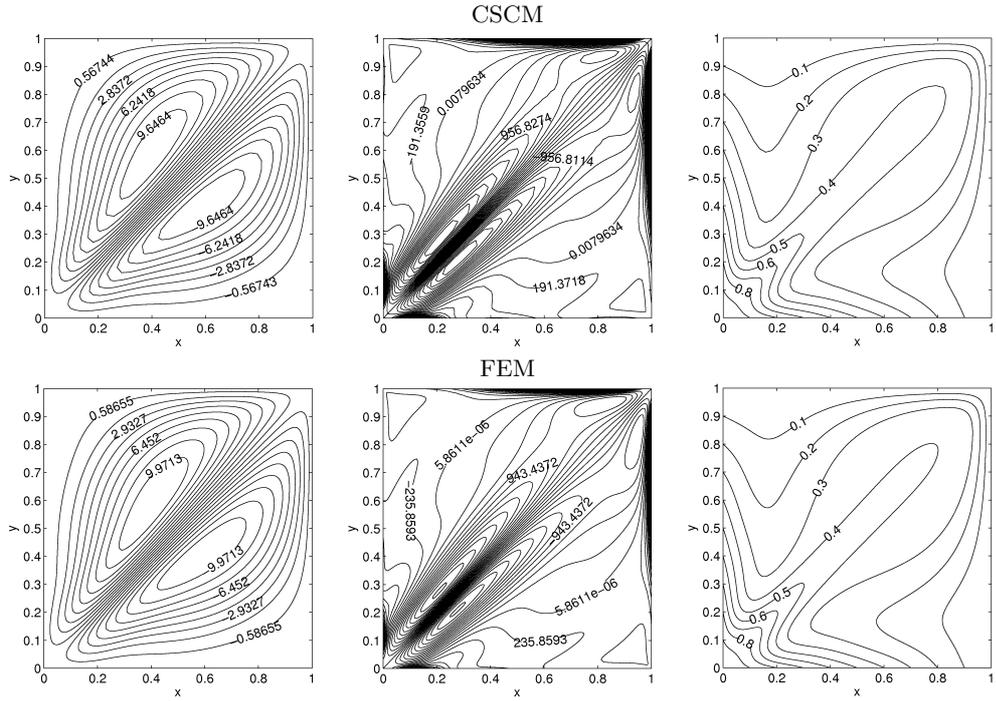
Figure 3.10: Problem 3.2.3: Streamlines (L), vorticity (M) and temperature (R) contours for $Ra = 10^6$ and $Ha = 100$, $\phi = 45$, $\varphi = 45$.
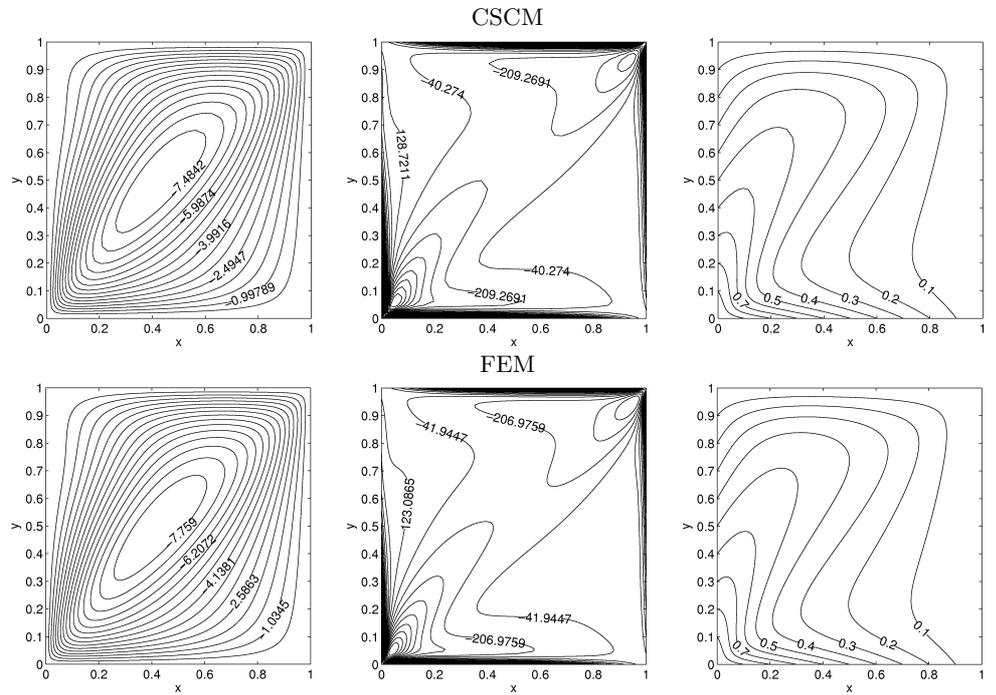
Figure 3.11: Problem 3.2.3: Streamlines (L), vorticity (M) and temperature (R) contours for $Ra = 10^6$ and $Ha = 100$, $\phi = -45$, $\varphi = 45$.

velocity boundary conditions allows the CSCM to capture the behaviors of the flow and temperature for high values of the characteristic parameters ($Ra = 10^6$ and $Ha = 100$). Consequently, the results show that the Chebyshev spectral collocation method can successively be applied for solving natural convection flow problems under the influence of an external magnetic field with different directions in inclined square cavities.

3.3 Application of CSCM to MHD flow and heat transfer between two parallel plates

This section considers the one-dimensional, unsteady MHD flow and heat transfer of a viscous, electrically conducting, incompressible fluid between two parallel plates. The non-dimensional equations governing the flow of an unsteady, incompressible and electrically conducting fluid which has temperature dependent viscosity are introduced in Section 1.1.4 as

$$\frac{\partial u}{\partial t} + Rv \frac{\partial u}{\partial y} = G + \frac{\partial}{\partial y}\left[\mu(T)\frac{\partial u}{\partial y}\right] - Ha^2 u,$$

$$\frac{\partial T}{\partial t} + Rv \frac{\partial T}{\partial y} = \frac{1}{Pr}\frac{\partial^2 T}{\partial y^2} + Ec\,\mu(T)\left(\frac{\partial u}{\partial y}\right)^2 + Ec\,Ha^2\,u^2, \tag{3.39}$$

$$-1 \le y \le 1,\ t > 0.$$

Here, u denotes the velocity of the fluid in x- direction which is fully developed and varies parabolically with respect to y, and T is the temperature of the fluid. Rv is the constant velocity component in the y- direction which may be considered as inflow/outflow parameter through the plates. $Rv = 0$ corresponds to the absence of inflow/outflow through plates at $y = \mp 1$. The dimensionless parameters Hartmann number Ha, Prandtl number Pr, Eckert number Ec and the pressure gradient G are given in Section 1.1.4. The initial and boundary conditions are,

$$u(y,0) = 0,\ T(y,0) = 0 \quad \text{on} \quad -1 \le y \le 1,$$

$$u(-1,t) = 0,\ T(-1,t) = 0,$$

$$u(1,t) = Ru,\ T(1,t) = 1,$$

where Ru is the velocity of the moving upper plate. A sketch of the problem domain is provided where the boundary conditions are also shown in Figure 3.12. The dynamic viscosity has exponential variation as

$$\mu(T) = e^{-aT} \tag{3.40}$$

where a is the viscosity parameter defined in Section 1.1.4.

The Chebyshev spectral collocation method is applied to the coupled MHD and energy equations (3.39) by discretizing the interval $[-1, 1]$ using the previously
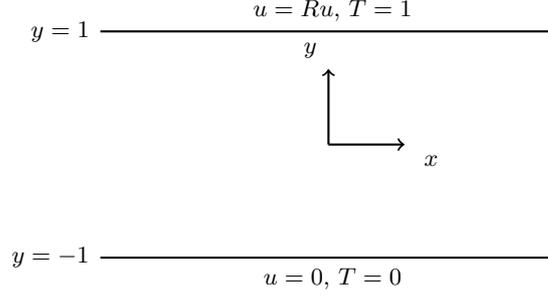
Figure 3.12: Domain and boundary conditions of Problem 3.3.

defined CGL points $x_j = \cos(\dfrac{j\pi}{N})$. The time derivatives of the velocity and temperature are discretized by using the unconditionally stable backward difference scheme

$$\dot{f}_{s+1} = \frac{f_{s+1} - f_s}{\Delta t} \qquad (3.41)$$

with equally spaced time levels Δt. When the CSCM approximations for the velocity u_N and for the temperature T_N are substituted, the discretized system of equations at the m-th time level are obtained as

$$\frac{(u_N)_j^{(m+1)} - (u_N)_j^{(m)}}{\Delta t} + Rv\ d_{ij}^{(1)}(u_N)_j^{(m+1)} = G + d_{ij}^{(1)}\ \mu_j^{(m)} d_{ij}^{(1)}(u_N)_j^{(m+1)}$$

$$+\mu_j^{(m)} d_{ij}^{(2)}(u_N)_j^{(m+1)} - Ha^2(u_N)_j^{(m+1)},$$

$$\frac{(T_N)_j^{(m+1)} - (T_N)_j^{(m)}}{\Delta t} + Rv\ d_{ij}^{(1)}(T_N)_j^{(m+1)} = \frac{1}{Pr} d_{ij}^{(2)}\ (T_N)_j^{(m+1)} \qquad (3.42)$$

$$+Ec\ \mu_j^{(m)}[d_{ij}^{(1)}(u_N)_j^{(m+1)}]^2 + Ec\ Ha^2[(u_N)_j^{(m+1)}]^2,$$

where $i, j = 0, .., N$ and $\mu_j = e^{-aT_j}$. Here, $d_{ij}^{(1)}$ and $d_{ij}^{(2)}$ are the coefficients of the first and the second order Chebyshev collocation differentiation matrices, respectively. These discretized equations are written as a system of matrix-vector equations for the first equation in (3.42)

$$[A]\ \{u_N\}^{(m+1)} = \frac{1}{\Delta t}\ \{u_N\}^{(m)} + G \qquad (3.43)$$

and for the second equation in (3.42)

$$[B]\ \{T_N\}^{(m+1)} = \frac{1}{\Delta t}\ \{T_N\}^{(m)} + \{F_N\}^{(m)} \qquad (3.44)$$

where the $(N+1) \times (N+1)$ matrices $[A]$ and $[B]$, and the $(N+1) \times 1$ vector

83

$\{F_N\}^{(m)}$ are defined as

$$[A] = (\frac{1}{\Delta t} + Ha^2)[I_N] + Rv\ [D_N^{(1)}] - [D_N^{(1)}]\ \{\Gamma_N\}^{(m)}\ [D_N^{(1)}] - \{\Gamma_N\}^{(m)}\ [D_N^{(2)}]$$

$$[B] = \frac{1}{\Delta t}[I_N] + Rv\ [D_N^{(1)}] - \frac{1}{Pr}[D_N^{(2)}]$$

$$\{F_N\}^{(m)} = Ec\ \{\Gamma_N\}^{(m)}\left([D_N^{(1)}]\ \{u_N\}^{(m+1)}\right)^2 + Ec\ Ha^2\ \left(\{u_N\}^{(m+1)}\right)^2 .$$

$[D_N^{(1)}]$ and $[D_N^{(2)}]$ are the first order and second order Chebyshev differentiation matrices, respectively, $[I_N]$ is the $(N+1)\times(N+1)$ identity matrix and $\{\Gamma_N\}$ is the viscosity vector with entries $\Gamma_i = \mu(T_i) = e^{-aT_i}$, where $i = 0,..,N$. The vector-matrix multiplication $\{\Gamma_N\}^{(m)}\ [D_N]^{(2)}$ is achieved by forming a new diagonal matrix with the diagonal entries $\{\Gamma_j\}^{(m)}$. In the source vector $\{F_N\}^{(m)}$ vector products are carried componentwise. The solutions which satisfy both of the conditions

$$\left|(u_N)_k^{(m+1)} - (u_N)_k^{(m)}\right| \le \varepsilon_s, \quad \left|(T_N)_k^{(m+1)} - (T_N)_k^{(m)}\right| \le \varepsilon_s$$

are taken as the steady-state solutions, where ε_s is a preassigned parameter, the superscript m is the time level and k denotes the k-th node, $k = 1,...,(N+1)^2$.

3.3.1 Numerical results

Numerical results are visualized in terms of velocity and temperature of the fluid for several values of viscosity parameter a, Hartmann number Ha, and for fixed plates $(Ru = 0)$ or moving upper plate $(Ru = 1)$ for depicting the influences on the flow and temperature. Also, inflow/outflow through plates is controlled with the parameter $(Rv = 0)$ or $(Rv \ne 0)$ which implies the absence or presence of convection. In numerical simulations, Prandtl number $Pr = 1$ and Eckert number $Ec = 0.2$ are taken as in [3, 4, 45]. The fluid is driven by a negative pressure gradient $G = 5$ when the walls are fixed $(Ru = 0)$. When the upper plate moves horizontally $(Ru \ne 0)$, the flow starts with both the movement of the upper wall and the pressure gradient. In the computations for all values of parameters such as Ha and a, $N = 12$ is set, and since implicit finite difference has been used for time derivatives, $\Delta t = 0.01$ is taken which does not have to be too small. The steady-state solutions are obtained with the convergence parameter as $\varepsilon_s = 10^{-6}$. Figure 3.13 shows the effect of variable viscosity $(\mu(T) = e^{-aT})$ parameter a on the velocity and temperature of the fluid for fixed Hartmann numbers, $Ha = 1$, 5 and 30. As a increases, both the velocity and the temperature, at the center line, increase, and also the time elapsed for reaching steady-state is increasing. The same figure also depicts the Ha effect on the centerline velocity and temperature when Ha is increased to 1, 5 and 30. As it is observed, increasing Hartmann number causes a decrease on the flow for all values of a, since the electromagnetic force opposite to fluid movement is augmented. On the other
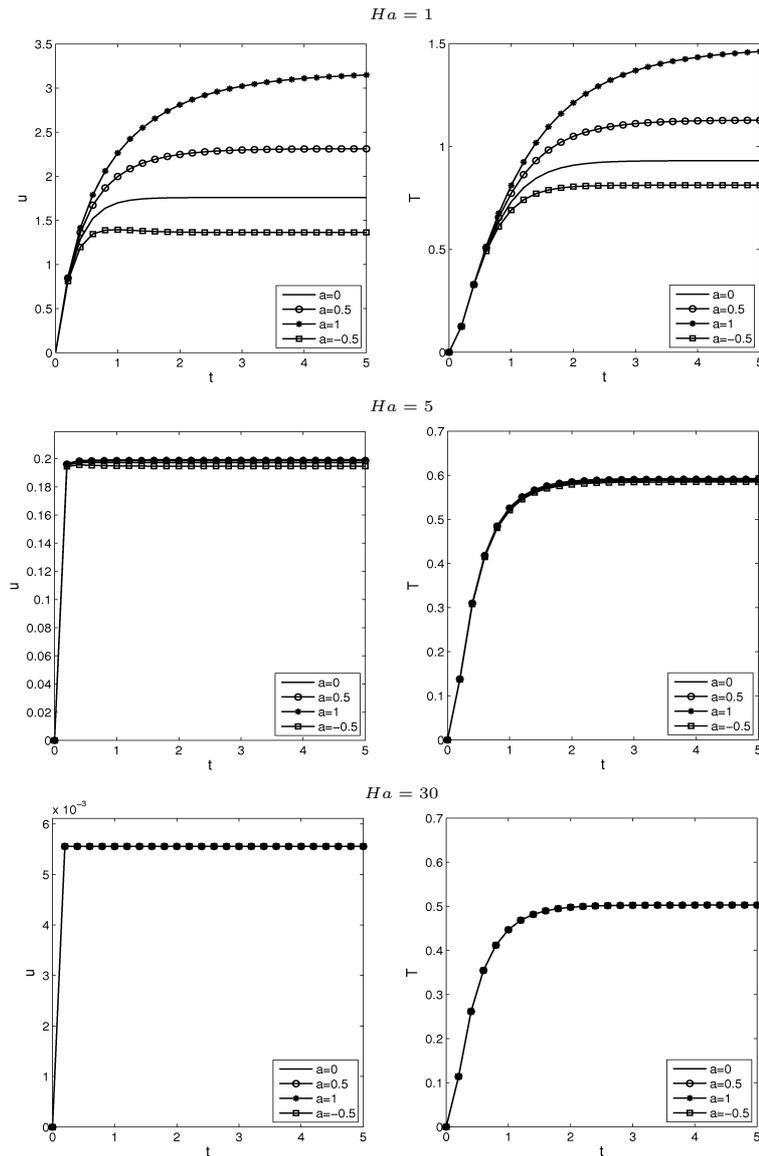
Figure 3.13: Problem 3.3: Centerline values of u (L) and T (R) for $Ru = 0$, $Ha = 1$, $Ha = 5$ and $Ha = 30$.

hand, the temperature field is less sensitive to an increase in Ha. The drop in the temperature magnitude is not as sharp as in the velocity and it almost settles down for a certain Ha (e.g. $Ha = 5$). For larger Ha values ($Ha \geq 5$) the effect of viscosity parameter disappears and both centerline velocity and temperature show the same behavior for all values of a, since the magnetic force dominates and controls the fluid flow.

In Figure 3.14, the influence of the viscosity parameter a on the velocity and temperature profiles at steady-state are illustrated for Ha values 1, 5 and 10. An increment of a increases both the velocity and temperature magnitudes. Also, velocity (flow) tries to pile up towards the upper plate especially for increasing values of Ha, and for large values of a. This is due to the contribution of the vari-
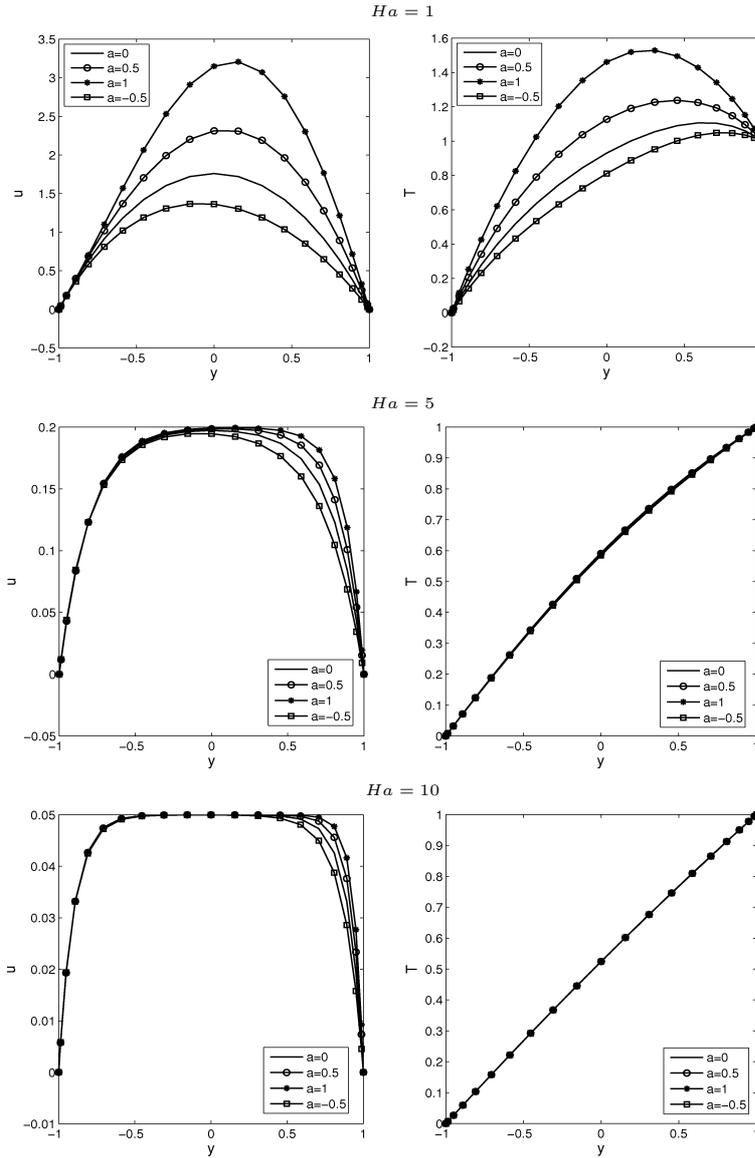
Figure 3.14: Problem 3.3: Steady state values of u (L) and T (R) for $Ru = 0$, $Ha = 1$, $Ha = 5$ and $Ha = 10$.

ation of viscosity with the temperature. Temperature shows an increasing profile from 0 value at lower plate to the value 1 at the upper plate. Again, for $Ha \geq 5$ electromagnetic effect overwrites the effect of variable viscosity. The steady-state velocity and temperature profiles are given in Figure 3.15, for increasing Ha for a fixed viscosity parameter $a = -0.5$. The drop in the velocity and temperature magnitudes is observed when Ha gets larger, and this decrease   is strong in the velocity.

Figure 3.16 shows the velocity contours for increasing time levels between $y = -1$ and $y = 1$, for a fixed a, and for increasing Ha values $0, 1, 2, 5, 10$, respectively. As Ha increases, boundary layer formation starts to develop near the plates at $y = \mp 1$. This is the well-known characteristic of MHD flow.
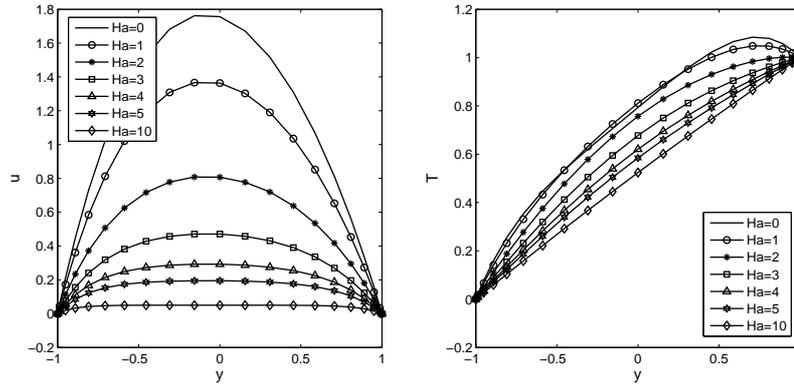
Figure 3.15: Problem 3.3: Steady state values of u and T for $a = -0.5$ and $Ru = 0$, $Rv = 0$.
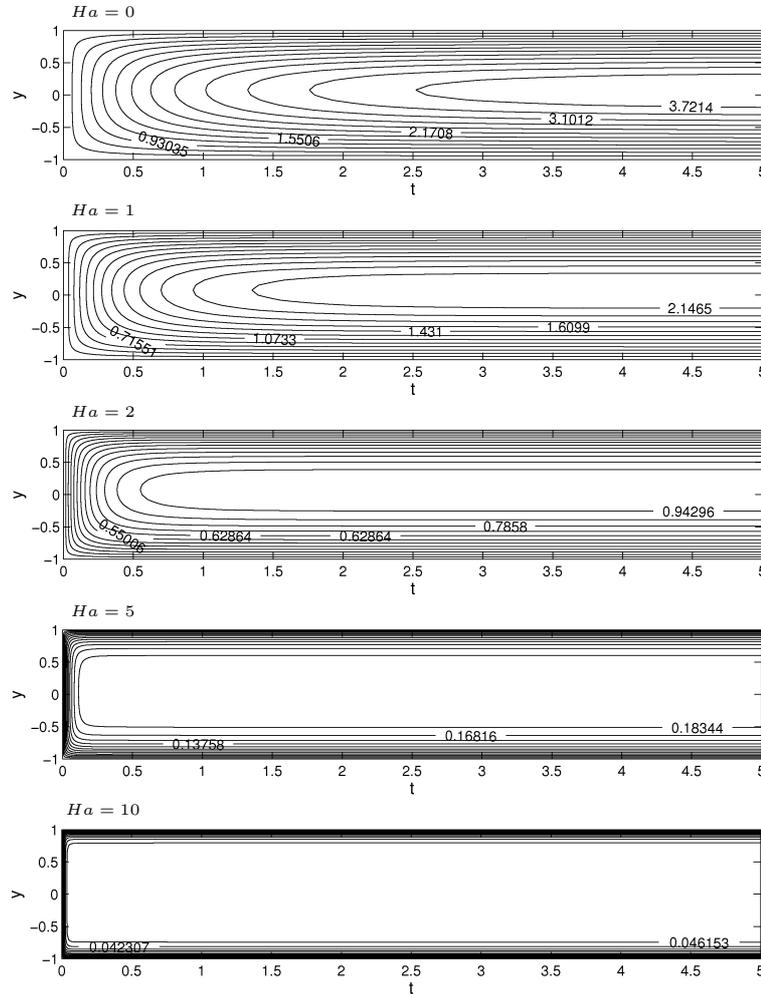
Figure 3.16: Problem 3.3: Contours of u for $a = 0.5$ and $Ru = 0$, $Rv = 0$.

Figure 3.17 depicts the mesh plot and level curves for the velocity and temperature with respect to $-1 \leq y \leq 1$ and $0 \leq t \leq 5$, for a fixed viscosity parameter $a = 0.5$, and for $Ha = 0$ and $Ha = 2$. Symmetrical behavior of velocity is seen with a

87

parabolic profile in the y-variation, reaching zero end conditions at $y = \mp 1$. The temperature level curves start from the cold plate at $y = -1$ and reach to the value 1 on the plate at $y = 1$. The decrease in both the velocity and the temperature as Ha increases is also well observed. The presence of the convection terms in the equations $(Rv \neq 0)$ indicate that the action of an inflow and outflow through the plates is permitted.
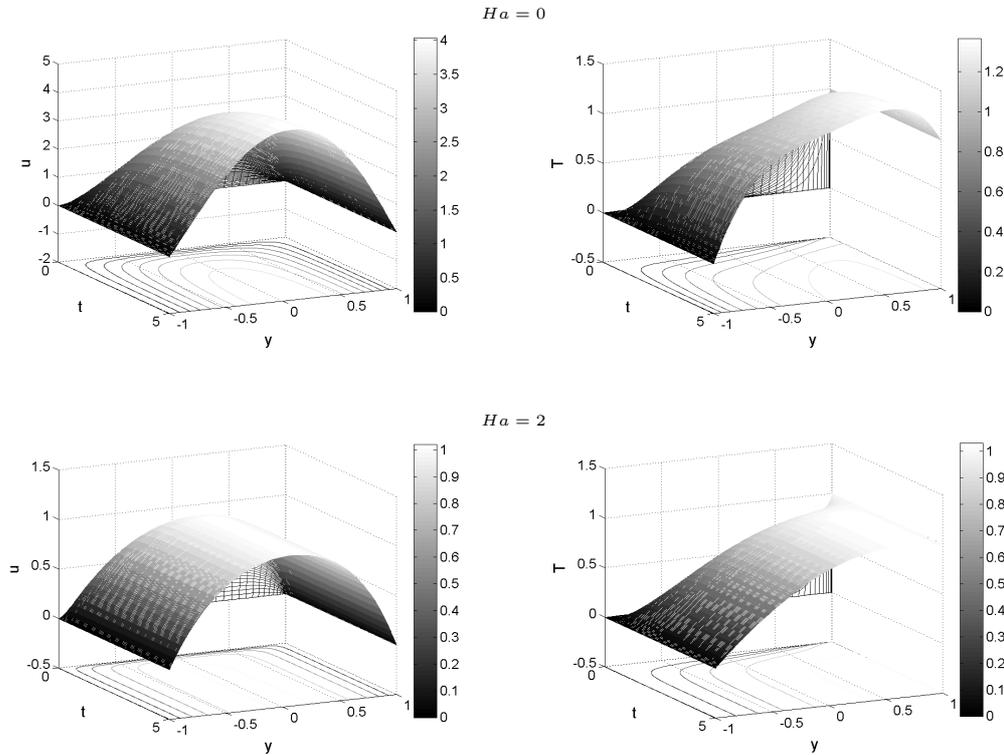
Figure 3.17: Problem 3.3: Mesh plot of u and T for $Ha = 0$ and $Ha = 2$, $a = 0.5$ and $Ru = 0$, $Rv = 0$.

Figure 3.18 shows the influence of this parameter Rv on the steady-state velocity and temperature profiles, for several viscosity parameters when $Ha = 2$. The distortion of flow through (close to) upper plate is more pronounced now due to the effect of convection. Figure 3.19 shows the steady velocity and temperature behaviors between the plates at $y = \mp 1$ for increasing inflow/outflow parameter Rv. Not only the drop in the magnitude but also the boundary layer formation is noticed when Rv increases, for the velocity and the temperature. This is due to the convection dominance of the governing fluid flow and temperature equations.

In Figures 3.20 and 3.21 the steady-state velocity and temperature profiles are presented when the upper plate is moving with a constant velocity $u = Ru = 1$ to the right. The convection parameter Rv is kept zero for observing the effect of movement of the upper wall only. $Ha = 1$ is taken in Figure 3.20 and the variation with respect to viscosity parameter is studied. When compared with Figure 3.14 ($Ha = 1$) which is the case $Ru = 0$, similar behavior is seen, however,
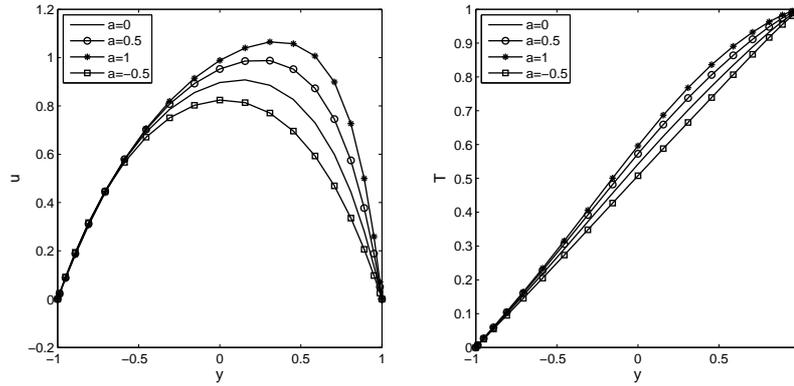
Figure 3.18: Problem 3.3: Steady-state values of u and T for $Ha = 2$ and $Ru = 0$, $Rv = 1$.

the velocity reaches the value 1 when $y = 1$ in this case. Temperature is not affected with the movement of the upper plate.
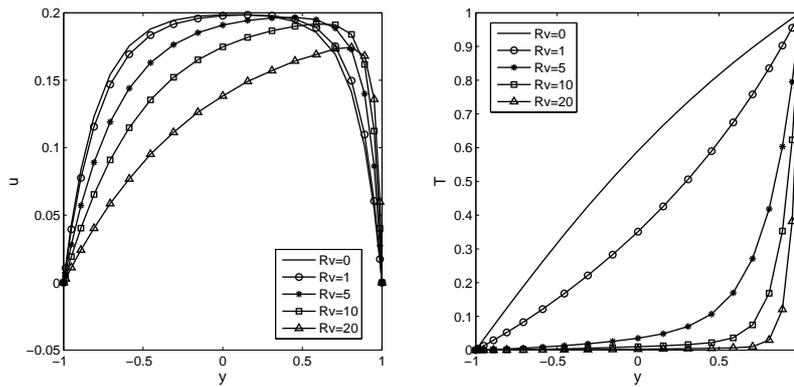
Figure 3.19: Problem 3.3: Steady-state values of u and T for $Ha = 5$ and $a = 0.5$ $Ru = 0$.
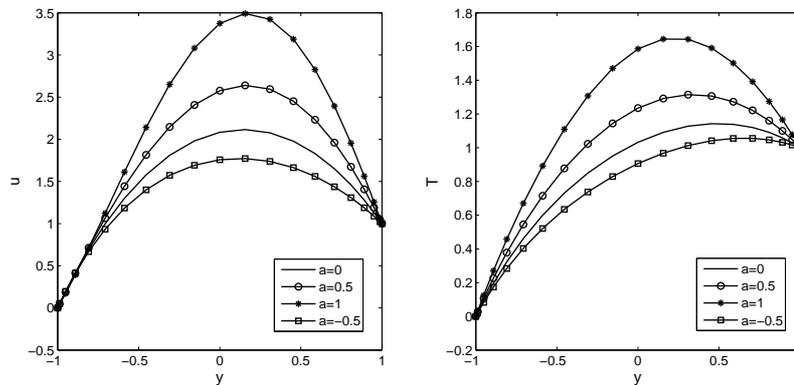
Figure 3.20: Problem 3.3: Steady-state values of u and T for $Ru = 1$ and $Ha = 1$, $Rv = 0$.

Figure 3.21 shows the variations of velocity and temperature with respect to Ha in the presence of movement of the upper plate. As Ha increases, there is a
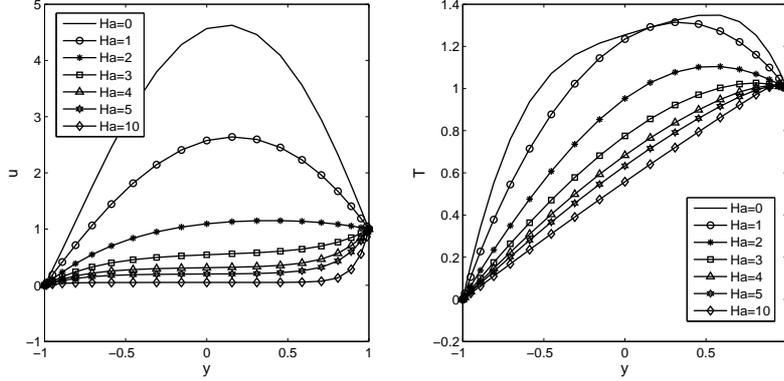
Figure 3.21: Problem 3.3: Steady-state values of u and T for $Ru = 1$ and $a = 0.5$, $Rv = 0$.

flattening tendency through the value zero, but close to the wall at $y = 1$, they all take the value 1. Again the temperature profile is not effected. The results are in good agreement with the results presented in [3].

3.4 Application of CSCM to MHD flow and heat transfer of a dusty fluid between two parallel plates

In this section, the CSCM application to MHD flow with heat transfer presented in the previous section, is extended to that the fluid contains solid particles. The unsteady MHD flow and heat transfer of a dusty fluid is considered where the electrically conducting fluid has temperature dependent viscosity. Both the fluid and dust particles are governed by the coupled set of momentum and energy equations. The governing equations in non-dimensional form are given as in Section 1.1.5

$$Re\frac{\partial u}{\partial t} = Re\ G + \frac{\partial}{\partial y}\left[\mu(T)\frac{\partial u}{\partial y}\right] - Ha^2 u - R(u - u_p),$$

$$\frac{\partial u_p}{\partial t} = \frac{1}{Re\ g}(u - u_p),$$

$$Re\frac{\partial T}{\partial t} = \frac{1}{Pr}\frac{\partial}{\partial y}\left(\kappa(T)\frac{\partial T}{\partial y}\right) + Ec\ \mu(T)\left(\frac{\partial u}{\partial y}\right)^2 + Ec\ Ha^2\ u^2 + \frac{2R}{3Pr}(T_p - T),$$

$$\frac{\partial T_p}{\partial t} = -L_T(T_p - T),$$

(3.45)

where $0 \leq y \leq 1$, $t > 0$. In the equations, u denotes the velocity of the fluid which is fully developed in x-direction and varies parabolically with respect to y. u_p is the velocity of the particles, T is the temperature of the fluid and T_p is the temperature of the particles.

90

$$\beta\frac{\partial u}{\partial y} = -u, \ \beta\frac{\partial u_p}{\partial y} = -u_p, \ T = T_p = 1$$

$y = 1$

y

$y = 0$

$$\beta\frac{\partial u}{\partial y} = u, \ \beta\frac{\partial u_p}{\partial y} = u_p, \ T = T_p = 0$$

x
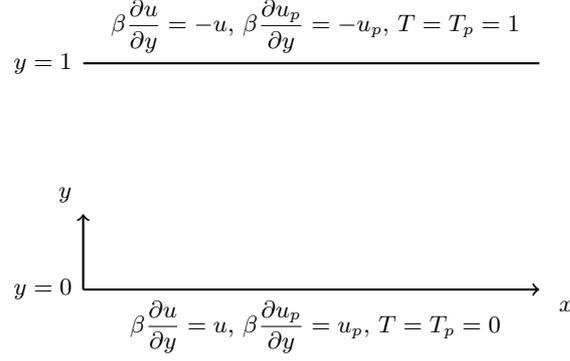
Figure 3.22: Domain and boundary conditions for Problem 3.4.

The initial and boundary conditions are,

$$u(y,0) = u_p(y,0) = 0, \ T(y,0) = T_p(y,0) = 0 \ \text{ on } \quad 0 \le y \le 1,$$

$$\beta\frac{\partial u}{\partial n} + \gamma u = 0 \ \text{ for } \ y = 0,1,$$

$$\beta\frac{\partial u_p}{\partial n} + \gamma u_p = 0 \ \text{ for } \ y = 0,1, \tag{3.46}$$

$$T(0,t) = T_p(0,t) = 0 \ \text{ and }$$

$$T(1,t) = T_p(1,t) = 1$$

where the Navier-slip parameters β and γ take several values resulting with Dirichlet, Neumann or mixed boundary conditions. The same collision effect near the boundaries as the fluid velocity is assumed in this study, as discussed in Section 1.1.5. Thus, the Navier-slip boundary conditions are imposed on both the fluid velocity u and the particles velocity u_p, consequently, $\gamma = \mp 1$ is taken and the fluid and particle velocity boundary conditions are employed as

$$\beta\frac{\partial u}{\partial y} = +u \ \text{ at } \ y = 0, \qquad \beta\frac{\partial u_p}{\partial y} = +u_p \ \text{ at } \ y = 0,$$

$$\beta\frac{\partial u}{\partial y} = -u \ \text{ at } \ y = 1, \qquad \beta\frac{\partial u_p}{\partial y} = -u_p \ \text{ at } \ y = 1,$$

for various constant values of Navier-slip parameter β. The sketch the problem configuration and the boundary conditions are shown in Figure 3.22.

The Chebyshev spectral collocation method is applied to the coupled MHD and energy equations (3.45). As the problem is defined on $[0,1]$, the CGL points $x_j = \frac{1}{2}\cos(\frac{j\pi}{N}) + \frac{1}{2}$ are used in the construction of the Chebyshev differentiation matrices, where $j = 0, ..., N$. For the time derivatives of the velocity and temperature, the unconditionally stable backward difference scheme (3.41) is used. The approximations u_N, u_{pN}, T_N and T_{pN} for u, u_p, T and T_p, respectively, are

substituted into (3.45) and the discretized system of equations in space and time are obtained

$$Re\ \frac{(u_N)_j^{(m+1)} - (u_N)_j^{(m)}}{\Delta t} = Re\ G + d_{ij}^{(1)}\ \mu_j^{(m)} d_{ij}^{(1)} (u_N)_j^{(m+1)} + \mu_j^{(m)} d_{ij}^{(2)} (u_N)_j^{(m+1)}$$

$$-(Ha^2 + R)(u_N)_j^{(m+1)} + R\ (u_{pN})_j^{(m)}\ ,$$

(3.47)

$$Re\ g\ \frac{(u_{pN})_j^{(m+1)} - (u_{pN})_j^{(m)}}{\Delta t} = (u_N)_j^{(m+1)} - (u_{pN})_j^{(m+1)}\ , \qquad (3.48)$$

$$Re\ \frac{(T_N)_j^{(m+1)} - (T_N)_j^{(m)}}{\Delta t} = \frac{1}{Pr} d_{ij}^{(1)} \kappa_j^{(m)} d_{ij}^{(1)} (T_N)_j^{(m+1)} + \frac{1}{Pr} \kappa_j^{(m)} d_{ij}^{(2)}\ (T_N)_j^{(m+1)}$$

$$+Ec\ \mu_j^{(m+1)} \left(d_{ij}^{(1)} (u_N)_j^{(m+1)}\right)^2 + Ec\ Ha^2 \left((u_N)_j^{(m+1)}\right)^2$$

$$+\frac{2R}{3Pr} \left((T_{pN})_j^{(m)} - (T_N)_j^{(m+1)}\right)\ ,$$

(3.49)

$$\frac{(T_{pN})_j^{(m+1)} - (T_{pN})_j^{(m)}}{\Delta t} = L_T\ \left((T_N)_j^{(m+1)} - (T_{pN})_j^{(m+1)}\right) \qquad (3.50)$$

where $i = j = 0, ..., N$. Here, $d_{ij}^{(1)}$ and $d_{ij}^{(2)}$ are the coefficients of the first order and the second order Chebyshev collocation differentiation matrices, respectively. The superscript m indicates the m-th time level.

These discretized equations result in the system of matrix-vector equations

$$[\bar{A}]\ \{u_N\}^{(m+1)} = \Delta t\ Re\ G + \Delta t\ R\ \{u_{pN}\}^{(m)} + Re\ \{u_N\}^{(m)} \qquad (3.51)$$

$$(Re\ g + \Delta t)\{u_{pN}\}^{(m+1)} = Re\ g\ \{u_{pN}\}^{(m)} + \Delta t\{u_N\}^{(m+1)} \qquad (3.52)$$

$$[\bar{B}]\ \{T_N\}^{(m+1)} = \Delta t\ Ec\ Pr\ \{\bar{F}_N\}^{(m)} + Re\ Pr\ \{T_N\}^{(m)} + (2\Delta t R/3)\{T_{pN}\}^{(m)}$$
(3.53)

$$(1 - \Delta t\ L_T)\{T_{pN}\}^{(m+1)} = \{T_{pN}\}^{(m)} + \Delta t\ L_T\ \{T_N\}^{(m+1)} \qquad (3.54)$$

where the $(N+1) \times (N+1)$ matrices $[\bar{A}]$ and $[\bar{B}]$ are defined as

$$[\bar{A}] = \left(Re + \Delta t(Ha^2 + R)\right) [I_N] - \Delta t\ \left([D_N^{(1)}]\ \{Z_N\}^{(m)}\ [D_N^{(1)}] + \{Z_N\}^{(m)}\ [D_N^{(2)}]\right)$$

$$[\bar{B}] = (Re\ Pr + 2\Delta t R/3) [I_N] - \Delta t\ \left([D_N^{(1)}]\ \{W_N\}^{(m)}\ [D_N^{(1)}] + \{W_N\}^{(m)}\ [D_N^{(2)}]\right)$$

and the $(N+1) \times 1$ vector $\{\bar{F}_N\}$ is given as

$$\{\bar{F}_N\}^{(m)} = \{Z_N\}^{(m)} \left[[D_N^{(1)}]\ \{u_N\}^{(m+1)}\right]^2 + Ha^2\ \left[\{u_N\}^{(m+1)}\right]^2\ .$$

92

As before, $[D_N^{(1)}]$ and $[D_N^{(2)}]$ are the first order and second order Chebyshev differentiation matrices, respectively, and $[I_N]$ is the $(N+1) \times (N+1)$ identity matrix. $\{Z_N\}$ is the viscosity vector $Z_i = \mu(T_i) = e^{-aT_i}$ and $\{W_N\}$ is the thermal conductivity vector $W_i = \kappa(T_i) = e^{bT_i}$ $i = 0, ..., N$. For the vector-matrix multiplication $\{Z_N\}^{(m)}$ $[D_N^{(2)}]$ a new diagonal matrix with the diagonal entries $Z_{N_j}^{(m)}$ is arranged. In the source vector $\{\bar{F}_N\}$, vector products are carried componentwise. The steady-state solutions are obtained when the differences between two successive time levels of all unknowns u_N, u_{pN}, T_N and T_{pN} on the whole problem domain are less then a preassigned parameter ε_s.

3.4.1 Numerical results

The velocity and the temperature behaviors for both the fluid and the particles are investigated for several values of viscosity parameter a, thermal conductivity parameter b, Navier-slip parameter β and Hartmann number Ha. In the computations, Prandtl number $Pr = 7.1$, Eckert number $Ec = 0.2$, Reynolds number $Re = 1$, particle concentration parameter $R = 0.5$, temperature relaxation parameter $L_T = 0.7$, and particle mass parameter $g_p = 0.8$ are taken as in [50]. The fluid is driven by a negative pressure gradient $G = 1$. The discretized systems of equations (3.51)-(3.54) are solved with $N = 12$, and the time step is taken as $\Delta t = 0.01$. The steady-state parameter is taken as $\varepsilon_s = 10^{-6}$. The velocity of the fluid u, particles velocity u_p, temperature of the fluid T and particles temperature T_p are shown in Figure 3.23 at steady-state for different viscosity parameter values $a = 0, 0.5, 1, 2$ when $Ha = 1$, $\beta = 1$ and $b = 0.01$. It is observed from the figure that as a increases, the velocities of both the fluid and particles increase, especially near the upper heated plate. The increase in velocities is relatively small near the lower cold plate compared to the upper plate. The temperature of the fluid and the particles have linear behavior from cold plate to heated plate, and for different a values this profile is not much affected.

Figure 3.24 shows the effect of the thermal conductivity parameter b on the steady-state values of u, u_p, T and T_p where $Ha = 1$, $a = 1$ and $\beta = 1$. It can be seen from the figure that the linear profile of the temperatures of both the fluid and the particles is diminishing when b is increased. The increase in the temperature leads to lower viscosities and therefore both the velocities of fluid and particles increase for higher values of b. The effect of the thermal conductivity on the velocities of the fluid and particles is not much pronounced as b varies. Both of them have parabolic profiles reaching smoothly from the cold lower plate to the hot upper plate.

In Figure 3.25, u, u_p, T and T_p profiles are depicted when the Navier-slip condition is imposed for both u and u_p on the plates. The $\beta = 0$ case which implies no-slip condition is obviously a parabolic profile taking zero values on the plates for u and u_p. For increasing values of Navier-slip parameter β, magnitudes of the fluid and particle velocities increase and the symmetry of the parabolas is slightly destroyed due to the slip on the upper plate. For larger values of β, the velocity

Figure 3.23: Problem 3.4: Steady-state solutions when $Ha = 1$, $b = 0.01$ and $\beta = 1$ for different viscosity parameter a: (a) u, (b) u_p, (c) T, (d) T_p.

profiles are almost linear. The temperature profiles, however, are not that much affected.

The variation of Hartmann number is also studied on the velocity and temperature behaviors, and the results are shown in Figure 3.26. It is observed that the Hartmann number does not have a significant effect on the temperature profiles. The velocity of both fluid and particles decrease as Hartmann number increases which amounts an increase in the intensity of the applied magnetic field. This is due to the Lorentz force rises when magnetic field is applied to an electrically conducting dusty fluid. This force slows down the motion of both fluid and dust particles.

Figure 3.27 illustrates the transient behaviors of u, u_p, T and T_p. The time dependent solutions show that both velocity and temperature fields increase progressively till the steady-state is reached before $t = 8$. The temperature increases due to the applied boundary condition and this increase in temperature causes the velocity to increase. When the temperature is reached to steady-state in the channel, the velocity profiles converge to steady-state as can be depicted from this figure.

In conclusion, in this chapter, numerical solutions to MHD and natural convection
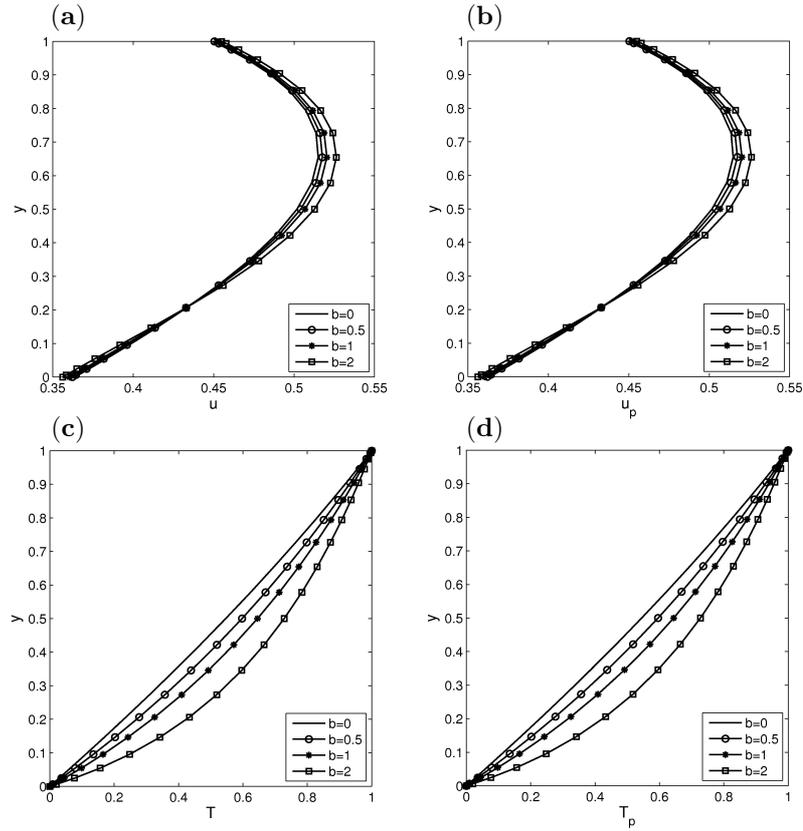
Figure 3.24: Problem 3.4: Steady-state solutions when $Ha = 1$, $a = 1$ and $\beta = 1$ for different thermal conductivity parameter b: (**a**) u, (**b**) u_p, (**c**) T, (**d**) T_p.

flow problems are obtained by using Chebyshev spectral collocation method. The Navier-Stokes and natural convection flow under magnetic field equations are solved, and both quantitative and qualitative comparison with the FEM results of Chapter 2 are provided. The lid-driven cavity flow problem is reconsidered for Re values up to 1000 and the outcomes are also compared with the previously obtained FEM results in terms of streamlines and vorticity contours. The given procedure failed to converge for higher values of Reynolds number within the maximum number of collocation points tested ($N = 50$) in this study. The discontinuity of the velocity boundary conditions is seem to be responsible for the divergence of the procedure. Furthermore, it is found that the dense structure of the collocation matrices especially for large number of nodes which is needed for high Re may also be the reason for this. The natural convection flow problem under the effect of an external magnetic field, however, is solved successively by using CSCM. The method is observed to capture the thin boundary layers especially in vorticity contours for high problem parameters (Ra and Ha). The flow behavior and temperature distribution in the cavity as well as the magnitudes of the contours of all of the unknowns are shown to be in excellent agreement with the FEM results.
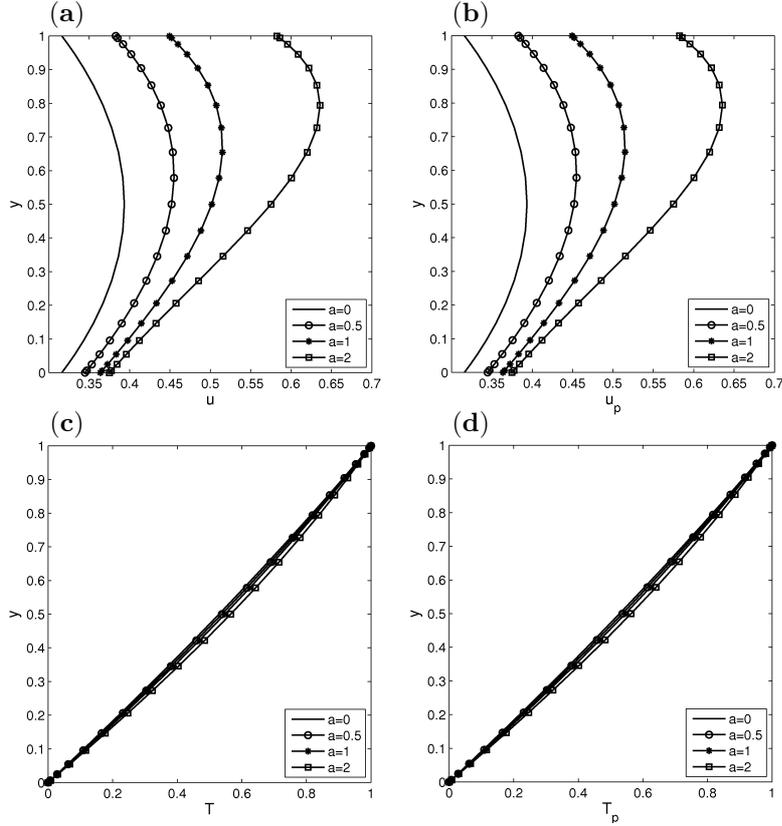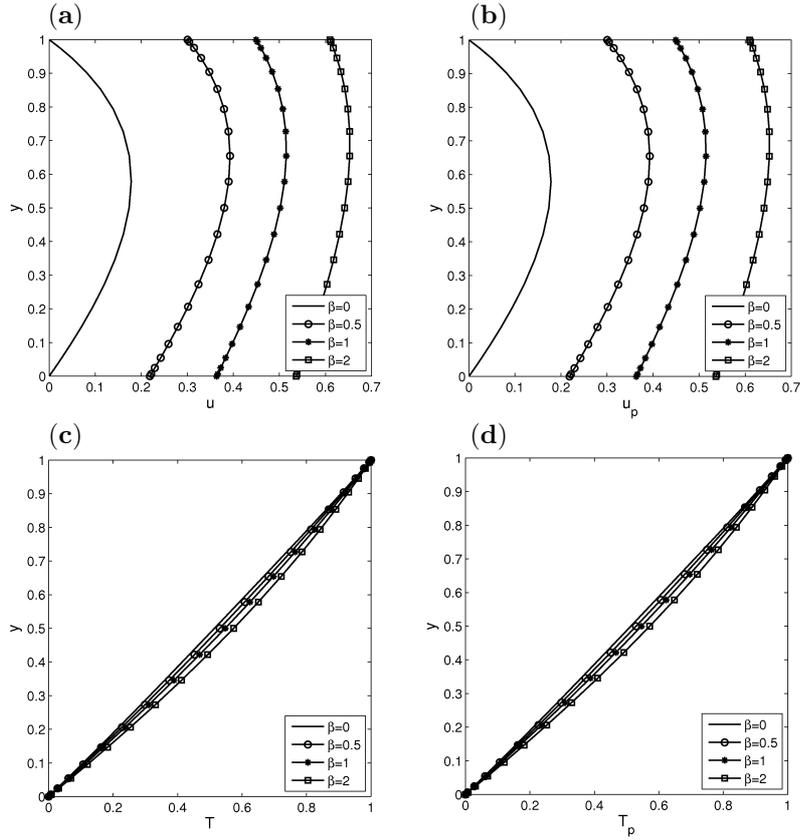
Figure 3.25: Problem 3.4: Steady-state solutions when $Ha = 1$, $a = 1$ and $b = 0.01$ for different Navier-slip parameter β: (a) u, (b) u_p, (c) T, (d) T_p.

The MHD flow with heat transfer of an electrically conducting incompressible fluid with temperature dependent viscosity is solved between two parallel insulating plates. The MHD flow of a dusty fluid is also considered between parallel plates imposing the Navier-slip conditions on velocities of both the fluid and particles. The effects of the viscosity parameter, Hartmann number, Navier-slip parameter and thermal conductivity parameter on the flow and heat transfer are investigated. The use of CSCM when it is combined with the unconditionally stable backward difference time integration scheme gives very good accuracy with considerably small number of collocation points, and quite large time steps. The ease of implementation and the convenience of CSCM with high order accuracy to especially one-dimensional problems are pronounced. This puts forth the essential aim of this chapter.
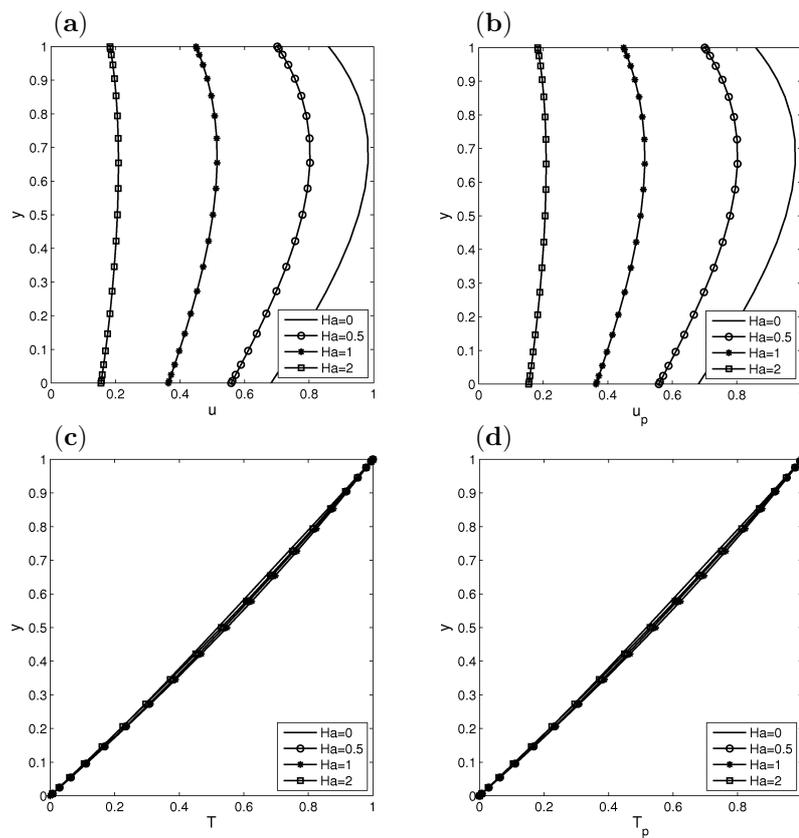
Figure 3.26: Problem 3.4: Steady-state solutions when $a = 1$, $b = 0.01$ and $\beta = 1$ for different Hartmann numbers: (**a**) u, (**b**) u_p, (**c**) T, (**d**) T_p.
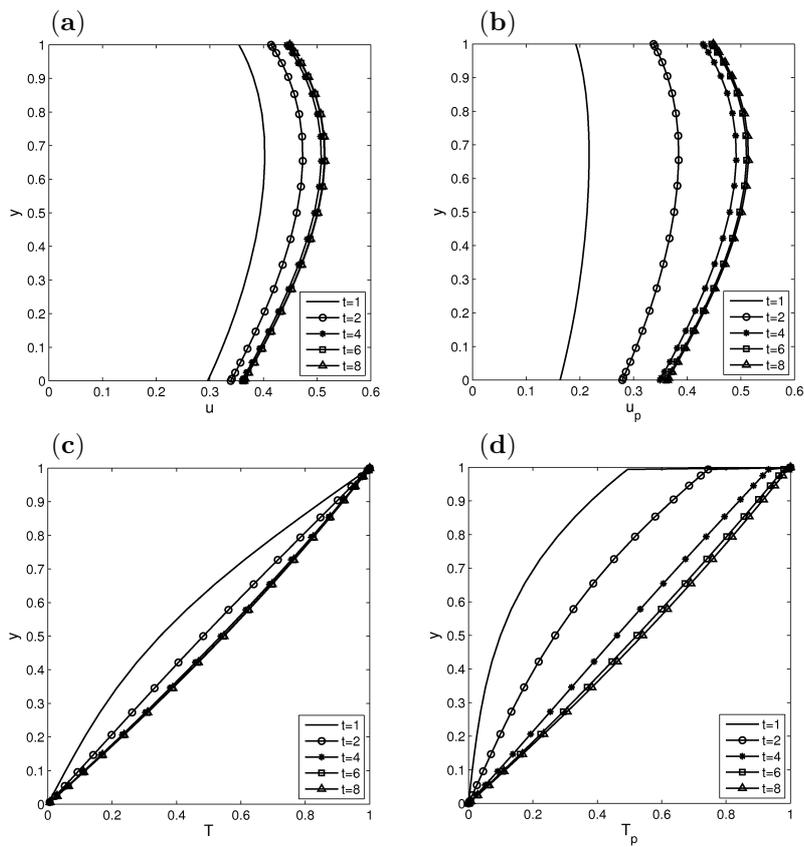
Figure 3.27: Problem 3.4: Transient solutions for $a = 1$, $Ha = 1$, $\beta = 1$, $b = 0.01$: (**a**) u, (**b**) u_p, (**c**) T, (**d**) T_p.

CHAPTER 4

FEM and BEM Solutions of Biomagnetic Flow Problems

In this chapter, numerical solutions to biomagnetic fluid flow and heat trans-
fer problems are presented. Biomagnetic fluids are introduced in Section 1.2 as
circulating fluids in living creatures which are influenced by the presence of the
magnetic fields. The flow field and heat transfer of biomagnetic fluids are in ac-
cordance with the fundamental principles of biomagnetic fluid dynamics (BFD)
which investigates the dynamics of biological fluids affected by magnetic fields. In
particular, the flow regimes covered in this chapter are two-dimensional and lam-
inar, and the fluid is taken as viscous, homogenous, incompressible and assumed
to be Newtonian. The flow is subjected to an external magnetic field which is
generated by a nodal source placed at a point closely below the lower plate. Blood
is considered to be a typical biomagnetic fluid due to the interaction of intercellu-
lar protein, cell membrane and hemoglobin, and hence, the physical properties of
blood are adopted in BFD models considered in the present study. Both steady
and unsteady flows are considered which take place between two impermeable
and electrically non-conducting plates (channels) in the cases of with/without a
constriction (stenosis). The equations governing the biomagnetic fluid flow are
derived from the continuity, momentum and energy equations which involve the
magnetization force terms due to the application of an external magnetic field.
The non-dimensional equations in terms of stream function ψ, vorticity w and
temperature T are introduced in Section 1.2 as

$$\nabla^2 \psi = -w$$

$$\frac{\partial w}{\partial t} = \nabla^2 w - Re \left\{ \frac{\partial w}{\partial x}\frac{\partial \psi}{\partial y} - \frac{\partial w}{\partial y}\frac{\partial \psi}{\partial x} \right\}$$

$$+ Mn_F ReH \left\{ \frac{\partial H}{\partial x}\frac{\partial T}{\partial y} - \frac{\partial H}{\partial y}\frac{\partial T}{\partial x} \right\} + Mn_M \frac{\partial}{\partial y}\left(H^2 \frac{\partial \psi}{\partial y} \right) \qquad (4.1)$$

$$\frac{\partial T}{\partial t} = \frac{1}{Pr}\nabla^2 T - Re\left\{\frac{\partial T}{\partial x}\frac{\partial \psi}{\partial y} - \frac{\partial T}{\partial y}\frac{\partial \psi}{\partial x}\right\}$$

$$+ Mn_F ReEcH(\varepsilon + T)\left\{\frac{\partial H}{\partial x}\frac{\partial \psi}{\partial y} - \frac{\partial H}{\partial y}\frac{\partial \psi}{\partial x}\right\}$$

$$+ Mn_M EcH^2\left(\frac{\partial \psi}{\partial y}\right)^2 + Ec\left\{\left(\frac{\partial^2 \psi}{\partial y^2} - \frac{\partial^2 \psi}{\partial x^2}\right)^2 + 4\left(\frac{\partial^2 \psi}{\partial x \partial y}\right)^2\right\}.$$

The non-dimensional parameters, Reynolds number Re, Prandtl number Pr, Eckert number Ec and the temperature number ε are defined in Section 1.2. The magnetic numbers arising from ferrohydrodynamics, Mn_F, and magnetohydrodynamics, Mn_M, are also given in the same section. The flow problems considered in this chapter, take place both in straight channels and in constricted channels. In the definitions of the problem domains containing constriction, the profiles of the lower and upper plates of the channels are defined as functions of x, where $y = F(x)$ defines the lower plate, and $y = G(x)$ is the function for the upper plate. The nodal magnetic source is placed at a point (a, b) outside of the channel close to the lower plate and the magnetic field intensity H is given by the relation

$$H(x, y) = \frac{|b|}{\sqrt{(x-a)^2 + (y-b)^2}} \ . \tag{4.2}$$

The flow at the entrance of the channel is assumed to be fully developed, and the velocity and the temperature have parabolic profiles, whereas the vorticity has a linear profile. On the lower and upper plates, no-slip boundary condition is imposed for the velocities in both directions $u = v = 0$, and Dirichlet type boundary conditions are imposed for the temperature where they are kept at constant temperatures. At the exit of the channel, the homogenous Neumann boundary conditions are assigned as $\partial R/\partial x = 0$ to indicate the continuity of behaviors of the flow and the temperature, where $R = \psi, w, T$. The problem configuration, magnetic field contours resulting from the nodal magnetic source and the boundary conditions are displayed in Figure 4.1.
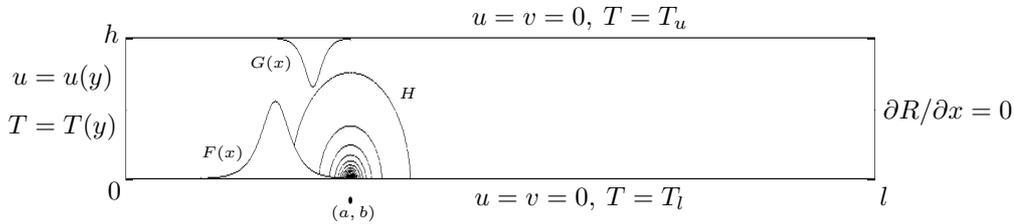
Figure 4.1: Problem configuration and boundary conditions for biomagnetic fluid flow.

In BFD models where the biomagnetic fluid is taken as poor conductor, the effect of the Lorentz force arising in MHD is small in comparison to the magnetization

100

force (see Section 1.2). Thus, in Equations (4.1), the MHD magnetic number Mn_M is taken as zero, the corresponding terms are dropped, and the nonzero magnetic number Mn_F is referred as Mn, and the resulting governing equations are given as

$$\nabla^2 \psi = -w$$

$$\frac{\partial w}{\partial t} = \nabla^2 w - Re\left\{\frac{\partial w}{\partial x}\frac{\partial \psi}{\partial y} - \frac{\partial w}{\partial y}\frac{\partial \psi}{\partial x}\right\} + MnReH\left\{\frac{\partial H}{\partial x}\frac{\partial T}{\partial y} - \frac{\partial H}{\partial y}\frac{\partial T}{\partial x}\right\}$$

$$\frac{\partial T}{\partial t} = \frac{1}{Pr}\nabla^2 T - Re\left\{\frac{\partial T}{\partial x}\frac{\partial \psi}{\partial y} - \frac{\partial T}{\partial y}\frac{\partial \psi}{\partial x}\right\}$$

$$+MnReEcH(\varepsilon + T)\left\{\frac{\partial H}{\partial x}\frac{\partial \psi}{\partial y} - \frac{\partial H}{\partial y}\frac{\partial \psi}{\partial x}\right\}$$

$$+Ec\left\{\left(\frac{\partial^2 \psi}{\partial y^2} - \frac{\partial^2 \psi}{\partial x^2}\right)^2 + 4\left(\frac{\partial^2 \psi}{\partial x\partial y}\right)^2\right\}.$$

(4.3)

In addition, if the flow is time independent and the nondimensionalization given in Section 1.2 is applied where the plates are kept at different temperatures, equations governing the nonconducting biomagnetic fluid flow and heat transfer, take the steady form

$$\nabla^2 \psi = -w$$

$$\nabla^2 w = Re\left\{\frac{\partial w}{\partial x}\frac{\partial \psi}{\partial y} - \frac{\partial w}{\partial y}\frac{\partial \psi}{\partial x}\right\} + MnReH\left\{\frac{\partial H}{\partial x}\frac{\partial T}{\partial y} - \frac{\partial H}{\partial y}\frac{\partial T}{\partial x}\right\}$$

$$\nabla^2 T = PrRe\left\{\frac{\partial T}{\partial x}\frac{\partial \psi}{\partial y} - \frac{\partial T}{\partial y}\frac{\partial \psi}{\partial x}\right\}$$

$$+MnPrReEcH(\varepsilon - T)\left\{\frac{\partial H}{\partial x}\frac{\partial \psi}{\partial y} - \frac{\partial H}{\partial y}\frac{\partial \psi}{\partial x}\right\}$$

$$+PrEc\left\{\left(\frac{\partial^2 \psi}{\partial y^2} - \frac{\partial^2 \psi}{\partial x^2}\right)^2 + 4\left(\frac{\partial^2 \psi}{\partial x\partial y}\right)^2\right\}.$$

(4.4)

In this study, the solution methodologies are firstly tested without the magnetization effect. In the absence of an external magnetic field, the magnetic number Mn in System (4.3) is taken as zero, hence the corresponding FHD terms drop.

Thus, Equations (4.3) are simplified further as

$$\nabla^2 \psi = -w$$

$$\frac{\partial w}{\partial t} = \nabla^2 w - Re \left\{ \frac{\partial w}{\partial x}\frac{\partial \psi}{\partial y} - \frac{\partial w}{\partial y}\frac{\partial \psi}{\partial x} \right\}$$

$$\frac{\partial T}{\partial t} = \frac{1}{Pr}\nabla^2 T - Re \left\{ \frac{\partial T}{\partial x}\frac{\partial \psi}{\partial y} - \frac{\partial T}{\partial y}\frac{\partial \psi}{\partial x} \right\} \qquad (4.5)$$

$$+ Ec \left\{ \left(\frac{\partial^2 \psi}{\partial y^2} - \frac{\partial^2 \psi}{\partial x^2} \right)^2 + 4 \left(\frac{\partial^2 \psi}{\partial x \partial y} \right)^2 \right\},$$

where the flow in this case is referred as biofluid flow. Similarly, the steady Equations (4.4), in the absence of the magnetic field ($Mn = 0$), take the form

$$\nabla^2 \psi = -w$$

$$\nabla^2 w = Re \left\{ \frac{\partial w}{\partial x}\frac{\partial \psi}{\partial y} - \frac{\partial w}{\partial y}\frac{\partial \psi}{\partial x} \right\}$$

$$\nabla^2 T = PrRe \left\{ \frac{\partial T}{\partial x}\frac{\partial \psi}{\partial y} - \frac{\partial T}{\partial y}\frac{\partial \psi}{\partial x} \right\} \qquad (4.6)$$

$$+ PrEc \left\{ \left(\frac{\partial^2 \psi}{\partial y^2} - \frac{\partial^2 \psi}{\partial x^2} \right)^2 + 4 \left(\frac{\partial^2 \psi}{\partial x \partial y} \right)^2 \right\}.$$

Finite element method (FEM) is applied for solving biomagnetic flow equations in all cases considered. That is, systems of equations (4.1), (4.3), (4.4), (4.5) and (4.6) are going to be solved by using FEM. The FEM application to BFD flow problems is mainly based on the FEM analysis of two-dimensional flows of incompressible viscous fluids presented in Chapter 2. Moreover, for the case of steady biomagnetic fluid flow (Equations (4.4)), application of dual reciprocity boundary element method (DRBEM) is also given. The rest of the chapter is organized as follows. In Section 4.1, the procedure for the calculation of the unknown vorticity wall values is given. Section 4.2, introduces the DRBEM formulation to steady biogmagnetic fluid flow equations. Sections 4.3, 4.4 and 4.5 lay out the FEM applications of Equations (4.4), (4.3) and (4.1), respectively, with several physical configurations. Numerical results and discussions to six test problems are considered in Section 4.6. Section 4.6.1 presents the DRBEM and FEM solutions to steady biomagnetic fluid flow problem where the fluid is considered to be electrically nonconducting. A detailed comparison of the two methods is provided in this section. Time dependent biomagnetic fluid flow is visualized by using FEM in Section 4.6.2. Section 4.6.3 presents the steady biomagnetic fluid flow problem in a straight channel where the fluid is considered to be electrically conducting and the governing equations are accordingly modified. The extended

model is also used in the subsequent sections 4.6.4, 4.6.5 and 4.6.6 where the flow behavior is examined on a channel with symmetrical constriction, a channel with an irregular constriction and a multiply stenosed channel, respectively.

4.1 Vorticity boundary conditions

In general, in the stream function-vorticity-temperature formulation of the fluid flow problems, the wall conditions for vorticity remain unknown. Particularly, in the channel flows considered in this chapter, the lower and upper wall boundary conditions of vorticity are unspecified. The no-slip boundary conditions for velocity are made use of in computing vorticity boundary conditions. In problem regions where the nodes are distributed regularly, the most common approach which is the finite difference method, can be employed to obtain the vorticity boundary conditions by incorporating these velocity boundary conditions. The finite difference procedure is based on Taylor's series expansion of stream function on a boundary point using inner stream function values. For problems defined between parallel plates, the nodes lie on lines normal to the boundaries, and hence the finite difference method is applied in the computation of the vorticity wall values.
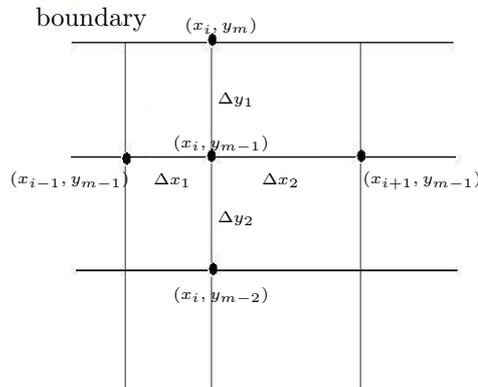
Figure 4.2: Inner nodes for calculation of vorticity boundary conditions.

In the derivation of vorticity wall conditions, four inner nodes are used which are distributed as shown in Figure 4.2. For a specific boundary point (x_i, y_m) the four inner points (x_{i-1}, y_{m-1}), (x_i, y_{m-1}), (x_{i+1}, y_{m-1}) and (x_i, y_{m-2}) are used in Taylor series expansion of the function, and using the stream function-vorticity relation $(\nabla^2 \psi = -\omega)$ the wall conditions (upper and lower) for voriticty are obtained as

$$\omega_{i,m} = a_1 \psi_{i-1,m-1} + a_2 \psi_{i,m-1} + a_3 \psi_{i+1,m-1} + a_4 \psi_{i,m-2} . \qquad (4.7)$$

The constants a_1, a_2, a_3 and a_4 are defined as

$$a_1 = \frac{-2}{\Delta x_1(\Delta x_1 + \Delta x_2)}, \qquad a_2 = \frac{2}{\Delta x_1 \Delta x_2} + \frac{2}{\Delta y_2(2\Delta y_1 + \Delta y_2)},$$

$$a_3 = \frac{-2}{\Delta x_2(\Delta x_1 + \Delta x_2)}, \qquad a_4 = \frac{-2}{\Delta y_2(2\Delta y_1 + \Delta y_2)} \; . \tag{4.8}$$

This method is applied to the problems with regular domains (i.e. regions between parallel plates) where a rectangular grid is used to discretize in the problems of Sections 4.6.1-4.6.4. In the regions where the node distribution is irregular, problems in Sections 4.6.5 and 4.6.6, a different methodology for obtaining unknown vorticity values is followed which is described in Section 4.5.1.

4.2   DRBEM Formulation of Steady Biomagnetic Fluid Flow

In this section, the DRBEM formulation of steady biomagnetic fluid flow equations given in (4.4) is presented. The boundary element method (BEM) is a boundary only discretization numerical scheme which is widely used for solving fluid flow problems. The method basically transforms the governing differential equations defined on the problem domain into integral equations which are defined on the boundary. Therefore, the method results in a system of algebraic equations which are very small in size compared to other domain discretization schemes as finite difference, finite element or finite volume methods. In the presence of nonlinear terms, convection terms and/or reaction terms in the differential equations, the dual reciprocity BEM (DRBEM) can be used. In DRBEM, the fundamental solution of the Laplace equation is used in transforming the differential equations into boundary integral equations. All the terms except Laplacian including nonlinearities are treated as inhomogeneity [16].

The DRBEM formulation for Equations (4.4) on the problem domain Ω with boundary $\partial\Omega$ are derived as follows. The terms except Laplacian in Equations (4.4) are taken to the right hand side of the equalities and are treated as the inhomogeneity of each equation. The stream function, vorticity and temperature equations in (4.4) are multiplied by the two-dimensional fundamental solution of Laplace equation

$$u^* = \frac{1}{2\pi} \ln(1/r)$$

and integrated over the domain Ω. Then, the use of the Green's second identity to the left hand side reduces the domain integral to boundary integrals [16] as

$$c_i \psi_i + \int_{\partial\Omega} (q^* \psi - u^* \frac{\partial \psi}{\partial n}) ds = -\int_{\Omega} (-w) u^* d\Omega$$

104

$$c_i w_i + \int_{\partial\Omega} (q^* w - u^* \frac{\partial w}{\partial n}) ds \;=\; -\int_{\Omega} \left(Re(\frac{\partial w}{\partial x}\frac{\partial \psi}{\partial y} - \frac{\partial w}{\partial y}\frac{\partial \psi}{\partial x}) \right.$$

$$\left. + MnReH(\frac{\partial H}{\partial x}\frac{\partial T}{\partial y} - \frac{\partial H}{\partial y}\frac{\partial T}{\partial x}) \right) u^* d\Omega \tag{4.9}$$

$$c_i T_i + \int_{\partial\Omega} (q^* T - u^* \frac{\partial T}{\partial n}) ds \;=\; -\int_{\Omega} \left\{ PrRe(\frac{\partial T}{\partial x}\frac{\partial \psi}{\partial y} - \frac{\partial T}{\partial y}\frac{\partial \psi}{\partial x}) \right.$$

$$+ MnPrReEcH(\varepsilon - T)(\frac{\partial H}{\partial x}\frac{\partial \psi}{\partial y} - \frac{\partial H}{\partial y}\frac{\partial \psi}{\partial x})$$

$$\left. + PrEc((\frac{\partial^2 \psi}{\partial y^2} - \frac{\partial^2 \psi}{\partial x^2})^2 + 4(\frac{\partial^2 \psi}{\partial x \partial y})^2) \right\} u^* d\Omega$$

where $q^* = \partial u^*/\partial n$, i is the source point and $c_i = \theta_i/2\pi$ is a constant with the internal angle θ_i at the source point. To transform the domain integrals on the right hand sides of Equations (4.9), the right hand side terms are approximated by using radial basis functions $f_j(x,y)$ as

$$b_1 = -w \;=\; \sum_{j=1}^{N+L} \alpha_j f_j(x,y) \tag{4.10}$$

$$b_2 = Re(\frac{\partial w}{\partial x}\frac{\partial \psi}{\partial y} - \frac{\partial w}{\partial y}\frac{\partial \psi}{\partial x}) + MnReH(\frac{\partial H}{\partial x}\frac{\partial T}{\partial y} - \frac{\partial H}{\partial y}\frac{\partial T}{\partial x}) \;=\; \sum_{j=1}^{N+L} \beta_j f_j(x,y) \tag{4.11}$$

$$b_3 \;=\; PrRe(\frac{\partial T}{\partial x}\frac{\partial \psi}{\partial y} - \frac{\partial T}{\partial y}\frac{\partial \psi}{\partial x}) + MnPrReEcH(\varepsilon - T)(\frac{\partial H}{\partial x}\frac{\partial \psi}{\partial y} - \frac{\partial H}{\partial y}\frac{\partial \psi}{\partial x})$$

$$+ PrEc((\frac{\partial^2 \psi}{\partial y^2} - \frac{\partial^2 \psi}{\partial x^2})^2 + 4(\frac{\partial^2 \psi}{\partial x \partial y})^2) = \sum_{j=1}^{N+L} \gamma_j f_j(x,y) \,. \tag{4.12}$$

The radial basis functions $f_j(x,y)$ depend on the problem geometry and are linked with the particular solutions $\hat{u}_j$ to the equation $\nabla^2 \hat{u}_j = f_j$, [16]. The coefficients α_j, β_j and γ_j are undetermined coefficients and, N and L are the numbers of boundary nodes and internal nodes, respectively. Now, the right hand side terms b_1, b_2 and b_3 involve the multiplication of the Laplacian of particular solution $\hat{u}_j$ with the fundamental solution u^*. Therefore, these terms can now be treated in a similar DRBEM approach and the boundary only integral equations

$$c_i \psi_i + \int_{\partial\Omega} (q^* \psi - u^* \frac{\partial \psi}{\partial n}) ds = \sum_{j=1}^{N+L} \alpha_j \left[c_i \hat{u}_{ji} + \int_{\partial\Omega} (q^* \hat{u}_j - u^* \hat{q}_j) ds \right]$$

$$c_i w_i + \int_{\partial\Omega} (q^* w - u^* \frac{\partial w}{\partial n}) ds = \sum_{j=1}^{N+L} \beta_j \left[c_i \hat{u}_{ji} + \int_{\partial\Omega} (q^* \hat{u}_j - u^* \hat{q}_j) ds \right] \tag{4.13}$$

$$c_i T_i + \int_{\partial\Omega} (q^* T - u^* \frac{\partial T}{\partial n}) ds = \sum_{j=1}^{N+L} \gamma_j \left[c_i \hat{u}_{ji} + \int_{\partial\Omega} q^* \hat{u}_j - u^* \hat{q}_j ds \right]$$

are obtained where $\hat{q} = \partial \hat{u}_j / \partial n$. The boundary is discretized using N linear elements and the DRBEM discretized equations (4.13) for stream function, vorticity and temperature equations are written in matrix-vector form

$$[H]\{\psi\} - [G]\{\frac{\partial \psi}{\partial n}\} = ([H][\hat{U}] - [G][\hat{Q}])\{\alpha\}$$

$$[H]\{w\} - [G]\{\frac{\partial w}{\partial n}\} = ([H][\hat{U}] - [G][\hat{Q}])\{\beta\} \qquad (4.14)$$

$$[H]\{T\} - [G]\{\frac{\partial T}{\partial n}\} = ([H][\hat{U}] - [G][\hat{Q}])\{\gamma\} .$$

The $(N + L) \times (N + L)$ enlarged matrices $[H]$ and $[G]$ are defined as

$$H_{ij} = c_i \delta_{ij} + \frac{1}{2\pi} \int_{\partial\Omega_j} \frac{\partial}{\partial n} \left(\ln(\frac{1}{r}) \right) ds, \quad H_{ii} = - \sum_{j=1, j\neq i}^{N} H_{ij}$$

$$G_{ij} = \frac{1}{2\pi} \int_{\partial\Omega_j} \ln(\frac{1}{r}) ds, \quad G_{ii} = \frac{l_e}{2\pi}(\ln(2/l_e) + 1)$$

where r is the distance between node-i and node-j, l_e is the length of the element and δ_{ij} is the Kronecker's delta function. The vectors $\{\hat{u}_j\}$ and $\{\hat{q}_j\}$ construct the columns of the $(N + L) \times (N + L)$ matrices $\hat{U}$ and $\hat{Q}$, respectively.

The $(N + L) \times 1$ vectors $\{\alpha\}$, $\{\beta\}$ and $\{\gamma\}$ are constructed by collocating b_1, b_2 and b_3 given in (4.10)-(4.12) at $N + L$ boundary and internal nodes as

$$[F]\{\alpha\} = \{b_1\}, \quad [F]\{\beta\} = \{b_2\}, \quad [F]\{\gamma\} = \{b_3\}$$

giving
$$\{\alpha\} = [F]^{-1}\{b_1\}, \quad \{\beta\} = [F]^{-1}\{b_2\}, \quad \{\gamma\} = [F]^{-1}\{b_3\}.$$

The matrix $[F]$ which is generally referred as the coordinate matrix, is the $(N + L) \times (N + L)$ matrix whose columns are constructed from functions f_j evaluated at $N + L$ points. The spatial derivatives of the unknowns ψ, w and T can also be calculated with the help of the coordinate matrix $[F]$ by approximating these unknowns also using radial basis functions f_j. Then,

$$\{\frac{\partial R}{\partial x}\} = [\frac{\partial F}{\partial x}][F]^{-1}\{R\}, \qquad \{\frac{\partial R}{\partial y}\} = [\frac{\partial F}{\partial y}][F]^{-1}\{R\} .$$

where R denotes ψ, w and T.

Therefore, the discretization of the boundary $\partial\Omega$ into N linear elements gives the final DRBEM discretized system

$$[H]\{\psi\} - [G]\{\frac{\partial \psi}{\partial n}\} = [C]\{-w\}$$

$$([H] - Re[C][B])\{w\} - [G]\{\frac{\partial w}{\partial n}\} = MnRe[C][D]\{T\} \qquad (4.15)$$

$$([H] - PrReEc[C][B] + MnPrReEc\varepsilon[C][D])\{T\} - [G]\{\frac{\partial T}{\partial n}\} =$$

$$MnPrReEc\varepsilon[C][D]\{\psi\} + EcPr[C]\{r_1\}\,.$$

The $(N+L) \times (N+L)$ matrix $[C]$ which appears in each of the above systems is

$$[C] = ([H][\hat{U}] - [G][\hat{Q}])[F]^{-1},$$

and the matrices $[B]$ and $[D]$ are defined as

$$[B] = ([\frac{\partial F}{\partial y}]\{\psi\})[\frac{\partial F}{\partial x}][F]^{-1} - ([\frac{\partial F}{\partial x}]\{\psi\})[\frac{\partial F}{\partial y}][F]^{-1}$$

and

$$[D] = \{H\}([\frac{\partial F}{\partial x}]\{H\})[\frac{\partial F}{\partial y}][F]^{-1} - \{H\}([\frac{\partial F}{\partial y}]\{H\})[\frac{\partial F}{\partial x}][F]^{-1}\,.$$

The $(N+L) \times 1$ vector $\{r_1\}$ involve the second order partial derivative approximations of the stream function, and is defined as

$$\{r_1\} = \left([\frac{\partial^2 F}{\partial y^2}][F]^{-1}\{\psi\} - [\frac{\partial^2 F}{\partial x^2}][F]^{-1}\{\psi\}\right)^2 + 4\left([\frac{\partial^2 F}{\partial x \partial y}][F]^{-1}\{\psi\}\right)^2\,.$$

Each system in Equations (4.15) consists of $N+L$ equations in $N+L$ unknowns. N unknowns on the boundary appear as function or its normal derivative values, and L unknown function values are at the interior nodes. Thus, for solving Equations (4.15), the corresponding boundary conditions are imposed in each system, and the system is rearranged so that the unknown values are displaced with the known values on the right hand side vector. More concisely, imposing the boundary conditions and shuffling the known and unknown values, each system is reduced to the form

$$[\tilde{A}]\{z\} = \{\tilde{b}\} \qquad (4.16)$$

where the vector $\{z\}$ contains the total N unknowns of $\{R\}$ or $\{\frac{\partial R}{\partial n}\}$ on the boundary, and L unknown values of $\{R\}$ at interior nodes, for $R = \psi, w, T$. Thus, the solution of the system (4.16) gives the unknown function values on the whole domain, and also the unknown derivative values on the boundary.

The coupled and nonlinear DRBEM equations (4.15) are solved by introducing an iterative procedure in which the stream function, vorticity and temperature equations are first reduced to the form given in (4.16) as described above. The sequential procedure starts by solving the stream function equation with an initial estimate for vorticity and imposing the given boundary conditions. The newly

calculated stream function values are used to calculate the lower and upper wall boundary conditions for vorticity by using Equation (4.7) given in Section 4.1. An initial estimate also for temperature (for the first iteration) is made use of, and the vorticity equation in (4.15) is solved. At this stage, an experimentally determined smoothing parameter λ is made use of for increasing the convergence rate of the iterative procedure as mentioned earlier in Section 2.1.2 of Chapter 2. The vorticity boundary values w_B, at the $(m+1)$-th iteration level are averaged by the corresponding values from the m-th level via the relation $w_B^{(m+1)} = \lambda w_B^{(m+1)} + (1-\lambda)w_B^{(m)}$ where $0 < \lambda < 1$. The final step in every iteration is to solve the temperature equation in (4.15). The iterative procedure is terminated when the convergence criteria between two successive iterations for all unknowns

$$\left| \psi_{ij}^{(m+1)} - \psi_{ij}^{(m)} \right| \leq \tau, \quad \left| w_{ij}^{(m+1)} - w_{ij}^{(m)} \right| \leq \tau, \quad \left| T_{ij}^{(m+1)} - T_{ij}^{(m)} \right| \leq \tau$$

is satisfied, where τ is the preassigned convergence tolerance and ij denotes the ij-th node varying from 1 to $N + L$ in the domain.

4.3   FEM Formulation of Steady Biomagnetic Fluid Flow

This section introduces the FEM application to the steady biomagnetic fluid flow equations given in (4.4). Basically, the fundamental steps presented in Chapter 2 are followed to obtain the FEM formulations. First, the weak form of the steady biomagnetic fluid flow equations is developed by multiplying the equations in (4.4) with the weight functions ω_1, ω_2 and ω_3 corresponding to the stream function, vorticity and temperature equations, respectively. The weight functions, as before, are assumed to be twice differentiable with respect to x and y, and directly satisfy the homogeneous Dirichlet boundary conditions (see Section 2.1 of Chapter 2). The weighted equations are integrated over the problem domain, and are set to zero

$$\int_\Omega \omega_1 (\nabla^2 \psi + w) d\Omega = 0,$$

$$\int_\Omega \omega_2 \left(\nabla^2 w - Re \left\{ \frac{\partial w}{\partial x} \frac{\partial \psi}{\partial y} - \frac{\partial w}{\partial y} \frac{\partial \psi}{\partial x} \right\} \right.$$

$$\left. -MnReH \left\{ \frac{\partial H}{\partial x} \frac{\partial T}{\partial y} - \frac{\partial H}{\partial y} \frac{\partial T}{\partial x} \right\} \right) d\Omega = 0,$$

(4.17)

$$\int_\Omega \omega_3 \left(\nabla^2 T - PrRe \left\{ \frac{\partial T}{\partial x} \frac{\partial \psi}{\partial y} - \frac{\partial T}{\partial y} \frac{\partial \psi}{\partial x} \right\} \right.$$

$$-MnPrReEcH(\varepsilon - T) \left\{ \frac{\partial H}{\partial x} \frac{\partial \psi}{\partial y} - \frac{\partial H}{\partial y} \frac{\partial \psi}{\partial x} \right\}$$

$$\left. -PrEc \left\{ \left(\frac{\partial^2 \psi}{\partial y^2} - \frac{\partial^2 \psi}{\partial x^2} \right)^2 + 4 \left(\frac{\partial^2 \psi}{\partial x \partial y} \right)^2 \right\} \right) d\Omega = 0.$$

The application of the divergence theorem reduces the derivative orders in Laplace terms, and yields

$$-\int_\Omega \left(\frac{\partial \omega_1}{\partial x} \frac{\partial \psi}{\partial x} + \frac{\partial \omega_1}{\partial y} \frac{\partial \psi}{\partial y} \right) d\Omega + \int_\Omega \omega_1 w \, d\Omega + \int_{\partial \Omega} \omega_1 \frac{\partial \psi}{\partial n} ds = 0,$$

$$-\int_\Omega \left(\frac{\partial \omega_2}{\partial x} \frac{\partial w}{\partial x} + \frac{\partial \omega_2}{\partial y} \frac{\partial w}{\partial y} \right) d\Omega + MnRe \int_\Omega \omega_2 H \left(\frac{\partial H}{\partial y} \frac{\partial T}{\partial x} - \frac{\partial H}{\partial x} \frac{\partial T}{\partial y} \right) d\Omega$$

$$+Re \int_\Omega \omega_2 \left(\frac{\partial w}{\partial y} \frac{\partial \psi}{\partial x} - \frac{\partial w}{\partial x} \frac{\partial \psi}{\partial y} \right) d\Omega + \int_{\partial \Omega} \omega_2 \frac{\partial w}{\partial n} ds = 0,$$

$$\int_\Omega \left(\frac{\partial \omega_3}{\partial x} \frac{\partial T}{\partial x} + \frac{\partial \omega_3}{\partial y} \frac{\partial T}{\partial y} \right) d\Omega + PrRe \int_\Omega \omega_3 \left(\frac{\partial T}{\partial x} \frac{\partial \psi}{\partial y} - \frac{\partial T}{\partial y} \frac{\partial \psi}{\partial x} \right) d\Omega$$

$$+MnPrReEc \int_\Omega \omega_3 H(\varepsilon - T) \left(\frac{\partial H}{\partial x} \frac{\partial \psi}{\partial y} - \frac{\partial H}{\partial y} \frac{\partial \psi}{\partial x} \right) d\Omega$$

$$+PrEc \int_\Omega \omega_3 \left\{ \left(\frac{\partial^2 \psi}{\partial y^2} - \frac{\partial^2 \psi}{\partial x^2} \right)^2 + 4 \left(\frac{\partial^2 \psi}{\partial x \partial y} \right)^2 \right\} d\Omega - \int_{\partial \Omega} \omega_3 \frac{\partial T}{\partial n} ds = 0.$$

$$(4.18)$$

In the above equations, the magnetic field intensity function $H(x, y)$ and its spatial derivatives $\dfrac{\partial H}{\partial x}$, $\dfrac{\partial H}{\partial y}$ enter as known values from definition (4.2).

For the problem region discretization, six-nodal triangular elements are used, and the unknowns ψ, w and T are approximated over an element by using the quadratic shape functions

$$\psi^e(x, y) \approx \sum_{i=1}^{6} \psi_i^e N_i^e(x, y), \quad w^e(x, y) \approx \sum_{i=1}^{6} w_i^e N_i^e(x, y),$$

$$(4.19)$$

$$T^e(x, y) \approx \sum_{i=1}^{6} T_i^e N_i^e(x, y).$$

where ψ_i^e, w_i^e and T_i^e are the nodal values of ψ, w and T over an element e, respectively. The shape functions N_i^e are given in area coordinates as

$$N_1^e = \xi_1(2\xi_1 - 1), \quad N_2^e = \xi_2(2\xi_2 - 1), \quad N_3^e = \xi_3(2\xi_3 - 1)$$

$$N_4^e = 4\xi_1\xi_2, \qquad N_5^e = 4\xi_2\xi_3, \qquad N_6^e = 4\xi_1\xi_3$$

(4.20)

where $\xi_i = A_i/A_e$, $(i = 1, 2, 3)$ are the linear shape functions given in local area coordinates for each element which are defined in Section 2.1 of Chapter 2.

The Galerkin approach is followed and the weight functions are taken as shape functions when Equations (4.18) are written for each element. The boundary integrals in the element level equations drop out as the shape functions vanish for Dirichlet type boundary conditions and also the normal derivative conditions are zero (homogenous Neumann type) at the exit of the channel, for all the unknowns. The integral equations (4.18) can now be written for any six-nodal triangular element Ω_e

$$-\int_{\Omega_e} \left(\frac{\partial N_i}{\partial x} \frac{\partial \psi}{\partial x} + \frac{\partial N_i}{\partial y} \frac{\partial \psi}{\partial y} \right) d\Omega_e + \int_{\Omega_e} N_i w d\Omega_e = 0 \,,$$

$$-\int_{\Omega_e} \left(\frac{\partial N_i}{\partial x} \frac{\partial w}{\partial x} + \frac{\partial N_i}{\partial y} \frac{\partial w}{\partial y} \right) d\Omega_e + Re \int_{\Omega_e} N_i \left(\frac{\partial w}{\partial y} \frac{\partial \psi}{\partial x} - \frac{\partial w}{\partial x} \frac{\partial \psi}{\partial y} \right) d\Omega_e$$

$$+ MnRe \int_{\Omega_e} N_i H \left(\frac{\partial H}{\partial y} \frac{\partial T}{\partial x} - \frac{\partial H}{\partial x} \frac{\partial T}{\partial y} \right) d\Omega_e = 0 \,,$$

(4.21)

$$\int_{\Omega_e} \left(\frac{\partial N_i}{\partial x} \frac{\partial T}{\partial x} + \frac{\partial N_i}{\partial y} \frac{\partial T}{\partial y} \right) d\Omega_e + PrRe \int_{\Omega_e} N_i \left(\frac{\partial T}{\partial x} \frac{\partial \psi}{\partial y} - \frac{\partial T}{\partial y} \frac{\partial \psi}{\partial x} \right) d\Omega_e$$

$$+ MnPrReEc \int_{\Omega_e} N_i H(\varepsilon - T) \left(\frac{\partial H}{\partial x} \frac{\partial \psi}{\partial y} - \frac{\partial H}{\partial y} \frac{\partial \psi}{\partial x} \right) d\Omega_e$$

$$+ PrEc \int_{\Omega_e} N_i \left\{ \left(\frac{\partial^2 \psi}{\partial y^2} - \frac{\partial^2 \psi}{\partial x^2} \right)^2 + 4 \left(\frac{\partial^2 \psi}{\partial x \partial y} \right)^2 \right\} d\Omega_e = 0 \,.$$

The integrals are evaluated on each element e, where $e = 1, ..., M_e$, and M_e is the total number of elements. The use of six-nodal triangular element results in 6×6 systems of matrix-vector equations for stream function, vorticity and temperature equations on each element. The assembly procedure is performed next, which connects all local element equations to the global equation system over the whole problem domain

$$[K]\{\psi\} = [M]\{w\}$$

$$-[K]\{w\} - Re[A]\{w\} = MnRe\{F_3\} \qquad (4.22)$$

$$-[K]\{T\} - PrRe[A]\{T\} + MnPrReEc[A_3]\{T\}$$

$$= MnPrReEc\varepsilon\{F_1\} + PrEc\{F_2\} \ .$$

The summation $\sum\limits_{e=1}^{M_e}$ implies the assembly task which results in the algebraic systems of equations with the size equals to the number of total nodes in the problem domain for each system.

The global matrices $[K]$, $[A]$, $[A_3]$ and $[M]$ are defined as

$$[K] \;=\; \sum_{e=1}^{M_e} \int_{\Omega_e} \left(\frac{\partial N_i^e}{\partial x}\frac{\partial N_j^e}{\partial x} + \frac{\partial N_i^e}{\partial y}\frac{\partial N_j^e}{\partial y} \right) d\Omega_e$$

$$[A] \;=\; \sum_{e=1}^{M_e} \int_{\Omega_e} N_i^e \left[(\sum_{k=1}^{6}\frac{\partial N_k^e}{\partial y}\psi_k^e)\frac{\partial N_j^e}{\partial x} - (\sum_{k=1}^{6}\frac{\partial N_k^e}{\partial x}\psi_k^e)\frac{\partial N_j^e}{\partial y} \right] d\Omega_e$$

$$[A_3] \;=\; \sum_{e=1}^{M_e} \int_{\Omega_e} N_i^e \left[\sum_{k=1}^{6}(\frac{\partial N_k^e}{\partial y}\psi_k^e)\sum_{l=1}^{6}(N_l^e H_l^e \frac{\partial H_l^e}{\partial x}) \right. \qquad (4.23)$$

$$\left. - \sum_{k=1}^{6}(\frac{\partial N_k^e}{\partial x}\psi_k^e)\sum_{l=1}^{6}(N_l^e H_l^e \frac{\partial H_l^e}{\partial y}) \right] N_j^e d\Omega_e$$

$$[M] \;=\; \sum_{e=1}^{M_e} \int_{\Omega_e} N_i^e N_j^e d\Omega_e, \qquad i,j = 1,...,6 \ .$$

The right hand side vectors $\{F_1\}$, $\{F_2\}$ and $\{F_3\}$ are given as

$$\{F_1\} \;=\; \sum_{e=1}^{M_e} \int_{\Omega_e} \left[\sum_{k=1}^{6}(\frac{\partial N_k^e}{\partial y}\psi_k^e)\sum_{l=1}^{6}(N_l^e H_l^e \frac{\partial H_l^e}{\partial x}) \right.$$

$$\left. - \sum_{k=1}^{6}(\frac{\partial N_k^e}{\partial x}\psi_k^e)\sum_{l=1}^{6}(N_l^e H_l^e \frac{\partial H_l^e}{\partial y}) \right] N_i^e d\Omega_e$$

$$\{F_2\} = \sum_{e=1}^{M_e} \int_{\Omega_e} \left[\left(\sum_{l=1}^{6} \frac{\partial^2 N_k^e}{\partial y^2} \psi_k^e - \sum_{l=1}^{6} \frac{\partial^2 N_k^e}{\partial x^2} \psi_k^e \right)^2 \right.$$

$$\left. +4 \left(\sum_{l=1}^{6} \frac{\partial^2 N_i^e}{\partial x \partial y} \psi_k^e \right)^2 \right] N_i^e d\Omega_e \qquad (4.24)$$

$$\{F_3\} = \sum_{e=1}^{M_e} \int_{\Omega_e} \left[\sum_{k=1}^{6} \left(\frac{\partial N_k^e}{\partial y} T_k^e \right) \sum_{l=1}^{6} \left(N_l^e H_l^e \frac{\partial H_l^e}{\partial x} \right) \right.$$

$$\left. - \sum_{k=1}^{6} \left(\frac{\partial N_k^e}{\partial x} T_k^e \right) \sum_{l=1}^{6} \left(N_l^e H_l^e \frac{\partial H_l^e}{\partial y} \right) \right] N_i^e d\Omega_e,$$

$$i = 1, ..., 6 \,.$$

A similar iterative procedure introduced in the previous section is employed to solve the coupled nonlinear systems (4.22) which results in a set of linear algebraic equations in each iteration. The stream function equation is solved with an initial estimate for vorticity at the first iteration, and imposition of the boundary conditions for stream function. Next, using the newly obtained stream function values, the lower and upper wall conditions for vorticity are calculated via Equation (4.7) given in Section 4.1. As the final step of each iteration, the temperature equation in (4.22) is solved with the imposition of the given boundary conditions. The iterative procedure is terminated when the convergence criteria between two successive iterations for all unknowns

$$\left| \psi_{ij}^{(m+1)} - \psi_{ij}^{(m)} \right| \le \tau, \quad \left| w_{ij}^{(m+1)} - w_{ij}^{(m)} \right| \le \tau, \quad \left| T_{ij}^{(m+1)} - T_{ij}^{(m)} \right| \le \tau$$

is met, where as before, τ is the preassigned convergence tolerance and ij denotes the ij-th node varying from 1 to the total number of nodes in the domain.

4.4 FEM Formulation of Unsteady Biomagnetic Fluid Flow

In this section, finite element model of the unsteady, electrically nonconducting biomagnetic fluid flow problem is developed. The flow and heat transfer equations given in (4.3) are solved. The weak form is obtained by multiplying each equation in (4.3) with the corresponding weight function ω_1 for stream function, ω_2 for vorticity, and ω_3 for temperature. The equations are integrated over the problem region and the divergence theorem is applied

$$-\int_\Omega \left(\frac{\partial \omega_1}{\partial x} \frac{\partial \psi}{\partial x} + \frac{\partial \omega_1}{\partial y} \frac{\partial \psi}{\partial y} \right) d\Omega + \int_\Omega \omega_1 w d\Omega + \int_{\partial\Omega} \omega_1 \frac{\partial \psi}{\partial n} ds = 0 \,,$$

$$\int_\Omega \omega_2 \frac{\partial w}{\partial t} d\Omega + \int_\Omega \left(\frac{\partial \omega_2}{\partial x} \frac{\partial w}{\partial x} + \frac{\partial \omega_2}{\partial y} \frac{\partial w}{\partial y} \right) d\Omega + Re \int_\Omega \omega_2 \left(\frac{\partial \psi}{\partial x} \frac{\partial w}{\partial y} - \frac{\partial w}{\partial y} \frac{\partial \psi}{\partial x} \right) d\Omega$$

$$- MnRe \int_\Omega \omega_2 H \left(\frac{\partial H}{\partial x} \frac{\partial T}{\partial y} - \frac{\partial H}{\partial y} \frac{\partial T}{\partial x} \right) d\Omega - \int_{\partial\Omega} \omega_2 \frac{\partial w}{\partial n} ds = 0 \,,$$

$$(4.25)$$

$$\int_\Omega \omega_3 \frac{\partial T}{\partial t} d\Omega + \frac{1}{Pr} \int_\Omega \left(\frac{\partial \omega_3}{\partial x} \frac{\partial T}{\partial x} + \frac{\partial \omega_3}{\partial y} \frac{\partial T}{\partial y} \right) d\Omega$$

$$+ Re \int_\Omega w_3 \left(\frac{\partial T}{\partial x} \frac{\partial \psi}{\partial y} - \frac{\partial T}{\partial y} \frac{\partial \psi}{\partial x} \right) d\Omega$$

$$- MnReEc \int_\Omega \omega_3 (\varepsilon + T) H \left(\frac{\partial H}{\partial x} \frac{\partial \psi}{\partial y} - \frac{\partial H}{\partial y} \frac{\partial \psi}{\partial x} \right) d\Omega$$

$$- Ec \int_\Omega \omega_3 \left(\left(\frac{\partial^2 \psi}{\partial y^2} - \frac{\partial^2 \psi}{\partial x^2} \right)^2 + 4 \left(\frac{\partial^2 \psi}{\partial x \partial y} \right)^2 \right) d\Omega - \frac{1}{Pr} \int_{\partial\Omega} \omega_3 \frac{\partial T}{\partial n} ds = 0 \,.$$

In general, there are two alternative ways to develop the finite element model of time dependent problems. In one approach, which is referred as the coupled formulation, time is treated as an additional coordinate along with the spatial coordinates. The other approach, which is referred as decoupled formulation, treats the time and spatial variations separately [59]. In the present study, the decoupled formulation is applied and the unknowns ψ, w and T are approximated over a six-nodal triangular element by using quadratic shape functions,

$$\psi^e(x, y, t) \approx \sum_{j=1}^6 \psi_j^e(t) N_j^e(x, y), \quad w^e(x, y, t) \approx \sum_{j=1}^6 w_j^e(t) N_j^e(x, y),$$

$$(4.26)$$

$$T^e(x, y, t) \approx \sum_{j=1}^6 T_j^e(t) N_j^e(x, y).$$

The quadratic shape functions N_j^e's are defined in (4.20) in area coordinates, and ψ_i^e, w_i^e and T_i^e are the time dependent nodal values of ψ, w, T, respectively. The Galerkin approach is followed where the weight functions w_i are taken as shape functions when the equations (4.25) are written for each element. The boundary integrals drop due to the property of shape functions to be vanished for Dirichlet boundary conditions, and zero normal derivative conditions at the exit. The integral equations (4.25) are written for a 6-nodal triangular element Ω_e, and after the assembly procedure for the total number of M_e elements, the following matrix-vector system of ordinary differential equations (ODEs) is obtained

$$[K]\{\psi\} = [M]\{w\}$$

$$[M]\{\dot{w}\} + [K]\{w\} + Re\,[A]\{w\} = MnRe\,\{F_3\} \qquad (4.27)$$

$$[M]\{\dot{T}\} + \frac{1}{Pr}[K]\{T\} + Re\,[A]\{T\} - MnReEc\,[A_3]\{T\}$$

$$= MnReEc\varepsilon\,\{F_1\} + Ec\,\{F_2\}\ .$$

The superposed dot in the vorticity and temperature equations, denotes the time derivative at nodal values for w and T. For the temporal discretization, the backward finite difference scheme which is defined by

$$\dot{u}\big|_{s+1} = \frac{\partial u}{\partial t}\Big|_{s+1} = \frac{u_{s+1} - u_s}{\Delta t}$$

is employed, where s indicates the time level. Thence, time discretized form of FEM system of algebraic equations take the form

$$[K]\{\psi\}_{s+1} = [M]\{w\}_s$$

$$[\hat{K}_1]\{w\}_{s+1} = \{\hat{F}_1\} \qquad (4.28)$$

$$[\hat{K}_2]\{T\}_{s+1} = \{\hat{F}_2\}$$

where $[\hat{K}_1]$ and $[\hat{K}_2]$ are

$$[\hat{K}_1] = [M] + \Delta t[K] + \Delta tRe[A],$$

$$[\hat{K}_2] = [M] + \frac{\Delta t}{Pr}[K] + \Delta tRe[A] - \Delta tMnReEc[A_3], \qquad (4.29)$$

and $\{\hat{F}_1\}$ and $\{\hat{F}_2\}$ are given as

$$\{\hat{F}_1\} = \Delta tMnRe\,\{F_3\} + [M]\{w\}_s\,,$$

$$\{\hat{F}_2\} = \Delta tMnReEc\varepsilon\,\{F_1\} + \Delta tEc\,\{F_2\} + [M]\{T\}_s\ . \qquad (4.30)$$

The matrices $[K]$, $[A]$, $[M]$, $[A_3]$ and the right hand side vectors $\{F_1\}$, $\{F_2\}$ and $\{F_3\}$ are defined in Section 4.3. The final algebraic system (4.28) is solved by the iterative procedure given in the previous section. Each iteration starts with solving the stream function equation, and then, the vorticity lower and upper wall conditions are approximated as given in Section 4.1. The vorticity equation is solved next to obtain all nodal values of the vorticity in the whole problem domain. The final step of each iteration is solving the temperature equation. The iterative procedure is terminated when the conditions

$$\left|(\psi_{ij})_{(s+1)} - (\psi_{ij})_{(s)}\right| \leq \tau,\ \ \left|(w_{ij})_{(s+1)} - (w_{ij})_{(s)}\right| \leq \tau,\ \ \left|(T_{ij})_{(s+1)} - (T_{ij})_{(s)}\right| \leq \tau$$

are satisfied, where ij denotes the ij-th node varying from 1 to the total number of nodes in the domain, and s is the time level. The solutions satisfying the above criteria are accepted as the steady-state solutions, with respect to the steady-state tolerance parameter τ.

4.5 FEM formulation of unsteady biomagnetic electrically conducting fluid flow

This section extends the FEM model for the unsteady biomagnetic electrically nonconducting fluid flow problem developed in the previous section in that the fluid is considered as electrically conducting. Accordingly, the governing equations given in (4.1) are taken into account. The FEM model of Section 4.4 is modified so that the FHD magnetic number Mn is replaced by Mn_F as appears in Equations (4.1), and the MHD terms in the vorticity and temperature equations are added. Therefore, the FEM discretized system (4.28) will be adapted and the MHD terms (with Mn_M) will be enrolled into the model. As a result, the FEM discretized model for Equations (4.1) is obtained as

$$[K]\{\psi\}_{s+1} = [M]\{w\}_s$$

$$[\hat{K}_1]\{w\}_{s+1} = \{\hat{F}_3\} \tag{4.31}$$

$$[\hat{K}_2]\{T\}_{s+1} = \{\hat{F}_4\}$$

where as before, s is the time level, $[\hat{K}_1]$ and $[\hat{K}_2]$ are defined in (4.29), with $M_n = Mn_F$, of the previous section whereas, and the matrices $[K], [A], [M], [A_3]$ are defined in Section 4.3. The right hand side vectors $\{\hat{F}_3\}$ and $\{\hat{F}_4\}$ are defined as follows

$$
\begin{aligned}
\{\hat{F}_3\} &= [M]\{w\}_s + \Delta t Mn_F Re\{F_3\}_s + \Delta t Mn_M\{F_4\}_{s+1}, \\
\{\hat{F}_4\} &= [M]\{T\}_s + \Delta t Mn_F Re Ec\varepsilon\{F_1\}_{s+1} \\
&\quad + \Delta t Mn_M Ec\{F_5\}_{s+1} + \Delta t Ec\{F_2\}_{s+1}.
\end{aligned} \tag{4.32}
$$

The vectors $\{F_1\}$, $\{F_2\}$ and $\{F_3\}$ are given in (4.24), where $\{F_4\}$ and $\{F_5\}$ are defined as

$$
\begin{aligned}
\{F_4\} &= \sum_{e=1}^{M_e} \int_{\Omega_e} \left[\sum_{k=1}^{6}\left(\frac{\partial N_k^e}{\partial y}\psi_k^e\right)\sum_{l=1}^{6}\left(N_l^e\frac{\partial(H_l^e)^2}{\partial y}\right) \right. \\
&\quad \left. + \sum_{l=1}^{6}\left(\frac{\partial^2 N_k^e}{\partial y^2}\psi_k^e\right)\sum_{l=1}^{6}\left(N_l^e(H_l^e)^2\right) \right] N_i^e d\Omega_e, \\
\{F_5\} &= \sum_{e=1}^{M_e} \int_{\Omega_e} \left(\sum_{k=1}^{6}\frac{\partial N_k^e}{\partial y}\psi_k^e\right)^2 \left(\sum_{l=1}^{6}N_l^e(H_l^e)^2\right) N_i^e d\Omega_e, \\
&\quad i = 1, ..., 6.
\end{aligned} \tag{4.33}
$$

The coupled equations (4.31) are solved by two distinctive iterative approaches. Specifically in both procedures, the stream function, vorticity and temperature equations are solved sequentially with the admission of arbitrary initial estimates for vorticity and temperature at the first iteration, and the process caries on until a previously assigned steady-state criteria is met. However, the vorticity wall conditions (the lower and upper walls) are calculated by using two different approaches depending on the problem geometry. This constitutes the main difference between the two iterative procedures. The biomagnetic fluid flow equations (4.1) are solved basically in three different channels, namely, a straight channel (Section 4.6.3), a symmetrically stenosed channel (Section 4.6.4) and a channel with irregular constriction patterns (Sections 4.6.5 and 4.6.6). In both straight and symmetrically stenosed channels, the method based on a finite difference approach given in Section 4.1 is applied in the computation of the vorticity wall values. In these configurations, the iterative progress is exactly the same as in the previous sections. However, in unsymmetrically stenosed channels in which the discretization yields irregularly distributed nodes, a different technique based on FEM is applied to evaluate the vorticity boundary values. The details of this iterative approach (followed in unsymmetrically stenosed channels) together with the computation of the vorticity wall conditions are presented in the following section.

4.5.1 Vorticity boundary conditions in irregularly stenosed regions and the iterative solution procedure

A technique for the computation of the unknown vorticity boundary conditions at the upper and lower walls, which is based on Taylor's series expansion of the stream function, is previously presented in Section 4.1. This finite difference method is one of the most commonly used procedure for computing vorticity boundary conditions. However, the finite difference method is limited to regular domains and is not convenient when the nodes in the problem domain are distributed in an irregular pattern. Thus, an approach based on FEM is applied in the present work. This approach basically follows the procedure given in the work of [21]. In this technique, mainly an iterative procedure is followed. Firstly, the vorticity values on the whole domain are assumed to be known. Having known the vorticity values from the previous (s-th) level and the stream function's boundary conditions, the stream function equation is solved using FEM modality

$$\{\psi\}_{s+1} = \left[K^{-1}\right]\left[M\right]\{w\}_s \qquad (4.34)$$

which gives the stream function values in the $(s+1)$-th iteration. Using these stream function values together with the known (inlet and outlet) vorticity boundary conditions, the equation

$$\{w\}_{s+1} = \left[M^{-1}\right]\left[K\right]\{\psi\}_{s+1} \qquad (4.35)$$

is now used to obtain the missing boundary values for vorticity. Note that Equation (4.35) is solved only for the unknown boundary conditions (upper and lower

plates), and the inverse matrix calculations are not exactly performed but an equation solver is applied instead. Having obtained the boundary conditions for the vorticity from Equation (4.35), and using the stream function values at the $(s+1)$-th level, second equation in (4.31) is solved to obtain the vorticity values on the whole domain at the $(s+1)$-th level. Finally, the stream function and vorticity solutions at the $(s+1)$-th level are used and the equation for temperature in (4.32) is solved to obtain the temperature values at the $(s+1)$-th level. This iterative procedure stops when the conditions

$$\left|(\psi_{ij})_{(s+1)} - (\psi_{ij})_{(s)}\right| \leq \tau, \quad \left|(w_{ij})_{(s+1)} - (w_{ij})_{(s)}\right| \leq \tau, \quad \left|(T_{ij})_{(s+1)} - (T_{ij})_{(s)}\right| \leq \tau$$

are satisfied, as mentioned earlier, ij denotes the ij-th node varying from 1 to the total number of nodes in the domain, and s is the time level. The solutions satisfying this criteria are taken as the steady-state solutions, with respect to τ.

4.6   Numerical Results

The numerical simulations for the biomagnetic fluid flow problems under the influence of a magnetic field in different channels, are presented in this section. The channels with various types of constrictions are defined individually in each problem section. The DRBEM and FEM methodologies are applied for solving various configurations of biomagnetic flow problems. Implicit backward difference scheme is made use of for temporal discretization in time dependent problems. In particular, Section 4.6.1 presents the numerical results obtained from DRBEM and FEM for steady biomagnetic fluid flow where the fluid is taken as electrically nonconducting. In Section 4.6.2, the results of the unsteady biomagnetic nonconducting fluid flow in a straight channel are presented. Then, the model is extended so that the fluid is electrically conducting, and the results concerning the unsteady biomagnetic fluid flow in a straight channel are given in Section 4.6.3. Next, the unsteady biomagnetic fluid flow is simulated in symmetrically stenosed, unsymmetrically stenosed, and finally in multi-stenosed channels in Sections 4.6.4, 4.6.5 and 4.6.6, respectively. The computational domain in each problem is determined by taking the length and the height of the channel as $l = 10$ and $h = 1$, respectively. In the FEM discretization of the irregularly stenosed channels, namely Problems 4.6.5 and 4.6.6, an open source FreeFem++ is made use of. The boundaries of the problem domain are defined as functions and the domain is triangulated using three-nodal linear elements using this software package. However, in this study, six-nodal quadratic triangular elements are used and hence, the three-nodal element coordinates data is modified so as to have six-nodal triangulation of the computational domain. The physical parameters, and the number of elements used in the discretization are provided in each problem separately. In each iteration of the solution procedures, the systems of algebraic equations resulting from both DRBEM and FEM discretizations are solved using a MATLAB code, where a sparse system solver function is involved in FEM models.

4.6.1 BEM and FEM applications for steady biomagnetic fluid flow

The DRBEM and FEM solutions of steady biomagetic fluid flow in a straight channel are presented in this section using both boundary and finite element methodologies which are introduced in Sections 4.2 and 4.3, respectively. The influence of a spatially varying magnetic field on the flow and heat transfer is investigated where the fluid is assumed to be a poor conductor. The governing equations given in (4.4) are taken into consideration. The flow at the entrance is assumed to be fully developed, and the velocity has a parabolic profile whereas, the temperature has a linear profile. On the lower and upper plates, the no-slip condition is imposed for velocities, and the plates are kept at constant temperatures. At the exit of the channel, homogenous Neumann boundary conditions are imposed as $\partial\psi/\partial x = 0$, $\partial w/\partial x = 0$, $\partial T/\partial x = 0$. Thus, the boundary conditions for stream function and temperature are given as

$$\psi(0,y) = 2y^2 - (4/3)y^3, \ \psi(x,0) = 0, \ \psi(x,1) = 2/3,$$
$$T(0,y) = 1 - y, \ T(x,0) = 1, \ T(x,1) = 0, \tag{4.36}$$

and the unavailable vorticity boundary conditions are calculated by the method given in Section 4.1.
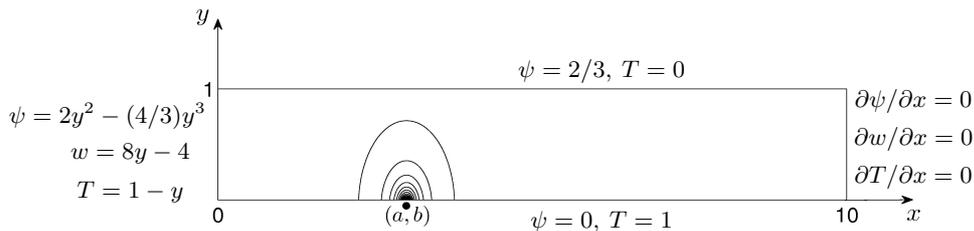

Figure 4.3: Domain configuration and boundary conditions for Problem 4.6.1.

The numerical simulations are performed taking $Pr = 20$, $\varepsilon = 8$, and $Ec = 2.476 \times 10^{-6}$ and the results are obtained for fixed Reynolds numbers ($Re = 50$ with DRBEM, $Re = 150$ with DRBEM and FEM, and $Re = 250$ with FEM). The external magnetic source is placed at the point $(a,b) = (2.5, -0.05)$. The resulting magnetic field contours together with the problem domain and boundary conditions are shown in Figure 4.3. The results obtained from each method are presented separately in the sequel.

The DRBEM discretized equations (4.15) are solved by the iterative procedure described in Section 4.2, and the results are obtained for the sets of Reynolds number, magnetic number values $Re = 50$, $Mn = 115, 215$; $Re = 50$, $Mn = 315$ and $Re = 150$, $Mn = 115$, using respectively, $N = 290$, $N = 330$ and $N = 330$ uniform linear boundary elements. The coordinate function is taken as $f = 1 + r$ in the computations.

In Figure 4.4, the steam function, vorticity and temperature contours are drawn for a fixed Reynolds number $Re = 50$ for the values of magnetic numbers (a) $Mn =$
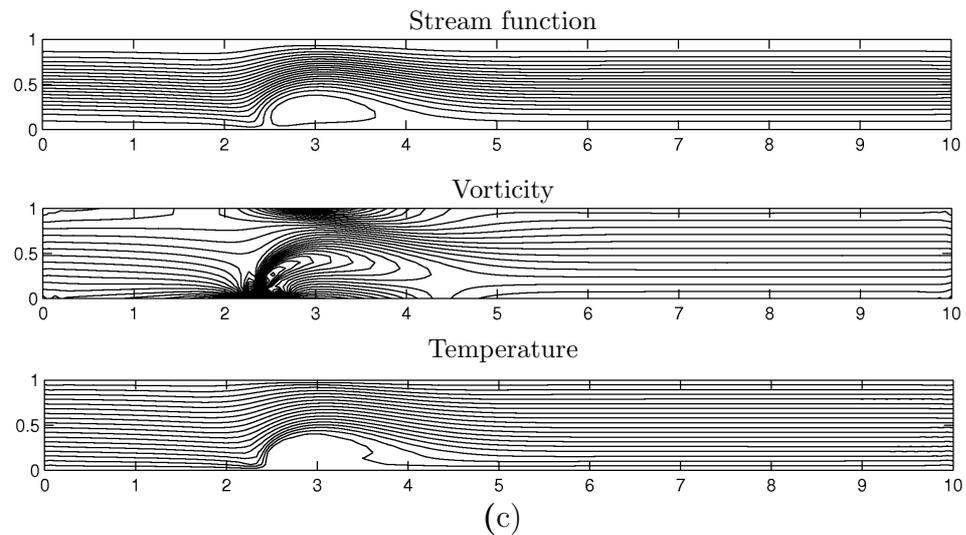
Stream function

Vorticity

Temperature

(a)

Stream function

Vorticity

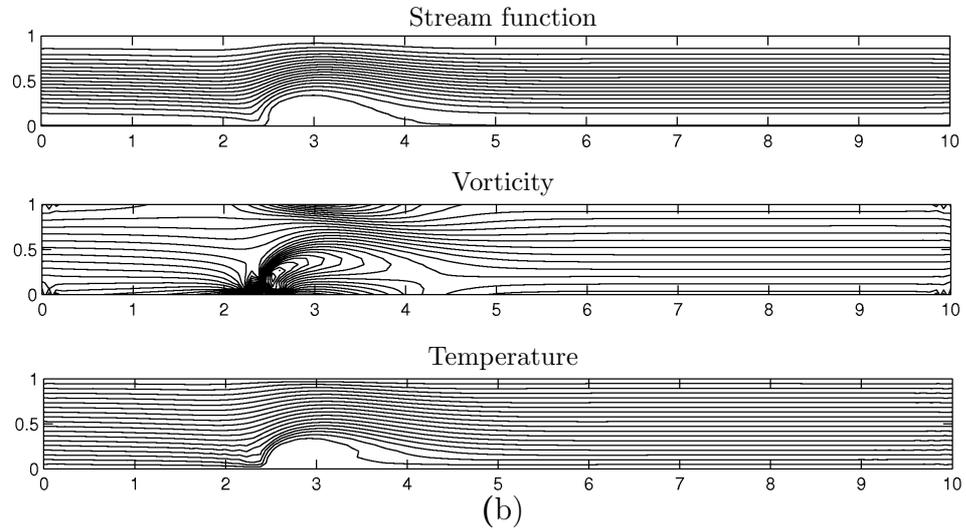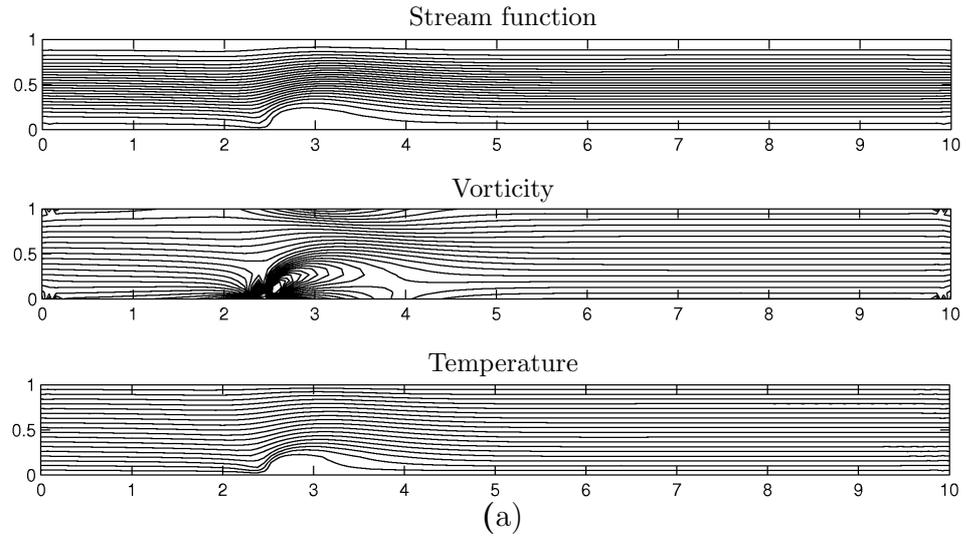Temperature

(b)

Stream function

Vorticity

Temperature

(c)

Figure 4.4: Problem 4.6.1: Effects of magnetic field on streamlines, vorticity contours and isotherms (DRBEM) for $Re = 50$, $(a)\, Mn = 115$, $(b)\, Mn = 215$, $(c)\, Mn = 315$.

115, $(b)\,Mn = 215$ and $(c)\,Mn = 315$. It is observed from the figure that the presence of the external field leads to a vortex formation for all of the unknowns close to magnetic source along the lower plate. The vortex which indicates a circulation and a decrease in the flow rate of the fluid, extends both horizontally and vertically as the intensity of the magnetic field increases. Consequently, the stagnant region spreads in the neighborhood of the magnetic source, and the temperature of the fluid increases to the temperature of the lower plate.
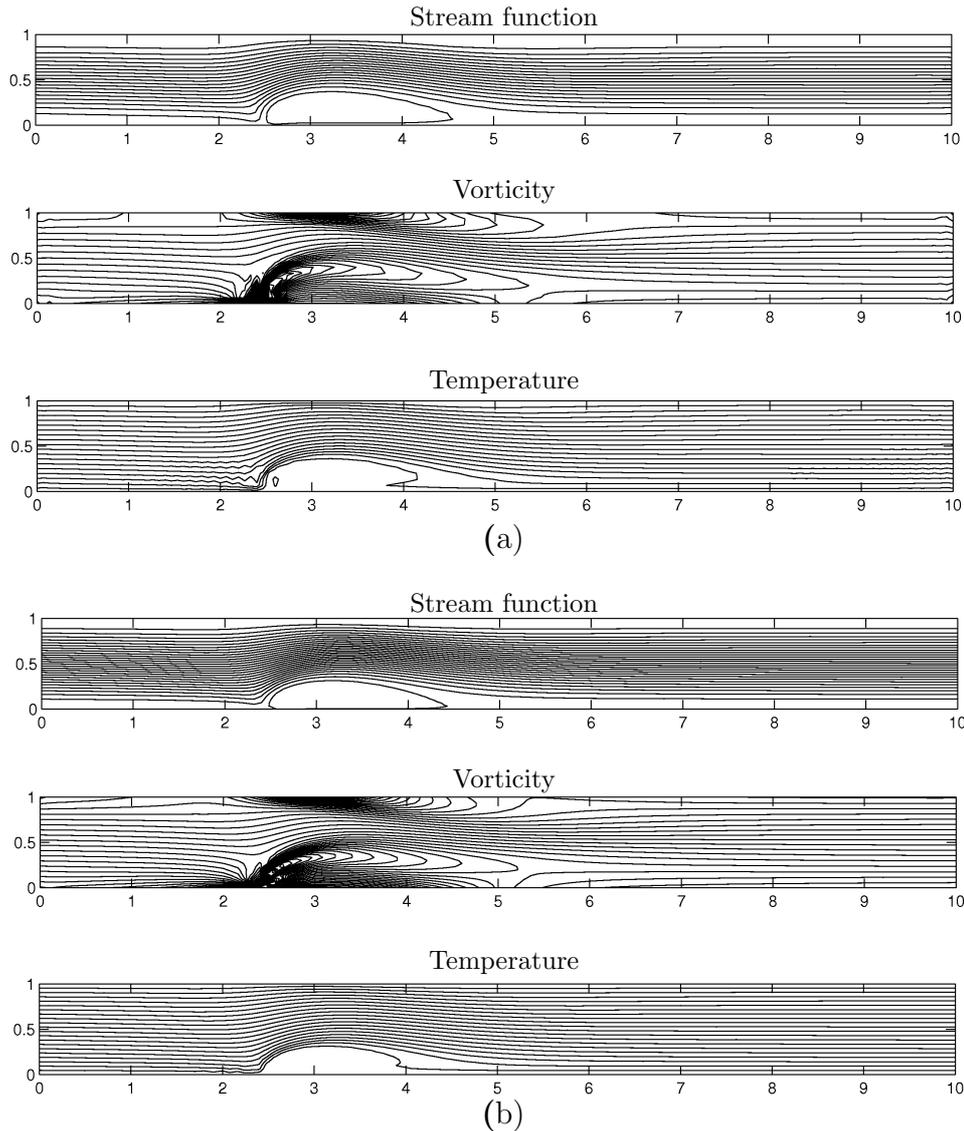
Figure 4.5: Problem 4.6.1: Streamlines, vorticity contours and isotherms for $Re = 150$, $Mn = 115$: (a) DRBEM, (b) FEM.

Figure 4.5 presents the streamlines, vorticity contours and isotherms for the values of $Re = 150$ and $Mn = 115$ obtained by (a) DRBEM and (b) FEM procedures. When Figure 4.5(a) and Figure 4.4(a) are compared, it can be seen that for a fixed magnetic number $(Mn = 115)$, increasing Reynolds number from 50 to 150

causes an extension of the vortices in the contours of all unknowns. Figures 4.5 (a) and (b) confirm that the obtained DRBEM and FEM results are in good agreement generally on the whole channel, especially in the region around the magnetic source for the given set of Reynolds and magnetic numbers, $Re = 150$ and $Mn = 115$. However, at the exit of the channel FEM gives smoother results than DRBEM especially for vorticity. In DRBEM solutions, some small discrepancies are noticed in the profiles of streamlines, isotherms and especially vorticity contours near the top and bottom corners at the exit of the channel. These are not expected physical behaviors, and may be due to the singularities in boundary conditions at the corners of the exit. A remedy for the unexpected oscillations can be increasing the number of the boundary elements, and inner nodes taken in the computations. However, the advantage of DRBEM actually lies in obtaining solutions with small number of elements compared to domain discretization methods such as FEM. In the present case, the numerical simulations are carried out using 1350 quadratic finite elements in FEM whereas in DRBEM, only 330 linear boundary elements are used to obtain the same behavior for the solution with an iteration tolerance 10^{-6} for a moderate value of $Re = 150$ (where the equations are mildly nonlinear). The results lead to a conclusion that the small computational advantage of DRBEM can successively made use of for capturing the behavior of the simplified biomagnetic flow problems in moderate Reynolds number values.
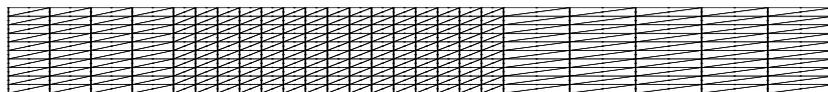

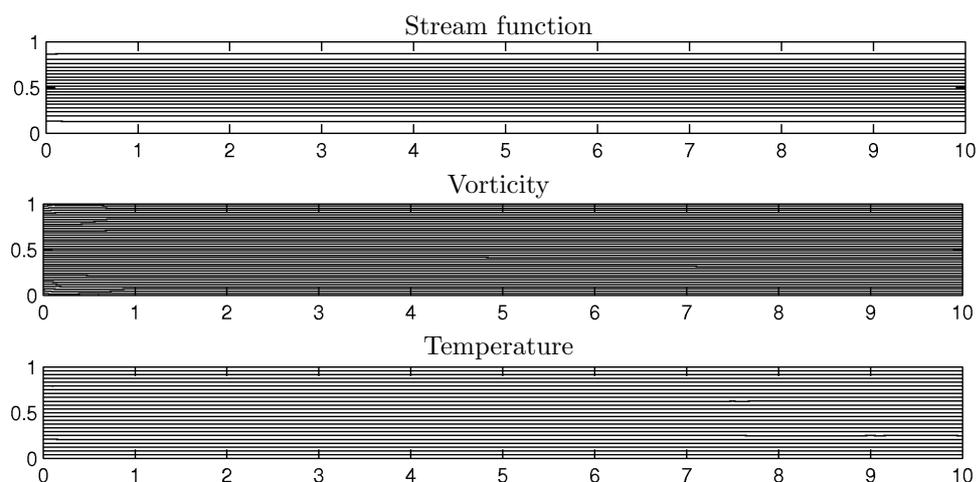Figure 4.6: Problem 4.6.1: A sample FEM discretization of the problem region using $M_e = 480$ elements.

Figure 4.7: Problem 4.6.1: Streamlines, vorticity contours and isotherms (FEM) for $Re = 250$, $Mn = 0$.
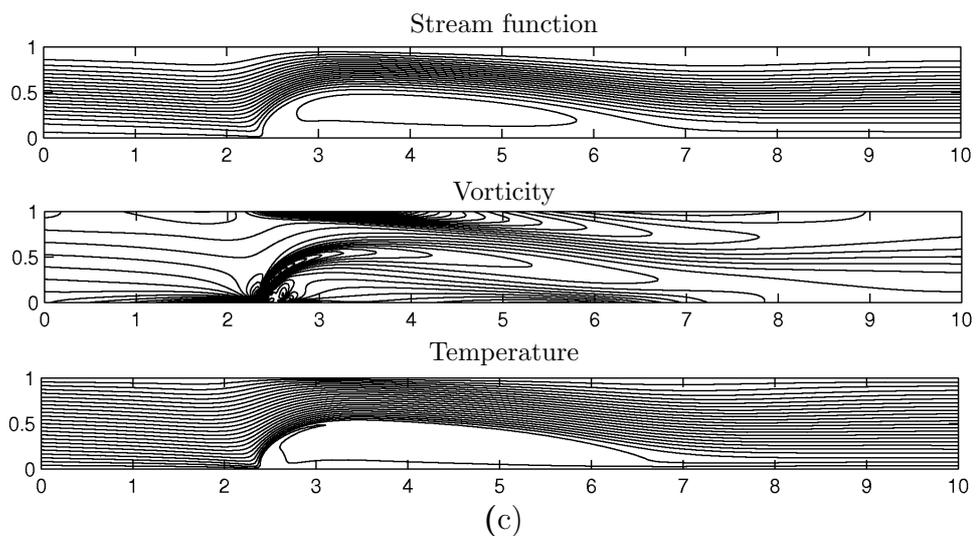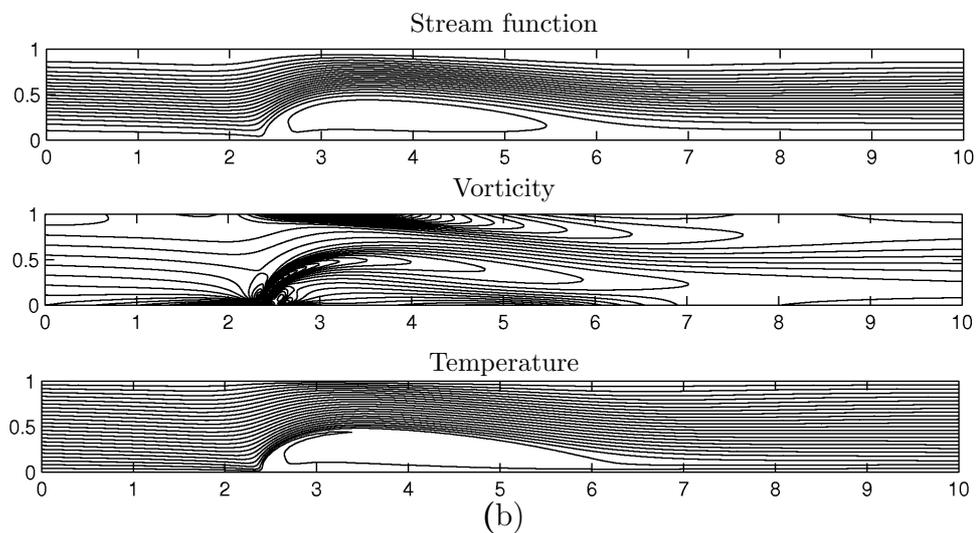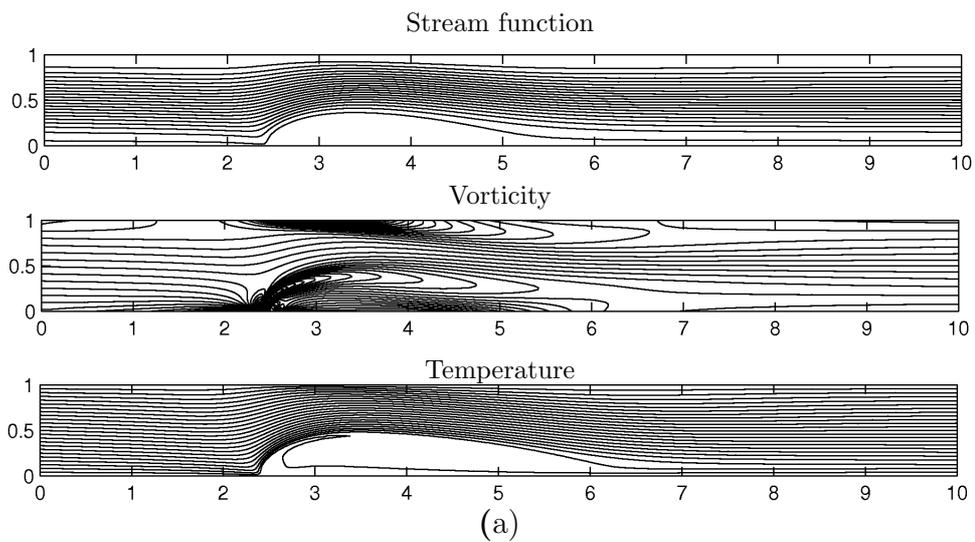
Figure 4.8: Problem 4.6.1: Effects of magnetic field on streamlines, vorticity contours and isotherms (FEM) for $Re = 250$, $(a)\,Mn = 115$, $(b)\,Mn = 215$, $(c)\,Mn = 315$.

In FEM solutions, as the characteristic behavior of the flow is expected to take place in the neighborhood of the magnetic source, this part of the channel, i.e. between $x = 2$ and $x = 6$, is discretized using more elements than the number of elements used outside where a linear flow profile is expected. Figure 4.6, illustrates a sample discretization of the problem domain using 480 elements. In the computations, the domain is discretized by using 3750 quadratic elements. The biomagnetic fluid is taken to be blood and hence, the characteristic parameters for a real blood flow are used which are $\bar{\rho} = 1050 kg/m^3$, $\bar{\mu} = 3.2 \times 10^{-3} kg/ms$, $\bar{u}_r = 3.81 \times 10^{-2}$. Thence, the corresponding Reynolds number under these conditions is taken as $Re = 250$, [47].

The numerical tests using FEM when $Re = 250$ are first performed in the absence of the magnetic field (biofluid flow) where $Mn = 0$ (Equations (4.6)), and the results are shown in Figure 4.7. The absence of the magnetic field effect results in a pure hydrodynamic flow, where all contours of the unknowns have a linear profile at steady-state, and this behavior can be depicted from Figure 4.7.

The effect of the externally applied magnetic field on the biomagnetic fluid flow is investigated via several test cases for Reynolds number $Re = 250$ with magnetic numbers $Mn = 115$, $Mn = 215$ and $Mn = 315$. When Reynolds number and the temperature difference between the upper plate and lower plate are fixed, increasing the magnetic number is equal to increasing the magnetic field strength applied at the point (a, b). Figure 4.8 shows this effect on the streamlines, vorticity contours and isotherms for (a) $Mn = 115$, (b) $Mn = 215$ and (c) $Mn = 315$. As it can be seen from the figure, a vortex is formed in the region around the magnetic source in stream function, vorticity and temperature contours. Moreover, it is observed that near the magnetic source, the lengths of the vortices extend horizontally along the lower plate and the temperature values increase due to an increase in Mn. In all cases, stream function, vorticity and temperature contours are affected close to the magnetic source region. However, as the strength and effect of the magnetic field decreases towards the exit of the channel, the contours regain their inlet profile.

4.6.2 Unsteady biomagnetic fluid flow in a straight channel

In this problem, the biomagnetic fluid flow and heat transfer problem is solved in a straight channel, where the fluid is considered as electrically nonconducting as in the previous problem. The governing equations given in (4.3) are accompanied with the boundary conditions, (see Figure 4.9)

$$\begin{aligned}
&\psi(0, y) = 2y^2 - (4/3)y^3, \psi(x, 0) = 0, \psi(x, 1) = 2/3 \\
&T(0, y) = y, T(x, 0) = 0, T(x, 1) = 1, \\
&w(0, y) = 8y - 4, \\
&\frac{\partial \psi}{\partial x} = 0, \frac{\partial T}{\partial x} = 0, \frac{\partial w}{\partial x} = 0, \quad x = 10.
\end{aligned} \quad (4.37)$$

The FEM discretized equations (4.27) given in Section 4.4 are solved by the procedure introduced in the same section. In the numerical simulations, $Pr = 25$, $Ec = 7.43 \times 10^{-7}$, $\varepsilon = 9$ are taken as in [76], and the magnetic source is placed at the point $(a, b) = (3, -0.05)$. In the numerical tests, the magnetic number values are taken as $Mn = 1312$, 5250, 32813 and 131250, and the corresponding Reynolds number values are taken as $Re = 100$, 50, 20 and 10, respectively. In the problem region discretization, $M_e = 4250$ quadratic triangular elements are used for $Mn = 1312$, 5250, and $M_e = 5250$ elements are used for $Mn = 32813$, 131250. The time step for $Mn = 1312$, 5250, and 32813 cases, is taken as $\Delta t = 10^{-3}$, whereas, for the highest magnetic number $Mn = 131250$, $\Delta t = 10^{-4}$ is taken in the computations.
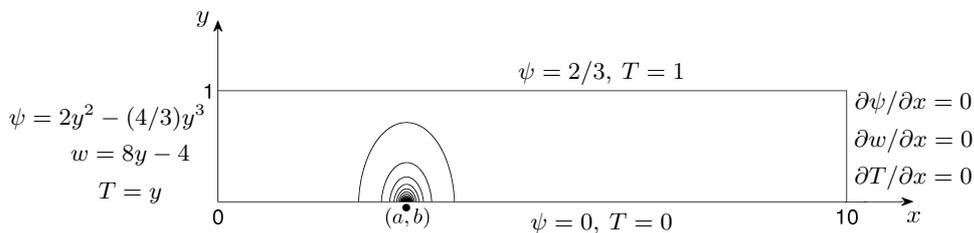

Figure 4.9: Domain configuration and boundary conditions for Problem 4.6.2.

Figure 4.10 shows the effect of the magnetic field on the streamlines, vorticity contours and isotherms at transient levels $(a)\, t = 0.2$ and $(b)\, t = 1.0$, and finally at steady-state $(c)\, t = 5$ for $Re = 100$ and $Mn = 1312$. It is seen that, at the very early stage when $t = 0.2$ a small vortex is formed in the close neighborhood of the nodal magnetic source for both stream function and temperature. In addition, a deformation around the magnetic source occurs in the vorticity behavior. The resulting vortex extends horizontally up to $x = 6$ with a time advance and the flow settles down at approximately $t = 5$ where the steady-state is reached according to the present convergence parameter, $(\tau = 10^{-6})$.

Figure 4.11 illustrates the steady-state profiles of streamlines, vorticity contours and isotherms for (a) $Mn = 5250$, (b) $Mn = 32813$ and (c) $Mn = 131250$. It is observed that the vortex formation also takes place close to the point where the nodal magnetic source is located for all these magnetic numbers. In addition to this vortex, a smaller vortex arises in the region between the entrance of the channel and the magnetic source point near the upper plate. An increase in the density of these vortices is observed as the magnetic number increases. The temperature of the fluid remains low around the magnetic source and close to the lower wall which is kept cold in the present problem. The temperature is higher in the region between the entrance and the point where the magnetic source is placed, and it increases more towards the upper wall which is heated. It is seen from the figures that this variation increases as well when Mn increases. The streamlines, vorticity and temperature contours are gaining their entrance profiles towards the exit of the channel where the effect of the magnetic field is diminishing.
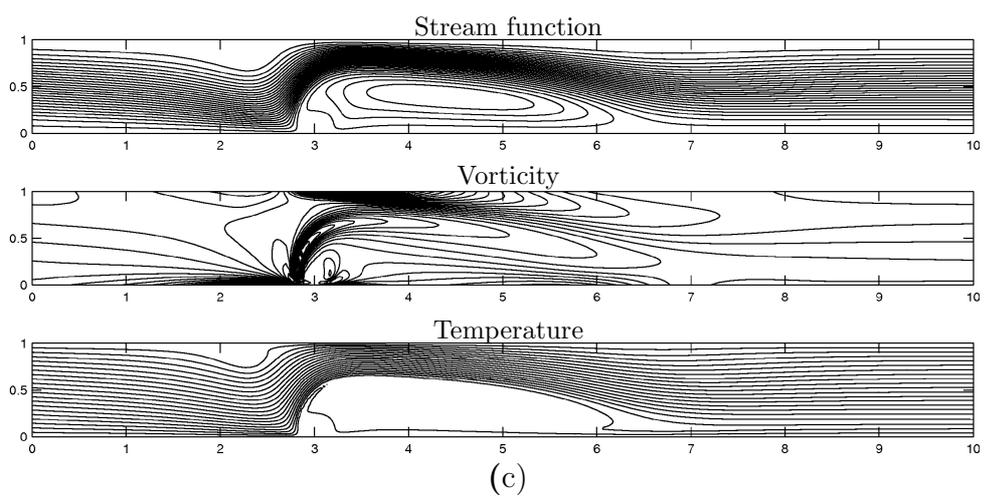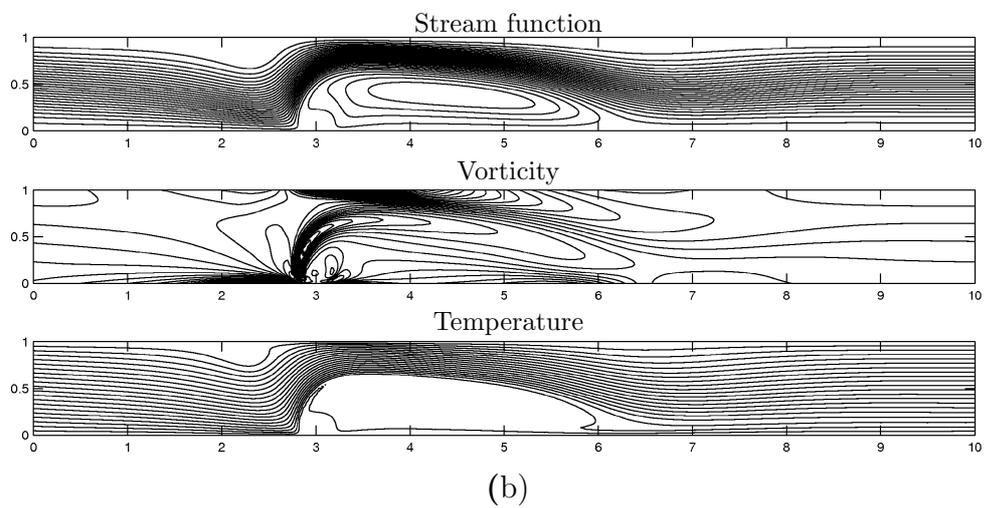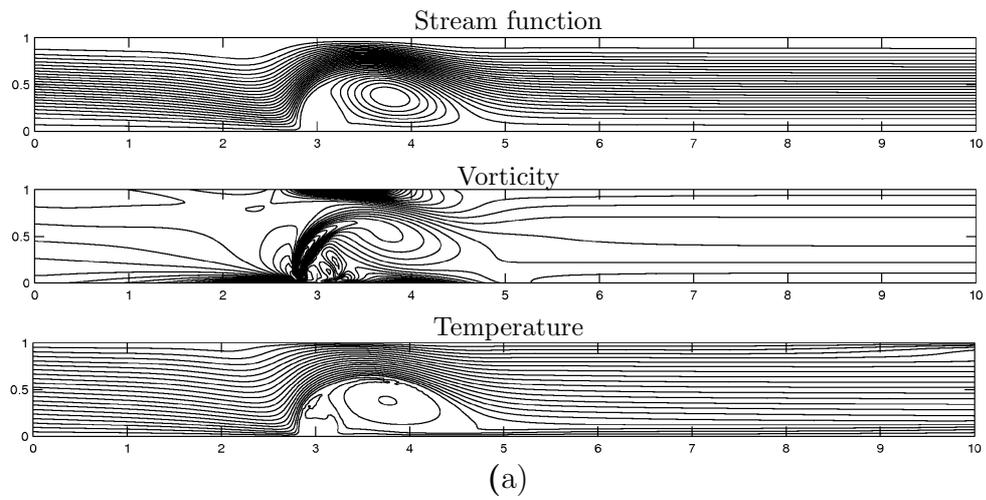
124

Figure 4.10: Problem 4.6.2: Time evaluation of stream function, vorticity and temperature contours for $Re = 100$, $Mn = 1312$ when (**a**) $t = 0.2$, (**b**) $t = 1.0$, (**c**) $t = 5.0$.
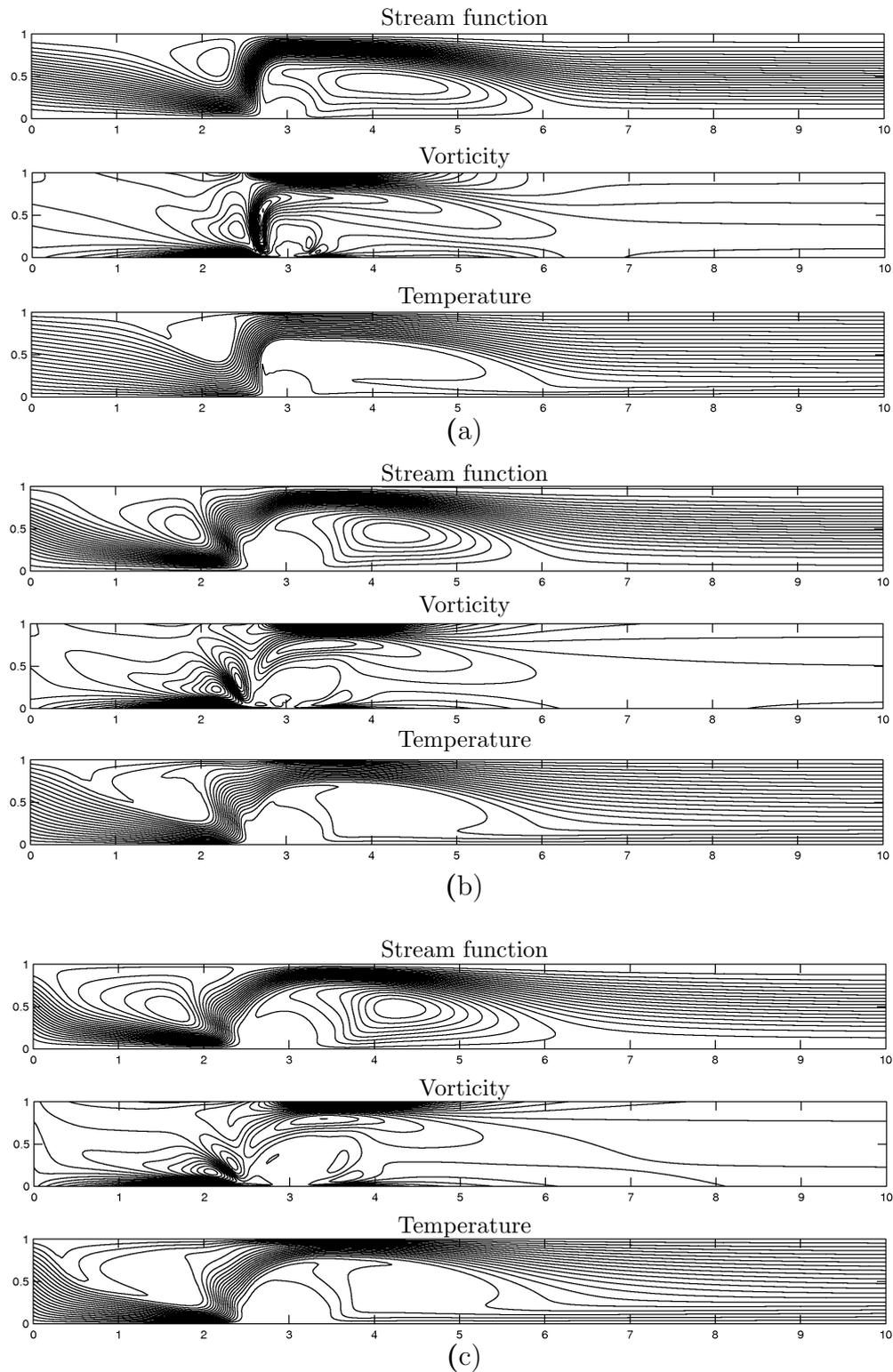
Figure 4.11: Problem 4.6.2: Stream function, vorticity contours and isotherms for (**a**) $Re = 50$, $Mn = 5250$, (**b**) $Re = 20$, $Mn = 32813$, (**c**) $Re = 10$, $Mn = 131250$.

4.6.3 Unsteady biomagnetic electrically conducting fluid flow in a straight channel

The electrically conducting biomagnetic fluid flow and heat transfer governed by Equations (4.1) is considered first in a straight channel in this problem. The FEM model (4.31) developed in Section 4.5 is solved by the iterative procedure described in the same section. The boundary conditions are as follows

$$
\begin{aligned}
&\psi(0,y) = 2y^2 - (4/3)y^3, \psi(x,0) = 0, \psi(x,1) = 2/3, \\
&T(0,y) = 4y(1-y), T(x,0) = 0, T(x,1) = 0, \\
&w(0,y) = 8y - 4,
\end{aligned}
\tag{4.38}
$$

together with the zero derivative conditions at the exit. The vorticity wall conditions are calculated by the method of Section 4.1. The problem domain with the boundary conditions together with the magnetic field contours are visualized in Figure 4.12.
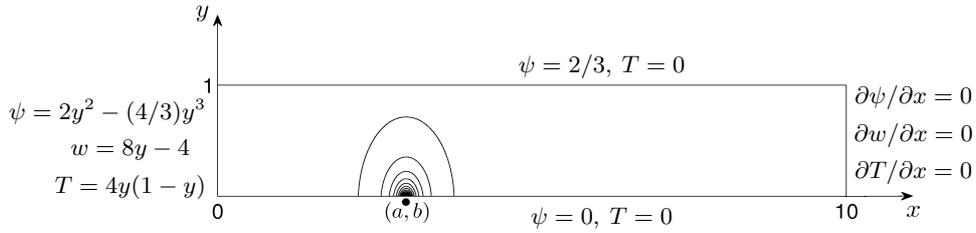

Figure 4.12: Domain configuration and boundary conditions for Problem 4.6.3.

The physical parameters are taken suitable to the real blood flow as $Pr = 25$, $Ec = 1.49 \times 10^{-8}$ and $\varepsilon = 77.5$ in the numerical simulations. The nodal magnetic source is placed at the point $(a,b) = (3, -0.05)$. Since the characteristic behavior of the flow is expected to take place around the region near the magnetic source, this region, where $2 \leq x \leq 6$, is discretized using more elements than used in other parts of the problem domain as in Problem 4.6.2. The numerical results presented in this section are obtained using $M_e = 2800$ quadratic triangular elements and $\Delta t = 0.001$ as time increment. The steady-state parameter is taken as $\tau = 10^{-6}$.

The streamlines, vorticity contours and isotherms for (a) $Mn_F = 82$, $Mn_M = 0.025$ and (b) $Mn_F = 164$, $Mn_M = 0.1$ are shown in Figure 4.13 where Reynolds number is fixed, $Re = 100$. As can be depicted from the figure, the effect of the magnetic field, similar to the previous cases, is the vortex formation in streamlines, equivorticity lines and isotherms. An increase in Mn, causes the vortices in all contours to extend in both directions, and as a consequence, the recirculation of the flow expands downstream of the channel. The temperature of fluid in the vortex region decreases to the temperature of the lower plate which has a zero temperature boundary condition. At the exit of the channel, as in the previous problems, the streamlines, vorticity contours and isotherms gain their inlet profile as the effect of the magnetic field is diminishing.
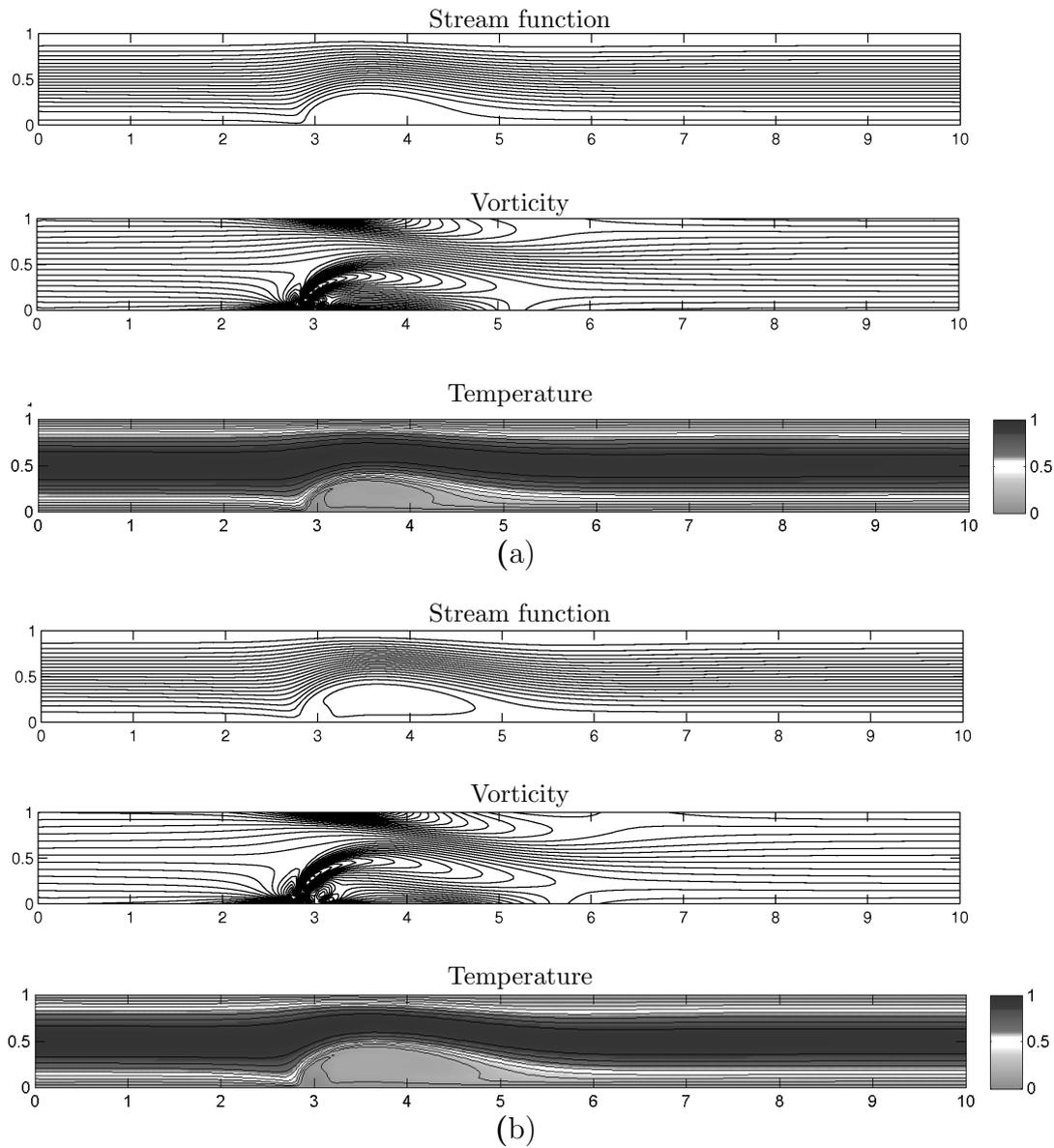
Figure 4.13: Problem 4.6.3 Effects of magnetic field on streamlines, vorticity contours and isotherms for $Re = 100$ (**a**) $Mn_F = 82$, $Mn_M = 0.025$, (**b**) $Mn_F = 164$, $Mn_M = 0.1$.

4.6.4 Unsteady biomagnetic fluid flow in a symmetrically stenosed channel

This section presents the biomagnetic fluid flow of an electrically conducting fluid and heat transfer in a symmetrically stenosed channel. The governing equations are given in (4.1) and the FEM model (4.31) developed in Section 4.5 is solved iteratively. The characteristic parameters are taken as in Problem 4.6.3, where $Pr = 25$, $\varepsilon = 77.5$ and $Ec = 1.49 \times 10^{-8}$. The convergence tolerance is set to be $\tau = 10^{-6}$ to achieve the steady-state. The problem domain boundaries are

defined by the functions

$$y_1(x) = A_1 \sec h(6(x - x_1)), \quad 0 \le x \le 10,$$

$$y_2(x) = 1 - A_2 \sec h(6(x - x_2)), \quad 0 \le x \le 10$$

for lower and upper plates, respectively. The positive constants A_1, A_2 control the degree of constriction of the channel, and B_1, B_2 are the constants controlling the length of the stenosed area. The positions of major constrictions at the lower and the upper plates are demonstrated by x_1 and x_2, respectively [75]. The boundary conditions are given by

Inflow $(x = 0, \quad 0 \le y \le 1)$
$\psi = 2y^2 - (4/3)y^3, \quad T = 4y(1 - y), \quad \omega = 8y - 4$

Outflow $(x = 10, \quad 0 \le y \le 1)$
$\dfrac{\partial \psi}{\partial x} = \dfrac{\partial T}{\partial x} = \dfrac{\partial \omega}{\partial x} = 0$

(4.39)

Lower plate $(y = y_1(x), \quad 0 \le x \le 10)$
$\psi = 0, \quad T = 0$

Upper plate $(y = y_2(x), \quad 0 \le x \le 10)$
$\psi = 2/3, \quad T = 0,$

and the required vorticity boundary conditions are derived by the method presented in Section 4.1. In the test problems, the computational domain is determined by taking $B_1 = B_2 = 6$, and $x_1 = x_2 = 3$. The numerical simulations are carried out first for the straight channel ($A_1 = A_2 = 0$), and then for the channel with the 40% degree of stenosis ($A_1 = A_2 = 0.2$) and 60% degree of stenosis ($A_1 = A_2 = 0.3$) to see the effect of the constriction on the fluid flow. Thus, the resulting channel is symmetrically constricted. The nodal magnetic source is placed at $(a, b) = (3.3, -0.05)$. The symmetrically stenosed channel (a representative 60% degree of stenosis) with boundary conditions and the resulting magnetic field contours are shown in Figure 4.14.
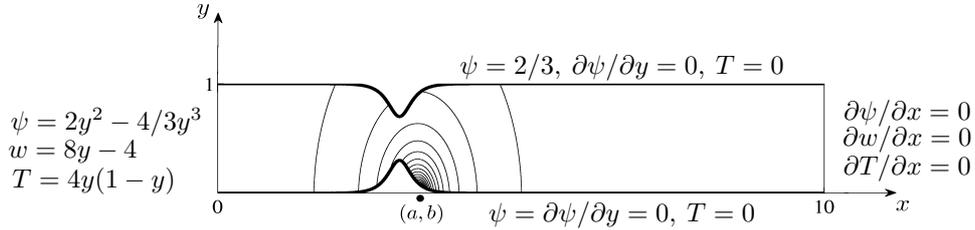

Figure 4.14: Symmetrically stenosed channel and the boundary conditions for Problem 4.6.4.

The characteristic behavior of the flow for the present case, is expected to take place in the neighborhood of the magnetic source and/or constriction. Therefore, the region around the magnetic source and/or constriction, i.e. between $x = 2$

and $x = 6$, is discretized using more elements than the number of elements used outside this region where a fully-developed flow profile is expected. Figures 4.15 and 4.16 show sample discretizations for 40% and 60% stenosed channels respectively, using 1088 elements. The domain is discretized by using 4352 quadratic triangular elements in the numerical simulations.
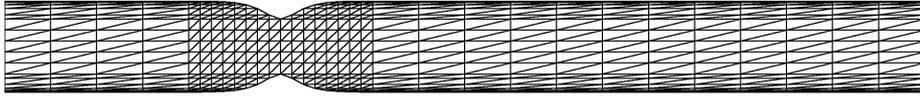

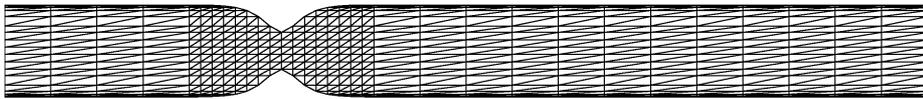Figure 4.15: A sample discretization of channel with 40% stenosis for Problem 4.6.4.

Figure 4.16: A sample discretization of channel with 60% stenosis for Problem 4.6.4.

Figures 4.17 and 4.18 display the fluid flows through the channels with stenosis of degrees 40% and 60%, respectively, for the biofluid flow (Equations (4.5)) (a) $Mn_F = Mn_M = 0$, and the biomagnetic flows (b) $Mn_F = 82$, $Mn_M = 0.025$, (c) $Mn_F = 164$, $Mn_M = 0.1$. It can be seen from Figures 4.17(a)-4.18(a) that the stream function, vorticity, and temperature behaviors are distorted from being straight lines due to the stenosis. The formation of two symmetric vortices downstream of the stenosis is noticed in the vorticity contours, whereas small deviations occur after the stenosis in both streamlines and temperature contours. On the other hand, in the absence of magnetic source as the degree of stenosis increases, the density and the extend of the vortices increase. Moreover, the increase in the degree of stenosis leads to the formation of two symmetric vortices downstream of the stenosis not only in the vorticity but also in the streamlines. When a magnetic source is placed close to stenosed area under the lower plate, a vortex formation is also observed immediately after the stenosed area in both streamlines and temperature profiles as in the case with no stenosis. In addition, the length of this vortex enlarges through the lower plate following an increase in both the intensity of the magnetic field and the degree of the stenosis for streamlines and isotherms. When the vorticity profile under the influence of a magnetic source is compared with the pure hydrodynamic flow case, it is observed that the presence of a magnetic source breaks the symmetry in the formation of vortices emanating from the stenosed area. That is, the lower vortex extends vertically due to the magnetic source in both 40% and 60% of stenosis cases. Thus, the upper vortices in the profiles of streamlines and isotherms shrink following the increase in the strength of the magnetic field for the case with 60%-stenosis. Moreover, the temperature values remain constant in the core of the vortices in all cases. The maximum temperature value is shifted towards the upper plate following the formation of a vortex in the magnetic source region as the intensity of the magnetic field increases.

Figure 4.17: Problem 4.6.4: Streamlines, vorticity contours and isotherms 40% stenosis for $Re = 100$, (**a**) $Mn_F = Mn_M = 0$, (**b**) $Mn_F = 82$, $Mn_M = 0.025$, (**c**) $Mn_F = 164$, $Mn_M = 0.1$.

In the case with 60%-stenosis, the simulations are carried for higher values of magnetic numbers $Mn_F = 656$, $Mn_M = 1.2$ and $Mn_F = 1312$, $Mn_M = 6.4$ (see Figure 4.19). As it is expected, an increase in the intensity of the magnetic field results in an extension of vortex along the lower plate. In all cases, the streamlines, vorticity contours and isotherms regain the entrance profiles at the downstream of the channel, away from the stenosed area and magnetic source, through the exit of the channel. These results are in good agreement with the results in the work of Tzirtzilakis [75].

Figure 4.18: Problem 4.6.4: Streamlines, vorticity contours and isotherms 60% stenosis for $Re = 100$, (**a**) $Mn_F = Mn_M = 0$, (**b**) $Mn_F = 82$, $Mn_M = 0.025$, (**c**) $Mn_F = 164$, $Mn_M = 0.1$.

The time evolution for the stream function, vorticity and temperature is investigated for the case of 60%-stenosis, when $Re = 100$ and $Mn_F = 82$, $Mn_M = 0.025$. The results in terms of the contours of the unknowns are shown in Figure 4.20. It is observed that the vortex formed close to lower plate is elongated horizontally as time advances until the flow settles down at approximately $t = 3$.
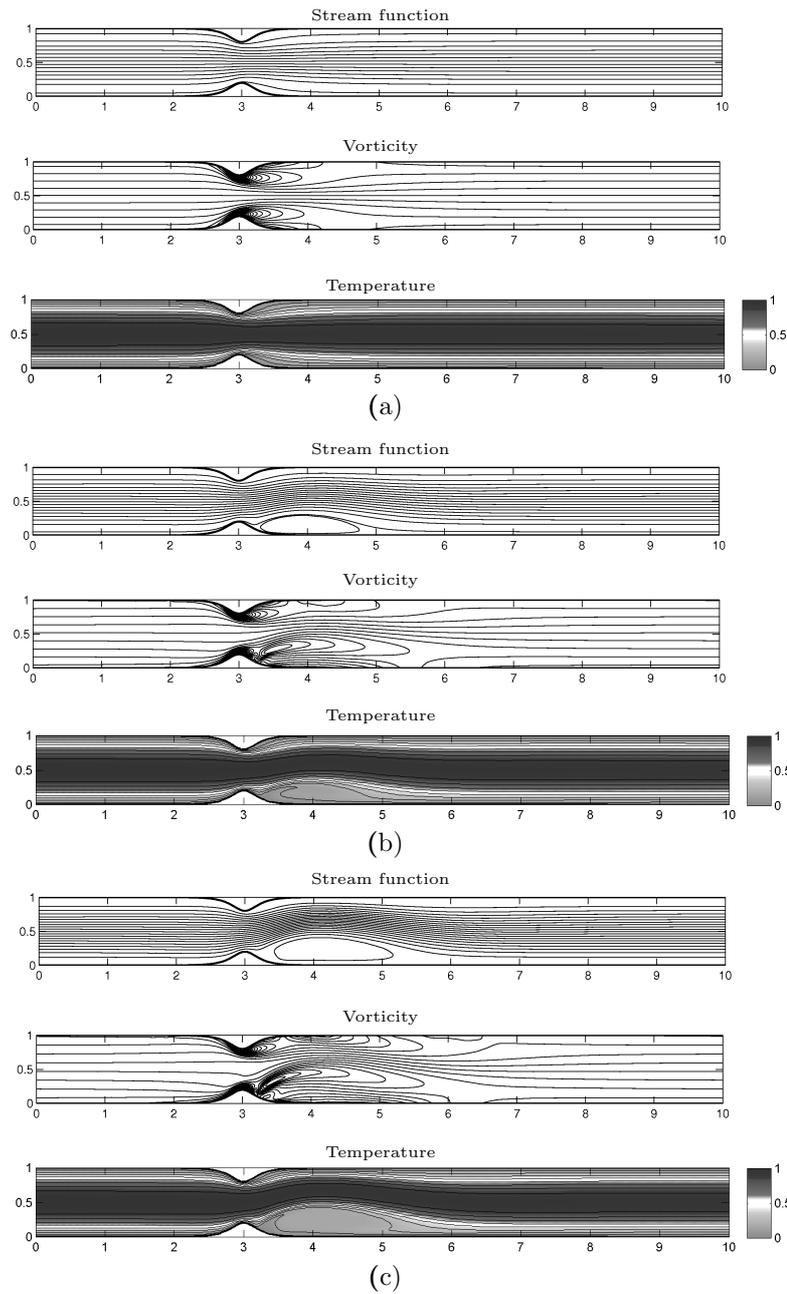
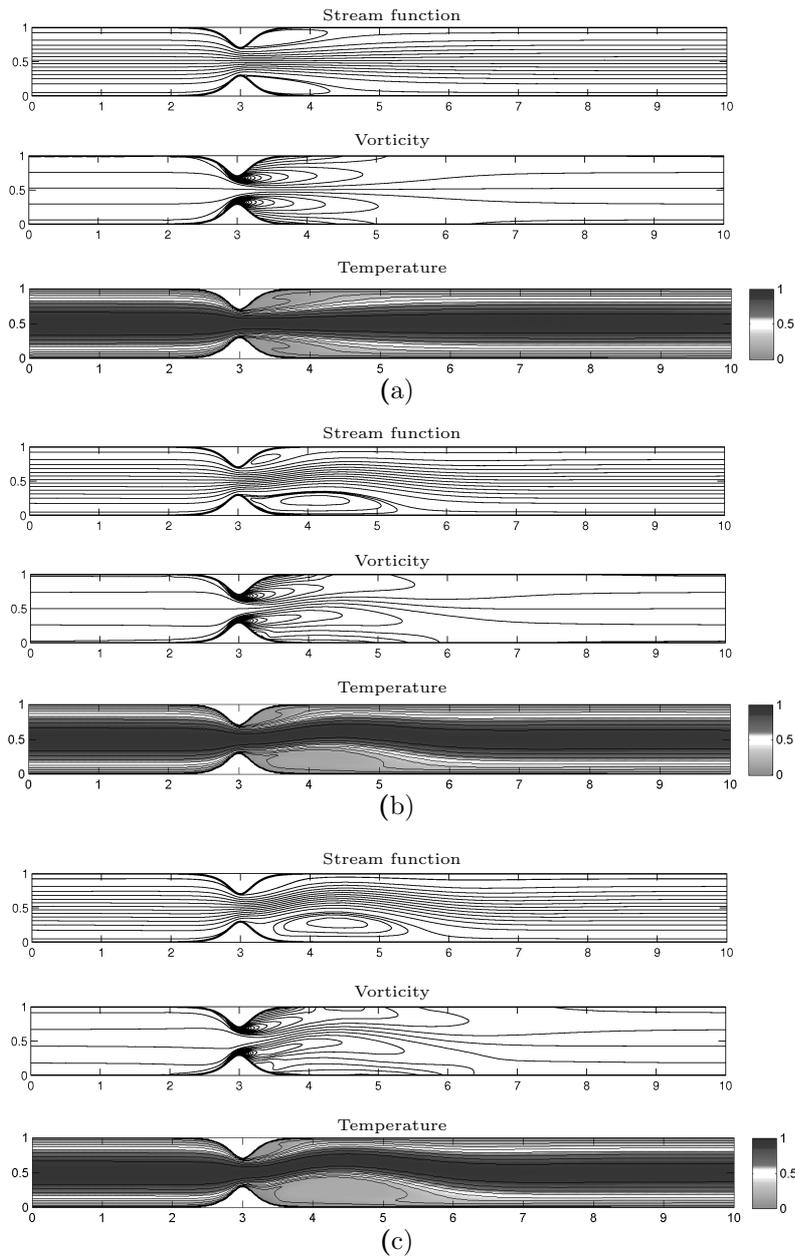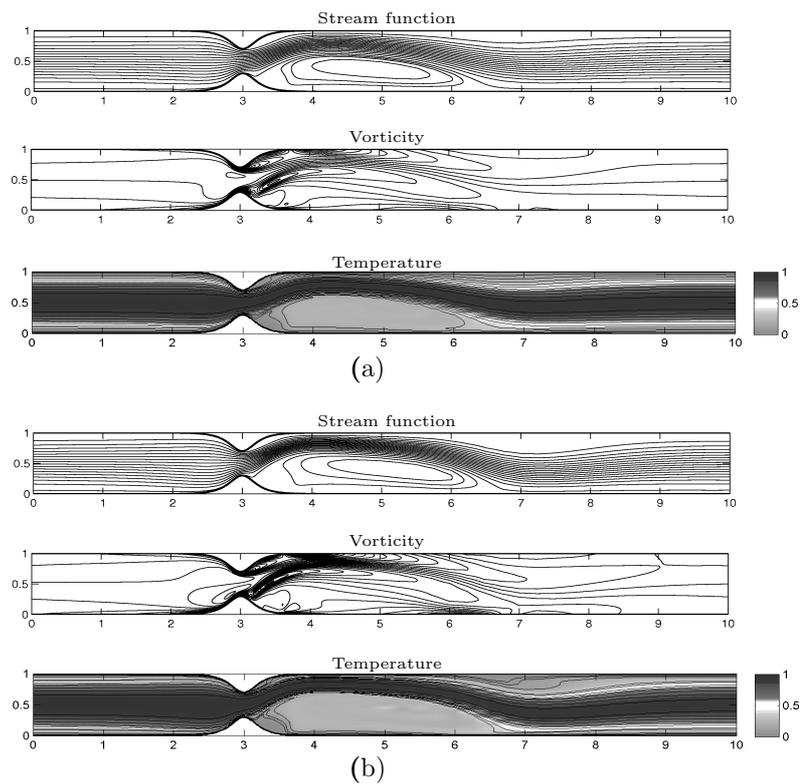Figure 4.19: Problem 4.6.4: Streamlines, vorticity contours and isotherms 60% stenosis for $Re = 100$, (**a**) $Mn_F = 656$, $Mn_M = 1.2$, (**b**) $Mn_F = 1312$, $Mn_M = 6.4$.
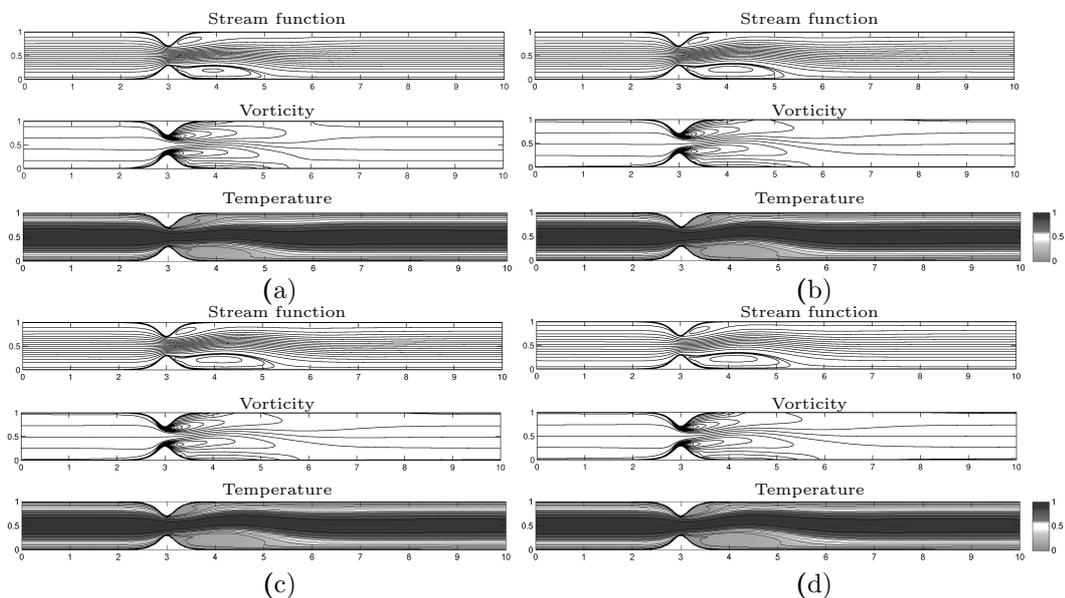

Figure 4.20: Problem 4.6.4: Time evolution for the streamlines, vorticity contours and isotherms, 60% stenosis, for $Re = 100$, $Mn_F = 82$, $Mn_M = 0.025$: (**a**) $t = 0.4$, (**b**) $t = 1.0$, (**c**) $t = 1.25$, (**d**) $t = 3.0$.

133

4.6.5 Unsteady biomagnetic fluid flow in an unsymmetrically stenosed channel

In this problem, the numerical simulations for the biomagnetic fluid flow under the influence of an externally applied magnetic field (Equations (4.1)) are carried out in a channel with an unsymmetrical stenosis. The computational domain is considered to have a severe stenosis with an unsymmetrical structure. Consequently, the lower and upper walls of the channel are defined as in Problem 4.6.4

$$y_1(x) = A_1 \sec h(B_1(x - x_1)), \ 0 \le x \le 10$$

and

$$y_2(x) = 1 - A_2 \sec h(B_2(x - x_2)), \ 0 \le x \le 10,$$

respectively. In the present test problem, however, the constants which control the degree of constriction of the channel are taken as $A_1 = 0.55$, $A_2 = 0.35$, whereas the constants controlling the length of the stenosed area are taken as $B_1 = 6$, $B_2 = 10$. The positions of the major constrictions at the lower and the upper plates are determined by $x_1 = 2$ and $x_2 = 2.5$. The computational domain for the given parameters is shown together with the magnetic field intensity H contours applied at $(3, -0.05)$, in Figure 4.21. The boundary conditions are given by

$$\begin{aligned} &\text{Inflow } (x = 0, \ \ 0 \le y \le 1) \\ &\psi = 2y^2 - (4/3)y^3, \ \ T = 4y(1-y), \ \ \omega = 8y - 4 \\[2mm] &\text{Outflow } (x = 10, \ \ 0 \le y \le 1) \\ &\frac{\partial \psi}{\partial x} = \frac{\partial T}{\partial x} = \frac{\partial \omega}{\partial x} = 0 \\[2mm] &\text{Lower plate } (y = y_1(x), \ \ 0 \le x \le 10) \\ &\psi = 0, \ \ T = 0 \\[2mm] &\text{Upper plate } (y = y_2(x), \ \ 0 \le x \le 10) \\ &\psi = 2/3, \ \ T = 0. \end{aligned} \tag{4.40}$$

The FEM model (4.31) of Equations (4.1) with the imposition of the provided boundary conditions given in (4.40) is solved iteratively. The iterative procedure including the computation of the vorticity wall conditions described in Section 4.5.1 is followed. The time step is taken as $\Delta t = 0.001$, and the iterations are terminated when the steady-state conditions are satisfied where $\tau = 10^{-4}$. As the characteristic behavior of the flow is expected to take place in the neighborhood of the constriction, the region around the constriction $(1 \le x \le 3.5)$ is discretized using more elements than the number of elements used outside this region. A sample discretization of the problem region using $M_e = 948$ is illustrated in Figure 4.22, whereas, the presented results are obtained by using 9574 elements.

The numerical tests are firstly conducted for the biofluid flow governed by Equations (4.5), for $Re = 100$ ($Mn_F = Mn_M = 0$), in order to investigate the effect of the constriction on the flow dynamics. The streamlines, vorticity contours

134
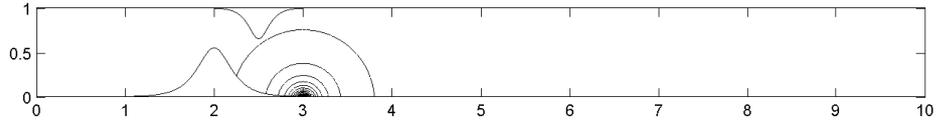
Figure 4.21: The magnetic field contours (channel with an irregular stenosis) for Problem 4.6.5.
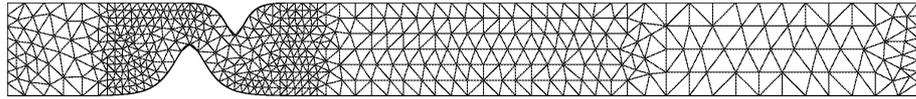
Figure 4.22: A sample discretization (channel with an irregular stenosis) for Problem 4.6.5.

and isotherms for this case are shown in Figure 4.23. It is well observed that the streamlines, vorticity contours and the isotherms are distorted from being straight lines in the region after the stenosis. A vortex following the circulation is formed downstream of the stenosis close to the upper wall in both streamlines and isotherm profiles. This physically indicates that fluid flow slows down after the constriction. Thus, the temperature of the fluid in the vortex region decreases to the temperature of the upper wall due to this circulation. On the other hand, the temperature is quite high close to the lower wall in the same region ($2.5 \leq x \leq 5$). On the other hand, the streamlines, vorticity contours and isotherms regain their inlet profiles towards the exit of the channel where the effect of the stenosis almost vanishes.
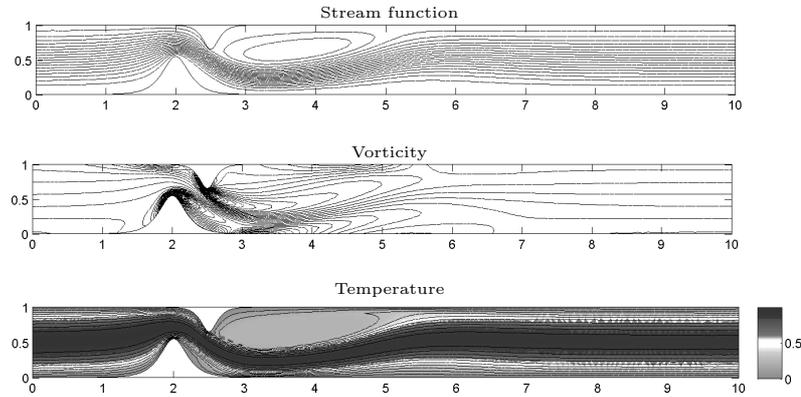
Figure 4.23: Problem 4.6.5: Streamlines, vorticity contours and isotherms, $Re = 100$, $Mn_F = 0$, $Mn_M = 0$.

Secondly, the effect of the location of the external nodal magnetic source on the flow field is investigated when $Mn_F = 82$, $Mn_M = 0.025$ by solving Equations (4.1) using FEM discretized Equations (4.31). The results are visualized in Figure 4.24 in terms of streamlines, vorticity contours and isotherms for (a) $a = 1$, (b) $a = 2.5$ and (c) $a = 3$. When the nodal magnetic source is placed at $(1, -0.05)$,

135
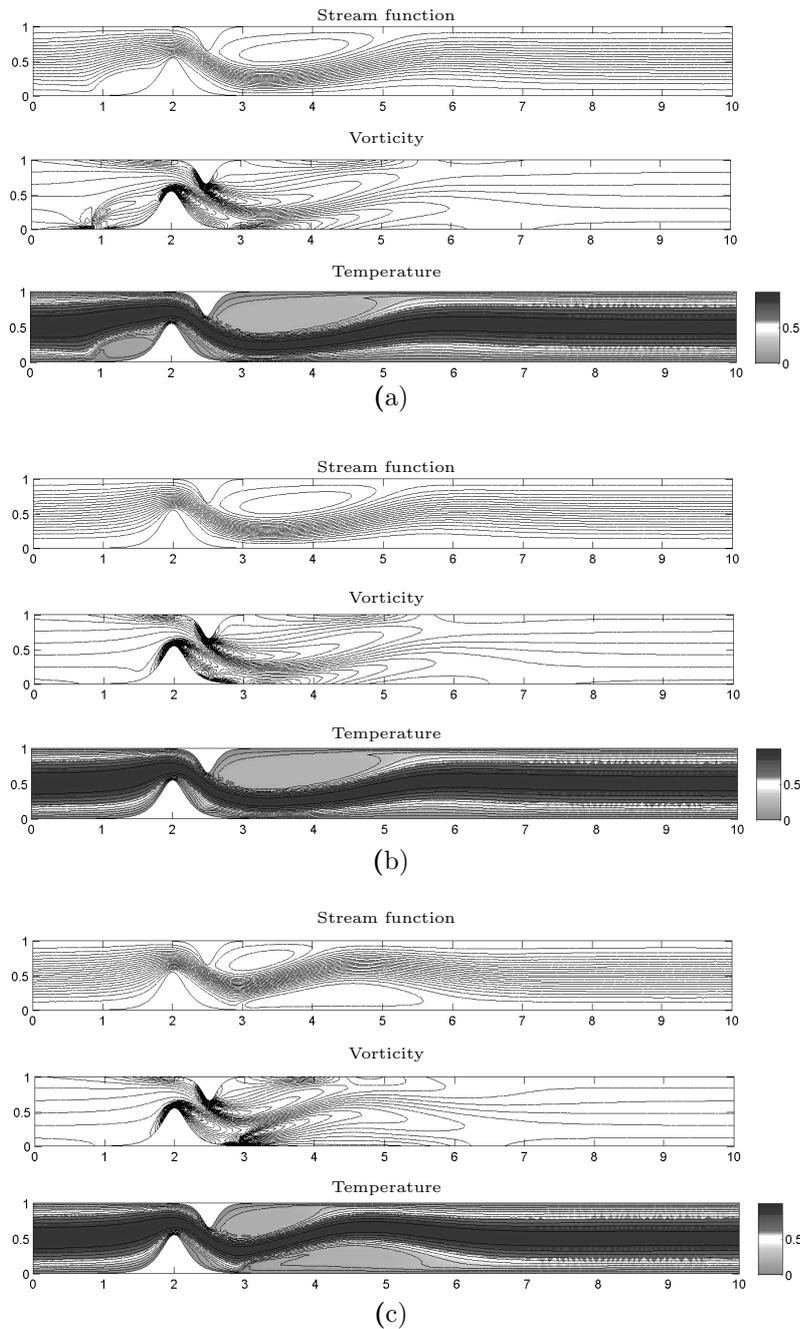
Figure 4.24: Problem 4.6.5: Streamlines, vorticity contours and isotherms for $Re = 100$, $Mn_F = 82$, $Mn_M = 0.025$, (**a**) $a = 1.0$, (**b**) $a = 2.5$, (**c**) $a = 3.0$.

it generates minor vortices in the contours of the unknowns, in the region before the stenosis. However, the flow shows the same behavior towards the downstream of the stenosis as in the case when $Mn_F = Mn_M = 0$. On the other hand, placing the magnet at $(2.5, -0.05)$ has no visible effect on the flow behavior when it is compared to the case of the pure hydrodynamic flow, since the effect of the magnetic field remains mainly outside of the problem domain. Finally, application of the magnetic field at the point $(3, -0.05)$ significantly alters the

136
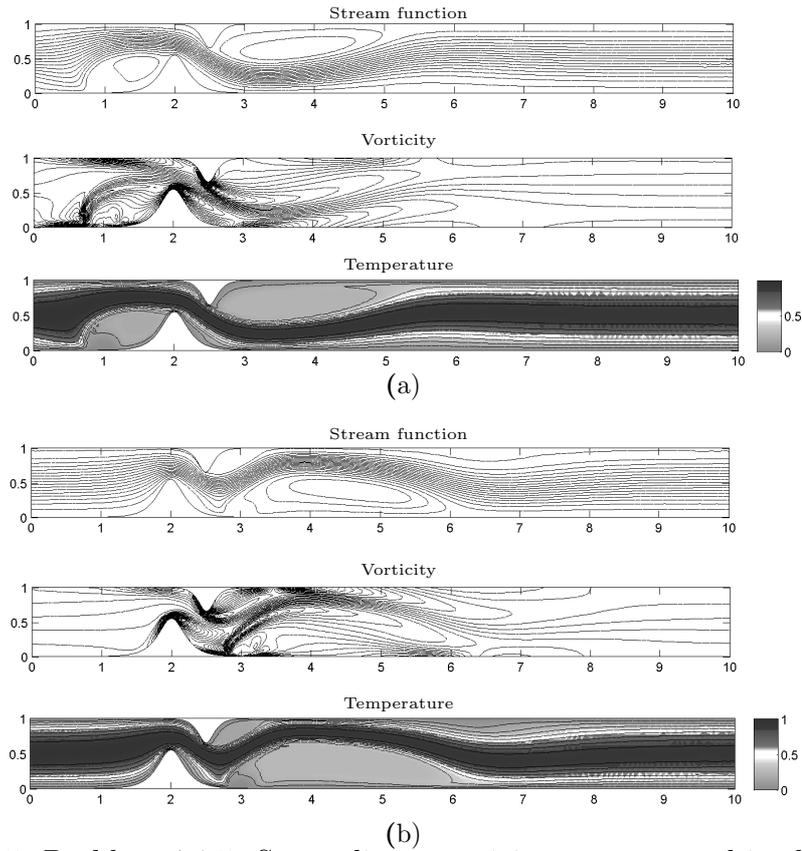
Figure 4.25: Problem 4.6.5: Streamlines, vorticity contours and isotherms, $Re = 100$, $Mn_F = 656$, $Mn_M = 1.2$: (**a**) $a = 1.0$, (**b**) $a = 3.0$.

flow field and the temperature distribution. The vortices close to upper wall in the pure hydrodynamic flow case are narrowed and shortened in length. In addition, formation of additional vortices is observed in streamlines and isotherms close to the lower wall where $3 \leq x \leq 6$. The problem is also solved for higher values of magnetic numbers, $Mn_F = 656$, $Mn_M = 1.2$, and the results are shown in Figure 4.25 for (a) $a = 1$ and (b) $a = 3$. When Figure 4.25(a) is compared with Figure 4.24(a), it is seen that increasing Mn_F, Mn_M results in extension, in both x- and y- directions, of the vortices prior to the stenosed region in the profiles of all unknowns, whereas the contours remain almost unchanged downstream of the stenosis. On the other hand, comparing Figure 4.25(b) and Figure 4.24(c) shows that the streamlines, vorticity contours and isotherms are notably affected with an increase in the magnetic numbers. That is, while the vortex formed along the lower plate extends in the y-direction towards the upper plate, the vortex occurred along the upper plate in the case when $Mn_F = 82$, almost vanishes with an increase in Mn_F value to 656.

In conjunction with the aforementioned results, the final test of the present problem is conducted for a fixed location of the magnetic source $(a, b) = (3, -0.05)$ in order to see the effect of increasing the magnetic numbers Mn_F and Mn_M on the flow behavior. Figure 4.26 shows the streamlines, vorticity contours and isotherms for (a) $Mn_F = 0$, $Mn_M = 0$, (b) $Mn_F = 82$, $Mn_M = 0.025$, (b) $Mn_F = 164$,

$Mn_M = 0.1$, and (d) $Mn_F = 656$, $Mn_M = 1.2$. As it is expected, the vortices in streamlines and isotherms formed due to application of magnetic field for the set of lowest values of magnetic numbers tested in this study ($Mn_F = 82$, $Mn_M = 0.025$), are extended in length and width as the magnetic numbers increase. This results in a rise of the fluid flow towards the upper wall. Moreover, the shifting effect of the magnetic field on the flow becomes stronger with an increase in magnetic numbers and hence, the vortices due to the stenosis which are close to the upper walls are narrowed down. Thus, the effect of the constriction on the resistance to the fluid flow decreases. In addition, the temperature close to the upper wall downstream of the stenosis increases by the shifted fluid flow in this region with an increase in magnetic effect. All streamlines, vorticity contours and isotherms are recovering their inlet profiles through the exit of the channel where the effects of both the stenosis and the magnetic source vanish.

4.6.6   Unsteady biomagnetic fluid flow in an multi-stenosed channel

The final test problem also deal with the biomagnetic fluid flow under the effect of an externally applied magnetic field which is governed by Equations (4.1). In the present case, the problem domain is taken as a channel with irregular multistenotic regions. Specifically, the channel first narrows down with a symmetric stenosis close to the entrance and recovers its initial width. Then, a severe constriction follows which is unsymmetrically spread in the middle of the channel. After the recovery of the second stenosis, the channel narrows down gradually so that the exit diameter is less than the entrance diameter. Thus, the lower and upper walls of the channel are defined by the formulas

$$y_1(x) = C_1 \left[1 - \cos(2\pi(x - D(x))/E(x))\right], \quad 0 \le x \le 10,$$

$$y_2(x) = 1 - C_2(x) \left[1 - \cos(2\pi(x - D(x))/E(x))\right], \quad 0 \le x \le 10,$$

respectively. Here, C_1 is a positive constant and taken as $C_1 = 0.075$. The piecewise-constant-valued functions C_2, D and E are defined as

$$C_2(x) = \begin{cases} 0.075, & \text{if } 5.8 < x \le 10 \\ 0.225, & \text{if } 3.2 < x \le 5.8 \\ 0.075, & \text{if } 0 \le x \le 3.2 \end{cases}, \quad D(x) = \begin{cases} 5.8, & \text{if } 5.8 < x \le 10 \\ 3.2, & \text{if } 3.2 < x \le 5.8 \\ 0, & \text{if } 0 \le x \le 3.2 \end{cases},$$

$$E(x) = \begin{cases} 7.2, & \text{if } 5.8 < x \le 10 \\ 2.6, & \text{if } 3.2 < x \le 5.8 \\ 3.2, & \text{if } 0 \le x \le 3.2 \end{cases}.$$

The resulting problem region can be seen in Figure 4.27.

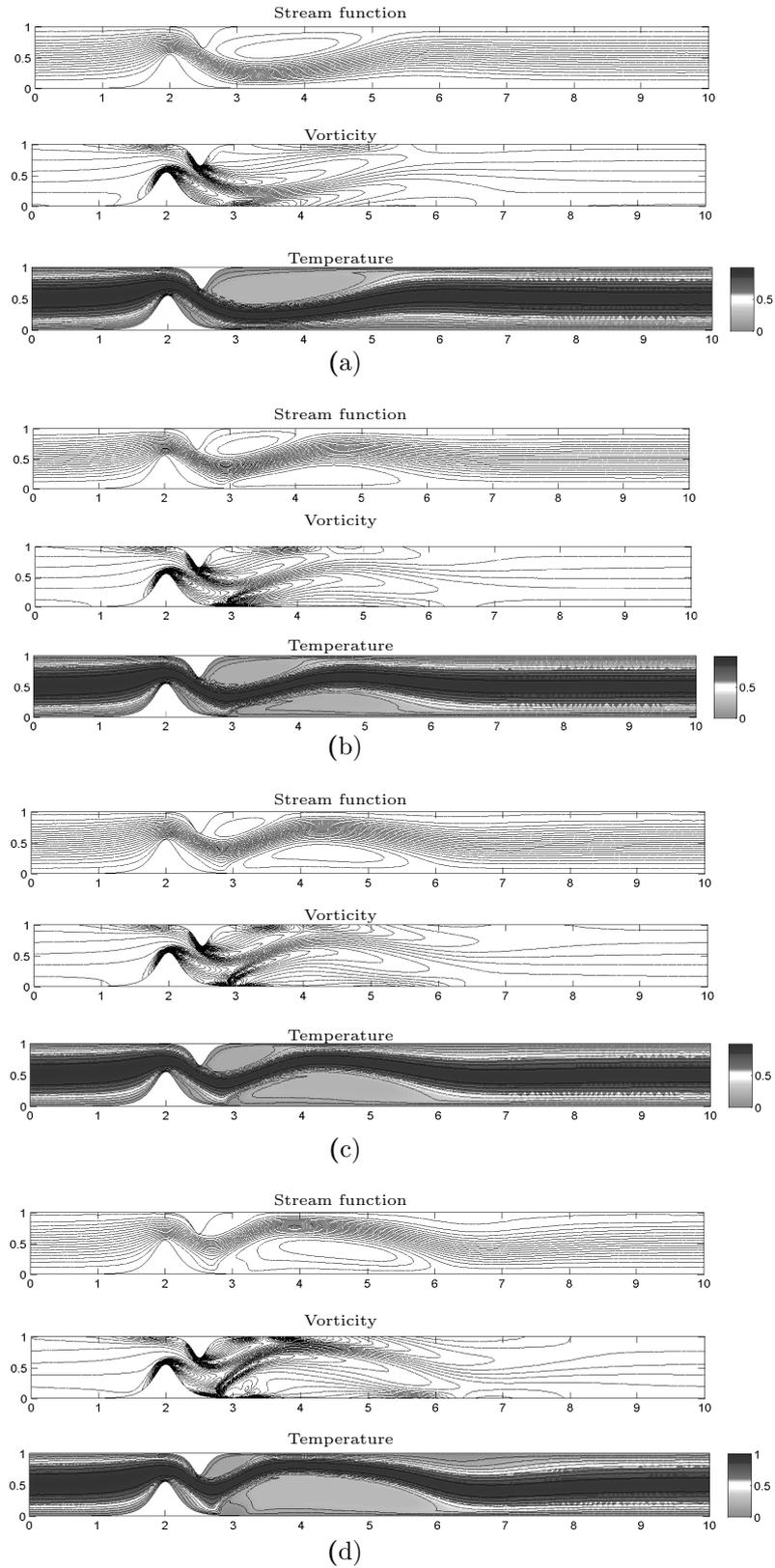Figure 4.26: Problem 4.6.5: Streamlines, vorticity contours and isotherms, $Re = 100$, $a = 3.0$: (**a**) $Mn_F = 0$, $Mn_M = 0$, (**b**) $Mn_F = 82$, $Mn_M = 0.025$, (**c**) $Mn_F = 164$, $Mn_M = 0.1$, (**d**) $Mn_F = 656$, $Mn_M = 1.2$.
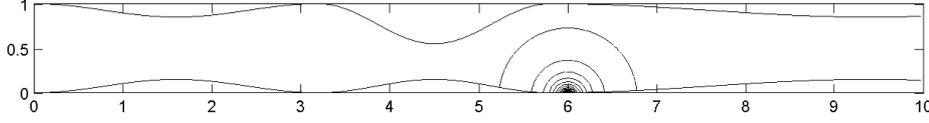
Figure 4.27: Multi-stenosed channel and the magnetic field contours for Problem 4.6.6.
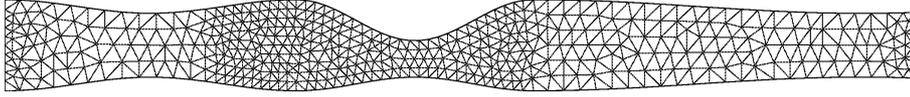
Figure 4.28: A sample discretization (multi-stenosed channel) for Problem 4.6.6.

The governing equations are accompanied by the boundary conditions

$$
\begin{aligned}
&\text{Inflow} \quad (x = 0, \quad 0 \le y \le 1) \\
&\psi = 2y^2 - (4/3)y^3, \quad T = 4y(1 - y), \quad \omega = 8y - 4 \\[6pt]
&\text{Outflow} \quad (x = 10, \quad 0 \le y \le 1) \\
&\frac{\partial \psi}{\partial x} = \frac{\partial T}{\partial x} = \frac{\partial \omega}{\partial x} = 0 \\[6pt]
&\text{Lower plate} \quad (y = y_1(x), \quad 0 \le x \le 10) \\
&\psi = 0, \quad T = 0 \\[6pt]
&\text{Upper plate} \quad (y = y_2(x), \quad 0 \le x \le 10) \\
&\psi = 2/3, \quad T = 0.
\end{aligned}
\tag{4.41}
$$

The iterative procedure described in Section 4.5.1 is followed for solving the FEM model (4.31), and the vorticity boundary conditions are accordingly calculated. The characteristic flow parameters, as in Problems 4.6.4 and 4.6.5, are taken suitable to the real blood flow, namely, $Pr = 25$, $\varepsilon = 77.5$, $Ec = 1.49 \times 10^{-8}$. In the computations, $M_e = 6970$ elements are used to discretize the problem region, where the majority of the elements are taken in the severe stenosis region. A sample discretizaion of the problem domain using 920 elements can be seen in Figure 4.28. The time step is taken as $\Delta t = 0.001$, and the steady-state solutions are reported when $\tau = 10^{-4}$.

The results of Problem 4.6.5 have proved that the flow is considerably affected when the magnetic source is placed closely after the stenosed region. Accordingly, in the present problem, the nodal magnetic source is placed after the major stenosed region, at $(a, b) = (6, -0.05)$ (see Figure 4.27).

Figures 4.29-4.31 present the streamlines, vorticity contours and isotherms, respectively, for (a) $Mn_F = 0$, $Mn_M = 0$, (b) $Mn_F = 82$, $Mn_M = 0.025$, (c) $Mn_F = 164$, $Mn_M = 0.1$, (d) $Mn_F = 656$, $Mn_M = 1.2$, and (e) $Mn_F = 1312$, $Mn_M = 6.4$. Figures 4.29 (a), 4.30 (a) and 4.31 (a) illustrate the effect of the constrictions in the channel on the pure hydrodynamic flow in the absence of the magnetic effect.

Figure 4.29: Problem 4.6.6: Streamlines for $Re = 100$: (**a**) $Mn_F = 0$, $Mn_M = 0$, (**b**) $Mn_F = 82$, $Mn_M = 0.025$, (**c**) $Mn_F = 164$, $Mn_M = 0.1$, (**d**) $Mn_F = 656$, $Mn_M = 1.2$, (**e**) $Mn_F = 1312$, $Mn_M = 6.4$.
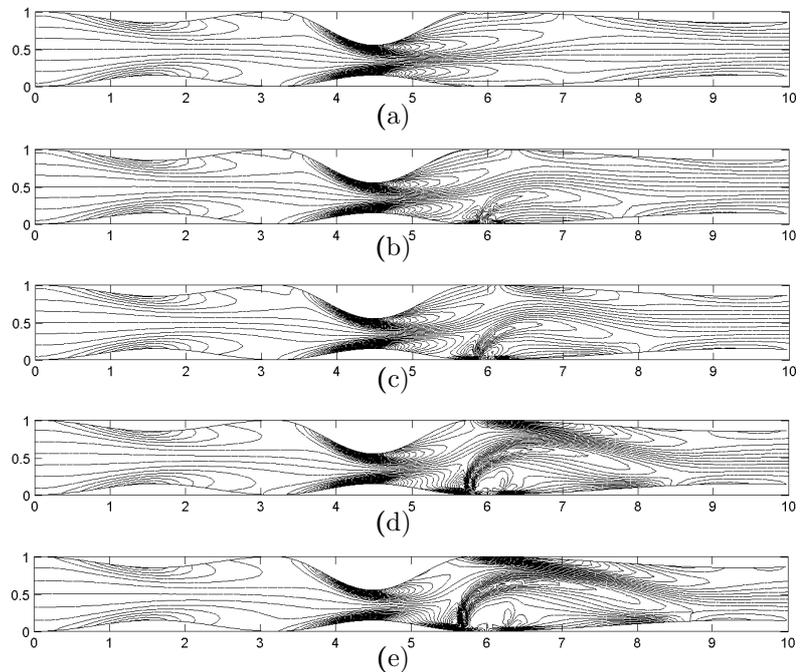
Figure 4.30: Problem 4.6.6: Vorticity contours for $Re = 100$: (**a**) $Mn_F = 0$, $Mn_M = 0$, (**b**) $Mn_F = 82$, $Mn_M = 0.025$, (**c**) $Mn_F = 164$, $Mn_M = 0.1$, (**d**) $Mn_F = 656$, $Mn_M = 1.2$, (**e**) $Mn_F = 1312$, $Mn_M = 6.4$.
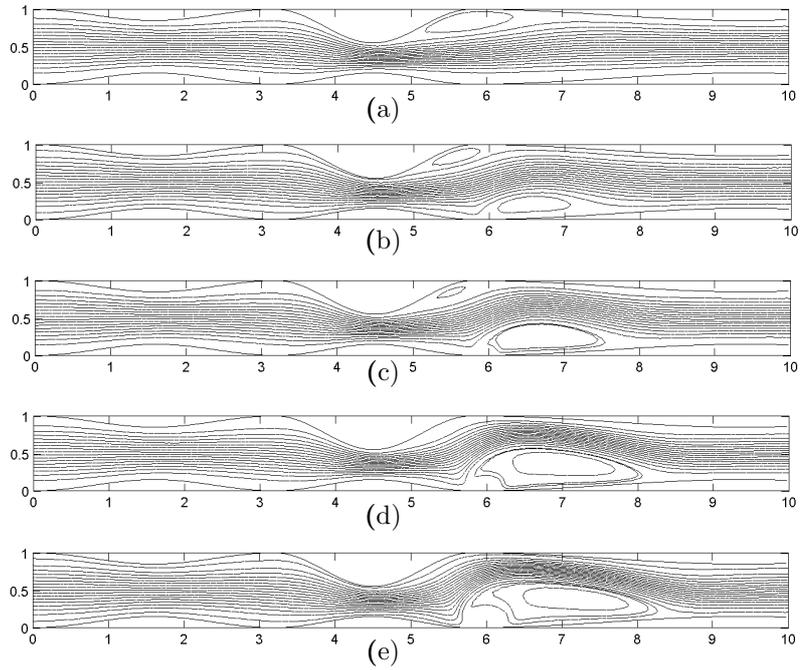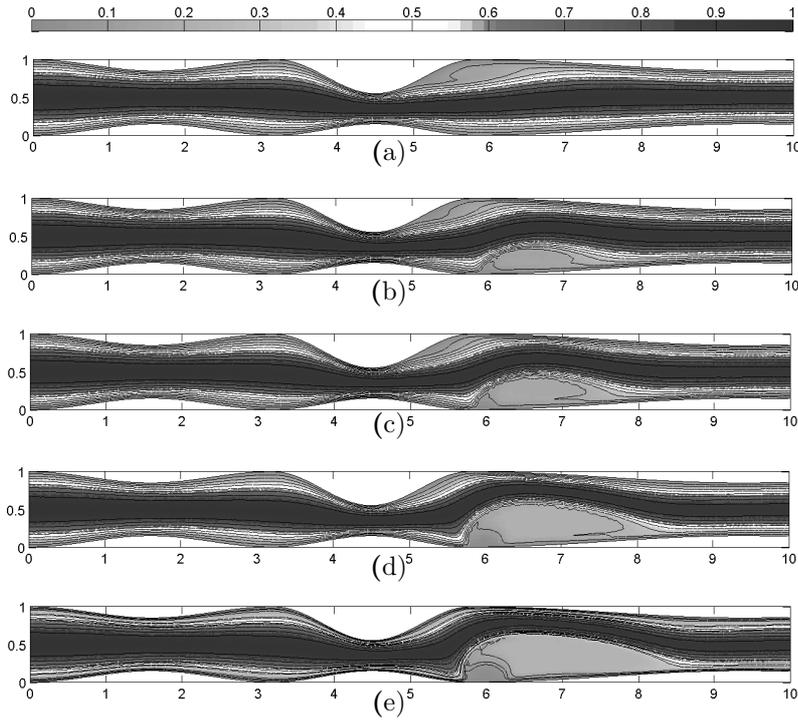
Figure 4.31: Problem 4.6.6: Isotherms for $Re = 100$: (**a**) $Mn_F = 0$, $Mn_M = 0$, (**b**) $Mn_F = 82$, $Mn_M = 0.025$, (**c**) $Mn_F = 164$, $Mn_M = 0.1$, (**d**) $Mn_F = 656$, $Mn_M = 1.2$, (**e**) $Mn_F = 1312$, $Mn_M = 6.4$.

As it can be seen from these figures, the inlet profiles of the streamlines and isotherms are sustained during the first mild stenosis. The distortion from being parallel lines is observed after the peak of the major stenosis. A vortex formation in both streamlines and isotherms is observed close to the upper wall downstream of the major stenotic region. The temperature has lower values in the vortex region compared to the center of the channel. The vorticity contours, on the other hand, are affected from the first narrowing down of the channel where a mild stenosis takes place. The circulation in the vorticity contours is close to the lower and upper walls, whereas the centerline contours remain parallel to the plates. A significant deformation after the major constriction region follows the reattachment of the vorticity contours. All streamlines, vorticity contours and isotherms are observed to regain their parallel profiles concordant with the narrowing down exit conditions. Application of a magnetic field affects the flow behavior even for low magnetic numbers ($Mn_F = 82$, $Mn_M = 0.025$) especially noticed in streamlines and isotherms (see Figures 4.29(b) , 4.30(b) and 4.31(b)). The presence of a magnetic source results in a vortex formation close to the lower wall where magnetic source is placed. As expected, similar behavior in streamlines, vorticity contours and isotherms is observed around the magnetic source region as the magnetic numbers increase. The vortices close to the lower wall enlarge with an increase in the magnetic numbers and hence, as a result of the shifting effect, the vortex close to upper wall diminishes for higher values of magnetic numbers ($Mn_F = 656$, $Mn_M = 1.2$ and $Mn_F = 1312$, $Mn_M = 6.4$). Thus, the resistance to the flow in the major constriction region is reduced. The vorticity contours are affected mostly at the magnetic source region, and the

142

deformations in other parts of the channel are relatively less. Similarly, the profile of the isotherms is greatly affected in the magnetic source region. That is, the temperature in the core of the vortex region due to the magnetic effect decreases as the vortex enlarges towards the upper wall, whereas the temperature increases along the upper plate downstream of the major stenosis with an increase in the magnetic numbers.

As a conclusion, in this chapter, the FEM solution to biomagnetic fluid flow and heat transfer between channels is presented for various physical configurations. Both electrically conducting and nonconducting fluid cases, and also steady and unsteady flow problems are separately considered where the equations are given in terms of stream function, vorticity and temperature. For the steady biomagnetic fluid flow model where the fluid is considered as a poor conductor, the DRBEM application is also introduced. The first applications of both FEM and DRBEM for solving biomagnetic fluid flow in channels, constitute one of the major novelties in this thesis. The obtained results indicate that FEM gives high accuracy for the characteristic flow parameters taken suitable to the real blood properties. The DRBEM results has put forth that the boundary only nature method can be applied to capture the flow behaviors for moderate parameter values at a small expense compared to FEM.

Moreover, the first applications of FEM are presented for the solution of the problem of biomagnetic fluid flow through channels with various stenotic regions. The flow under the effect of the external magnetic field is considered on straight, symmetrically constricted and irregularly multi-stenosed channels.

Two different methodologies are implemented for the computation of the missing vorticity boundary conditions at the lower and upper walls. For the regularly dis-cretized (straight and symmetrically stenosed) regions, a finite difference method based on Taylor series expansion of the stream function using four inner nodes is applied. However, in the cases where the problem region is irregularly discretized, an approach based on FEM is used to compute the vorticity wall conditions which is also a new contribution in handling unknown vorticity wall values. Iterative solution procedure is used in solving the resulting systems of equations in all problems.

The effects of the stenotic regions, intensity of the magnetic field and location of the nodal magnetic source on the flow and heat transfer are examined in details. The numerical results have shown that both the stenosis in the channel and the external magnetic field cause a formation of vortices in different places and various sizes. The vortices extend in both horizontal and vertical directions with an increase in the magnetic field intensity. The temperature values generally remain constant through the vortex regions depending on the boundary condition of the plate which is close to the vortex. The results concerning straight channels and symmetrically stenosed channels show a very good agreement with the available results in the literature. It is seen that the application of the external magnetic field after a severe stenosis region, can be employed to recover the flow pattern distracted due the constriction.

CHAPTER 5

CONCLUSION

In this study, numerical solutions of hydrodynamic and magnetohydrodynamic flow problems are presented. The primary focus is on finite element method application using irregular mesh with quadratic triangular elements, yet Chebyshev spectral collocation method (for flows between parallel plates) and dual reciprocity boundary element method (for biomagnetic fluid flows) implementations are also presented. In particular, the fundamental steps of FEM application to incompressible fluid flow and natural convection flow equations in terms of stream function, vorticity and temperature are given in Chapter 2. Some benchmark problems including lid-driven cavity flow and natural convection flow under a magnetic field in inclined enclosures are solved using FEM. The efficiency of the method is proved through a test problem for which the exact solution is available. The lid-driven cavity flow problem solutions are obtained for laminar flow regimes up to Reynolds number value $Re = 2000$, and furthermore, the numerical solutions are presented for higher Re values as 5000 and 10000 for showing the efficiency of the FEM algorithm and capability of the code prepared in the thesis. Next, FEM solutions of natural convection flow in inclined enclosures in the presence of an oblique magnetic field are presented. The second order derivatives of stream function in the vorticity equation entailed the use of quadratic triangular elements in the discretizations. The influence of the externally applied oblique magnetic field is investigated, and the results for large values of Rayleigh and Hartmann number up to $Ra = 10^6$ and $Ha = 100$ are presented. The increase in Re for the lid-driven cavity flow and the increase in Ra in natural convection flow have common effects. The stagnant regions are developed at the center of the enclosure for the flow, and boundary layers are formed for all unknowns. The results indicated that, it is the external magnetic field which is more powerful controlling the flow behavior than the buoyancy force in natural convection flow.

The Chebyshev spectral collocation method is used especially for solving unidirectional MHD flow and heat transfer problems between parallel plates because of its simplicity in applications. The N-S equations with exact solution, lid-driven square cavity and natural convection flow under a magnetic field problems are also solved, and the results are compared both quantitatively and qualitatively with the FEM results obtained before. The lid-driven cavity flow results are given for Re values up to 1000. For higher values of Re, the number of collocation points needs to be further increased than the one used ($N = 50$), and this

loses the practicality and small cost of the method in terms of computations. The dense structure of collocation matrices for large N, and the discontinuity of the velocity boundary conditions may be the reason for not having convergence for $Re \geq 1000$. The natural convection flow under the effect of an external magnetic field is solved successively by using CSCM. The method is observed to capture the thin boundary layers especially in vorticity contours for high values of problem parameters (Ra and Ha). The flow behavior and temperature distribution in the cavity as well as the magnitudes of the contours of all of the unknowns are shown to be in excellent agreement with the FEM results. Moreover, as a new application of CSCM, the MHD flows with heat transfer are solved between two parallel insulating plates. The fluid is considered as electrically conducting, incompressible and having temperature dependent viscosity. The MHD flow of a dusty fluid is also considered between parallel plates imposing the Navier-slip conditions on velocities of both the fluid and dust particles. The effects of the viscosity parameter, Hartmann number, Navier-slip parameter and thermal conductivity parameter on the flow and heat transfer are investigated. It was shown that the use of CSCM with the unconditionally stable backward difference time integration scheme, provides a high accuracy with a considerably small number of collocation points, and quite large time steps. The ease of implementation and the convenience of CSCM with high order accuracy to especially one-dimensional problems are pronounced.

The FEM solution to biomagnetic fluid flow (blood flow) and heat transfer in channels between (parallel) plates under the effect of a magnetic source is presented for various physical configurations in the last part of the thesis. DRBEM application is also introduced for the steady biomagnetic fluid flow model where the fluid is considered as a poor conductor. FEM analysis is provided for both electrically conducting and nonconducting fluid cases, and also steady and unsteady flow problems. The results indicated that FEM gives high accuracy for the characteristic flow parameters taken suitable to the real blood properties. The DRBEM results have put forth that the boundary only nature of BEM can be applied to capture the flow behaviors for moderate values of the parameters at a small expense compared to FEM. Moreover, FEM applications are presented for the solution of the problem of biomagnetic fluid flow through channels with various stenotic regions for the first time in this thesis. The biomagnetic fluid flow under the effect of the external magnetic field is solved in straight, symmetrically constricted and irregularly-multiply-stenosed channels. Two different methodologies are implemented for the computation of the unknown vorticity boundary conditions at the lower and upper walls. First, the finite difference method based on Taylor series expansion of the stream function using four inner nodes, is applied on regularly discretized straight and symmetrically stenosed channels. Second, an approach based on FEM is used in irregularly discretized regions. The resulting systems of equations in all problems are solved iteratively, and the effects of the stenotic regions, intensity of the magnetic field and location of the magnetic source on the flow and heat transfer are examined. The numerical results have shown that both the stenosis in the channel and the external magnetic field cause a formation of vortices in different places and various sizes. It was observed that the vortices extend in both horizontal and vertical direc-

tions with an increase in the magnetic field intensity. The temperature values generally remain constant through the vortex regions depending on the boundary condition of the plate which is close to the vortex. The results indicated that the application of the external magnetic field after a severe stenosis region, can be employed to recover the flow pattern distracted due the constriction. The FEM solution to biomagnetic fluid flow exposed to an external magnetic source in irregularly-multiply-stenosed channels, constitutes a major new contribution in the thesis.

Further investigations could be concentrated on obtaining solutions for biomagnetic fluid flows in stenosed channels by coupling the FEM and DRBEM numerical procedures. The finite element method is suitable in the stenosed area since it can use very fine mesh, and at the rest of the channel only the boundary can be discretized by using DRBEM since the flow and temperature show almost uniform behavior. Also, for highly conducting fluids, the induced magnetic field inside the fluid must be taken into consideration. Thus, the flow equations are going to be solved together with the induced current equations in coupled form.

REFERENCES

[1] M. Abramowitz and I. A. Stegun, *Handbook of Mathematical Functions*, Dover, New York, 1972.

[2] R. A. Alpher, Heat transfer in magnetohydrodynamic flow between parallel plates, International Journal of Heat and Mass Transfer, 3, pp. 108–112, 1961.

[3] H. A. Attia, Transient MHD flow and heat transfer between two parallel plates with temperature dependent viscosity, Mechanics Research Communications, 26, pp. 115–121, 1999.

[4] H. A. Attia, On the effectiveness of variation in the physical variables on the steady MHD flow between parallel plates with heat transfer, International Journal for Numerical Methods in Engineering, 65, pp. 224–235, 2006.

[5] H. A. Attia, The effect of variable properties on the unsteady Couette flow with heat transfer considering the Hall effect, Communications in Nonlinear Science and Numerical Simulation, 13, pp. 1596–1604, 2008.

[6] H. A. Attia, Unsteady hydromagnetic Couette flow of dusty fluid with temperature dependent viscosity and thermal conductivity, International Journal of Non-Linear Mechanics, 43, pp. 707–715, 2008.

[7] H. A. Attia and N. A. Kotb, MHD flow between two parallel plates with heat transfer, Acta Mechanica, 117, pp. 215–220, 1996.

[8] F. Auteri, L. Quartapelle, and L. Vigevano, Accurate ω-ψ spectral solution of the singular driven cavity problem, Journal of Computational Physics, 180, pp. 597–615, 2002.

[9] E. Barragy and G. F. Carey, Stream function-vorticity driven cavity solution using p finite elements, Computers & Fluids, 26, pp. 435–468, 1997.

[10] R. Bhargava, O. A. Beg, S. Sharma, and J. Zueco, Finite element study of nonlinear two-dimensional deoxygenated biomagnetic micropolar flow, Communications in Nonlinear Science and Numerical Simulation, 15, pp. 1210–1223, 2010.

[11] Y. Bilgen and R. B. Yedder, Natural convection in enclosure with heating and cooling by sinusoidal temperature profiles on one side, International Journal of Heat and Mass Transfer, 50, pp. 139–150, 2007.

[12] J. Blazek, *Computational Fluid Dynamics: Principles and Applications*, ELSEVIER, Philadelphia, 1977.

[13] O. Botella and R. Peyret, Benchmark spectral results on the lid-driven cavity flow, Computers & Fluids, 27, pp. 421–433, 1998.

[14] J. P. Boyd, *Chebyshev and Fourier Spectral Methods*, Dover, New York, 2000.

[15] C. A. Brebbia and J. Dominguez, *Boundary Elements: An Introductory Course*, Computational Mechanics Publications, Southampton, Boston, 1992.

[16] C. A. Brebbia, P. W. Partridge, and L. C. Wrobel, *The Dual Reciprocity Boundary Element Method*, Computational Mechanics Publications, Southampton, Boston, 1992.

[17] O. D. Burggraf, Analytical and numerical studies of the structure of steady separated flows, Journal of Fluid Mechanics, 24, pp. 113–151, 1966.

[18] A. J. Chamkha, Unsteady laminar hydromagnetic fluid-particle flow and heat transfer in channels and circular pipes, International Journal of Heat and Fluid Flow, 21, pp. 740–746, 2000.

[19] A. J. Chamkha, Hydromagnetic combined convection flow in a vertical lid-driven cavity with internal heat generation or absorption, Numerical Heat Transfer, Part A, 41, pp. 529–546, 2002.

[20] T. J. Chung, *Computational Fluid Dynamics*, Cambridge University Press, New York, 2010.

[21] G. Comini, M. Manzan, and C. Nonino, Finite element solution of the stream function-vorticity equations for incompressible two-dimensional flows, International Journal for Numerical Methods in Fluids, 19, pp. 513–525, 1994.

[22] G. De Vahl Davis, Natural convection of air in a square cavity: A bench mark numerical solution, International Journal for Numerical Methods in Fluids, 3, pp. 249–264, 1983.

[23] H. Ding, C. Shu, K. S. Yeo, and D. Xu, Development of least-square-based two-dimensional finite-difference schemes and their application to simulate natural convection in a cavity, Computers & Fluids, 33, pp. 137–154, 2004.

[24] L. Dragos, *Magnetofluid Dynamics*, Abacus Press: Tunbridge Wells, Kent, 1975.

[25] M. C. Ece and E. Büyük, Natural convection flow under a magnetic field in an inclined square enclosure differentialy heated on adjacent walls, Meccanica, 42, pp. 435–449, 2007.

[26] P. Eguía, J. Zueco, E. Granada, and D. Patiño, NSM solution for unsteady MHD Couette flow of a dusty conducting fluid with variable viscosity and electric conductivity, Applied Mathematical Modelling, 35, pp. 303–316, 2011.

[27] E. Erturk, T. C. Corke, and C. Gökçöl, Numerical solutions of 2-D steady incompressible driven cavity flow at high Reynolds numbers, International Journal for Numerical Methods in Fluids, 48, pp. 747–774, 2005.

[28] G. Evans, J. Blackledge, and P. Yardley, *Numerical Methods for Partial Differential Equations*, Springer, Great Britain, 1999.

[29] R. Ganguly, A. P. Gaind, S. Sen, and I. K. Puri, Analyzing ferrofluid transport for magnetic drug targeting, Journal of Magnetism and Magnetic Materials, 289, pp. 331–334, 2005.

[30] J. P. Garandet, T. Alboussiere, and R. Moreau, Buoyancy driven convection in a rectangular enclosure with a transverse magnetic field, International Journal of Heat and Mass Transfer, 35, pp. 741–748, 1992.

[31] M. Gay and L. T. Zhang, Numerical studies of blood flow in healthy, stenosed, and stented carotid arteries, International Journal for Numerical Methods in Fluids, 61, pp. 453–472, 2009.

[32] U. Ghia, N. Ghia, and C. T. Shin, High-Re solutions for incompressible flow using the Navier-Stokes equations and a multigrid method, Journal of Computational Physics, 48, pp. 387–411, 1982.

[33] D. Gottlieb and S. A. Orszag, *Numerical analysis of spectral methods: Theory and Applications*, SIAM, Philadelphia, 1977.

[34] F. M. Hady, R. A. Mohamed, and A. Mahdy, MHD free convection flow along a vertical wavy surface with heat generation or absorption effect, International Communications in Heat and Mass Transfer, 33, pp. 1253–1263, 2006.

[35] Y. Haik, V. Pai, and C. J. Chen, Development of magnetic device for cell separation, Journal of Magnetism and Magnetic Materials, 194, pp. 254–261, 1999.

[36] Y. Haik, V. Pai, and C. J. Chen, Apparent viscosity of human blood in a high static magnetic field, Journal of Magnetism and Magnetic Materials, 225, pp. 180–186, 2001.

[37] T. Hayat, Z. Abbas, M. Sajid, and S. Asghar, The influence of thermal radiation on MHD flow of a second grade fluid, International Journal of Heat and Mass Transfer, 50, pp. 931–941, 2007.

[38] T. Hayat and M. Qasim, Influence of thermal radiation and joule heating on MHD flow of a Maxwell fluid in the presence of thermophoresis, International Journal of Heat and Mass Transfer, 53, pp. 4780–4788, 2010.

[39] M. A. Ikbal, Viscoelastic blood flow through arterial stenosis-effect of variable viscosity, International Journal of Non-Linear Mechanics, 47, pp. 888–894, 2012.

[40] S. C. Kakarantzas, I. E. Sarris, A. P. Grecos, and N. S. Vlachos, Magnetohydrodynamic natural convection in a vertical cylindrical cavity with sinusoidal upper wall temperature, International Journal of Heat and Mass Transfer, 52, pp. 250–259, 2009.

[41] C. Karcher, Y. Kolesnikov, O. Andreev, and A. Thess, Natural convection in a liquid metal heated from above and influenced by a magnetic field, European Journal of Mechanics - B/Fluids, 21, pp. 75–90, 2002.

[42] S. Kenjeres, Numerical analysis of blood flow in realistic arteries subjected to strong non-uniform magnetic fields, International Journal of Heat and Fluid Flow, 29, pp. 752–764, 2008.

[43] S. A. Krashan and Y. Haik, Numerical simulation of biomagnetic fluid downstream an eccentric stenotic orifice, Physics of Fluids, 18, pp. 113601–1–113601–10, 2006.

[44] J. Li and H. Huang, Effect of magnetic field on blood flow and heat transfer through a stenosed artery, in *Proceedings of the 3rd Conference on Biomedical Engineering and Informatics*, pp. 2028–2032, 2010.

[45] J. A. Lima, J. N. N. Quaresma, and E. N. Macedo, Integral transform analysis of MHD flow and heat transfer in parallel-plates channels, International Communications in Heat and Mass Transfer, 34, pp. 420–431, 2007.

[46] D. C. Lo, D. L. Young, and C. C. Tsai, High resolution of 2D natural convection in a cavity by the DQ method, Journal of Computational and Applied Mathematics, 203, pp. 219–236, 2007.

[47] V. C. Loukopoulos and E. E. Tzirtzilakis, Biomagnetic channel flow in spatially varying magnetic field, International Journal of Engineering Science, 42, pp. 571–590, 2004.

[48] S. Mahmud and R. A. Fraser, Magnetohydrodynamic free convection and entropy generation in a square porous cavity, International Journal of Heat and Mass Transfer, 47, pp. 3245–3256, 2004.

[49] T. K. Maikap, T. R. Mahapatra, P. Niyogi, and A. K. Ghosh, Numerical study of magnetohydrodynamic laminar flow separation in a channel with smooth expansion, International Journal for Numerical Methods in Fluids, 59, pp. 495–518, 2009.

[50] O. D. Makinde and T. Chinyoka, MHD transient flows and heat transfer of dusty fluid in a channel with variable physical properties and Navier slip condition, Computers and Mathematics with Applications, 60, pp. 660–669, 2010.

[51] M. T. Matthews and J. M. Hill, Newtonian flow with nonlinear Navier boundary condition, Acta Mechanica, 191, pp. 195–217, 2007.

[52] A. R. Mitchell and R. Wait, *The Finite Element Method in Partial Differential Equations*, John-Wiley & Sons, 1978.

152

[53] P. Neofytou and D. Drikakis, Effects of blood models on flows through a stenosis, International Journal for Numerical Methods in Fluids, 43, pp. 597–635, 2003.

[54] R. S. Newbower, Magnetic fluids in the blood, Magnetics, IEEE Transactions, 9, pp. 447–450, 1973.

[55] S. D. Nigam and S. N. Singh, Heat transfer by laminar flow between parallel plates under the action of transverse magnetic field, Quarterly Journal of Mechanics and Applied Mathematics, 13, pp. 85–97, 1960.

[56] H. F. Oztop, M. Oztop, and Y. Varol, Numerical simulation of magneto-hydrodynamic buoyancy-induced flow in a non-isothermally heated square enclosure, Communications in Nonlinear Science and Numerical Simulation, 14, pp. 770–778, 2009.

[57] C. Pozrikidis, *Introduction to Finite and Spectral Element Methods using MATLAB*, Chapman and Hall/CRC, Boca Raton, 2005.

[58] J. Rasoul and P. Prinos, Natural convection in an inclined enclosure, International Journal of Numerical Methods for Heat and Fluid Flow, 7, pp. 438–478, 1997.

[59] J. N. Reddy, *An introduction to the finite element method*, The McGraw-Hill Companies, New York, 2006.

[60] R. E. Rosensweig, Magnetic fluids, Annual Review of Fluid Mechanics, 19, pp. 437–461, 1987.

[61] S. Roy and T. Basak, Finite element analysis of natural convection flows in a square cavity with non-uniformly heated wall(s), International Journal of Engineering Science, 43, pp. 668–680, 2005.

[62] N. Rudraiah, R. M. Barron, M. Venkatachalappa, and C. K. Subbaraya, Effect of a magnetic field on free convection in a rectangular enclosure, International Journal of Engineering Science, 33, pp. 1075–1084, 1995.

[63] N. Rusli, A. K. B. Hong, E. H. Kasiman, A. Yassin, and N. Amin, Numerical computation of a two-dimensional biomagnetic channel flow, International Journal of Modern Physics, 9, pp. 178–192, 2012.

[64] M. Sahin and R. G. Owens, A novel fully implicit fnite volume method applied to the lid-driven cavity problem-part i: High reynolds number flow calculations, Journal for Numerical Methods in Fluids, 42, pp. 57–77, 2003.

[65] I. Saidu, M. W. Yusuf, I. J. Uwanta, and A. Iguda, MHD effects on convective flow of dusty viscous fluid with fraction in a porous medium, Australian Journal of Basic and Applied Sciences, 4, pp. 6094–6105, 2010.

[66] I. E. Sarris, G. K. Zikos, A. P. Grecos, and N. S. Vlachos, On the limits of validity of the low magnetic reynolds number approximation in MHD natural-convection heat transfer, Numerical Heat Transfer, Part B, 50, pp. 157–180, 2006.

[67] M. Sathiyamoorthy and A. Chamkha, Effect of magnetic field on natural convection flow in a liquid gallium filled square cavity for linearly heated side wall(s), International Journal of Thermal Sciences, 49, pp. 1856–1865, 2010.

[68] K. K. Singh, Unsteady flow of a conducting dusty fluid through a rectangular channel with time dependent pressure gradient, Indian Journal of Pure and Applied Mathematics, 8, pp. 1124–1131, 1976.

[69] W. F. Spotz and G. F. Carey, High-order compact scheme for the steady stream function-vorticity equations, International Journal for Numerical Methods in Engineering, 38, pp. 3497–3512, 1995.

[70] P. Sreeharireddy, A. S. Nagarajan, and M. Sivaiah, MHD flow of a dusty viscous conducting liquid between two parallel plates, Journal of Scientific Research, 1, pp. 220–225, 2009.

[71] E. Sweet, K. Vajravelu, R. A. Van Gorder, and I. Pop, Analytical solution for the unsteady MHD flow of a viscous fluid between moving parallel plates, Communications in Nonlinear Science and Numerical Simulation, 16, pp. 266–273, 2011.

[72] L. N. Trefethen, *Spectral Methods in Matlab*, Siam, Philadelphia, 2000.

[73] K. Tzirakis, Y. Papaharilaou, D. Giordano, and J. Ekaterinaris, Numerical investigation of biomagnetic fluids in circular ducts, International Journal for Numerical Methods in Biomedical Engineering, 2013.

[74] E. E. Tzirtzilakis, A mathematical model for blood flow in magnetic field, Physics of Fluids, 17, pp. 077103–1–077103–15, 2005.

[75] E. E. Tzirtzilakis, Biomagnetic fluid flow in a channel with stenosis, Physica D, 237, pp. 66–81, 2008.

[76] E. E. Tzirtzilakis, A simple numerical methodology for BFD problems using stream function vorticity formulation, Communications in Numerical Methods in Engineering, 24, pp. 683–700, 2008.

[77] E. E. Tzirtzilakis and M. A. Xenos, Biomagnetic fluid flow in a driven cavity, Meccanica, 48, pp. 187–200, 2013.

[78] P. A. Voltairas, D. I. Fotiadis, and L. K. Michalis, Hydrodynamics of magnetic drug targeting, Journal of Biomechanics, 35, pp. 813–821, 2002.

CURRICULUM VITAE

PERSONAL INFORMATION

Surname, Name: Türk, Önder
Nationality: Turkish
Date and Place of Birth: July 29, Antakya
Marital Status: Single
Phone: +903122105610
Fax: +903122102985

EDUCATION

Degree	Institution	Year of Graduation
M.S.	Institute of Applied Mathematics, METU	2008
B.S.	Department of Mathematics, METU	2001
High School	Antakya Merkez 23 Temmuz L.	1996

PROFESSIONAL EXPERIENCE

Year	Place	Enrollment
2008-2013	Institute of Applied Mathematics, METU	Research Assistant

PUBLICATIONS

Journal Publications

1. Önder Türk, Canan Bozkaya and Münevver Tezer-Sezgin, A FEM approach to biomagnetic fluid flow in irregularly and multiple stenosed channels, Computers & Fluids, 2013, in review.

2. Önder Türk, Münevver Tezer-Sezgin and Canan Bozkaya, Finite Element Study of Biomagnetic Fluid Flow in a Symmetrically Stenosed Channel, Journal of Computational and Applied Mathematics, 259, pp. 760-770, 2014.

3. Münevver Tezer-Sezgin, Canan Bozkaya and Önder Türk, BEM and FEM based Numerical Simulations for Biomagnetic Fluid Flow, Engineering Analysis with Boundary Elements, 37, pp. 1127-1135, 2013.

4. Önder Türk, Münevver Tezer-Sezgin, Chebyshev Spectral Collocation Method for Unsteady Mhd Flow and Heat Transfer of a Dusty Fluid Between Parallel Plates, Numerical Heat Transfer, Part A: Applications, 64, pp. 597-610, 2013.

5. Önder Türk, Münevver Tezer-Sezgin, FEM solution of natural convection flow in square enclosures under magnetic field, International Journal of Numerical Methods for Heat & Fluid Flow, 23, pp. 844-866, 2013.

Abstracts in International Conferences

1. Önder Türk, M. Tezer-Sezgin, Canan Bozkaya, "Biofluid flow in a channel with stenosis", International Conference on Applied and Computational Mathematics (ICACM), Ankara, Turkey, September 3-6, 2012.

2. Önder Türk, M. Tezer-Sezgin, Canan Bozkaya, "Biomagnetic Fluid Flow Between Parallel Plates in the Presence of Magnetic Field ", BIOCOMP-2012, Mathematical Modeling and Computational Topics in Biosciences, Vietri sul Mare, June 4-8, 2012.

3. M. Tezer-Sezgin, Önder Türk, Canan Bozkaya,"FEM Solution to Unsteady Biomagnetic Fluid Flow in a Channel ", BIOCOMP-2012, Mathematical Modeling and Computational Topics in Biosciences, Vietri sul Mare, June 4-8, 2012.

4. Canan Bozkaya, Önder Türk, M.Tezer-Sezgin, "A Numerical Solution to Biomagnetic Channel Flow with DRBEM ", BIOCOMP-2012, Mathematical Modeling and Computational Topics in Biosciences, Vietri sul Mare, June 4-8, 2012.

5. Önder Türk, M. Tezer-Sezgin, "FEM Solution of Natural Convection Flow in the Presence of Magnetic Field ", Inter. School on MHD and Fusion Applic. (ISMFA 2011), Marmaris, Turunç, Turkey, September 9-16, 2011.

6. Önder Türk, "Chebyshev spectral collocation method for unsteady MHD flow and heat transfer between parallel plates ", 24th Biennial Conf. on Numerical Analy. (NACONF 2011), Glasgow, UK, June 28-July 1, 2011.

7. M. Tezer-Sezgin, Önder Türk, "MHD Flow and Heat Transfer Between Parallel Plates with Navier-Slip Wall Condition ", 24th Biennial Conf. on Numerical Analy. (NACONF 2011), Glasgow, UK, June 28-July 1, 2011.

8. Önder Türk, M. Tezer-Sezgin, "Chebyshev Spectral Method Solution of Natural Convection Flow under Magnetic Field ", 7th.Inter. Cong. on Indust. and Appl. Math.(ICIAM 2011), Vancouver, B.C., Canada, July 18-22, 2011.

9. Önder Türk, "FEM Solution of Natural Convection Flow Under a Magnetic Field ", International Congress on Computational and Applied Mathematics, (ICCAM 2010), Leuven, Belgium, July 5-9, 2010.

10. Önder Türk, M.Tezer-Sezgin, "FEM Solution of Diffusion-Convection-Reaction Equations in Air Pollution ", ENUMATH 2009, 8-th European Conference on Numerical Mathematics and Advanced Applications, Uppsala, Sweden, July 3-5, 2009.

Projects

1. TÜBITAK (Scientific and Technical Research Council of Turkey), Daralma gösteren damar boyunca akan biyomanyetik akışkan modelinin sonlu ve sınır elemanları yöntemleri ile çözümü, 111T269, Researcher, November, 2011 - November, 2013.

2. METU BAP, İçinde parçacıklar bulunduran sıvıların zamana bağımlı magnetohidrodinamik akışı ve ısı transferi, BAP-07-05-2011-101, Researcher, January, 2011 - December, 2011.

3. METU BAP, Numerical solution of liquid metal magnetohydrodynamics (MHD) flow with heat transfer, BAP-07-05-2010-00-01, Researcher, January, 2010 - December, 2010.